# Natural and anthropogenic fluid migration pathways in marine sediments

Dissertation

zur Erlangung des Doktorgrades

der Mathematisch-Naturwissenschaftlichen Fakultät

der Christian-Albrechts-Universität zu Kiel

vorgelegt von

Christoph Böttner

Kiel, 2019

Erster Gutachter: Prof. Dr. Christian Berndt

Zweiter Gutachter: Prof. Dr. Gerhard Bohrmann

Tag der mündlichen Prüfung: 07.02.2020

Zum Druck genehmigt am: ……………………

………………………….
Der Dekan

## Erklärung

Hiermit erkläre ich, dass die vorliegende Doktorarbeit selbständig, abgesehen von der Beratung durch die Betreuer, und ohne Zuhilfenahme unerlaubter Hilfsmittel erstellt habe. Weder diese Arbeit noch eine ähnliche Arbeit wurde im Rahmen eines Prüfungsverfahrens veröffentlicht und oder zur Veröffentlichung vorgelegt. Ferner versichere ich, dass die Arbeit unter Einhaltung der Regeln guter wissenschaftlicher Praxis der Deutschen Forschungsgemeinschaft angefertigt wurde. Des Weiteren wurde mir kein akademischer Grad entzogen.

Kiel, den 03.12.2019

Christoph Böttner

# Abstract

Fluids are an important agent in nearly all geologic processes that shape the planet Earth. Fluid abundance and composition are governed by flow along permeable beds or natural and anthropogenic structures in the subsurface including faults, wells, and chimneys/pipes. Spatial and temporal variations in fluid flow activity modify total fluxes between geosphere, cryosphere, hydrosphere, and atmosphere. These fluxes have broad implications for geological processes including the formation of natural resources or the occurrence of geohazards including landslides, earthquakes and blowouts. They further play a crucial role for the global carbon cycles and the climate system. A qualitative and quantitative understanding of fluid flow in the subsurface is therefore important to assess the role of fluids in the Earth system and to quantify fluxes from the geosphere into the hydro- and atmosphere. In this Ph.D. thesis I use an integrated, interdisciplinary approach to study natural and anthropogenic fluid migration pathways in marine sediments in the North Sea, the convergent Hikurangi margin, and a section of the ancient Tethys margin which is now exposed near Varna, Bulgaria. The applied methods include conventional 3D seismic, high-resolution 3D seismic, and 2D seismic data as well as hydroacoustic, sedimentological, unmanned aerial vehicle-based photogrammetric and geochemical data. In each of the studied systems, natural and/or anthropogenic fluid migration pathways allow the transport of significant amounts of fluids through marine sediments towards the seafloor. Often the co-existence of multiple pathways enables the fluids to bypass permeability barriers within the Earth’s crust resulting in the formation of structurally complex flow systems. Focused fluid flow along normal faults in the Hikurangi margin likely plays an active role in the subduction drainage system, influences the slope stability and the morphotectonic evolution of the margin. Results from the Eocene Tethys margin show that focused fluid flow in marine sediments is possible in unconsolidated sands if seepage is focused at the top of faulted units and the flux rate is high enough. This stands in contrast to the general assumption that focused fluid flow in marine sediments is limited to low-permeable sediments. In the marine environment the term fluid flow is often used to exclusively refer to the flow of hydrocarbons. However, geochemical data from the North Sea and the Tethys margin indicate that the involved fluids are of different origin including compaction-related dehydration and submarine groundwater discharge. In each of the investigated cases, the temporal and spatial evolution of fluid flow is not fully addressed yet, especially with regard to vertical fluid conduits or the safety of subsurface drilling and storage operations. The results of my thesis highlight that the investigation of fluid migration pathways requires an interdisciplinary approach which may indicate the origin of the fluids, help understand the fluxes of fluids from the geosphere into the hydrosphere and atmosphere of the past, present and future and reveal the resulting consequences for the global carbon cycles and the climate system.

## Zusammenfassung

Fluide sind ein wichtiger Bestandteil fast aller geologischen Prozesse, die den Planeten Erde prägen. Die Fluidfülle und -zusammensetzung werden durch Fluidflüsse entlang permeabler Schichten oder natürlicher und anthropogener Strukturen im Untergrund bestimmt, einschließlich Störungen, Bohrlöchern und fokussierten Fluidstrukturen. Räumliche und zeitliche Variationen der Fluidströmungsaktivität verändern die Gesamtflüsse zwischen Geosphäre, Kryosphäre, Hydrosphäre und Atmosphäre. Diese Fluidflüsse haben weitreichende Auswirkungen auf geologische Prozesse, einschließlich der Bildung natürlicher Ressourcen oder des Auftretens von Georisiken wie Erdrutschen, Erdbeben und Blowouts. Sie spielen zudem eine entscheidende Rolle für die globalen Kohlenstoffkreisläufe und das Klimasystem. Ein qualitatives und quantitatives Verständnis der Fluidströmung im Untergrund ist daher wichtig, um die Rolle von Fluiden im Erdsystem zu beurteilen und Flüsse aus der Geosphäre in die Hydro- und Atmosphäre zu quantifizieren. In dieser Doktorarbeit verwende ich einen integrierten, interdisziplinären Ansatz, um natürliche und anthropogene Fluidmigrationswege in marinen Sedimenten in der Nordsee, den konvergenten Hikurangi-Kontinentalrand und einen Abschnitt des alten Tethys-Kontinentalrands zu untersuchen, der heute in der Nähe von Varna, Bulgarien, exponiert ist. Zu den angewandten Methoden gehören konventionelle 3D-Seismik, hochauflösende 3D-Seismik und 2D-Seismik sowie hydroakustische, sedimentologische, drohnenbasierte photogrammetrische und geochemische Daten. In jedem der untersuchten Systeme ermöglichen natürliche und/oder anthropogene Fluidmigrationswege den Transport bedeutender Fluidmengen durch marine Sedimente in Richtung Meeresboden. Häufig ermöglicht die Koexistenz mehrerer Migrationswege, dass Fluide Permeabilitätsbarrieren innerhalb der Erdkruste umgehen, was zur Bildung strukturell komplexer Fluidsysteme führen kann. Ein fokussierter Fluidstrom entlang von Abschiebungen im Hikurangi-Kontinentalrand spielt wahrscheinlich eine aktive Rolle in der Entwässerung der Subduktionszone, beeinflusst die Hangstabilität und die morphotektonische Entwicklung der Subduktionszone. Die Ergebnisse aus dem Tethys Kontinentalrand im Eozän zeigen, dass ein fokussierter Fluidstrom in marinen Sedimenten in unverfestigten Sanden möglich ist, wenn der Gasaustritt an der Obergrenze frakturierter Einheiten fokussiert ist und die entsprechende Flussrate hoch genug ist. Dies steht im Gegensatz zu der allgemeinen Annahme, dass sich fokussierte Fluidströmungen in marinen Sedimenten auf niedrigpermeable Sedimente beschränken. In der marinen Umwelt wird der Begriff Fluidströmung oft verwendet, um sich ausschließlich auf den Fluss von Kohlenwasserstoffen zu beziehen. Geochemische Daten aus der Nordsee und dem Kontinentalrand der Tethys deuten jedoch darauf hin, dass die beteiligten Fluide unterschiedlichen Ursprungs sein können, einschließlich kompaktionsbedingter Dehydrierung und submarinem Grundwasserausfluss. Die zeitliche und räumliche Entwicklung dieser Fluidströmungssysteme ist jedoch noch nicht ausreichend untersucht, insbesondere im Hinblick auf fokussierte Fluidstrukturen oder die Sicherheit von unterirdischen Bohr- und Speichervorhaben. Die Ergebnisse meiner Dissertation zeigen, dass die Untersuchung von Fluidmigrationswegen einen interdisziplinären Ansatz erfordert, der die Herkunft der Fluide anzeigen kann, hilft, die Flüsse von Fluiden aus der Geo- in die Hydro- und Atmosphäre der Vergangenheit, Gegenwart und Zukunft zu verstehen und die daraus resultierenden Folgen für die globalen Kohlenstoffkreisläufe und das Klimasystem aufzuzeigen.

# Table of Content

# 1. Introduction

Guanziling hot spring, which is enriched in methane that ignites immediately, southern Taiwan (J. Karstens).

## 1.1. Motivation

Fluids play a crucial role for many geologic processes in the Earth system. The formation of natural resources such as water or hydrocarbons, the occurrence of geohazards including landslides and earthquakes, or the seabed ecology are just some examples that are largely governed by the abundance and composition of the available fluids. Spatial and temporal variations in fluid flow activity modify total fluxes between geosphere, cryosphere, hydrosphere, and atmosphere with wide implications for the global carbon cycle and the climate system. Greenhouse gas emissions from marine sediments directly influence global warming, which will be one of the grand challenges for the next decades to centuries (Ciais et al., 2013; Saunois et al., 2016, IPCC, 2018). In 2007, the Intergovernmental Panel on Climate Change (IPCC) has therefore acknowledged geological fluxes of greenhouse gases as an important source and added oceanic and land-based emissions to their inventory (Denman et al, 2007; Etiope et al., 2008; Ciais et al., 2013; Saunois et al., 2016). However, especially in the marine environment, a qualitative and quantitative understanding of fluid flow in the subsurface and the release of fluid into the hydrosphere and atmosphere is challenged by the inaccessibility of offshore regions and associated difficulties in monitoring over sufficient spatial and temporal scales. This results in large uncertainties in quantifying and attributing emissions from marine natural geological sources.

In the marine environment, fluids are transported by either diffusive or focused flow through the Earth’s crust. Structures that support focused fluid flow include natural features such as faults or fracture networks and anthropogenic features such as hydrocarbon wells or other subsurface operations. Millions of hydrocarbon wells and other subsurface operations penetrate through marine sediments. Where fluid accumulations exist in the subsurface, drilling may become life threatening (e.g. North Sea blowout 22/4B, 1990, Leifer & Judd, 2015), but may also form effective fluid migration pathways through the overburden (Gurevich et al., 1993). Although the interpretation of seismic chimneys and pipes as vertical fluid conduits is well-established, very little is known about their internal architecture, nature and hydraulic parameters, especially their permeability (Karstens et al., 2017). The permeability of faults and fractures is an important controlling factor for the temporal and spatial variability of seafloor seepage (Talukder, 2012). In active continental margins, tectonic deformation and subduction-related processes such as compaction and dehydration result in a complex hydrological regime (Saffer & Tobin, 2011). Often, the role of upper-plate faulting for the hydrodynamic and tectonic evolution of the forearc is poorly understood.

In the present and future world, a good understanding of fluid migration through marine sediments may become crucial with respect to two societal challenges. First, the possible storage of large amounts of $CO_2$ in marine saline aquifers is considered a key mitigation strategy to reduce CO2 concentrations in the atmosphere (Metz et al., 2005; IPCC, 2018). Good knowledge on natural fluid flow in theses settings is required to identify potential leakage pathways from $CO_2$ storage reservoirs through the overburden and towards the seafloor.

Second, with the exacerbation of effects of climate change, water becomes a more important resource in many places around the world. In 2019, water shortages already threaten major coastal cities around the globe (Taniguchi et al., 2002; Cohen et al., 2010; Post et al., 2013; Berndt & Micallef, 2019). However, very little is understood with respect to flow and discharge of submarine groundwater and potential sustainable usage of the offshore resources.

### 1.1.1. Earth climate and global warming

Global warming and climate change have been in the focus of scientific research over the last decades. Due to the grand challenge that climate global warming represents for the society, the climate science community has organized itself since 1988 as the Intergovernmental Panel on Climate Change (IPCC). The main aim of the IPCC is to provide a scientific basis for climate change, investigate the correlation between anthropogenic greenhouse gas emissions and global warming, but also to recommend mitigation strategies for the consequences of climate change to society, stakeholders, as well as policy and decision makers.

Earth climate has experienced continuous change throughout the last 65 million years and beyond which is documented in the geologic record for example by variations in oxygen ($\delta^{18}O$) and carbon ($\delta^{13}C$) isotopes of deep-sea sediments (Zachos, 2001). Natural factors such as the change in eccentricity, obliquity and precession of the Earth’s orbital geometry determine the amount and incident of solar radiation reaching the Earth’s surface. Plate tectonics and the perpetual motion of the Earth’s surface control the total area and global distribution of landmasses and volcanism (Zachos, 2001). Removing these natural factors from the temperature trend of the last thousand years reveals a correlation between anthropogenic greenhouse gas emissions and the pronounced global warming of the 20th century (Crowley, 2000). The radiative properties of the atmosphere are heavily influenced by the concentrations of greenhouse gases. Carbon dioxide, methane and nitrous oxide, are the main greenhouse gases. Their concentration in the atmosphere has significantly increased since the beginning of the Industrial era (pre-industrial defined as the beginning of the year 1750), primarily due to anthropogenic emissions (Figure 1.1; Ciais et al., 2013). In 2018, the annual global average carbon dioxide concentration in the Earth’s atmosphere was 407.4 ± 0.1 parts per million (ppm), which is, based on ice core data, higher than at any point in the last 800,000 years (Blunden & Arndt, 2018).

The rising concentrations of greenhouse gases since pre-industrial times correlate with an increase in global mean surface temperature. The decade 2006–2015 was 0.87°C warmer than the average over the 1850–1900 period (IPCC, 2018). The estimated anthropogenic global warming is currently increasing at 0.2°C per decade due to past and ongoing greenhouse gas emissions (IPCC, 2018). Global warming occurs generally faster over land than over the ocean and may reach extremes in land regions and seasons, i.e. in the Arctic, where warming is two to three times faster than the global annual average (IPCC, 2018). The current global warming manifests itself in an increase of temperature extremes, droughts and precipitation deficits, heavy precipitation, partial melting of the Greenland and Antarctic ice sheets (IPCC, 2018). For many human and ecological systems, the sea level rise of up to 0.77 m by 2100 amplifies the exposure of small islands, low-lying coastal areas and deltas to risks such as saltwater intrusions, flooding, and damage to infrastructure (IPCC, 2018).

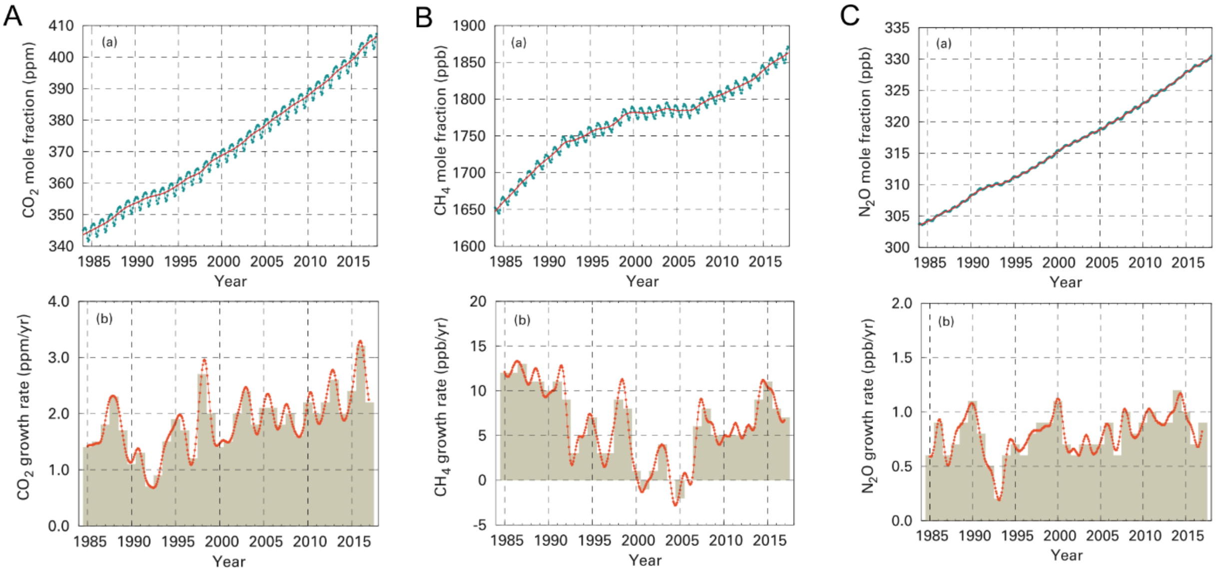

**Figure 1.1**. Globally averaged mole fractions and its growth rate from 1984 to 2017 for (**A**) carbon dioxide, (**B**) methane, and (**C**) nitrous oxide (modified after WMO, 2018).

The best analogue for present-day global warming is the massive release of light hydrocarbons and rising methane concentrations in the atmosphere during the Paleocene-Eocene thermal maximum (PETM), which correlated with a rise in the global temperature (Zachos, 2001). Though contentious, the sudden release of light hydrocarbons may be explained by the release of methane from gas hydrates, pore water venting, turbidite oxidation, or metamorphism of marine sediments due to volcanic intrusions (Zachos, 2001; Higgins & Schraag, 2006; Dickens, 2011).

Mitigation pathways to limit global warming to 1.5°C and reaching net zero $CO_2$ emissions include the reduction of non-$CO_2$ greenhouse gas emission, primarily methane (e.g. 50% from the oil and gas industry; IEA, 2019), energy demand reductions, decarbonization of electricity and other fuels, electrification of energy end use, deep reductions in agricultural emissions, and some form of carbon dioxide removal with carbon storage on land or sequestration in geological reservoirs (IPCC, 2018). Carbon dioxide removal via carbon dioxide capture and storage (CCS) is a key mitigation technology that includes the separation of $CO_2$ from industrial and energy-related sources, transport to a storage location and long-term isolation from the atmosphere (e.g. Metz et al., 2005). Though CCS is not the solution to reduce $CO_2$ concentration in the atmosphere to tolerable amounts, the technology may provide time for the development and implementation of sustainable energy sources.

### 1.1.2. Methane – the most common greenhouse gas in marine sediments

The global methane ($CH_4$) budget remains poorly constrained both in terms of understanding the source and the quantity of methane emissions. Atmospheric inversion models (top-down approaches) describe the quantification of atmospheric methane concentrations and subsequent attribution to the various sources and sinks (IPCC: Ciais et al., 2013). Process-based models (bottom-up estimates) rely on quantification of individual processes and subsequent calculations of atmospheric methane concentrations (IPCC: Ciais et al., 2013). Top-down approaches of global emissions for the decade 2003-2012 estimate 540-568 Tg ($CH_4$) $yr^{-1}$ while bottom-up approaches predict 596-884 Tg ($CH_4$) $yr^{-1}$ (Saunois et al., 2016). The large discrepancies between top-down and bottom-up estimates of global sources and sinks highlight the lack of good constraints. Since 2014, the atmospheric concentrations of methane increased at nearly double the rate observed in 2007 while the causes remain subject of scientific debate (Fletcher & Schaefer, 2019).

Anthropogenic methane sources (340–360 Tg ($CH_4$) $yr^{-1}$; Saunois et al., 2016) contributed approximately half of the total methane emissions in the decade 2003-2012. The anthropogenic emissions include agriculture and waste (178–206 Tg ($CH_4$) $yr^{-1}$), fossil fuels (114–133 Tg ($CH_4$) $yr^{-}1$) as well as biomass and biofuel burning (27–35 Tg ($CH_4$) $yr^{-1}$). The impact of anthropogenic methane emissions on climate change is receiving ever-increasing attention (Saunois et al., 2016) as societies attempt to make the energy transition from coal to natural gas and further on to renewables.

Natural methane sources, which contribute 194–296 Tg ($CH_4$) $yr^{-1}$ to the global emissions (Saunois et al., 2016), are mainly attributed to natural wetlands (153–227 Tg ($CH_4$) $yr^{-1}$). Other terrestrial emissions, which come from fresh water, wild animals, termites, wildfires, permafrost, vegetation and geological processes, contribute a further 104–297 Tg ($CH_4$) $yr^{-1}$ to the budget (Saunois et al., 2016). Little is known about the oceanic sources, which are believed to contribute 5–25 Tg ($CH_4$) $yr^{-1}$ (Saunois et al., 2016). The oceanic sources, which are only estimated by bottom-up approaches, are categorized into two very general groups: (1) geological and (2) others, e.g. hydrates (Saunois et al., 2016). In the following, I will present different approaches to estimate the contribution of marine methane release to the global methane budget, which thus represent bottom-up estimates.

Methane is the most common gas in marine sediments and appears in the form of free gas, gas hydrates or dissolved in porewater. Methane found in marine sediments may be biogenic, derived from microbial degradation of organic matter, or thermogenic, generated in deep hydrocarbon reservoirs by thermal cracking of kerogens (Whiticar, 2000). The carbon and hydrogen isotope signatures and the relative proportions of methane and more mature hydrocarbons (e.g. ethane, propane, butane) can help distinguish between the two sources (Whiticar, 2000). Large amounts of methane in marine sediments are stored in gas hydrates, ice-like clathrates that are stable under high pressure and low temperatures (Kvenvolden, 1988). Estimates of the global gas hydrate inventory are poorly constrained and range from 3 to 4,000,000 Gt of carbon (Kvenvolden, 1988; Kvenvolden, 1993; Milkov, 2004; Burwicz et al., 2011; Piñero et al., 2013). Realistic estimates of natural oceanic methane emissions require a profound understanding of fluid flow systems, including spatial and temporal variations, internal architecture and preferential migration pathways through the overburden to constrain the contribution of natural greenhouse gas sources from the offshore environment (Etiope et al., 2008; Talukder, 2012, Landrø et al., 2019).

The understanding of natural migration pathways of methane and their hydraulic parameters (i.e. porosity and permeability) becomes important in another societal context. The geological storage of carbon dioxide in marine saline aquifers is considered a key technology (carbon dioxide capture and storage – CCS) to mitigate anthropogenic emissions of greenhouse gases into the atmosphere. Due to the lack of natural systems, where gas-phase carbon dioxide migrates through clastic sediments, the migration of methane through marine sediments is used to gain understanding about subsurface carbon dioxide migration (e.g. Grimstad et al., 2009; Landrø et al., 2019; Marín-Moreno et al., 2019). Both, methane and carbon dioxide are trapped in water-filled sediments by capillary interfaces. However, there are some differences in the behavior of these gases in the subsurface. In the gas-phase, at depths less than 500 m, carbon dioxide is 3 to 4 times denser than methane. At depths greater than 500 m, carbon dioxide is 10 to 14 times denser as it enters the liquid and dense phases. At 500 m depth, the gas-phase of methane is 2.5 times more buoyant than carbon dioxide (Naylor et al., 2011; Landrø et al., 2019). In addition, methane is 100 times less soluble in water than carbon dioxide. This marked difference in solubility will lead to greater losses of carbon dioxide gas due to dissolution along migration pathways (Cevatoglu et al., 2015). Despite these differences, the migration of methane is still considered a reasonable analogue for the migration of carbon dioxide in shallow sediments (i.e. less than 1000 m; Landrø et al., 2019).

### 1.1.3. Carbon dioxide capture and storage (CCS)

CCS is considered a key technology for reducing anthropogenic emissions of carbon dioxide ($CO_2$) into the atmosphere and for limiting global warming to 2° C above pre-industrial levels (IPCC, 2018). The aim is to capture $CO_2$ from large single sources (combustion sites) such as fossil fuel power plants, oil and gas production and other high-emitting industries (e.g. steel, cement, fertilizer) and then transport and store it safely in suitable geological formations. To reach the 2°C Paris climate target by 2060, about 14% of the cumulative emissions reductions must derive from CCS (Global CCS Institute, 2018). To achieve even more ambitious $CO_2$ reduction goals and limit global warming to 1.5° C above pre-industrial levels would require active carbon dioxide removal from the atmosphere by combining bioenergy with CCS (BECCS) and removals in agriculture, forestry and other land use industries (IPCC, 2018).

There are three main methods for carbon dioxide capturing at large single sources: (1) Pre-combustion, which chemically strips off carbon and leaves hydrogen to burn, (2) Post-combustion, which separates the $CO_2$ with the use of chemical solvents, and (3) Oxy-combustion, which burns coal or gas in denitrified air to yield only $CO_2$ and water (Metz et al., 2005; Haszeldine, 2009; Boot-Handford et al., 2014; Bui et al., 2018). Pre-combustion capture is mainly applied in fertilizer manufacturing and hydrogen combustion but can involve power plants that gasify coal and chemically shift methane or syngas to hydrogen (Metz et al., 2005;

Haszeldine, 2009). Oxy-combustion separates oxygen from air with established cryogenic methods and burns coal or gas in a mixture of that oxygen to enable a much easier separation of the $CO_2$ without a solvent (Haszeldine, 2009). This technology has, to date, only been employed for demonstration sites, but may reach commercial status in the near future (Boot-Handford et al., 2014; Bui et al., 2018). Post-combustion is the most-commonly applied method as it has been used successfully for decades for separating $CO_2$ from natural gas (Metz et al., 2005; Bui et al., 2018). Post-combustion uses chemical solvents to separate $CO_2$ from flue gases in the air produced by the combustion of the primary fuel at large single sources (Metz et al., 2005; Boot-Handford et al., 2014), i.e. by wet scrubbing of combustion products with aqueous amine solutions before they are vented into the atmosphere (Gibbins & Chalmer, 2008).

Transportation is an important factor of CCS. All power plants that are not located above geological storage sites require suitable transportation technologies (Metz et al., 2005). Transportation technologies for $CO_2$ are well established (Bui et al., 2018). $CO_2$ is either transported via on- or offshore pipelines (Noothout et al., 2014) or via ship, e.g. within the “Northern Lights” full-scale CCS project in Norway (Northern Lights, web link in reference list; Global CCS Institute, 2018). In October 2019, the London Protocol Parties adopted a resolution to allow provisional application of an amendment to Article 6 of the Protocol to allow sub-seabed geological formations for sequestration projects to be shared across national boundaries. The London Protocol provides a legal framework for parties to effectively prevent pollution of the sea caused by dumping or incineration at sea of wastes and other matter. Activities such as carbon dioxide capture and storage in sub-seabed geological formations and marine geoengineering activities, and ocean fertilization, are included within the London Protocol framework (IMO, 2019).

In general, geological storage is accomplished by injecting $CO_2$ into the rock formation below the surface (Metz et al., 2005). Potential geological storage formations include in marine saline aquifers, basalt layers, deep un-mineable coal beds, depleted oil and gas reservoirs or producing oil reservoirs as part of enhanced oil recovery ($CO_2$-EOR) operations (Figure 1.2; Metz et al., 2005; Matter et al., 2011). $CO_2$-EOR is used by the oil and gas industry since the 1970s (Haszeldine, 2009).

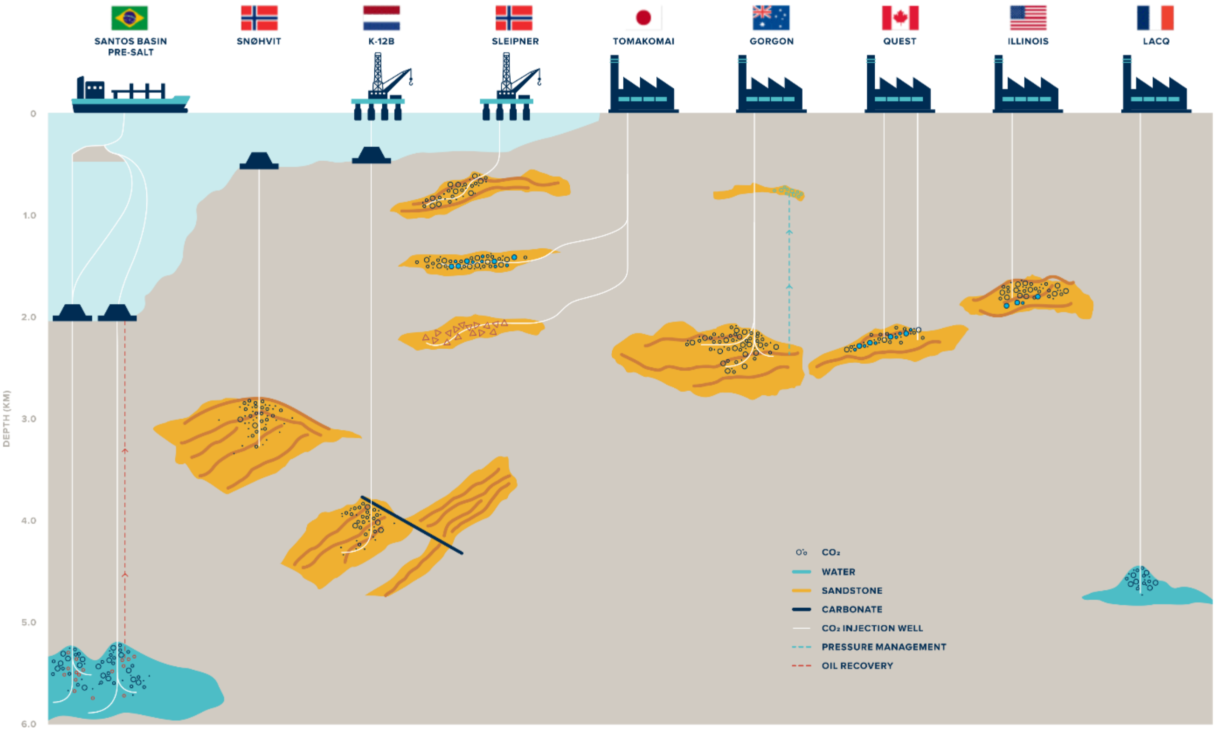

**Figure 1.2.** Illustration of $CO_2$ storage operations around the world. $CO_2$ has been injected and stored across many geological settings e.g. marine aquifers (e.g. Snøvhit, Sleipner, Quest, Illinois), basalt layers (e.g. Tomakomai), deep un-mineable coal beds, depleted oil and gas reservoirs (e.g. K-12B, Gorgon, Lacq) or producing oil reservoirs as part of enhanced oil recovery (e.g. Santos Basin Pre-Salt) using different injection methods (Global CCS Institute, 2018).

In 2018, 43 large-scale facilities for CCS were active, 18 of which were in commercial operation, 5 were under construction and 20 were in various stages of development (Global CCS Institute, 2018). Most of these facilities have the purpose of enhanced oil recovery ($CO_2$-EOR), where injection of $CO_2$ is used to increase the rate of oil extraction. Only a few are dedicated solely to storage. Globally, by 2018 more than 230 Mt of $CO_2$ had been successfully captured and injected deep underground and the cumulative storage rates reached approximately 40 million tonnes (metric tons) per annum (Mt/a) (Global CCS Institute, 2018). The IEA highlighted that globally 450 Mt/a could be captured, utilized and stored with a commercial incentive of US$40 per tonne of $CO_2$ (Global CCS Institute, 2018).

Europe has the third highest number of large-scale projects of which Snøvhit, country (0.7 Mt/a) and Sleipner, country (1 Mt/a) are operational (Bui et al., 2018). Both projects use geological storage in suitable formations for the industrial-scale implementation of CCS. In Europe these are saline aquifers and depleted hydrocarbon reservoirs in the North Sea Basin (Haszeldine, 2009). North Sea storage formations include the Utsira Formation, a marine saline aquifer with a storage potential of 20 to 60 Gt (Lindeberg et al, 2009). More than 18 Mt of $CO_2$ has been injected into the Utsira Formation at the Sleipner CCS site since 2006 (Furre et al., 2017).

CO2 storage in marine saline aquifers, which have the highest global storage potential, may represent the most favorable geological storage opportunity (Metz et al., 2005; Michael et al., 2010). However, the storage of $CO_2$ in the pore space of sedimentary rocks requires impermeable seals (cap rock) above the storage formations. For an efficient long-term storage of $CO_2$, the integrity of the cap rock is a crucial requirement. Leakage from storage formations can result from a variety of processes. First, accumulation of $CO_2$ beneath the cap rock may lead to critical overpressure and fracturing of the cap rock. When permeability barriers hinder the equilibration of overpressure by diffuse flow, pore fluids may form focused fluid conduits that breach the sealing cap rock and transport fluids and overpressure towards shallower reservoirs or the surface (Berndt 2005; Chadwick et al., 2009; Karstens & Berndt, 2015). Second, $CO_2$ can be released from failures of the injection well or along abandoned wells due to faulty casings/annuli or through the fractured surrounding rock (Gurevich et al., 1993; Gasda et al., 2004; Nordbotten et al., 2005; Vielstädte et al., 2015). Third, CO2 release can also be triggered by seismic activity that leads to faulting and fracturing of the subsurface (Gurevich et al., 1993; Metz et al., 2005; Zoback & Gorelick, 2012, 2015; Ajayi et al., 2019).

The different leakage pathways through the overburden require a careful evaluation in terms of the risks of $CO_2$ leakage from geological storage formations. Geotechnical incidents at the sub-seafloor injection site Tordis (Norwegian North Sea) in 2008 and the onshore injection site In Salah (Algeria) between 2004 and 2011 highlight the importance of detailed surveying prior to—and careful monitoring during—the $CO_2$ injection (Eidvin and Øverland, 2009; White et al., 2014). In the case of focused fluid flow conduits in particular, very little is known about the efficiency for $CO_2$ transfer, the long-term behavior and their physical properties, especially the permeability (Karstens et al., 2017). If these structures affect potential CCS sites, they may pose a potential risk for the long-term integrity of storage formations (Nicoll, 2011; Karstens et al., 2017; Andersen et al., 2017; Marin-Moreno et al., 2019).

### 1.1.4. STEMM-CCS

My thesis was conducted within the framework of the **St**rategies for **E**nvironmental **M**onitoring of **M**arine **C**arbon **C**apture and **S**torage (STEMM-CCS) project. The project was funded by European Commission (2016-2020) on an international level with a multi-disciplinary approach to deliver new approaches, methodologies, and tools for the safe operation of offshore CCS sites. The key objectives are to produce new tools and techniques for monitoring, quantification and assessing $CO_2$ emissions. The project generates new knowledge about the caprock integrity by direct investigation of natural geological and anthropogenic fluid flow features. STEMM-CCS also implements the first marine ecological baseline study, incorporating geochemical and biological variability, for CCS demonstration projects offshore.

The natural fluid flow systems investigated during the project include geological (volcanic) release of $CO_2$ from the seafloor around Panarea (Italy), methane release from the Scanner pockmark area (offshore United Kingdom) and the Nyegga pockmark field (offshore Norway). A key component of the project was an experiment in the North Sea at the Goldeneye depleted gas field (Connelly, 2019). At Goldeneye, a manmade fluid escape feature was created by release of $CO_2$ through a drill hole approximately 3 m beneath the seafloor. During the experiment, a large variety of monitoring and quantification techniques were tested and measured against baseline studies of the sediment and water column. The baselines enabled a separation of the natural $CO_2$ signal from the manmade $CO_2$ signal. In the unlikely event of leakage from an industrial scale project, the developments and techniques of the STEMM-CCS project will help stakeholders, including regulatory bodies, policymakers, industry groups, academia and the wider CCS community, to detect and quantify $CO_2$ release from the seafloor.

The STEMM-CCS project consists of eight work packages (WPs) coordinated and managed by WP8. WP1 deals with technical logistics and equipment development. Its main objective was to coordinate, design, develop, manufacture and deploy the seabed drill rig for the $CO_2$ release experiment at the Goldeneye site, as well as to deliver mooring integrate sensors and functionality for seabed landers. WP2 designs and implements techniques for baseline studies at CCS sites and identifies appropriate biological and chemical indices for the impact of the unlikely event of leakage from an industrial-scale CCS site. Modelling approaches are also included in WP2 to extend the spatially and temporally limited field observations.

WP3 investigates leakage pathways through the overburden at natural seepage sites and evaluates the risks of $CO_2$ leakage from geological storage formations. The main objectives are to determine (I) the efficiency of leakage pathways for CO2 transfer, (II) the $CO_2$ permeability of chimney structures, (III) how long chimney structures remain open for $CO_2$ transfer and (IV) the physical properties, especially the permeability, of chimney structures.

WP4 deals with leakage detection, localization and quantification. The aim of the WP is to implement efficient and accurate detection methods, and to trace and quantify $CO_2$ leakage from storage reservoirs in the marine environment. The main objectives are to detect, locate and quantify $CO_2$ leakage from the controlled release experiment from the sub-seabed to the water column and to assess the value of artificial and natural tracers of $CO_2$ in the marine environment. The findings from the experiment are complemented by nested model systems to assess the dispersion of $CO_2$ and tracers in the sediments and water column. WP5 develops new technologies and optimizes current methods (e.g. seabed imaging) to investigate the release experiment and provide decision support tools for future mitigation strategies.

WP6 and WP7 are dedicated to international collaboration and knowledge sharing. STEMM-CCS is aiming to maximize the exposure and dissemination of project outputs to an international audience of CCS stakeholders including industry, regulators, governments and researchers. This is ensured within these WPs by facilitating interaction between project scientists and stakeholders, and training of postgraduate and postdoctoral researchers.

My doctorate study was conducted within the framework of WP3. I further contributed to WP2 and WP7.

## 1.2. Fluid flow in marine sediments

The transport of fluids through marine sediments is primarily governed by pressure gradients and permeability contrasts (Berndt, 2005). In general, Darcy's law defines fluid flow through sedimentary basins (Whitaker, 1986). Darcy's law proved to be a specific solution of the Navier-Stokes-equation and more specifically describes the effective transport of fluid phases through permeable beds from deeper strata towards the surface dependent on the permeability of rocks, the viscosity of the fluids and the driving pressure gradient (Whitaker, 1986). Permeability is the rock property that describes how easily fluids can move through them.

While fluid migration in marine sediments is primarily governed by diffusive flow through permeable beds described by Darcy's law, seismic data have revealed the presence of focused fluid flow conduits in various geological settings around the world, manifesting themselves in a wide range of seismic anomalies (Cartwright et al., 2007; Løseth et al., 2009; Andresen, 2012; Karstens & Berndt, 2015). Focused fluid flow is primarily directed upwards and can occur when pore pressure exceeds the combined least principal stress and tensile strength of the sediment to induce hydrofracturing (Hubbert & Willis, 1957). Pore pressure may not need to exceed the least principal stress to enable fluid flow, if flow is focused along normal faults that can be reactivated before pore fluid pressure reaches the level of the least compressive stress. Aside from the Mohr-Coulomb failure criterion, fluids may also start to move if the pore pressure overcomes the capillary entry pressure and capillary failure occurs (Clayton & Hay, 1994). Both types of seal bypass commonly occur in areas where the fluid pressure is increased, i.e. by compaction, rapid loading, hydrothermal activity, or diagenetic processes (Berndt, 2005). Once migration pathways have formed, they may remain conductive for further gas migration from deeper strata towards the surface for millions of years (Dumke et al., 2014).

In marine sediments, fluids originate from a variety of sources that can lead to overpressure in pore space and subsequent vertical migration of fluids (Osborne & Swarbrick, 1997; Berndt, 2005). These sources include burial of seawater during sedimentation (Dugan & Flemings, 2000; Flemings et al., 2003), dehydration of minerals (Osborne & Swarbrick, 1997), hydrothermal venting from volcanic activity (Kulm & Suess, 1990; Svensen et al., 2004), tectonic compression (Saffer & Tobin, 2011), dissociation of gas hydrates (Kvenvolden; 1993; Dickens et al., 1997; Suess et al., 1999) or compaction of sediments (Berndt et al., 2003; Cartwright et al., 2003). Fresh or brine water systems can cause overpressure in the offshore realm because of their potentiometric head (e.g. artesian well; Bachu & Underschultz, 1993; Osborne & Swarbrick, 1997). Submarine groundwater aquifers charged with meteoric water, from onshore or during the geological past, are another example of fluid movement through marine sediments. These aquifers have become more important as increasing water shortages threaten major coastal cities around the world (Taniguchi et al., 2002; Cohen et al., 2010; Post et al., 2013; Berndt & Micallef, 2019).

Fluid flow in marine sediments plays a crucial role for the global carbon cycle and climate system, water and hydrocarbon resources, as well as natural and exploration-related geohazards.

The complex fluxes of hydrocarbons between the geosphere, biosphere, hydrosphere and atmosphere have a significant impact on the global carbon cycles (Judd & Hovland, 2007). Greenhouse gas emissions, including carbon dioxide and methane from marine sediments, and the production and burning of hydrocarbons, have a direct influence on the climate (IPCC: Ciais et al., 2013; Saunois et al., 2016). A large portion of marine methane is bound in gas hydrates, which are sensitive to changes in temperature and pressure conditions (Kvenvolden, 1988). The dissociation gas hydrates can have implications for global climate (Nisbet, 1990; Ruppel & Kessler, 2017) and the exacerbation of effects of climate change such as ocean acidification (Biastoch et al. 2011). Though contentious, it has also been long suggested that there is a link between gas hydrates and submarine slope stability (Carpenter, 1981) which can have implications for local infrastructure and coastal communities. Drilling incidents, such as Figge Maar crater/B1 blowout (Kornfeld, 1964; Thathje et al., 1999) or 22/4B blowout (Leifer & Judd, 2015), and leakage from decommissioned wells (Vielstädte et al., 2017) have large impact on the local environment but also add to the regional hydrocarbon budgets.

### 1.2.1. The manifestation of fluid flow in seismic refection data

Seismic reflectivity is sensitive to fluid in the pore space of marine sediments, especially gas, as it has a strong influence on seismic velocities and energy absorption of seismic waves (White, 1975; Domenico, 1977). Hydrocarbon-related fluid flow systems may thus manifest themselves in seismic data as anomalies in the subsurface (Berndt, 2005; Cartwright et al., 2007; Løseth et al., 2009; Andresen, 2012; Karstens & Berndt, 2015). Such seismic anomalies may be associated with vertical to sub-vertical fluid conduits, sediment deformation (e.g. sediment mobilization, polygonal faulting), gas hydrates or gas accumulations. For fresh water-related fluid flow systems, seismic data may provide valuable information about the geometry and character of aquifers (Taniguchi et al., 2002; Cohen et al., 2010; Post et al., 2013).

Three-dimensional (3D) seismic data have substantially advanced the knowledge of subsurface fluid migration features, which were previously often discarded as poorly imaged zones and seismic artifacts in two-dimensional (2D) seismic data (Cartwright & Huuse, 2005). Conventional 3D seismic data sets acquired for exploration purposes have shed light on the nature and architecture of geological features associated with fluid flow in sedimentary basins. With advancements in computational power, recording and processing of conventional 3D seismic data and 3D seismic attributes, the interpretation and understanding of focused fluid flow has reached a new age. However, the resolution of conventional seismic data, spatially (often >=12.5 m) and vertically (frequency dependent, e.g. for a dominant frequency of 40 Hz: 10 m), is often not sufficient to image the seismic expression of fluid flow systems in detail. Multi-frequency surveys with different sources (e.g. Bolt Gun, GI-Gun, Chirp, Boomer, and Sparker; e.g. Bull et al., 2018) and ultra-high resolution (one-meter-scale, e.g. P-cable; Lebedeva-Ivanova et al., 2018) complement conventional seismic data and have led to a better understanding of the nature and internal architecture of fluid flow systems.

Direct hydrocarbon indicators (DHI) highlight areas in seismic data where gas accumulates (see Figure 1.3). Such DHIs include:

- Acoustic blanking, which describes the energy absorption of a seismic wave due to the presence of free gas and the subsequent amplitude dimming of underlying reflectors, i.e. dim spots (White, 1975; Løseth et al., 2009).
- Velocity pushdown is an apparent depression of seismic reflectors (in the time domain) due to the decrease of seismic velocities in the accumulated gas phase above the reflectors (White, 1975; Domenico, 1977).
- Bright spots are high amplitude seismic reflections. In the case of a polarity reversal (with respect to the seafloor) they usually indicate the existence of free gas in the pore space (White, 1975; Domenico, 1976).
- Flat spots indicate a fluid contact (oil/gas, gas/water, oil/water) and manifest themselves in seismic data as horizontal (high-amplitude) reflections that cut dipping strata (Løseth et al., 2009).
- Bottom-simulating reflections (BSR) are reflections that can cross-cut sedimentary strata and that broadly mimic the seafloor. They can be gas hydrate or diagenesis related (Shipley et al., 1979; Holbrook et al., 1996, Berndt et al., 2004; Figure 1.3B). A negative polarity BSR (by far the most common) indicates the presence of gas hydrates by highlighting the acoustic impedance contrast between gas hydrates and the underlying free gas (Bangs et al., 1993; Hornbach et al., 2003).

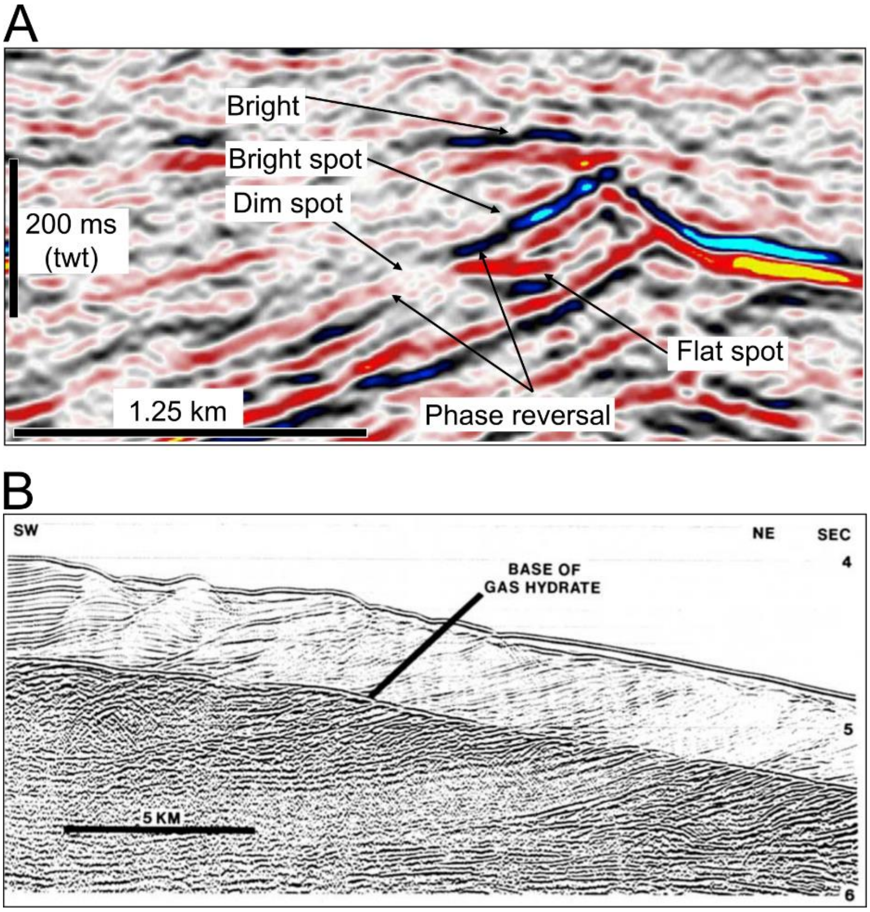

**Figure 1.3.** (**A**) Seismic anomalies associated with gas in the subsurface (Løseth et al., 2009) and (**B**) early multichannel seismic reflection profile showing a bottom simulating reflection (BSR) related to gas hydrates in the subsurface (Shipley et al., 1979).

Changes in the continuity of seismic reflections or structural deformation may develop in layers or geological structures, in which fluid migration altered the pre-existing sediments (Løseth et al., 2009). However, not all of these seismic indicators necessarily provide evidence for hydrocarbon accumulations as they may also be caused by abrupt changes in stratigraphy or low-velocity rocks (Ensley, 1984).

### 1.2.2. Focused fluid flow

Fluid flow systems in marine sediments comprise three main structural elements: the source, a seal-bypass system and seepage/venting at the seafloor. From a source in deeper strata, leakage may be focused through a seal-bypass system that transports fluids vertically towards shallow/overlying strata (Cartwright et al., 2007).

In general, cross-formational fluid flow in the subsurface is typically associated with

(I) Vertical fluid conduits (Berndt et al., 2003; Cartwright et al., 2007; Løseth et al., 2009; Andresen, 2012; Karstens & Berndt, 2015; Figure 1.4)

(II) Wells from hydrocarbon exploration and other subsurface operations (Gurevich et al., 1993; Gasda et al., 2004; Nordbotten et al., 2004; Vielstädte et al., 2015; Figure 1.4).

(III) Structure-controlled flow along faults or fractured zones (Behrmann, 1991; Gurevich et al., 1993; Aydin, 2000; Cartwright et al., 2007; Saffer & Tobin, 2011; Figure 1.4).

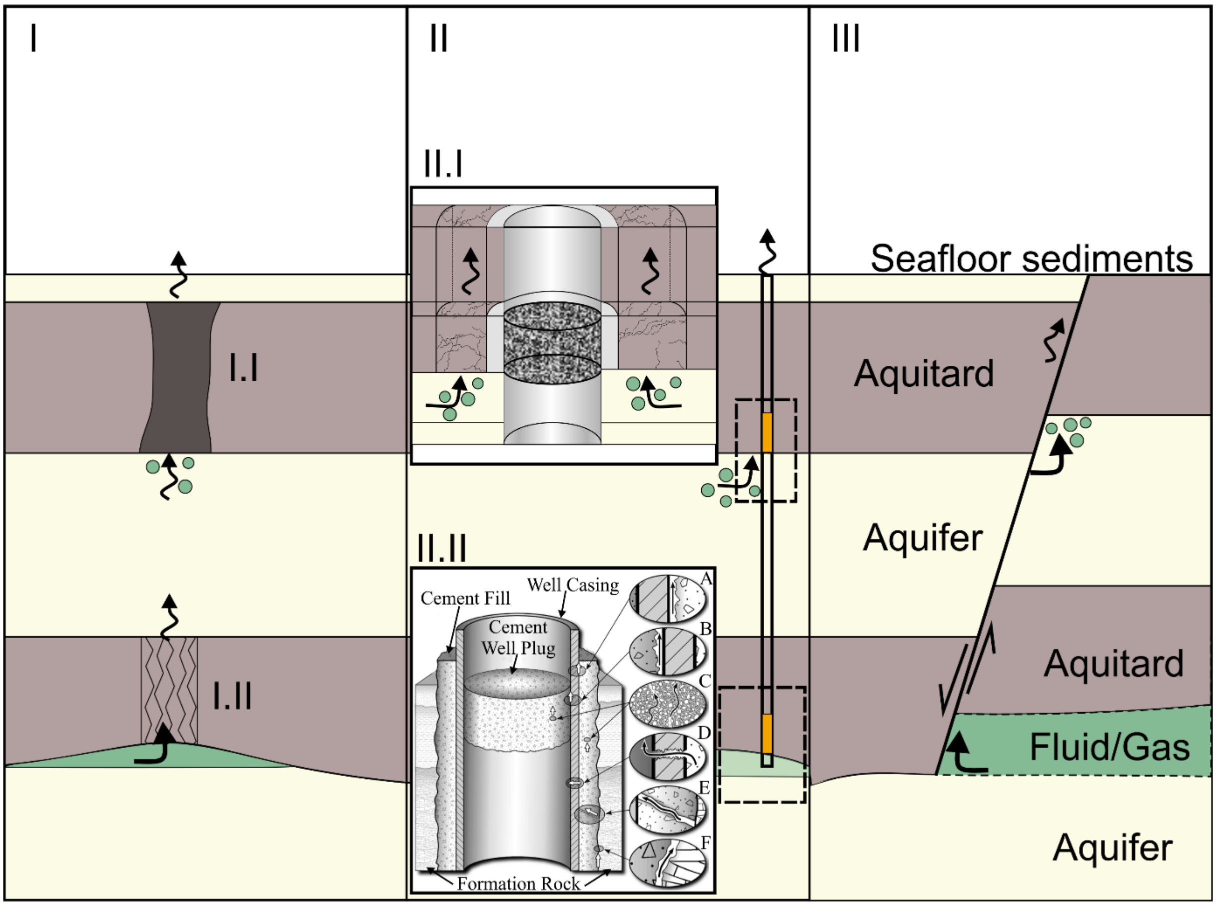

**Figure 1.4.** Schematic sketch of fluid migration pathways in marine sediments. (**I**) Vertical fluid conduits which manifest in seismic data as amplitude anomalies (Seismic pipes & chimneys). These structures are known from sediment basins around the world and are interpreted as the seismic image of (**I.II**) gas filled fracture networks or as (**I.II**) injections of fluids or fluidized sediments. **(II)** Wells from hydrocarbon exploration and other subsurface operations. Leakage may occur either (**II.I**) through the fractured surrounding of the borehole and/or (**II.II**) through faulty casings and/or annuli of the well: (A) Between casing and cement; (B) between cement plug and casing; (C) through the cement pore space as a result of cement degradation; (D) through casing as a result of corrosion; (E) through fractures in cement; and (F) between cement and rock (modified after Gasda et al., 2004). **(III)** Structure-controlled flow along faults and fractured zones in the subsurface.

The nature and internal architecture of fluid flow systems, especially their hydraulic properties, are poorly constrained by direct observations. Flow varies in both space and time (e.g. Clayton & Dando, 1996; Leifer et al., 2004; Moss & Cartwright, 2010; Chand et al., 2012; Krämer et al., 2017; Karstens et al., 2018) and the complex flow pathways through the overburden make it very difficult to characterize a particular system (Hornbach et al., 2007; Karstens & Berndt, 2015). In many sedimentary basins, fluid flow systems consist of a combination of various fluid migration pathway types and may develop complex internal architectures (Gay et al., 2007; Karstens & Berndt, 2015). Natural and anthropogenic fluid migration pathways through the overburden may thus have major implications for the availability of resources such as water or hydrocarbons and for the long-term integrity of future—and current—CCS sites.

### 1.2.3. Fluid flow through pipes & chimneys

Vertical fluid conduits may form where localized overpressure breaches the sealing cap rock (permeability barrier) and thereby transport fluids and overpressure towards shallower reservoirs or the surface (Berndt, 2005; Cartwright et al., 2007; Karstens & Berndt, 2015). Focused fluid conduits manifest themselves in seismic data as vertical amplitude anomalies known as chimney or pipe structures (Cartwright et al., 2007; Løseth et al., 2009; Andresen, 2012; Karstens & Berndt, 2015). Pipes and chimneys are interpreted as the seismic manifestation of gas filled fracture networks (e.g.; Granli et al., 1999; Arntsen et al., 2007) or as injections of fluids or fluidized sediments (e.g. Huuse et al., 2010; Andresen 2012; Karstens & Berndt, 2015; Figure 1.4).

Pipe and chimney structures are known from sediment basins around the world and are very common above hydrocarbon reservoirs (Heggland, 2007; Karstens et al., 2019), crosscutting the overlying strata and forming hydraulic connections between permeable reservoirs at various depths (Karstens & Berndt, 2015). Originally, seismic chimneys or gas chimneys were described as zones of chaotic reflections with dimmed or wiped-out zones and bright spots at different stratigraphic levels (e.g. Ekosfisk or Tommeliten, North Sea; Hovland & Sommerville, 1985; Granli et al., 1999). These “classical” chimneys are wide features (several km diameter) and show a complex internal architecture (see Figure 1.5A). Seismic pipes differ from these gas chimneys by being narrower and having distinct vertical oriented boundaries (e.g. Nyegga, Norway; Mienert et al., 1998; Figure 1.5B). The terms chimney and pipe for vertical amplitude anomalies have become arbitrary and are used interchangeably in the literature. However, both types of seismic anomalies are associated with fluid conduits in the subsurface that provide a hydraulic connection from deeper strata to shallower strata, or the seabed (Cartwright et al., 2007; Løseth et al., 2009; Andresen, 2012).

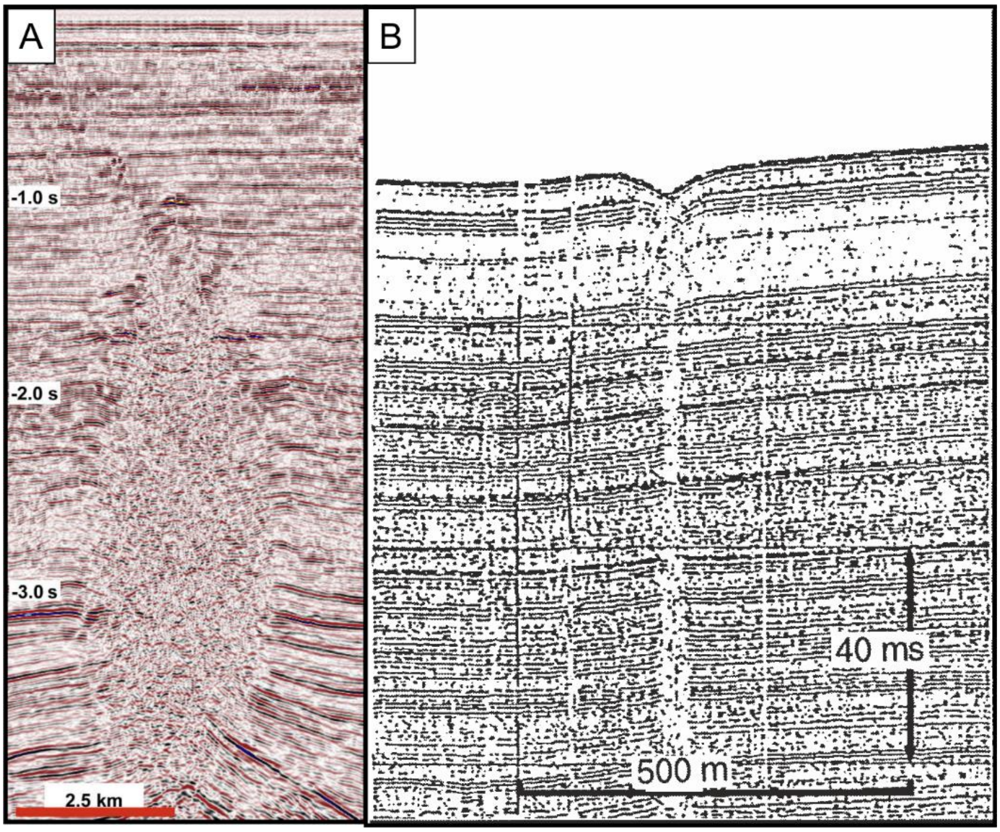

**Figure 1.5.** (**A**) Seismic chimney structure above the Tommeliten field (Løseth et al., 2009) and (**B**) seismic pipes structure below the Nyegga area on the mid-Norwegian margin (Mienert et al., 1998).

Although seismic pipes and chimneys are common features in seismic reflection data and their interpretation as focused fluid flow conduits is well established, their nature and in particular their permeability is poorly understood. They may pose a leakage risk for sub-seafloor storage operations, which is directly controlled by the permeability of focused fluid conduits (Karstens et al., 2017; Marín-Moreno et al., 2019). The permeability may vary significantly depending on the type of affected sediments, the age of the conduits and the migrating fluids. Cementation and compaction may seal a focused fluid conduit entirely with time and even high-resolution seismic data are not capable of resolving the internal architecture of such structures.

Seismic data analysis represents an effective method to map fluid accumulations in the subsurface, identify permeability barriers and constrain subsurface geometries of entire fluid flow systems. However, the scales of focused fluid conduits imaged with seismic data (e.g. Cartwright et al., 2007; Løseth et al., 2009; Andresen, 2012; Karstens & Berndt, 2015) is generally much larger than those found in onshore outcrops of fossil seep sites (Clari et al., 2004; De Boever et al., 2006a, 2006b; Capozzi et al., 2015 and references therein). Seismic chimneys and pipes are often hundreds of meters in diameter (Berndt, 2005; Cartwright et al., 2007; Løseth et al., 2009; Andresen, 2012; Karstens & Berndt, 2015), while the largest known fossilized hydrocarbon-derived carbonate conduits are only up to 10 m high and more than 1 m in diameter, spread over a comparatively small area (e.g. 300 x 800 m) (De Boever et al., 2006a, 2006b). To date, only onshore outcrops of sand intrusions, which form due to the remobilization of sediments during rapid fluid discharge or strong seismic activity (Hurst et al., 2011), have been observed to reach similar dimensions (tens of meters wide, hundreds of meters high) to their corresponding seismic anomalies (Huuse et al. 2005; Ross et al. 2014). Examples of such sand intrusions can be observed in the Kodachrome Basin, Utah, USA (Ross et al., 2014), or at the giant sandstone pipes in SE Utah (Huuse et al., 2005). Linking seismic signatures with field observations needs to overcome the observational gap between seismic and field geological data to give insight into the formation processes.

### 1.2.4. Fluid flow along wells

There are millions of wells from hydrocarbon exploration and other subsurface operations in continental shelves worldwide (Kang et al., 2016). In the North Sea alone, there are 20,507 hydrocarbon-related wells of which 6,689 are currently decommissioned (Appendix Table S1). These wells may hydraulically connect deeper strata with the overburden or seabed and thus represent potential anthropogenic (man-made) fluid migration pathways in the sedimentary succession. Drilling into over-pressured gas pockets has led to massive blowouts e.g. the 22/4B blowout in the Central North Sea (Figure 1.6; Leifer & Judd, 2015) or the B1 “Figge Maar” blowout (Kornfeld, 1964; Thathje et al., 1999) in the southeastern North Sea. Even drilling through less pressurized gas pockets and fluid accumulations may trigger focused fluid migration through the overburden and lead to gas release at the seafloor, into the hydrosphere, and consequently atmosphere (Gurevich et al., 1993; Gasda et al., 2004; Vielstädte et al., 2015).

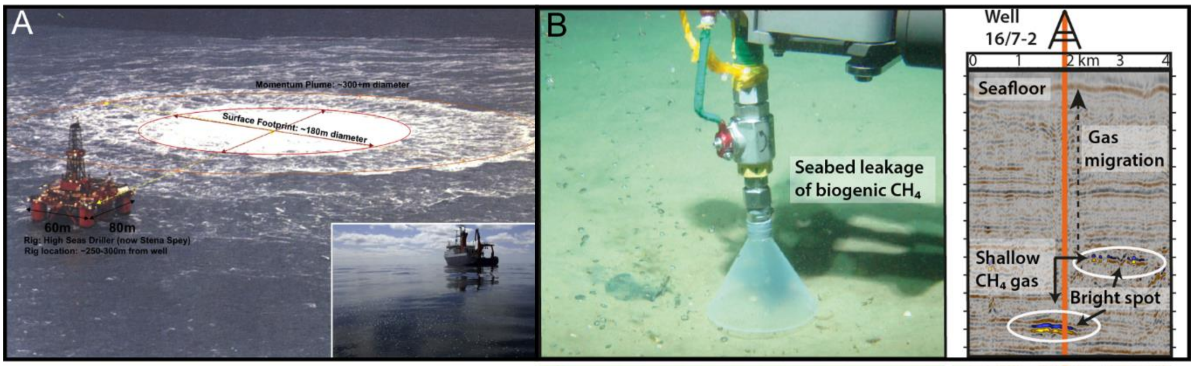

Figure 1.6. (**A**) The 22/4b blowout, November 1990. Leifer & Judd (2015) show the approximate diameters of bubble surfacing footprint and momentum plume. Inset shows the 22/4b surface bubble plume expression during 2005 Alkor cruise (photo by Peter Linke). (**B**) The first methane emission measurements at offshore wells in the Central North Sea (CNS) conducted by Vielstädte et al. (2015, 2017) showing that considerable amounts of biogenic methane originating from shallow gas accumulations in the overburden of deep reservoirs are vented into the North Sea, potentially releasing a total of 3−17 kt of methane per year into the North Sea.

Emissions of greenhouse gases (primarily methane) from wells and other subsurface operations may add to the global/regional greenhouse gas budgets and counteract efforts to mitigate emissions from fossil fuel infrastructure (Figure 1.6; Vielstädte et al., 2017). In the context of CCS, wells that penetrate $CO_2$ storage formations may represent potential leakage pathways (Gasda et al., 2004; Metz et al., 2005; Nordbotten et al., 2005; Kopp et al., 2010). Prolonged leakage along numerous wells that penetrate $CO_2$ storage formations may reduce the efficiency of long-term $CO_2$ storage (Vielstädte et al., 2019).

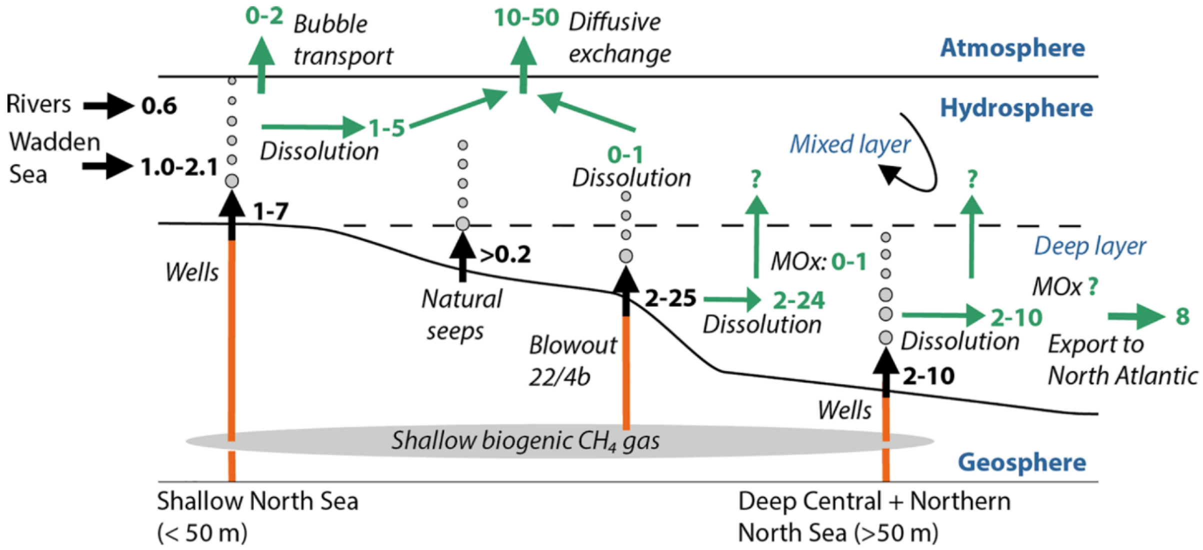

Figure 1.7. Methane budget with sources (black arrows) and sinks (green arrows) of the North Sea by Vielstädte et al. (2017). Emissions given in kt yr$^{-1}$ of methane. Leakage from shallow gas pockets along drilled wells (orange arrows) is a significant methane input into the North Sea (Vielstädte et al., 2017).

There are two leakage types associated with wells and other subsurface operations. Leakage may occur through faulty casings and/or annuli of wells (Type 1) or through the fractured surrounding along a well (Type 2). Leakage through faulty well casings and/or annuli is commonly referred to as “well integrity issues” (Celia & Bachu, 2003; Gasda et al., 2004). In these Type 1 cases, migration pathways may open in various ways: in the micro annulus between casing and annular cement, the micro annulus between cement plug and casing, as cracks or channels in cement plugs, as ruptures or pits in casing resulting in connection between annular cement and wellbore, as cracks or channels in annular cement resulting in connections between formation and casing, or through the micro annulus between annular cement and formation (Gasda et al., 2004). In the other case (Type 2), leakage occurs along the fractured surrounding parallel to the well bore outside the well casing (Gurevich et al., 1993). Currently no quantitative data exist for leakage through the fractured surroundings of well paths.

Similar to seismic pipes and chimneys, the effective permeability of wells is the key physical parameter for leakage risk assessment. In early studies on leakage through abandoned wells, little to no quantitative data on effective permeabilities existed and the studies had to rely on a stochastic framework (Celia et al., 2011). Newer approaches quantified the effective permeabilities of abandoned wells with specific field measurements, but well permeability still ranges from nanodarcies to hundreds of millidarcies (Postma et al., 2019). Direct measurements of methane release from decommissioned wells span 2 orders of magnitude. Onshore, release rates are highest for unplugged wells in the proximity of coal areas, i.e. 0.5 t yr$^{-1}$ of $CH_4$ (Kang et al., 2016). Offshore release rates measured at decommissioned wells in proximity to shallow gas accumulations are one order of magnitude higher than on land, i.e. 1-19 t $yr^{-1}$ of $CH_4$ (Vielstädte et al., 2015). The highest release rates (19 t $yr^{-1}$ of $CH_4$) were measured at an abandoned well that spatially correlates with a seismic chimney structure in the subsurface (Vielstädte et al., 2015). However, in the offshore realm, very few data exist on leakage from wells and other subsurface operations and independent emission estimates are scarce. All other information on methane emissions from fossil fuel infrastructure almost always originates from the oil and gas industry itself. In the U.S., studies have shown that the numbers surrounding methane emissions provided by the industry are too low (Allen et al., 2013; Miller et al., 2013).

Well attributes, such as geographic location, age, drilling date (spud date), production and abandonment, may be used as proxies to assess the leakage propensity of wells (Kang et al., 2016; Townsend-Small et al., 2016). Onshore, wells show a correlation of leakage with well attributes, i.e. geographic location, age, and proximity to shallow gas accumulations (Kang et al., 2016). However, basic information, such as the number of wells or their location, even in regions with a long history of oil and gas exploration and production, are often poorly documented (e.g. Kang et al., 2016; Townsend-Small et al., 2016). Offshore, the few publicly available measurements indicate that the presence of shallow gas accumulations (free gas in the upper 1000 m) is the most important factor for the tendency of wells to leak (Vielstädte et al., 2015). Machine learning approaches (Montague et al., 2018) and numerical probabilistic approaches (Orlic et al., 2018) can help understand which parameters (e.g. well attributes, reservoir characteristics) can be used to assess the well integrity and help predict the likelihood of wells leaking. Seismic data can also help identify gas accumulations in the subsurface and define areas where leakage is more likely (White, 1975; Anstey, 1977; Karstens & Berndt, 2015; Marfurt & Alves, 2015).

### 1.2.5. Fluid flow along faults

Faults are the most widespread and common structure with respect to focused fluid flow systems (Cartwright et al., 2007). Their role for the hydrodynamic system depends on the permeability contrast between the fault rock and surrounding damage zone and the adjacent strata (Aydin, 2000). Faults may act as conduits when their damage zone is more permeable than their host sequence, irrespective of their absolute displacement and rupture history. In these cases, fluid flow along the fault can be semi-permanent (Hooper, 1991; Cartwright et al., 2007).

Fault activity and therefore also fault permeability is linked to pore-pressure. Increasing pore pressure acting against an initially sealed fault reduces the strength of the fault and may ultimately result in fault rupture and a (temporal) increase in permeability and subsequent leakage of fluids from depth (Wiprut & Zoback, 2000; Grollimund & Zoback, 2003; Abrams, 2005; Egholm et al., 2008). Thus, faults have an active role in controlling the expulsion of fluids when they act as conduits for processes such as mineral dehydration reactions and compacting sediments (Saffer & Bekins, 1999; Screaton et al., 2002), e.g. for polygonal faults in ultra-low permeability sealing sequences (Cartwright et al., 2007). When pore pressure is reduced, the faults may seal again (Sibson, 1992). This leads to a complex and often intertwined relationship between fluid flow and fault activity.

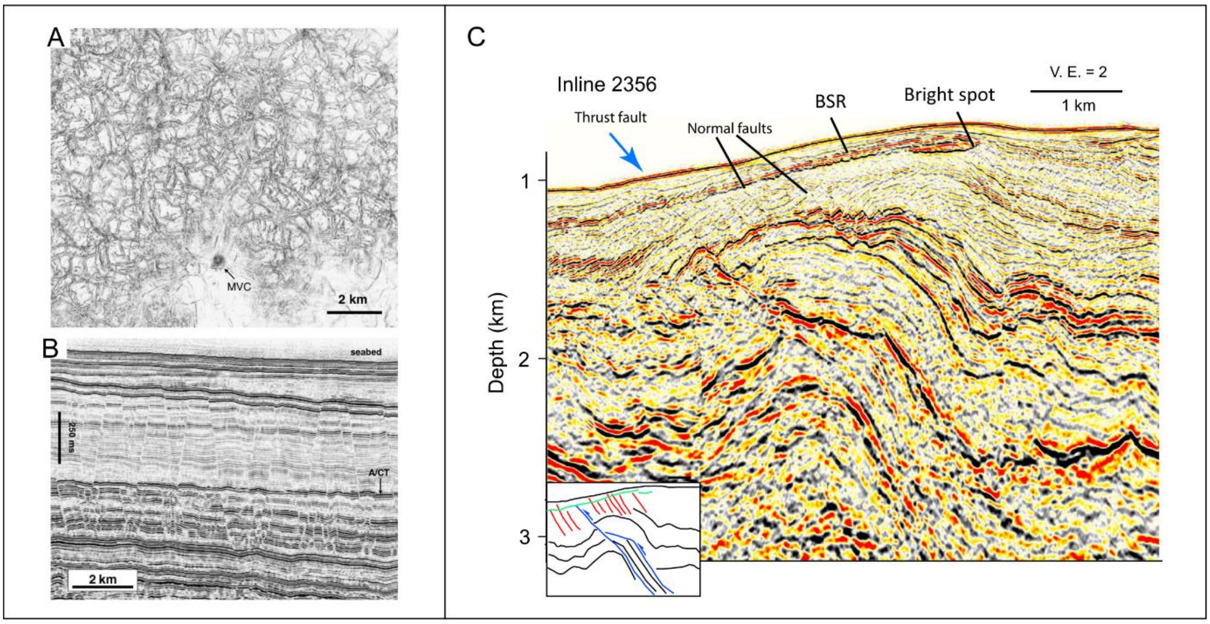

Figure 1.8. (A) Horizontal slice of 3D seismic attribute (Variance) of classical polygonal faulting and a mud volcano conduit (MVC). Faults are likely to act as conduits during their formation (Cartwright et al., 2007). (B) 3D seismic data profile through polygonal faulting with bottom simulating reflection caused by opal A/CT diagenesis (Cartwright et al., 2007). (C) Inline of 3D seismic data at the Costa Rican subduction margin showing normal faults within the slope cover and thrust faults within the margin wedge. A BSR and bright spots indicate migration of fluids through the margin (Bangs et al., 2015).

Faults are considered a major leakage pathway through sealing formations above CCS storage formations (Gurevich et al., 1993; Metz et al., 2005). Leakage through undetected faults and fractures constitutes a hazard to drinking-water aquifers, ecosystems, acidification of soils, displacement of oxygen in soils and release of $CO_2$ in low-lying areas with little wind may harm humans and animals (Metz et al., 2005). The injection of large volumes of $CO_2$ during industrial-scale CCS operations may lead to elevated pore pressures and subsequently higher probabilities of fault reactivation and earthquakes (Zoback & Gorelick, 2012, 2015).

In subduction-zones, tectonic deformation in combination with compaction dewatering and thermal dehydration results in a complex hydrogeological regime (Saffer & Tobin, 2011). Fluid production can vary over relatively short spatial and temporal scales in response to changes in sediment accumulation and compressional deformation (e.g. Watson et al., 2019). The resulting variations in pore-pressure within a subduction-zone may support a broad range of fault behavior spanning the full spectrum from large earthquake ruptures to aseismic creep (Saffer, 2017; Bürgmann, 2018). Upper-plate normal faults in marine forearcs likely play a significant role for the dewatering of the subduction-zone and the vertical-flow and possible seafloor seepage of hydrocarbons (Behrmann, 1991; Ranero et al., 2008). Such faults have long been considered a tectonic feature primarily associated with erosive margins. However, increasing coverage of marine seismic data has proven that similar features also exist in accretionary margins, such as Cascadia (McNeill et al., 1997), Makran (Grando and McClay, 2007), Nankai (Gulick et al., 2010; Moore et al., 2013) or Central Chile (Geersen et al., 2011, 2016), where horizontal compression usually results in folding and thrust-faulting. Leakage from these faults is likely episodic, driven by large subduction zone earthquakes or subducting seamounts (Geersen et al., 2016; Pecher et al., 2017). However, there is a general lack of understanding of the role and importance of normal faulting for the structural and tectonic evolution of accretionary margins and their role in fluid migration through marine sediments.

### 1.3. Detection & attribution of fluid flow

Fluid flow through marine sediments has numerous manifestations on the seafloor. Seepage and venting of fluids from the seafloor can involve gas, oil, water and sediments, and the consequent seeping/venting structures are referred to as "cold seeps" if the released fluids are not derived from hydrothermal venting (Judd & Hovland, 2007; Talukder, 2012; Ceramicola et al., 2018). Since King and McLean discovered pockmarks ("cone-like depressions") in 1970 on the Nova Scotia Shelf, offshore Canada, submarine cold seeps have been in the focus of scientific investigation (Judd & Hovland, 2007). Increasing seismic and hydroacoustic data coverage and quality reveal the abundance and nature of different seepage and venting types. The nature of cold seeps is determined by the released fluids, the release rate and physical conditions at the seafloor (Judd & Hovland, 2007).

Seepage and venting of methane can be associated with pockmarks (Hovland & Sommerville, 1985; Judd et al., 1994; Gay et al., 2007; Judd & Hovland, 2007), flares in hydroacoustic data (Judd & Hovland, 1992; Schneider von Deimling et al., 2007), chemosynthetic biological communities (Dando et al., 1991; Austen et al., 1993; Berndt 2005; Niemann et al., 2005; Wegener et al., 2008), methane-derived authigenic carbonates in the form of slabs, mounds and/or chimneys (Ritger et al., 1987, Kulm & Suess, 1990, Bohrmann et al., 1998; Boetius et al., 2000; Díaz del Río et al., 2003), mud diapirs/volcanoes (Kopf, 2002; Bohrmann et al., 2003; Van Rensbergen et al., 2005; Hensen et al., 2007) and hydrate mounds (Haeckel et al., 2004; Andreassen et al., 2017).

Anaerobic oxidation of methane (AOM) is an important sink and filter for methane. AOM is mainly mediated by anaerobic, methanotrophic archaea and sulfate reducing bacteria (e.g. Boetius et al., 2000). Bicarbonate is a byproduct of the involved reactions and can lead to the precipitation of methane-derived authigenic carbonates (MDAC), which are a clear indicator for continuous, long-lasting hydrocarbon seepage. MDAC can form crusts/slabs, mounds, tubular concretions or chimneys, which have been documented in many settings around the world and are often found in pockmarks (Boetius, et al., 2000; Judd & Hovland, 2007).

Pockmarks can be meters to hundreds of meters in diameter, meters to tens of meters in depth and affect the local environment, morphodynamics, biochemistry and ecology (Dando et al., 1991; Berndt 2005; Niemann et al., 2005; Judd & Hovland, 2007; Wegener et al., 2008). The morphology and size of pockmarks vary largely and they are often reshaped by local bottom-currents (e.g. King & McLean, 1970; Hovland, 1983; Judd & Hovland, 2007). The most renowned definition of pockmarks by Judd & Hovland (2007) distinguishes between circular and elliptical pockmarks, elongated and asymmetric pockmarks, merged composite pockmarks (pockmark complexes), pockmark strings, small unit pockmarks (possibly around larger centric pockmarks) and giant pockmarks. However, this model does not consider the pockmark forming processes or evolution over time. Especially the morphological parameters, e.g. depth and diameter, for individual classes are poorly constrained, which results in ambiguous description of similar sized pockmarks at one or several sites, e.g. relative descriptions of pockmarks as "unusually large" pockmarks in the Central North Sea block 15/25 (Judd et al., 1994). The primary model for pockmark formation is venting of hydrocarbons (Judd & Hovland, 2007), but they may also form due to the release of water from submarine groundwater discharge (Whiticar, 2002; Nardelli et al., 2017; Goff, 2019), purely sedimentological mechanisms (e.g. Dugan & Flemings, 2002; Paull et al., 2002), or biological processes (e.g. Mueller, 2015)

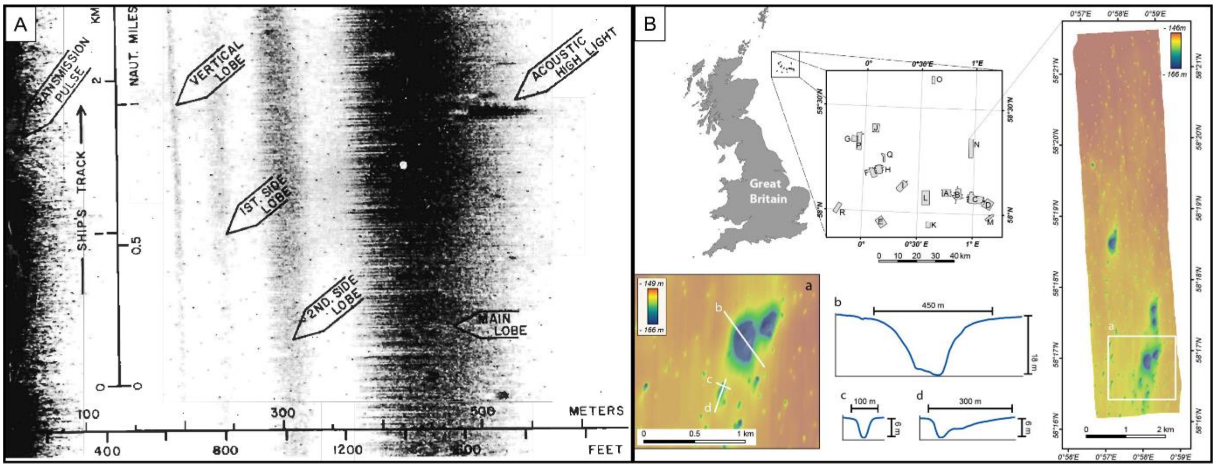

Figure 1.9. (**A**) The earliest description of pockmarks from side scan sonar data by King & McLean, 1970. (**B**) Recent semi-automated analyses of pockmarks applied to 18 different data sets in the Central North Sea (Gafeira et al., 2018).

The interest in submarine groundwater discharge (SGD) has increased over recent decades (e.g. Taniguchi et al., 2002; Burnett et al., 2006; Cuthbert et al., 2019; Gustafson et al., 2019). Even in Roman times, SGD was used as a source of fresh water (Judd & Hovland, 2007) and it has become an important source of fresh water in recent decades around the world (Moosdorf & Oehler, 2017). SGD may transport large amounts of nutrients from land to sea, sometimes far into the shelf region, and likely has a significant impact on the local environment and ecosystems (Cohen et al., 2010; Moore, 2010; Lecher et al., 2016). SGD can also be enriched in methane (Bugna et al. 1996; Cable et al. 1996; Dulaiova et al. 2010), which then leads to a combined submarine methane-groundwater discharge (Lecher et al., 2016). Detection, attribution and quantification of SGD are mainly conducted with optical systems, geochemical water-column investigation of tracers (radium & radon isotopes), dissolved silicon, remote sensing, geochemical analyses (e.g. methane, chloride) of the water column and sediment samples as well as seepage meters (Taniguchi et al., 2002; Burnett et al., 2006), however, very few geophysical studies dealing with SGD have been conducted to date, most of which are based on geoelectric or controlled sourced electromagnetic surveys (Stieglitz, 2005; Viso et al., 2010; Gustafson et al., 2019).

Leakage attribution is key for understanding the source of fluids that migrate through the overburden. For hydrocarbon-related cold seeps, the carbon ($\delta^{13}C$) and hydrogen ($\delta^{18}O$) isotope signatures and the relative proportions of methane and higher order hydrocarbons (e.g. ethane, propane, butane) in water and gas samples can help distinguish between shallow biogenic and deep thermogenic sources (Whiticar, 2000). The depth and character of the source are important to understand the complex fluid flow systems comprising different types of fluid migration pathways through the overburden, and to untangle their temporal and spatial evolution.

Effective monitoring strategies for anthropogenic features such as hydrocarbon wells and other subsurface operations may include direct measurements and indirect methods. Direct measurements of the released fluids with remotely operated vehicles (ROVs) are important for attribution of these fluids the particular source. The carbon and oxygen isotope ratios can help distinguish between leakage from deep reservoirs, which may be linked to well integrity issues (Celia & Bachu, 2003; Gasda et al., 2004), and leakage from shallow gas accumulations (in less than 1000 m below the seafloor), which is likely the result of focused fluid flow along the fractured surrounding of the well (Gurevich et al., 1993). Indirect methods may include evaluation of seismic, hydroacoustic and well attribute data to determine areas where leakage is more likely. Probabilistic (machine learning) approaches may help predict the propensity of wells to leak on land and in the ocean (e.g. Nogues et al., 2012; Montague et al., 2018). Effective monitoring strategies for wells and other subsurface operations would thus not only help to estimate greenhouse gas emissions, but also help to understand the processes involved, e.g. whether and how quickly well barriers degrade (in the case of leakage from the deep reservoirs).

## 1.4. Thesis outline

This thesis consists of seven chapters including an introduction, five manuscripts dealing with different aspects of focused fluid flow in marine sediments and a concluding chapter. I authored four of the presented manuscripts (Chapter 2-4, 6) and contributed relevant input to the other manuscript (Chapter 5). The manuscripts have been published, submitted or are planned to be submitted to peer-review journals.

**Chapter 2** deals with the migration of fluids along pipes and chimneys in the North Sea and emphasizes the correct attribution of fluids involved in pockmark formation in the Witch Ground Basin, Central North Sea. The chapter uses a combination of 2D and 3D seismic reflection, multibeam bathymetric, geochemical and sedimentological data to map and describe pockmarks in the Witch Ground Basin (central North Sea), characterize associated sedimentological and fluid migration structures, and analyze the related methane release. Based on morphological and structural differences of more than 1500 pockmarks, we defined two classes of pockmarks which formed independently from another corresponding to at least two different sources of fluids. Chapter 2 concludes that greenhouse gas emissions from pockmark fields cannot be based on pockmark numbers and present-day fluxes but require an analysis of the pockmark forming processes through geological time. Chapter 2 is published in Geochemistry, Geophysics, Geosystems as:

Böttner, C., Berndt, C., Reinardy, B.T.I., Geersen, J., Karstens, J., Bull., J.M., Callow, B.J., Lichtschlag, A., Schmidt, M., Elger, J., Schramm, B., Haeckel, M. (2019). Pockmarks in the Witch Ground Basin, Central North Sea. *Geochemistry, Geophysics, Geosystems*, *20*(4), 1698-1719.

**Chapter 3** deals migration of fluids along wells, in particular greenhouse gases (methane) emissions from decommissioned marine hydrocarbon wells in the North Sea. The chapter focuses on different leakage pathways in relation to hydrocarbon wells and other subsurface operations. The leakage of greenhouse gases from hydrocarbon wells and other subsurface operations may counteract efforts to mitigate greenhouse gas emissions. Chapter 3 present an approach for assessing methane release from marine decommissioned wells. The chapter finds a significant correlation between the presence of shallow gas accumulations in the vicinity of wells and gas release at the seafloor. Chapter 3 conclude that methane release from hydrocarbon wells represents a major source in the North Sea and formulates suggestions for drilling practice improvements and future monitoring strategies. Chapter 3 is currently under review at the International Journal of Greenhouse Gas Control as:

Böttner, C., Haeckel, M., Schmidt, M., Berndt, C., Vielstädte, L., Karstens, J., Weiß, T. (2019, in Review). Decommissioned hydrocarbon wells as a source for greenhouse gas release: sources, rates, and mitigation strategies. *International Journal of Greenhouse Gas Control*.

**Chapter 4 & 5** deal with the migration of fluids along faults in the Hikurangi Margin, New Zealand, and the importance of the advected fluids for slope stability. Chapter 4 documents widespread marine forearc extension in the Hikurangi Margin, New Zealand. The chapter gives insight into the processes that cause extension in the marine forearc of accretionary margins and evaluates the evoked models against findings from 2D and 3D reflection seismic data. Chapter 4 suggests that normal faults play an important role in the structural and tectonic evolution of accretionary margins, including the northern Hikurangi forearc. Chapter 5 investigates the Tuaheni Landslide Complex, which is located above the normal faults identified in Chapter 4. The high-angle normal faults act as fluid migration pathways and likely advect fluids from depth towards a basal shear zone. Chapter 5 is one of the most detailed studies of a landslide so far and gives insight into the fluid flow system and potential basal shear zone development. Chapter 4 is published in Tectonics and in Earth and Planetary Science Letters as:

Böttner, C., Gross, F., Geersen, J., Crutchley, G. J., Mountjoy, J. J., & Krastel, S. (2018). Marine Forearc Extension in the Hikurangi Margin: New Insights From High-Resolution 3-D Seismic Data. *Tectonics*, 37(5), 1472-1491.

Gross, F., Mountjoy, J. J., Crutchley, G. J., Böttner, C., Koch, S., Bialas, J., ... & Huhn, K. (2018). Free gas distribution and basal shear zone development in a subaqueous landslide–Insight from 3D seismic imaging of the Tuaheni Landslide Complex, New Zealand. *Earth and Planetary Science Letters*, 502, 231-243.

**Chapter 6** deals with an onshore outcrop of focused fluid conduits. The documented pipes are the largest hydrocarbon-derived carbonate conduits known globally and are well-exposed in unconsolidated sand and sandstones. The chapter investigates the relationship between faults and pipe formation in the area and formulates a new model for focused fluid flow in high permeable sand formations. Chapter 6 is currently prepared for submission to EGU Solid Earth: Faults, fractures, and fluid flow in the shallow crust – Special Issue as

Böttner, C., Callow, B.J., Schramm, B., Gross, F., Geersen, J., Schmidt, M., Vasilev, A., Petsinski, P., Berndt, C. (in prep.). Quantifying features of a fluid flow systems using customer-grade UAV imagery. *Solid Earth, Faults, fractures, and fluid flow in the shallow crust – Special Issue, European Geosciences Union, Munich, Germany.*

**Chapter 7** summarizes the results from this thesis, give and outlook for potential future and already planned follow-up research and recommendations for future fluid flow related studies.

## 1.5. References

Abrams, M. A. (2005). Significance of hydrocarbon seepage relative to petroleum generation and entrapment. *Marine and Petroleum Geology*, *22*(4), 457-477.

Ajayi, T., Gomes, J. S., & Bera, A. (2019). A review of CO 2 storage in geological formations emphasizing modeling, monitoring and capacity estimation approaches. *Petroleum Science*, 1-36.

Allen, D. T., Torres, V. M., Thomas, J., Sullivan, D. W., Harrison, M., Hendler, A., ... & Lamb, B. K. (2013). Measurements of methane emissions at natural gas production sites in the United States. *Proceedings of the National Academy of Sciences*, *110*(44), 17768-17773.

Andersen, O. A., Nilsen, H. M., & Gasda, S. E. (2017). Vertical equilibrium flow models with fully coupled geomechanics for CO2 storage modeling, using precomputed mechanical response functions. *Energy Procedia*, *114*, 3113-3131.

Andreassen, K., Hubbard, A., Winsborrow, M., Patton, H., Vadakkepuliyambatta, S., Plaza-Faverola, A., ... & Mienert, J. (2017). Massive blow-out craters formed by hydrate-controlled methane expulsion from the Arctic seafloor. *Science*, *356*(6341), 948-953.

Andresen, K. J. (2012). Fluid flow features in hydrocarbon plumbing systems: What do they tell us about the basin evolution?. *Marine Geology*, *332*, 89-108.

Anstey, N. A. (2013). *Seismic interpretation: the physical aspects*. Springer Science & Business Media.

Arntsen, B., Wensaas, L., Løseth, H., & Hermanrud, C. (2007). Seismic modeling of gas chimneys. *Geophysics*, *72*(5), SM251-SM259.

Austen, M. C., Warwick, R. M., & Ryan, K. P. (1993). Astomonema southwardorum sp. nov., a gutless nematode dominant in a methane seep area in the North Sea. *Journal of the Marine Biological Association of the United Kingdom*, *73*(3), 627-634.

Aydin, A. (2000). Fractures, faults, and hydrocarbon entrapment, migration and flow. *Marine and petroleum geology*, *17*(7), 797-814.

Bachu, S., & Underschultz, J. R. (1993). Hydrogeology of formation waters, northeastern Alberta Basin. *AAPG Bulletin*, *77*(10), 1745-1768.

Bangs, N. L., Sawyer, D. S., & Golovchenko, X. (1993). Free gas at the base of the gas hydrate zone in the vicinity of the Chile triple junction. *Geology*, *21*(10), 905-908.

Bangs, N. L., McIntosh, K. D., Silver, E. A., Kluesner, J. W., & Ranero, C. R. (2015). Fluid accumulation along the Costa Rica subduction thrust and development of the seismogenic zone. *Journal of Geophysical Research: Solid Earth*, *120*(1), 67-86.

Behrmann, J. H. (1991). Conditions for hydrofracture and the fluid permeability of accretionary wedges. *Earth and Planetary Science Letters*, *107*(3-4), 550-558.

Berndt, C. (2005). Focused fluid flow in passive continental margins. *Philosophical Transactions of the Royal Society A: Mathematical, Physical and Engineering Sciences*, *363*(1837), 2855-2871.

Berndt, C., Bünz, S., & Mienert, J. (2003). Polygonal fault systems on the mid-Norwegian margin: a long-term source for fluid flow. *Geological Society, London, Special Publications*, *216*(1), 283-290.

Berndt, C., Bünz, S., Clayton, T., Mienert, J., & Saunders, M. (2004). Seismic character of bottom simulating reflectors: examples from the mid-Norwegian margin. *Marine and Petroleum Geology*, *21*(6), 723-733.

Berndt, C., Micallef, A. (2019). Could offshore groundwater rescue coastal cities?.. *Nature*, **574** (36).

Biastoch, A., Treude, T., Rüpke, L. H., Riebesell, U., Roth, C., Burwicz, E. B., ... & Wallmann, K. (2011). Rising Arctic Ocean temperatures cause gas hydrate destabilization and ocean acidification. *Geophysical Research Letters*, *38*(8).

Blunden, J., & Arndt, D. S. (2019). State of the climate in 2018. *Bulletin of the American Meteorological Society*, *100*(9), Si-S306.

Boetius, A., Ravenschlag, K., Schubert, C. J., Rickert, D., Widdel, F., Gieseke, A., ... & Pfannkuche, O. (2000). A marine microbial consortium apparently mediating anaerobic oxidation of methane. *Nature, 407*(6804), 623.

Bohrmann, G., Greinert, J., Suess, E., & Torres, M. (1998). Authigenic carbonates from the Cascadia subduction zone and their relation to gas hydrate stability. *Geology*, *26*(7), 647-650.

Bohrmann, G., Ivanov, M., Foucher, J. P., Spiess, V., Bialas, J., Greinert, J., ... & Blinova, V. (2003). Mud volcanoes and gas hydrates in the Black Sea: new data from Dvurechenskii and Odessa mud volcanoes. *Geo-Marine Letters*, *23*(3-4), 239-249.

Boot-Handford, M. E., Abanades, J. C., Anthony, E. J., Blunt, M. J., Brandani, S., Mac Dowell, N., ... & Haszeldine, R. S. (2014). Carbon capture and storage update. *Energy & Environmental Science*, *7*(1), 130-189.

Bugna, G. C., Chanton, J. P., Cable, J. E., Burnett, W. C., & Cable, P. H. (1996). The importance of groundwater discharge to the methane budgets of nearshore and continental shelf waters of the northeastern Gulf of Mexico. *Geochimica et Cosmochimica Acta*, *60*(23), 4735-4746.

Bui, M., Adjiman, C. S., Bardow, A., Anthony, E. J., Boston, A., Brown, S., ... & Hallett, J. P. (2018). Carbon capture and storage (CCS): the way forward. *Energy & Environmental Science*, *11*(5), 1062-1176.

Bull, J., Berndt, C., Minshull, T., Henstock, T., Bayrakci, G., Gehrmann, R., ... & Callow, B. (2018). Constraining the physical properties of chimney/pipe structures within sedimentary basins. *14th International Conference on Greenhouse Gas Control Technologies, Melbourne, Australia. 21 - 25 Oct 2018.* 8 pp

Bürgmann, R. (2018). The geophysics, geology and mechanics of slow fault slip. *Earth and Planetary Science Letters*, *495*, 112-134.

Burnett, W. C., Aggarwal, P. K., Aureli, A., Bokuniewicz, H., Cable, J. E., Charette, M. A., ... & Moore, W. S. (2006). Quantifying submarine groundwater discharge in the coastal zone via multiple methods. *Science of the total Environment*, *367*(2-3), 498-543.

Burwicz, E. B., Rüpke, L. H., & Wallmann, K. (2011). Estimation of the global amount of submarine gas hydrates formed via microbial methane formation based on numerical reaction-transport modeling and a novel parameterization of Holocene sedimentation. *Geochimica et Cosmochimica Acta*, *75*(16), 4562-4576.

Cable, J. E., Bugna, G. C., Burnett, W. C., & Chanton, J. P. (1996). Application of 222Rn and CH4 for assessment of groundwater discharge to the coastal ocean. *Limnology and Oceanography*, *41*(6), 1347-1353.

Capozzi, R., Negri, A., Reitner, J., & Taviani, M. (2015). Carbonate conduits linked to hydrocarbon-enriched fluid escape. *Marine and Petroleum Geology*, (66), 497-500.

Carpenter, G. (1981). Coincident sediment slump/clathrate complexes on the US Atlantic continental slope. *Geo-Marine Letters*, *1*(1), 29-32.

Cartwright, J. (2007). The impact of 3D seismic data on the understanding of compaction, fluid flow and diagenesis in sedimentary basins. *Journal of the Geological Society*, *164*(5), 881-893.

Cartwright, J., & Huuse, M. (2005). 3D seismic technology: the geological 'Hubble'. *Basin Research*, *17*(1), 1-20.

Cartwright, J., James, D., & Bolton, A. (2003). The genesis of polygonal fault systems: a review. *Geological Society, London, Special Publications*, *216*(1), 223-243.

Celia, M. A., & Bachu, S. (2003, January). Geological sequestration of CO2: is leakage unavoidable and acceptable?. In *Greenhouse Gas Control Technologies-6th International Conference* (pp. 477-482). Pergamon.

Celia, M. A., Nordbotten, J. M., Court, B., Dobossy, M., & Bachu, S. (2011). Field-scale application of a semi-analytical model for estimation of CO2 and brine leakage along old wells. *International Journal of Greenhouse Gas Control*, *5*(2), 257-269.

Ceramicola, S., Dupré, S., Somoza, L., & Woodside, J. (2018). Cold seep systems. In *Submarine geomorphology* (pp. 367-387). Springer, Cham.

Cevatoglu, M., Bull, J. M., Vardy, M. E., Gernon, T. M., Wright, I. C., & Long, D. (2015). Gas migration pathways, controlling mechanisms and changes in sediment acoustic properties observed in a controlled sub-seabed CO2 release experiment. *International Journal of Greenhouse Gas Control*, *38*, 26-43.

Chadwick, R. A., Noy, D., Arts, R., & Eiken, O. (2009). Latest time-lapse seismic data from Sleipner yield new insights into CO2 plume development. *Energy Procedia*, *1*(1), 2103-2110.

Chand, S., Thorsnes, T., Rise, L., Brunstad, H., Stoddart, D., Bøe, R., ... & Svolsbru, T. (2012). Multiple episodes of fluid flow in the SW Barents Sea (Loppa High) evidenced by gas flares, pockmarks and gas hydrate accumulation. *Earth and Planetary Science Letters*, *331*, 305-314.

Ciais, P., Sabine, C., Bala, G., Bopp, L., Brovkin, V., Canadell, J., ... & Jones, C. (2013). Carbon and other biogeochemical cycles. In Climate change 2013: the physical science basis. Contribution of Working Group I to the *Fifth Assessment Report of the Intergovernmental Panel on Climate Change* (pp. 465-570). Cambridge University Press.

Clari, P., Cavagna, S., Martire, L., & Hunziker, J. (2004). A Miocene mud volcano and its plumbing system: a chaotic complex revisited (Monferrato, NW Italy). *Journal of Sedimentary Research*, *74*(5), 662-676.

Clayton, C. J., & Dando, P. R. (1996). Comparison of seepage and seal leakage rates. In Schumacher, D., Abrams, M. A., eds., *Hydrocarbon migration and its near surface expression: AAPG Memoi*r 66, p. 169-171.

Clayton, C. J., & Hay, S. J. (1994). Gas migration mechanisms from accumulation to surface. *Bulletin of the Geological Society of Denmark*, 41(1), 12-23

Cohen, D., Person, M., Wang, P., Gable, C. W., Hutchinson, D., Marksamer, A., ... & Evans, R. L. (2010). Origin and extent of fresh paleowaters on the Atlantic continental shelf, USA. *Groundwater*, *48*(1), 143-158.

Connelly, D. (2019). RRS James Cook Cruise JC180 25 April-30 May 2019. Strategies for the Environmental Monitoring of Marine Carbon Capture and Storage, STEMM-CCS.

Crowley, T. J. (2000). Causes of climate change over the past 1000 years. *Science*, *289*(5477), 270-277.

Cuthbert, M. O., Gleeson, T., Moosdorf, N., Befus, K. M., Schneider, A., Hartmann, J., & Lehner, B. (2019). Global patterns and dynamics of climate–groundwater interactions. *Nature Climate Change*, *9*(2), 137-141.

Dando, P. R., Austen, M. C., Burke Jr, R. A., Kendall, M. A., Kennicutt, M. C., Judd, A. G., ... & Southward, A. J. (1991). Ecology of a North Sea pockmark with an active methane seep. *Marine Ecology Progress Series*, 49-63.

De Boever, E., Swennen, R., & Dimitrov, L. (2006a). Lower Eocene carbonate cemented chimneys (Varna, NE Bulgaria): Formation mechanisms and the (a) biological mediation of chimney growth?. *Sedimentary Geology*, *185*(3-4), 159-173.

De Boever, E., Swennen, R., & Dimitrov, L. (2006b). Lower Eocene carbonate-cemented “chimney” structures (Varna, Bulgaria)—control of seepage rates on their formation and stable isotopic signature. *Journal of Geochemical Exploration*, *89*(1-3), 78-82.

Denman, K.L., Brasseur, G., Chidthaisong, A., Ciais, P., Cox, P.M., Dickinson, R.E., Hauglustaine, D., Heinze, C., Holland, E., Jacob, D., Lohmann, U., Ramachandran, S., da Silva Dias, P.L., Wofsy, S.C. and Zhang, X. (2007). *Couplings between changes in the climate system and biogeochemistry*. In: *Climate Change 2007: The Physical Science Basis. Contribution of Working Group I to the Fourth Assessment Report of the Intergovernmental Panel on Climate Change* [S. Solomon, D. Qin, M. Manning, Z. Chen, M. Marquis, K.B. Averyt, M. Tignor and H.L. Miller, (eds.)], Cambridge University Press, Cambridge and New York, NY, USA.

Dıaz-del-Rıo, V., Somoza, L., Martınez-Frias, J., Mata, M. P., Delgado, A., Hernandez-Molina, F. J., ... & León, R. (2003). Vast fields of hydrocarbon-derived carbonate chimneys related to the accretionary wedge/olistostrome of the Gulf of Cádiz. *Marine geology*, *195*(1-4), 177-200.

Dickens, G. R. (2011). Down the rabbit hole: Toward appropriate discussion of methane release from gas hydrate systems during the Paleocene-Eocene thermal maximum and other past hyperthermal events. *Climate of the Past*, *7*(3), 831-846.

Dickens, G. R., Castillo, M. M., & Walker, J. C. (1997). A blast of gas in the latest Paleocene: Simulating first-order effects of massive dissociation of oceanic methane hydrate. *Geology*, *25*(3), 259-262.

Domenico, S. N. (1976). Effect of brine-gas mixture on velocity in an unconsolidated sand reservoir. *Geophysics*, *41*(5), 882-894.

Domenico, S. N. (1977). Elastic properties of unconsolidated porous sand reservoirs. *Geophysics*, *42*(7), 1339-1368.

Dugan, B., & Flemings, P. B. (2000). Overpressure and fluid flow in the New Jersey continental slope: Implications for slope failure and cold seeps. *Science*, *289*(5477), 288-291.

Dugan, B., & Flemings, P. B. (2002). Fluid flow and stability of the US continental slope offshore New Jersey from the Pleistocene to the present. *Geofluids*, *2*(2), 137-146.

Dulaiova, H., Camilli, R., Henderson, P. B., & Charette, M. A. (2010). Coupled radon, methane and nitrate sensors for large-scale assessment of groundwater discharge and non-point source pollution to coastal waters. *Journal of Environmental Radioactivity*, *101*(7), 553-563.

Dumke, I., Berndt, C., Crutchley, G. J., Krause, S., Liebetrau, V., Gay, A., & Couillard, M. (2014). Seal bypass at the Giant Gjallar Vent (Norwegian Sea): Indications for a new phase of fluid venting at a 56-Ma-old fluid migration system. *Marine Geology*, 351, 38-52.

Egholm, D. L., Clausen, O. R., Sandiford, M., Kristensen, M. B., & Korstgård, J. A. (2008). The mechanics of clay smearing along faults. *Geology*, *36*(10), 787-790.

Eidvin, T., & Øverland, J. A. (2009). Faulty geology halts project. *Norwegian Continental Shelf*, *2*, 35-36.

Ensley, R. A. (1984). Comparison of P-and S-wave seismic data: A new method for detecting gas reservoirs. *Geophysics*, *49*(9), 1420-1431.

Etiope, G., Lassey, K. R., Klusman, R. W., & Boschi, E. (2008). Reappraisal of the fossil methane budget and related emission from geologic sources. *Geophysical Research Letters*, *35*(9).

Flemings, P. B., Long, H., Dugan, B., Germaine, J., John, C. M., Behrmann, J. H., ... & Expedition, I. O. D. P. (2008). Pore pressure penetrometers document high overpressure near the seafloor where multiple submarine landslides have occurred on the continental slope, offshore Louisiana, Gulf of Mexico. *Earth and Planetary Science Letters*, 269(3), 309-325.

Fletcher, S. E. M., & Schaefer, H. (2019). Rising methane: A new climate challenge. *Science*, *364*(6444), 932-933.

Furre, A. K., Eiken, O., Alnes, H., Vevatne, J. N., & Kiær, A. F. (2017). 20 Years of Monitoring CO2-injection at Sleipner. *Energy procedia*, *114*, 3916-3926.

Gafeira, J., Dolan, M., & Monteys, X. (2018). Geomorphometric characterization of pockmarks by using a GIS-based semi-automated toolbox. *Geosciences*, *8*(5), 154.

Gasda, S. E., Bachu, S., & Celia, M. A. (2004). Spatial characterization of the location of potentially leaky wells penetrating a deep saline aquifer in a mature sedimentary basin. *Environmental geology*, *46*(6-7), 707-720.Gay et al., 2007

Geersen, J., Behrmann, J. H., Völker, D., Krastel, S., Ranero, C. R., Diaz-Naveas, J., & Weinrebe, W. (2011). Active tectonics of the South Chilean marine fore arc (35 S–40 S). *Tectonics*, *30*(3).

Geersen, J., Scholz, F., Linke, P., Schmidt, M., Lange, D., Behrmann, J. H., ... & Hensen, C. (2016). Fault zone controlled seafloor methane seepage in the rupture area of the 2010 M aule earthquake, C entral C hile. *Geochemistry, Geophysics, Geosystems*, *17*(11), 4802-4813.

Gibbins, J., & Chalmers, H. (2008). Carbon capture and storage. *Energy policy*, *36*(12), 4317-4322.

Global CCS Institute (2018). The Global Status of CCS: 2018, Melbourne, Australia. Retrieved from https://www.globalccsinstitute.com/resources/global-status-report/.

Goff, J. A. (2019). Modern and fossil pockmarks in the New England Mud Patch: Implications for submarine groundwater discharge on the middle shelf. *Geophysical Research Letters*.

Grando, G., & McClay, K. (2007). Morphotectonics domains and structural styles in the Makran accretionary prism, offshore Iran. *Sedimentary Geology*, *196*(1-4), 157-179.

Granli, J. R., Arntsen, B., Sollid, A., & Hilde, E. (1999). Imaging through gas-filled sediments using marine shear-wave data. *Geophysics*, *64*(3), 668-677.

Grimstad, A. A., Georgescu, S., Lindeberg, E., & Vuillaume, J. F. (2009). Modelling and simulation of mechanisms for leakage of CO2 from geological storage. *Energy Procedia*, *1*(1), 2511-2518.

Grollimund, B., & Zoback, M. D. (2003). Impact of glacially induced stress changes on fault-seal integrity offshore Norway. *AAPG bulletin*, *87*(3), 493-506.

Gulick, S. P., Bangs, N. L., Moore, G. F., Ashi, J., Martin, K. M., Sawyer, D. S., ... and Taira, A. (2010). Rapid forearc basin uplift and megasplay fault development from 3D seismic images of Nankai Margin off Kii Peninsula, Japan. *Earth and Planetary Science Letters*, *300*(1), 55-62.

Gurevich, A. E., Endres, B. L., Robertson Jr, J. O., & Chilingar, G. V. (1993). Gas migration from oil and gas fields and associated hazards. *Journal of Petroleum Science and Engineering*, *9*(3), 223-238.

Gustafson, C., Key, K., & Evans, R. L. (2019). Aquifer systems extending far offshore on the US Atlantic margin. *Scientific Reports*, *9*(1), 8709.

Haeckel, M., Suess, E., Wallmann, K., & Rickert, D. (2004). Rising methane gas bubbles form massive hydrate layers at the seafloor. *Geochimica et Cosmochimica Acta*, *68*(21), 4335-4345.

Haszeldine, R. S. (2009). Carbon capture and storage: how green can black be?. *Science*, *325*(5948), 1647-1652.

Heggland, R. (1997). Detection of gas migration from a deep source by the use of exploration 3D seismic data. *Marine Geology*, *137*(1-2), 41-47.

Hensen, C., Nuzzo, M., Hornibrook, E., Pinheiro, L. M., Bock, B., Magalhães, V. H., & Brückmann, W. (2007). Sources of mud volcano fluids in the Gulf of Cadiz—indications for hydrothermal imprint. *Geochimica et Cosmochimica Acta*, *71*(5), 1232-1248.

Higgins, J. A., & Schrag, D. P. (2006). Beyond methane: towards a theory for the Paleocene–Eocene thermal maximum. *Earth and Planetary Science Letters*, *245*(3-4), 523-537.

Holbrook, W. S., Hoskins, H., Wood, W. T., Stephen, R. A., & Lizarralde, D. (1996). Methane hydrate and free gas on the Blake Ridge from vertical seismic profiling. *Science*, *273*(5283), 1840-1843.

Hooper, E. C. D. (1991). Fluid migration along growth faults in compacting sediments. *Journal of Petroleum Geology*, *14*, 161-180.

Hornbach, M. J., Holbrook, W. S., Gorman, A. R., Hackwith, K. L., Lizarralde, D., & Pecher, I. (2003). Direct seismic detection of methane hydrate on the Blake Ridge. *Geophysics*, *68*(1), 92-100.

Hornbach, M. J., Ruppel, C., & Van Dover, C. L. (2007). Three-dimensional structure of fluid conduits sustaining an active deep marine cold seep. *Geophysical Research Letters*, *34*(5).

Hovland, M. (1983). Elongated depressions associated with pockmarks in the western slope of the Norwegian Trench. *Marine Geology*, *51*(1-2), 35-46.

Hovland, M., & Sommerville, J. H. (1985). Characteristics of two natural gas seepages in the North Sea. *Marine and Petroleum Geology*, 2(4), 319-326.

Hubbert, M.K., Willis, D.G., 1957. Mechanic of hydraulic fracturing. *Trans. Soc. Pet. Eng*. AIME1957, 153–168.

Hurst, A., Scott, A., & Vigorito, M. (2011). Physical characteristics of sand injectites. *Earth-Science Reviews*, *106*(3-4), 215-246.

Huuse, M., Jackson, C. A. L., Van Rensbergen, P., Davies, R. J., Flemings, P. B., & Dixon, R. J. (2010). Subsurface sediment remobilization and fluid flow in sedimentary basins: an overview. *Basin Research*, *22*(4), 342-360.

Huuse, M., Shoulders, S. J., Netoff, D. I., & Cartwright, J. (2005). Giant sandstone pipes record basin-scale liquefaction of buried dune sands in the Middle Jurassic of SE Utah. *Terra Nova*, *17*(1), 80-85.

IEA (2012). World Energy Outlook 2012, World Energy Outlook, World Energy Outlook. OECD Publishing. doi:10.1787/weo-2012-en

IEA (2019, July 16). IEA launches new tool for tracking oil and gas-related methane emissions worldwide. Retrieved from https://www.iea.org/newsroom/news/2019/july/iea-launches-new-tool-for-tracking-oil-and-gas-related-methane-emissions.html.

IMO (2019, October 14). Addressing barriers to transboundary carbon capture and storage. Retrieved from http://www.imo.org/en/MediaCentre/PressBriefings/Pages/22-CCS-LP-resolution .aspx?ct=t(CCSA_Daily_Bulletin_Tuesday_25_April_2014_25_2017_).

IPCC (2018). Global Warming of 1.5°C. *An IPCC Special Report on the impacts of global warming of 1.5°C above pre-industrial levels and related global greenhouse gas emission pathways, in the context of strengthening the global response to the threat of climate change, sustainable development, and efforts to eradicate poverty* [Masson-Delmotte, V., P. Zhai, H.-O. Pörtner, D. Roberts, J. Skea, P.R. Shukla, A. Pirani, W. Moufouma-Okia, C. Péan, R. Pidcock, S. Connors, J.B.R. Matthews, Y. Chen, X. Zhou, M.I. Gomis, E. Lonnoy, T. Maycock, M. Tignor, and T. Waterfield (eds.)]. In Press.

Judd, A. G., & Hovland, M. (1992). The evidence of shallow gas in marine sediments. *Continental Shelf Research*, *12*(10), 1081-1095.

Judd, A. G., Long, D., & Sankey, M. (1994). Pockmark formation and activity, UK block 15/25, North Sea. *Bulletin of the Geological Society of Denmark*, 41(1), 34-49.

Judd, A., & Hovland, M. (2007). Seabed fluid flow: the impact on geology, biology and the marine environment. *Cambridge University Press*.

Kang, M., Christian, S., Celia, M. A., Mauzerall, D. L., Bill, M., Miller, A. R., ... & Jackson, R. B. (2016). Identification and characterization of high methane-emitting abandoned oil and gas wells. *Proceedings of the National Academy of Sciences*, *113*(48), 13636-13641.

Karstens, J., & Berndt, C. (2015). Seismic chimneys in the Southern Viking Graben–Implications for palaeo fluid migration and overpressure evolution. *Earth and Planetary Science Letters*, *412*, 88-100.

Karstens, J., Ahmed, W., Berndt, C., & Class, H. (2017). Focused fluid flow and the sub-seabed storage of CO2: Evaluating the leakage potential of seismic chimney structures for the Sleipner CO2 storage operation. *Marine and Petroleum Geology*, *88*, 81-93.

Karstens, J., Haflidason, H., Becker, L. W., Berndt, C., Rüpke, L., Planke, S., ... & Mienert, J. (2018). Glacigenic sedimentation pulses triggered post-glacial gas hydrate dissociation. *Nature communications*, *9*(1), 635.

Karstens, J., Müller, P., Berndt, C., & Patruno, S. (2019). Deep-seated focused fluid migration as indicator for hydrocarbon leads in the East Shetland Platform, North Sea Province. *Geological Society, London, Special Publications*, *494*, SP494-2019.

King, L. H., & Maclean, B. (1970). Pockmarks on the Scotian Shelf. *Geological Society of America Bulletin*, *81*, 3141.

Kopf, A. J. (2002). Significance of mud volcanism. *Reviews of Geophysics*, *40*(2), 2-1.

Kopp, A., Binning, P. J., Johannsen, K., Helmig, R., & Class, H. (2010). A contribution to risk analysis for leakage through abandoned wells in geological CO2 storage. *Advances in Water Resources*, *33*(8), 867-879.

Kornfeld, J. A. (1964). Wild blowout taps first North Sea gas. *World Oil*, 78.

Krämer, K., Holler, P., Herbst, G., Bratek, A., Ahmerkamp, S., Neumann, A., ... & Winter, C. (2017). Abrupt emergence of a large pockmark field in the German Bight, southeastern North Sea. *Scientific reports*, *7*(1), 5150.

Kulm, L. D., & Suess, E. (1990). Relationship between carbonate deposits and fluid venting: Oregon accretionary prism. *Journal of Geophysical Research: Solid Earth*, *95*(B6), 8899-8915.

Kvenvolden, K. A. (1988). Methane hydrate—a major reservoir of carbon in the shallow geosphere?. *Chemical geology*, *71*(1-3), 41-51.

Kvenvolden, K. A. (1993). Gas hydrates—geological perspective and global change. *Reviews of geophysics*, *31*(2), 173-187.

Landrø, M., Wehner, D., Vedvik, N., Ringrose, P., Løhre, N. L., & Berteussen, K. (2019). Gas flow through shallow sediments—A case study using passive and active seismic field data. *International Journal of Greenhouse Gas Control*, *87*, 121-133.

Lebedeva-Ivanova, N., Polteau, S., Bellwald, B., Planke, S., Berndt, C., & Stokke, H. H. (2018). Toward one-meter resolution in 3D seismic. *The Leading Edge*, *37*(11), 818-828.

Lecher, A. L., Kessler, J., Sparrow, K., Garcia-Tigreros Kodovska, F., Dimova, N., Murray, J., ... & Paytan, A. (2016). Methane transport through submarine groundwater discharge to the N orth P acific and A rctic Ocean at two A laskan sites. *Limnology and Oceanography*, *61*(S1), S344-S355.

Leifer, I., & Judd, A. (2015). The UK22/4b blowout 20 years on: Investigations of continuing methane emissions from sub-seabed to the atmosphere in a North Sea context. *Marine and Petroleum Geology*, *68*, 706-717.

Leifer, I., Boles, J. R., Luyendyk, B. P., & Clark, J. F. (2004). Transient discharges from marine hydrocarbon seeps: spatial and temporal variability. *Environmental Geology*, *46*(8), 1038-1052.

Lindeberg, E., Vuillaume, J. F., & Ghaderi, A. (2009). Determination of the CO2 storage capacity of the Utsira formation. *Energy Procedia*, *1*(1), 2777-2784.

Løseth, H., Gading, M., & Wensaas, L. (2009). Hydrocarbon leakage interpreted on seismic data. *Marine and Petroleum Geology*, *26*(7), 1304-1319.

Marfurt, K. J., & Alves, T. M. (2015). Pitfalls and limitations in seismic attribute interpretation of tectonic features. *Interpretation*, *3*(1), SB5-SB15.

Marín-Moreno, H., Bull, J. M., Matter, J. M., Sanderson, D. J., & Roche, B. J. (2019). Reactive transport modelling insights into CO2 migration through sub-vertical fluid flow structures. *International Journal of Greenhouse Gas Control*, *86*, 82-92.

Matter, J. M., Broecker, W. S., Gislason, S. R., Gunnlaugsson, E., Oelkers, E. H., Stute, M., ... & Axelsson, G. (2011). The CarbFix Pilot Project–storing carbon dioxide in basalt. *Energy Procedia*, *4*, 5579-5585.

McNeill, L. C., Piper, K. A., Goldfinger, C., Kulm, L. D., & Yeats, R. S. (1997). Listric normal faulting on the Cascadia continental margin. *Journal of Geophysical Research: Solid Earth*, *102*(B6), 12123-12138.

Metz, B., Davidson, O., De Coninck, H., Loos, M., & Meyer, L. (2005). *IPCC special report on carbon dioxide capture and storage*. Intergovernmental Panel on Climate Change, Geneva (Switzerland). Working Group III.

Michael, K., Golab, A., Shulakova, V., Ennis-King, J., Allinson, G., Sharma, S., & Aiken, T. (2010). Geological storage of CO2 in saline aquifers—A review of the experience from existing storage operations. *International Journal of Greenhouse Gas Control*, *4*(4), 659-667.

Mienert, J., Posewang, J., & Baumann, M. (1998). Gas hydrates along the northeastern Atlantic margin: possible hydrate-bound margin instabilities and possible release of methane. *Geological Society, London, Special Publications*, *137*(1), 275-291.

Milkov, A. V. (2004). Global estimates of hydrate-bound gas in marine sediments: how much is really out there?. *Earth-Science Reviews*, *66*(3-4), 183-197.

Miller, S. M., Wofsy, S. C., Michalak, A. M., Kort, E. A., Andrews, A. E., Biraud, S. C., ... & Miller, B. R. (2013). Anthropogenic emissions of methane in the United States. *Proceedings of the National Academy of Sciences*, *110*(50), 20018-20022.

Montague, J. A., Pinder, G. F., & Watson, T. L. (2018). Predicting gas migration through existing oil and gas wells. *Environmental Geosciences*, *25*(4), 121-132.

Moore, G. F., Boston, B. B., Sacks, A. F., & Saffer, D. M. (2013). Analysis of normal fault populations in the Kumano Forearc Basin, Nankai Trough, Japan: 1. Multiple orientations and generations of faults from 3-D coherency mapping. *Geochemistry, Geophysics, Geosystems*, *14*(6), 1989-2002.

Moore, W. S. (2010). The effect of submarine groundwater discharge on the ocean. *Annual review of marine science*, *2*, 59-88.

Moosdorf, N., & Oehler, T. (2017). Societal use of fresh submarine groundwater discharge: An overlooked water resource. *Earth-Science Reviews*, *171*, 338-348.

Moss, J. L., & Cartwright, J. (2010). The spatial and temporal distribution of pipe formation, offshore Namibia. *Marine and Petroleum Geology*, *27*(6), 1216-1234.

Mueller, R. J. (2015). Evidence for the biotic origin of seabed pockmarks on the Australian continental shelf. *Marine and Petroleum Geology*, *64*, 276-293.

Nardelli, B. B., Budillon, F., Watteaux, R., Ciccone, F., Conforti, A., De Falco, G., ... & Iudicone, D. (2017). Pockmark morphology and turbulent buoyant plumes at a submarine spring. *Continental Shelf Research*, *148*, 19-36.

Naylor, M., Wilkinson, M., & Haszeldine, R. S. (2011). Calculation of CO2 column heights in depleted gas fields from known pre-production gas column heights. *Marine and Petroleum Geology*, *28*(5), 1083-1093.

Nicoll, G. D. (2012). Evaluation of the Nordland Group overburden as an effective seal for the Sleipner CO2 storage site (offshore Norway) using analytical and stochastic modelling techniques. *Doctoral dissertation*, Heriot-Watt University, Edinburgh, United Kingdom.

Niemann, H., Elvert, M., Hovland, M., Orcutt, B., Judd, A., Suck, I., ... & Boetius, A. (2005). Methane emission and consumption at a North Sea gas seep (Tommeliten area). *Biogeosciences Discussions*, *2*(4), 1197-1241.

Nisbet, E. G. (1990). The end of the ice age. *Canadian Journal of Earth Sciences*, *27*(1), 148-157.

Nogues, J. P., Court, B., Dobossy, M., Nordbotten, J. M., & Celia, M. A. (2012). A methodology to estimate maximum probable leakage along old wells in a geological sequestration operation. *International Journal of Greenhouse Gas Control*, *7*, 39-47.

Noothout, P., Wiersma, F., Hurtado, O., Macdonald, D., Kemper, J., & van Alphen, K. (2014). CO2 Pipeline infrastructure–lessons learnt. *Energy Procedia*, *63*, 2481-2492.

Nordbotten, J. M., Celia, M. A., & Bachu, S. (2004). Analytical solutions for leakage rates through abandoned wells. *Water Resources Research*, *40*(4).

Nordbotten, J. M., Celia, M. A., & Bachu, S. (2005). Injection and storage of CO 2 in deep saline aquifers: analytical solution for CO 2 plume evolution during injection. *Transport in Porous media*, *58*(3), 339-360.

Orlic, B., Chitu, A., Brunner, L., Koenen, M., Wollenweber, J., & Schreppers, G. J. (2018, August). Numerical investigations of cement interface debonding for assessing well integrity risks. In *52nd US Rock Mechanics/Geomechanics Symposium*. American Rock Mechanics Association.

Osborne, M. J., & Swarbrick, R. E. (1997). Mechanisms for generating overpressure in sedimentary basins: a reevaluation. *AAPG bulletin*, *81*(6), 1023-1041.

Paull, C., Ussler Iii, W., Maher, N., Greene, H. G., Rehder, G., Lorenson, T., & Lee, H. (2002). Pockmarks off Big Sur, California. *Marine Geology*, *181*(4), 323-335.

Pecher, I. A., Villinger, H., Kaul, N., Crutchley, G. J., Mountjoy, J. J., Huhn, K., ... & Coffin, R. B. (2017). A fluid pulse on the Hikurangi subduction margin: Evidence from a heat flux transect across the upper limit of gas hydrate stability. *Geophysical Research Letters*, *44*(24), 12-385.

Pinero, E., Marquardt, M., Hensen, C., Haeckel, M., & Wallmann, K. (2013). Estimation of the global inventory of methane hydrates in marine sediments using transfer functions. *Biogeosciences (BG)*, *10*(2), 959-975.

Post, V. E., Groen, J., Kooi, H., Person, M., Ge, S., & Edmunds, W. M. (2013). Offshore fresh groundwater reserves as a global phenomenon. *Nature*, *504*(7478), 71-78.

Postma, T. J., Bandilla, K. W., & Celia, M. A. (2019). Estimates of CO2 leakage along abandoned wells constrained by new data. *International Journal of Greenhouse Gas Control*, *84*, 164-179.

Ranero, C. R., Grevemeyer, I., Sahling, H., Barckhausen, U., Hensen, C., Wallmann, K., ... & McIntosh, K. (2008). Hydrogeological system of erosional convergent margins and its influence on tectonics and interplate seismogenesis. *Geochemistry, Geophysics, Geosystems, 9*(3).

Ritger, S., Carson, B., & Suess, E. (1987). Methane-derived authigenic carbonates formed by subduction-induced pore-water expulsion along the Oregon/Washington margin. *Geological Society of America Bulletin*, *98*(2), 147-156.

Ross, J. A., Peakall, J., & Keevil, G. M. (2014). Facies and flow regimes of sandstone-hosted columnar intrusions: Insights from the pipes of Kodachrome Basin State Park. *Sedimentology*, *61*(6), 1764-1792.

Ruppel, C. D., & Kessler, J. D. (2017). The interaction of climate change and methane hydrates. *Reviews of Geophysics*, *55*(1), 126-168.

Saffer, D. M. (2017). Mapping fluids to subduction megathrust locking and slip behavior. *Geophysical Research Letters*, *44*(18), 9337-9340.

Saffer, D. M., & Bekins, B. A. (1999). Fluid budgets at convergent plate margins: Implications for the extent and duration of fault-zone dilation. *Geology, 27*(12), 1095-1098.

Saffer, D. M., & Tobin, H. J. (2011). Hydrogeology and mechanics of subduction zone forearcs: Fluid flow and pore pressure. *Annual Review of Earth and Planetary Sciences*, *39*, 157-186.

Saunois, M., Bousquet, P., Poulter, B., Peregon, A., Ciais, P., Canadell, J. G., ... & Janssens-Maenhout, G. (2016). The global methane budget 2000–2012. *Earth System Science Data (Online)*, 8(2).

Schneider von Deimling, J., Brockhoff, J., & Greinert, J. (2007). Flare imaging with multibeam systems: Data processing for bubble detection at seeps. *Geochemistry, Geophysics, Geosystems, 8*(6).

Screaton, E., Saffer, D., Henry, P., & Hunze, S. (2002). Porosity loss within the underthrust sediments of the Nankai accretionary complex: Implications for overpressures. *Geology*, *30*(1), 19-22.

Shipley, T. H., Houston, M. H., Buffler, R. T., Shaub, F. J., McMillen, K. J., Ladd, J. W., & Worzel, J. L. (1979). Seismic evidence for widespread possible gas hydrate horizons on continental slopes and rises. *AAPG bulletin*, *63*(12), 2204-2213.

Sibson, R. H. (1992). Implications of fault-valve behaviour for rupture nucleation and recurrence. *Tectonophysics*, *211*(1-4), 283-293.

Stieglitz, T. (2005). Submarine groundwater discharge into the near-shore zone of the Great Barrier Reef, Australia. *Marine Pollution Bulletin*, *51*(1-4), 51-59.

Suess, E., Torres, M. E., Bohrmann, G., Collier, R. W., Greinert, J., Linke, P., ... & Zuleger, E. (1999). Gas hydrate destabilization: enhanced dewatering, benthic material turnover and large methane plumes at the Cascadia convergent margin. *Earth and Planetary Science Letters*, *170*(1-2), 1-15.

Svensen, H., Planke, S., Malthe-Sørenssen, A., Jamtveit, B., Myklebust, R., Eidem, T. R., & Rey, S. S. (2004). Release of methane from a volcanic basin as a mechanism for initial Eocene global warming. *Nature*, *429*(6991), 542.

Talukder, A. R. (2012). Review of submarine cold seep plumbing systems: leakage to seepage and venting. *Terra Nova*, *24*(4), 255-272.

Taniguchi, M., Burnett, W. C., Cable, J. E., & Turner, J. V. (2002). Investigation of submarine groundwater discharge. *Hydrological Processes*, *16*(11), 2115-2129.

Thatje, S., Gerdes, D., & Rachor, E. (1999). A seafloor crater in the German Bight and its effects on the benthos. *Helgoland Marine Research*, *53*(1), 36.

Townsend-Small, A., Ferrara, T. W., Lyon, D. R., Fries, A. E., & Lamb, B. K. (2016). Emissions of coalbed and natural gas methane from abandoned oil and gas wells in the United States. *Geophysical Research Letters*, *43*(5), 2283-2290.

Van Rensbergen, P., Depreiter, D., Pannemans, B., Moerkerke, G., Van Rooij, D., Marsset, B., ... & Magalhaes, V. (2005). The El Arraiche mud volcano field at the Moroccan Atlantic slope, Gulf of Cadiz. *Marine Geology*, *219*(1), 1-17.

Vielstädte, L., Haeckel, M., Karstens, J., Linke, P., Schmidt, M., Steinle, L., & Wallmann, K. (2017). Shallow gas migration along hydrocarbon wells–An unconsidered, anthropogenic source of biogenic methane in the North Sea. *Environmental science & technology*, *51*(17), 10262-10268.

Vielstädte, L., Linke, P., Schmidt, M., Sommer, S., Haeckel, M., Braack, M., & Wallmann, K. (2019). Footprint and detectability of a well leaking CO2 in the Central North Sea: Implications from a field experiment and numerical modelling. *International Journal of Greenhouse Gas Control*, *84*, 190-203.

Viso, R., McCoy, C., Gayes, P., & Quafisi, D. (2010). Geological controls on submarine groundwater discharge in Long Bay, South Carolina (USA). *Continental Shelf Research*, *30*(3-4), 335-341.

Watson, S. J., Mountjoy, J. J., Barnes, P. M., Crutchley, G. J., Lamarche, G., Higgs, B., ... & Mitchell, J. (2019). Focused fluid seepage related to variations in accretionary wedge structure, Hikurangi margin, New Zealand. *Geology*.

Wegener, G., Shovitri, M., Knittel, K., Niemann, H., Hovland, M., & Boetius, A. (2008). Biogeochemical processes and microbial diversity of the Gullfaks and Tommeliten methane seeps (Northern North Sea*). Biogeosciences Discussions*, 5(1), 971-1015.

Whitaker, S. (1986). Flow in porous media I: A theoretical derivation of Darcy's law. *Transport in porous media*, *1*(1), 3-25.

White, J. A., Chiaramonte, L., Ezzedine, S., Foxall, W., Hao, Y., Ramirez, A., & McNab, W. (2014). Geomechanical behavior of the reservoir and caprock system at the In Salah CO2 storage project. *Proceedings of the National Academy of Sciences*, *111*(24), 8747-8752.

White, J. E. (1975). Computed seismic speeds and attenuation in rocks with partial gas saturation. *Geophysics*, 40(2), 224-232.

Whiticar, M. J. (2000). Can stable isotopes and global budgets be used to constrain atmospheric methane budgets?. In *Atmospheric methane* (pp. 63-85). Springer, Berlin, Heidelberg.

Whiticar, M. J. (2002). Diagenetic relationships of methanogenesis, nutrients, acoustic turbidity, pockmarks and freshwater seepages in Eckernförde Bay. *Marine Geology*, *182*(1-2), 29-53.

Wiprut, D., & Zoback, M. D. (2000). Fault reactivation and fluid flow along a previously dormant normal fault in the northern North Sea. *Geology*, *28*(7), 595-598.

WMO (2018, November 22). The State of Greenhouse Gases in the Atmosphere based on global observations through 2017. *WMO Greenhouse Gas Bulletin*, World Meteorological Organization, Geneva, Switzerland.

Zachos, J., Pagani, M., Sloan, L., Thomas, E., & Billups, K. (2001). Trends, rhythms, and aberrations in global climate 65 Ma to present. *science*, *292*(5517), 686-693.

Zoback, M. D., & Gorelick, S. M. (2012). Earthquake triggering and large-scale geologic storage of carbon dioxide. *Proceedings of the National Academy of Sciences*, *109*(26), 10164-10168.

Zoback, M. D., & Gorelick, S. M. (2015). To prevent earthquake triggering, pressure changes due to CO2 injection need to be limited. *Proceedings of the National Academy of Sciences*, *112*(33), E4510-E4510.

## 2. Pockmarks in the Witch Ground Basin, Central North Sea

Christoph Böttner, Christian Berndt, Benedict T. I. Reinardy, Jacob Geersen, Jens Karstens, Jonathan M. Bull, Ben J. Callow, Anna Lichtschlag, Mark Schmidt, Judith Elger, Bettina Schramm, Matthias Haeckel

Published in 2018 Geochemistry, Geophysics, Geosystems, 20(4), 1698-1719.

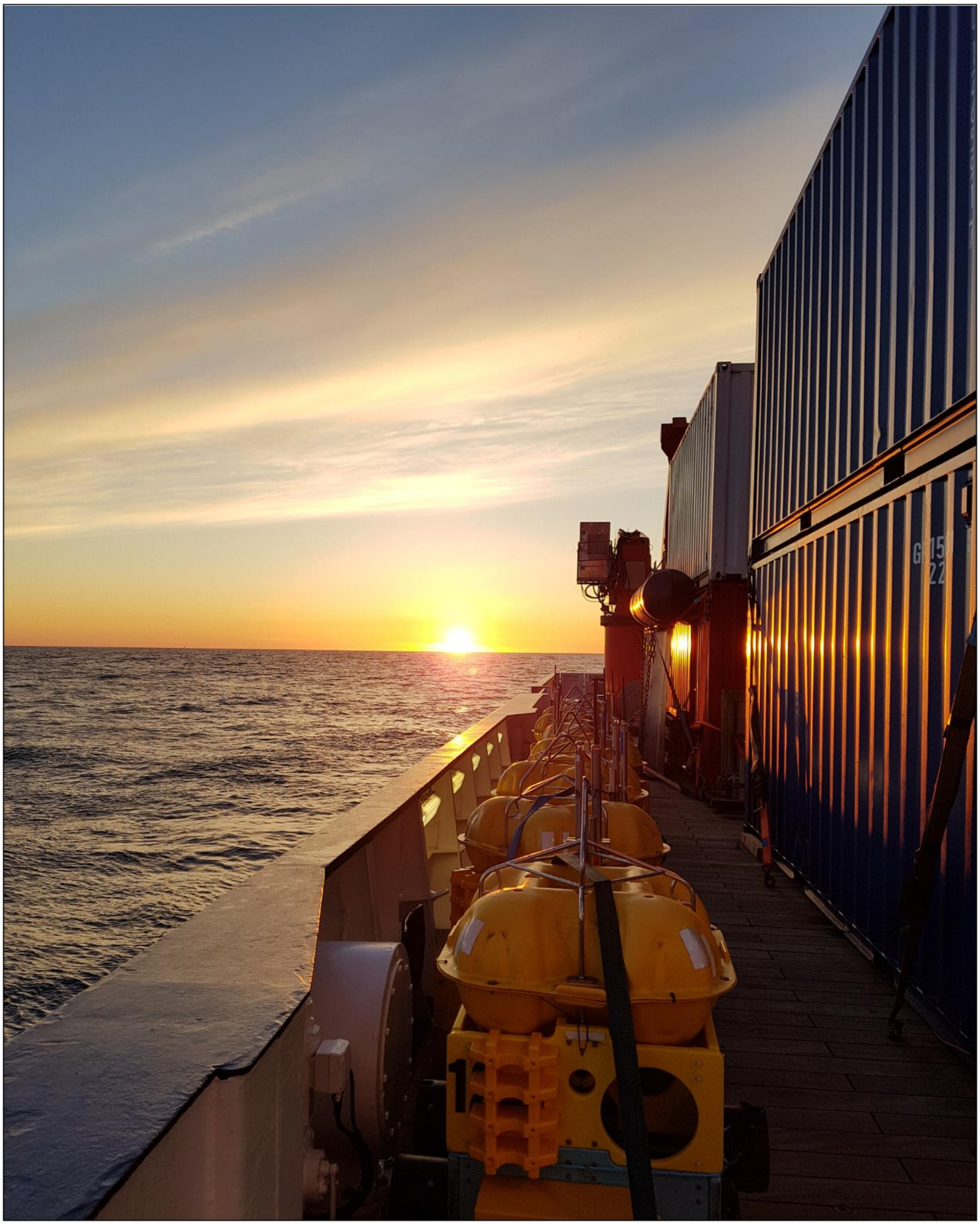

Sundown during MSM63 – PERMO to the Central North Sea.

**Key Points**

1. Marine geophysical data document > 1500 pockmarks of two morphological classes in the Witch Ground Basin, central North Sea.
2. Class 1 pockmarks are continuously active and supplied through seismic pipe structures by deeply sourced methane.
3. Class 2 pockmarks form at specific stratigraphic horizons suggesting intermittent venting triggered by pressure and temperature changes.

## 2.1. Abstract

Marine sediments host large amounts of methane ($CH_4$), which is a potent greenhouse gas. Quantitative estimates for methane release from marine sediments are scarce, and a poorly constrained temporal variability leads to large uncertainties in methane emission scenarios. Here, we use 2D and 3D seismic reflection, multibeam bathymetric, geochemical and sedimentological data to (I) map and describe pockmarks in the Witch Ground Basin (central North Sea), (II) characterize associated sedimentological and fluid migration structures, and (III) analyze the related methane release. More than 1500 pockmarks of two distinct morphological classes spread over an area of 225 km². The two classes form independently from another and are corresponding to at least two different sources of fluids. Class 1 pockmarks are large in size (> 6 m deep, > 250 m long, and > 75 m wide), show active venting, and are located above vertical fluid conduits that hydraulically connect the seafloor with deep methane sources. Class 2 pockmarks, which comprise 99.5 % of all pockmarks, are smaller (0.9-3.1 m deep, 26-140 m long, and 14-57 m wide) and are limited to the soft, fine-grained sediments of the Witch Ground Formation and possibly sourced by compaction-related dewatering. Buried pockmarks within the Witch Ground Formation document distinct phases of pockmark formation, likely triggered by external forces related to environmental changes after deglaciation. Thus, greenhouse gas emissions from pockmark fields cannot be based on pockmark numbers and present-day fluxes but require an analysis of the pockmark forming processes through geological time.

## 2.2. Plain language summary

Marine sediments host large amounts of methane ($CH_4$), which is a potent greenhouse gas. The amount of methane released into the atmosphere is, however, largely unknown making it difficult to implement this methane source in climate models. Here we use geophysical, geochemical and sedimentological data to map the distribution of fluid escape structures in the central North Sea. More than 1500 pockmarks, which are circular to semi-circular depressions of the seafloor, indicate fluid flow from the subsurface. There are two distinct morphological classes of pockmarks corresponding to at least two different fluid sources. Class 1 pockmarks are large, show active venting, and are located above vertical fluid conduits in the subsurface, which feed fluids from deeper strata. Class 2 pockmarks, which comprise 99.5 % of all pockmarks, are smaller and limited to the soft sediments directly below the seafloor. Older pockmarks in the subsurface document distinct phases of pockmark formation, likely triggered

by external forces after the retreat of ice in the North Sea. The amount of methane released from natural geological sources based on pockmark numbers may be wrong as these do not take into account the origin and composition of released fluids.

## 2.3. Introduction

Earth's climate is highly sensitive to the release of potent greenhouse gases such as methane ($CH_4$) into to atmosphere. Methane has been released during climatic changes including the steepest known natural temperature increase on Earth at the Paleocene-Eocene Thermal Maximum around 55.5 Ma ago (Svensen et al., 2004; Dickens, 2011) but also during and after the Younger Dryas-Preboreal abrupt warming event at the beginning of the Holocene (about 11600 cal. years BP; Petrenko et al., 2017). However, current and future methane emissions remain poorly constrained and bottom up as well as top down approaches for the quantification of methane emissions have large uncertainties (Petrenko et al., 2017; Dean et al., 2018). The global methane emission from natural geological sources shows a wide range in estimates [33-75 Tg $CH_4$ $yr^{-1}$] (Etiope et al., 2008; Ciais et al., 2013), which highlights the large uncertainties involved in attributing and quantifying methane emissions.

Marine sediments host large amounts of methane in the form of free gas, hydrates or dissolved in porewater. There is evidence for direct contribution of methane from shallow marine sediments to the atmospheric methane budget and hence to climate change (Judd et al., 2002; Etiope et al., 2008). Methane formed in marine sediments may either be biogenic (derived from microbial degradation of organic matter) or thermogenic (generated in deep hydrocarbon reservoirs by thermal cracking of kerogens; Whiticar, 2000). The carbon and hydrogen isotope signatures and the relative proportions of methane and more mature hydrocarbons (e.g. ethane, propane, butane) can help distinguish between the two sources (Whiticar, 2000). Methane from both onshore and offshore micro- and macro-seeps contributes to the atmospheric methane budget and can be supplied by geothermal, volcanic or sedimentary sources (Etiope et al., 2008; Saunois et al., 2016; Dean et al., 2018). In the marine environment, methane may accumulate in the subsurface, when gas pressure exceeds the ambient hydrostatic pressure and the methane forms gas bubbles, which may be released by diffusion or episodic ebullition (Boudreau et al., 2005; Maeck et al., 2013; Krämer et al., 2017). However, the global significance of marine methane sources and their impact on the global methane budget remains poorly constrained (Ciais et al., 2013; Etiope et al., 2008; Petrenko et al., 2017).

One manifestation of focused fluid migration at the seafloor are circular to semi-circular depressions known as pockmarks, which may form in response to venting of fluids from the seafloor (Judd & Hovland, 2007). Pockmarks may be meters to hundreds of meters in diameter, meters to tens of meters in depth and affect the local environment, morphodynamics, biochemistry and ecology (Dando et al., 1991; Berndt 2005; Niemann et al., 2005; Judd & Hovland, 2007; Wegener et al., 2008). Increasing high-resolution bathymetric data coverage reveals the wide abundance of pockmarks at the seafloor in various structural and geologic settings (e.g. Hovland et al., 2002; Brothers et al., 2012; Gafeira et al., 2018). Understanding the processes that control the formation and activity of pockmarks is crucial to estimate the contribution of methane from natural geological sources to the atmospheric methane budget and its impact on climate change.

Pockmarks often form on top of focused fluid conduits, which manifest in seismic data as seismic chimneys or pipes and are characterized by circular shaped amplitude anomalies with dimmed reflections and bright spots at different depth levels (Cartwright et al., 2007; Løseth et al., 2009; Andresen, 2012; Karstens & Berndt, 2015). The terms seismic chimneys or pipes and pockmarks are attributed to the localized release of overpressure in the subsurface through hydraulic connection of deeper strata with the seafloor (Cole et al., 2000; Hustoft et al., 2009). Pockmarks that formed above pipe and chimney structures are observed globally, for example at the Vestnesa Ridge NW off Svalbard (Hustoft et al., 2009; Plaza-Faverola et al., 2017), in the Nyegga pockmark field on the continental Norwegian margin (Karstens et al., 2018), offshore Nigeria (Løseth et al., 2010), in the Western Nile Deep Sea Fan (Moss et al., 2012) and in the Lower Congo Basin (Gay et al., 2007).

The aim of this study is to analyze pockmark-forming processes in the Witch Ground Basin, central North Sea (Figure 2.1). We first map the abundant pockmarks and characterize them based on their morphology and subsurface pre-conditions. Secondly, we determine the source of fluids that contribute to pockmark formation in the Witch Ground Basin and investigate the interrelation of fluid flow and depositional processes during their formation. This includes determining if there are different sources of fluids, if they are located at different depths and if they provide different types of fluids. Subsequently we constrain the timing and the recurrence rate of pockmark formation in the Witch Ground Basin.

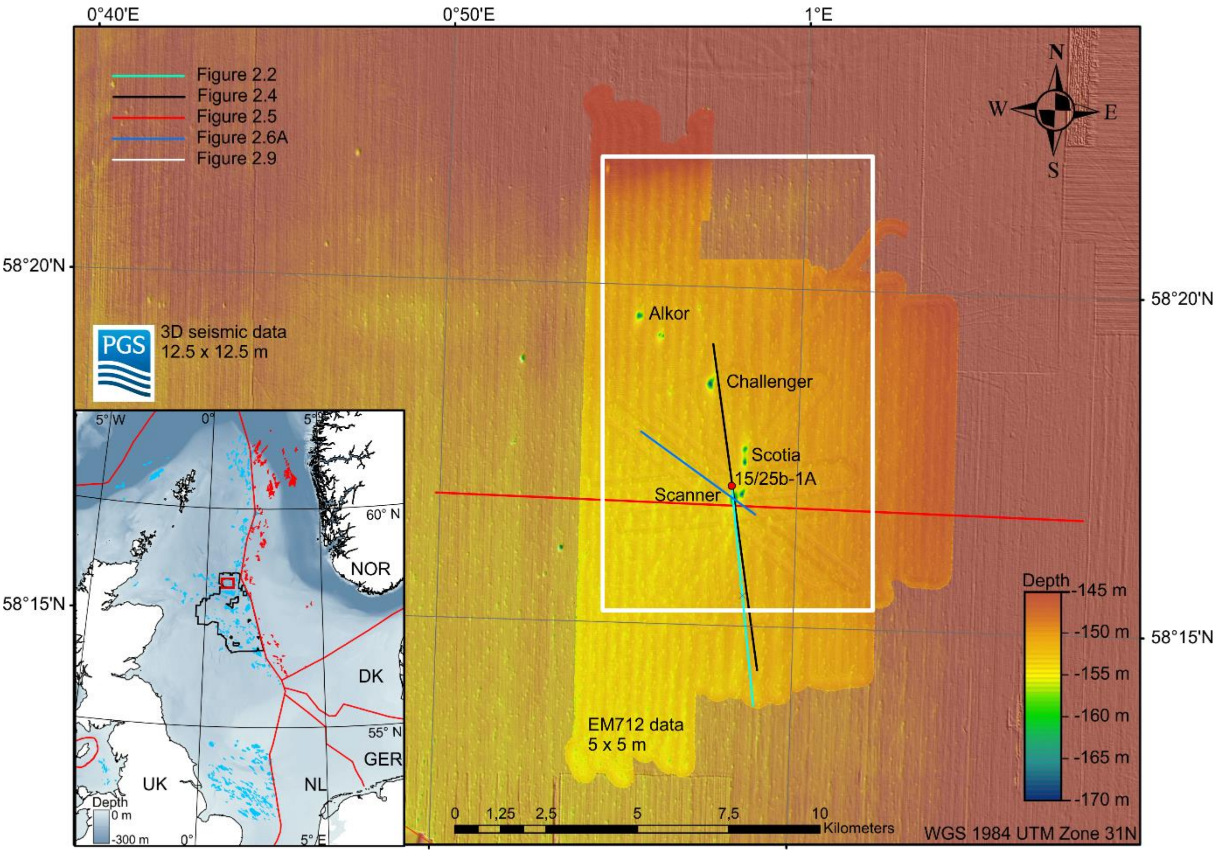

**Figure 2.1.** Bathymetric grid of the Witch Ground Basin, central North Sea. The shown bathymetry is a compilation of 3D reflection seismic data (converted with 1500 m/s constant velocity, 12.5 x 12.5 m lateral resolution) and EM712 (5 x 5 m lateral resolution). Locations for additional figures are indicated, turquoise line = Figure 2.2, black line = Figure 2.4c, red line = Figure 2.5b, blue line = Figure 2.6a, white line = Figure 2.9a-c. (**INSET**) The inset shows the location of the study area (red box) within the North Sea (EMODnet bathymetric map projected in UTM zone 31, WGS84). The black line outlines the PGS "CNS MegaSurveyPlus". Colored polygons show Norwegian (red, Norwegian Petroleum Directorate Open Data) and UK (blue, Oil and Gas Authority Open Data) hydrocarbon fields.

## 2.4. Regional setting

### 2.4.1. Pockmarks in the central North Sea

The North Sea is affected by focused flow of hydrocarbons from deep thermogenic sources, strongly mixed with microbially formed shallow methane (Chand et al., 2017; Karstens & Berndt, 2015). Three decades of extensive surveying and seafloor mapping in the Witch Ground Basin has revealed abundant "normal" pockmarks and multiple "unusually large" pockmarks. These pockmarks indicate significant flow of fluids from shallow marine sediments (Hovland & Sommerville, 1985; Judd et al., 1994; Gafeira et al., 2018). The term "normal" pockmark describes pockmarks that are more than 5 m in diameter and found in isolation where free gas pockets in the subsurface degas cyclically (Hovland et al., 2010).

The so-called "unusually large" pockmarks are complexes of pockmarks that are >100 m in diameter and >10 m deep. They are located in UK block 15/25 and include the Scanner, Scotia, Challenger and Alkor pockmark complexes, of which Scanner and Scotia comprise two large adjacent pockmarks (Judd et al., 1994; Gafeira & Long, 2015). Ongoing seepage is interpreted from repeated water column imaging (multiple cruises from 1983-2005; Dando et al., 1991; Judd et al., 1994; Judd & Hovland, 2007; Gafeira & Long, 2015) and visual evidence of emerging bubbles (Remotely operated vehicles, 1985, 2004; submarine Jago, 1990; Gafeira & Long, 2015). Methane derived-authigenic carbonates (MDAC) (Hovland & Irwin, 1989; Dando et al., 1991), bacterial mats (Dando et al., 1991; Pfannkuche, 2005), and seep-associated fauna (Dando et al., 1991; Austen et al., 1993) indicate long-lasting seepage from these unusually large pockmarks.

The “normal” pockmarks formed in the soft, fine-grained sediments of the Witch Ground Formation and have been identified across the Witch Ground Basin (Stoker & Long, 1984; Long, 1992; Judd et al., 1994; Sejrup et al., 1994; Gafeira et al., 2018). Their morphometry deviates strongly from the large pockmarks, as they are mostly less than 3 m deep and 20-40 m wide. The density ranges from less than 5 pockmarks per square kilometer at the outer parts of the Witch Ground Basin, to almost 30 pockmarks per square kilometer at the center, where water depth exceeds 150 m (Gafeira et al., 2018). There is seismic evidence that these normal pockmarks occur in tiers at distinct stratigraphic layers and not only at the surface (Stoker & Long, 1984). Previous studies indicate that the density of pockmarks per tier increases with decreasing burial depth (Long, 1992). The lack of evidence for seepage from repeated water column imaging suggests intermittent activity of these normal pockmarks assuming they are formed by seepage (Judd et al., 1994; Gafeira & Long, 2015).

### 2.4.2. Stratigraphy of the Witch Ground Basin

The Witch Ground Basin is located above the Witch Ground Graben, which is a major structural feature that developed between Triassic and Early Cretaceous times (Andrews et al., 1990). During the Late Jurassic and Early Cretaceous, the basin was a major sediment depo-center (Andrews et al., 1990). Clays with interbeds of sandstone and limestone dominate the Paleogene and Neogene sequences (Figure 2.2). The Witch Ground Basin was again a deposition center during the Quaternary (~ 600 m of sediment). The shallow sediments and especially the Early Pleistocene sediments of the Aberdeen Ground Formation show evidence for subglacial, glaciomarine and marine conditions (Sejrup et al., 1987; Stoker & Bent, 1987; Buckley, 2012; 2016; Rose et al., 2016; Reinardy et al., 2017; Rea et al., 2018). On seismic reflection sections, the Aberdeen Ground Formation is characterized by laterally continuous, high amplitude reflections (Ottesen et al., 2014). The top of the Aberdeen Ground Formation is defined by a regional glacial unconformity and dissection by a large number of tunnel valleys. The age of this unconformity is poorly constrained but it is thought to correspond to the advance of grounded ice into the North Sea Basin during the Mid Pleistocene Transition (~1.2-0.5 Ma) (further referred to as R4; Reinardy et al., 2017). The tunnel valleys that dissect the unconformity are part of the overlying Ling Bank Formation. This unit comprises a multitude of glacial tunnel valleys with different phases of erosion and deposition with poorly constrained ages. Comparison with tunnel valleys of onshore mainland Europe where the valley infill and associated facies have been dated to the Holsteinian interglacial corresponding to **M**arine

**I**sotope **S**tage (MIS) 11, gives a minimum age for formation of the stratigraphically lowest set of tunnel valleys in the North Sea during the Elsterian glaciation (MIS 12) (Stewart & Lonergan, 2011). The upper Mid to Late Pleistocene sedimentary succession consists of the Coal Pit, Swatchway and Witch Ground Formations (Figure 2.2). The Coal Pit Formation comprises glacial till with hard, dark grey to brownish-grey, muddy, pebbly sands or sandy muds deposited between MIS 3-6 (Andrews et al., 1990; Graham et al., 2010; Stoker et al., 2011). The Swatchway Formation comprises silty sandy clays with rare pebbles; possibly proximal glaciomarine sediments deposited during MIS2-3. The uppermost finely laminated, glaciomarine sediments of the Witch Ground Formation were deposited during MIS 1-2 (Stoker et al., 2011). The upper part of the Witch Ground Formation comprises Holocene age sediments, which were reworked during the past 8 ka, when sedimentation decreased or ceased to virtually no sediment input into the Witch Ground Basin (Erlenkeuser, 1979; Johnson & Elkins, 1979).

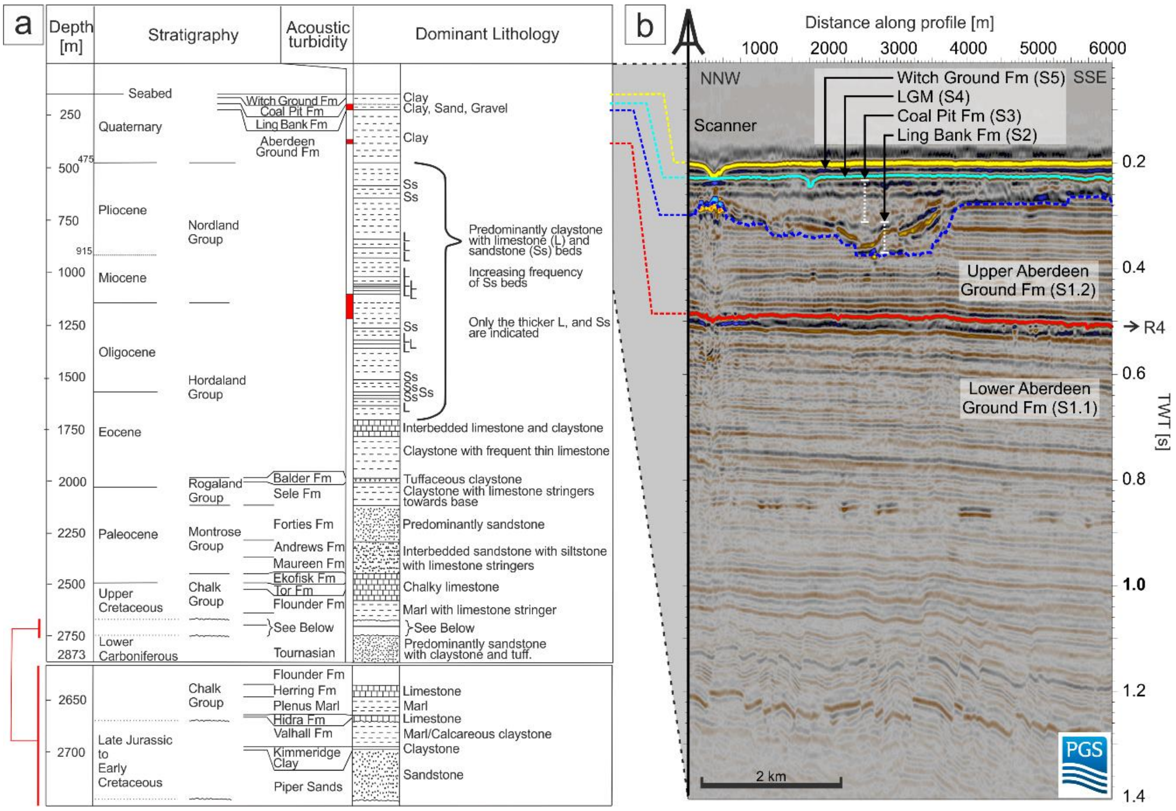

**Figure 2.2. (a)** Stratigraphic and lithological summary of well 15/25b-1A, located 400 m northwest of the western Scanner pockmark (modified after Judd et al., 1994). (**b)** 6 km-long representative seismic profile from conventional 3D seismic data from north-northwest to south-southeast. The seismic profile shows major stratigraphic units lower Aberdeen Ground Formation (S1.1), R4 reflector, upper Aberdeen Ground Formation (S1.2), Ling Bank Formation (S2), Coal Pit Formation (S3), last glacial maximum deposits (LGM, S4) and the Witch Ground Formation (S5). The image shows distance along profile on the x-axis and two-way traveltime (TWT) on the y-axis. 1.4 s TWT correspond to a minimum depth of 1050 m (at 1500 m/s seismic velocity). The location of the profile is given in Figure 2.1.

## 2.5. Methods

### 2.5.1. Seismic reflection data

We used an extensive 3D industry seismic data set (“CNS MegaSurveyPlus” provided by PGS) that covers > 22,000 km$^2$ of the central to northern North Sea down to 1.5 s two-way traveltime (TWT, Figure 2.1). The 3D pre-stack time-migrated seismic amplitude data (full fold stack) extends approximately 200 km from north to south and 140 km from east to west. The vertical resolution is approximately 20 m with an inline and crossline spacing of 12.5 m. Datasets like this have proven to be useful to identify fluid flow systems, including their geometry, permeability barriers and fluid accumulations, as they manifest in seismic data as amplitude anomalies (Karstens & Berndt, 2015).

We have used seismic attributes to enhance seismic interpretation including the Kingdom Suite Symmetry attribute, which is a post-stack, post migration structural feature detection tool (e.g. fracture detection) based on a 3D log-Gabor filter array (Yu et al., 2015). This attribute is highly sensitive to seismic amplitude variations and therefore correlates with curvatures and discontinuities associated with geological structures, e.g. faults, fractures and discontinuous events (Böttner et al., 2018). In addition, we use the root-mean-square (RMS) amplitude calculated over a time window of ± 50 ms around the picked horizon (see horizon in Figure 2.2b, dashed blue line). RMS amplitude is a post-stack attribute that highlights areas with direct hydrocarbon indicators such as bright spots by calculating the root of squared amplitudes divided by the number of samples per specified time window.

In addition, we acquired high-resolution 2D seismic reflection data during research cruise MSM63 in April/May 2017 onboard RV Maria S. Merian (Figure 2.1, red/black lines). The aim of the seismic survey was to increase seismic resolution, map the fluid flow systems and to image the presumed subsurface fracture networks. The seismic profiles were acquired with a two-105/105-in$^3$-GI-Gun-array shot at 210 bar every 5 seconds and a 150 m-long streamer with 96 channels and 1.5625 m channel spacing. The resulting shot point distance is approximately 8.75-12.5 m at 3.5-5 kn ship speed. The frequency range of the two-GI-Gun-array is 15-500 Hz. The processing included geometry and delay corrections, static corrections, binning to 1.5625 m and bandpass filtering with corner frequencies of 25, 45, 420, and 500 Hz. Furthermore, a normal-move-out-correction (with a constant velocity of 1488 m/s calculated from CTD measurements) was applied and the data were stacked and then migrated using a 2D Stolt algorithm (1500 m/s constant velocity model). The vertical resolution of the processed data is approximately 6-7 m near the seafloor.

### 2.5.2. Seismostratigraphic framework

Fluid flow in this area strongly depends on the local and regional stratigraphy and subsequent sediment properties. We have compiled a stratigraphic framework with seismic reflection data, industry well 15/25b-1A (Figure 2.2a), British Geological Survey boreholes BH77/2, BH86/26, BH04/01 (Figure 2.1) and information from literature (Holmes, 1977; Judd et al., 1994; Graham et al., 2010; Sejrup et al., 2014; Reinardy et al., 2017). We are able to tie most seismo-stratigraphic units within our stratigraphic framework to previously published lithostratigraphic units (Figure 2.2). Formation names and their ages utilize the North Sea Quaternary lithostratigraphic framework (Stoker et al., 2011). The seismostratigraphic unit S1.1 corresponds to the lower Aberdeen Ground Formation (MIS 100-21), S1.2 to the upper Aberdeen Ground Formation (MIS 21-13), S2 inside the tunnel valleys to the Ling Bank Formation (MIS 12-10), which is unconformably overlain by regional glacigenic sediments deposited during Mid Pleistocene (MIS 6; Reinardy et al., 2017), S3 to the Coal Pit Formation (MIS 6-3), S4 to the upper Swatchway or lower Witch Ground Formation (MIS 3-2) and S5 to the Witch Ground Formation (MIS 2-1). However, previous interpretations and stratigraphic units likely include sediments of different provenance due to lower resolution data. Possible reworking and disturbance by fluvial, glacial and marine processes further complicate the interpretation of lithostratigraphic units in this part of the Witch Ground Basin (Sejrup et al., 2014).

### 2.5.3. Hydroacoustic data

The shallow seismic stratigraphy was imaged by sub-bottom profiler data acquired during cruise MSM63 (Figure 2.1, blue/black line) using Parasound P70 with 4 kHz as the secondary low frequency to obtain seismic images of the upper 100 m below the seafloor with very high vertical resolution (< 15 cm). We applied a frequency filter (low cut 2 kHz, high cut 6 kHz, 2 iterations) and calculated the envelope within the seismic interpretation software IHS Kingdom. In addition, further sub-bottom profiler (SBP) data was acquired during cruise JC152 (onboard RV James Cook in August 2017) using a Chirp. The Chirp SBP produces a sweep, which lasts 0.035 s; the normalized zero-phase Klauder wavelet from the autocorrelation of the sweep shows a temporal length of 0.00075 s, allowing further processing. The bandwidth ranges from 2.8-6 kHz, with a central frequency of 4.4 kHz. The combination of both systems and the subsequent integrated data set enables a detailed analysis of the shallow sedimentary succession up to 50 m below the seafloor. Both systems are further referred to as echosounder.

Bathymetric data were acquired with the EM712 system mounted to the hull of RV Maria S. Merian (Figure 2.1). The survey was designed to provide high-resolution bathymetry with 5 x 5 m resolution. We processed the data using MB Systems software (Caress & Chayes, 2017) and included statistical evaluation of soundings that increased the signal-to-noise ratio. The sound velocity profile for multibeam processing was measured at the beginning and at the end of the cruise.

### 2.5.4. Semi-automated picking of pockmarks

To delineate pockmarks within the MSM63 bathymetric data we used a workflow that combines multiple ArcGIS geoprocessing tools (also compare Gafeira et al., 2012, 2018). In a first step, all depressions shallower than 18 m were filled with the “fill” tool. Subsequently the original grid was subtracted from the filled grid and all areas that have changed vertically by 0.5 m or more were classified. The “raster to polygon” tool was then used to draw polygons around the classified areas. Afterwards, the areas were calculated for all polygons and those comprising < 500 m² were deleted. This removed a vast quantity of polygons from the outer regions of single swath transects where the noise level within the multibeam data increased. After this step, the polygon dataset was manually inspected and all polygons that did not encircle pockmarks were manually removed. This manual editing step was necessary due to the presence of some large (> 500 m²) noisy regions within the multibeam data. Subsequently all empty areas within individual polygons were removed with the “Eliminate Polygon Part” tool. This removed the bathymetric noise within single pockmarks. The outlines of the polygons were then smoothed with the “smooth polygon” tool using a polynomial approximation with exponential kernel (PEAK) algorithm and a 100 m smoothing tolerance. Finally, the depth, the orientation and length of the longest and shortest axis, the perimeter, and the distance to the closest neighbor pockmarks were calculated for each pockmark defined by a polygon.

### 2.5.5. Sediment sampling

Shallow sediment samples were taken at the southwestern edge of the western Scanner pockmark during R/V Poseidon cruise POS518 (Leg 2) using a 6 m-long gravity corer (Linke & Haeckel, 2018). At the core location, the shallow sedimentary succession thins out, thus allowing the sampling of the underlying stratigraphic layers. The cores were split in 1 m segments of archive and working halves.

The working halves were sampled for physical sediment properties, element composition of solid phase, and chemical composition of porewater. Porewater was extracted from sediment in 30 cm intervals using Rhizons (0.2 µm, Rhizosphere Research Products, e.g. Seeberg-Elverfeldt et al., 2005). Sulfate and chloride concentrations of sampled porewater were determined by Ion Chromatography (IC) equipped with a conductivity sensor (Eco IC, Metrohm; Metrosep A Supp5 – 100/4.0). Analytical precision is ~1 % (1σ) measured by repeated analysis of IAPSO (International Association for the Physical Sciences of the Oceans). Total organic carbon content ($C_{org}$), C/N-ratio, and inorganic carbon content ($CaCO_3$) were determined by combustion of sediment samples in a EURO Element Analyzer (C/N/S configuration), prior and after removal of inorganic carbon with 1 M HCl. The analytical data is given in % of the total weight of dried sediment with an accuracy of 3 %. Calculated C/N-ratios are given in atom-ratios. Dissolved methane concentrations were determined by headspace sampling according to Sommer et al. (2009). 3 $cm^3$ of sediment are transferred into a 22 ml head space vial and closed with a crimped rubber septum after adding 6 ml of saturated sodium chloride solution. Equilibrated headspace gases were analyzed by injecting 100 µl of headspace gas into a Shimadzu gas chromatograph (GC-2014) equipped with a packed Haysep-Q (80/100, 8ft) column and a flame ionization detector. Analytical data is given with 2 % (1σ) accuracy. Sediment porosity was determined by weight difference due to loss of water from ~5 $cm^3$ wet sediment samples during freeze-drying.

The archive halves were used to measure the relative abundance of the elements Ca, Fe, S, Rb, Zr, and Cl at the British Ocean Sediment Core Research Facility (BOSCORF, Southampton, UK) using the ITRAX core-scanning X-ray fluorescence system (Cox Analytical; Croudace et al., 2006). This was done in 1-mm intervals using a molybdenum X-ray tube at 30 sec measurements time, 30 kV and 40 mA. Element abundances are presented as total counts normalized to counts per second (cps) and a running average of 1 cm was applied to the results. Physical properties (resistivity, magnetic susceptibility and density) of the sediments were measured on the archive halves using the GEOTEK multi-sensor core logger (MSCL) at 1 cm intervals.

## 2.6. Results

### 2.6.1. Seafloor morphology

High-resolution bathymetric data reveal abundant depressions of the seafloor in various shapes and sizes in the Witch Ground Basin. These abundant depressions occur in water depths between 120-180 m over an area 225 km$^2$ and we interpret them as pockmarks (Figure 2.3). Where pockmarks are absent, the seafloor is characterized by linear and curvilinear depressions, which we interpret as iceberg plough marks (Figure 2.3a). We identified 1679 individual pockmarks within our bathymetric grid. The derived morphological parameters are summarized in Table 2.1.

**Table 2.1:** Statistical analyses of geomorphological parameters derived from 1679 individual pockmarks in our survey area.

| PARAMETER | MIN. | MAX. | MEAN | STD. | PERCENTAGE IN |
|---|---|---|---|---|---|
| AREA [M$^2$] | 503 | 660991 | 7039 | 48998 | 99% in 503-56038 m² |
| LENGTH [M] | 13 | 1106 | 83 | 57 | 93% in 26-140 m |
| WIDTH [M] | 6 | 464 | 36 | 22 | 92% in 14-57 m |
| MAX. DEPTH [M] | 0.55 | 17.77 | 2.0 | 1.1 | 87% in 0.9-3.1 m |
| PERIMETER [M] | 32 | 2439 | 196 | 128 | 94% in 68-324 m |
| NEIGHBORING | 0 | 583 | 102 | 60 | 69 % in 42-162 m |
| WATER DEPTH [M] | 144 | 155 | 151 | 2 | 61% in 149-153 m |

Note: Minimum, Maximum, Mean, standard deviation, and percentage within range of: area, length (a-axis), width (b-axis), maximum depth (from threshold), perimeter, neighboring distance, and water depth at center point of respective pockmark.

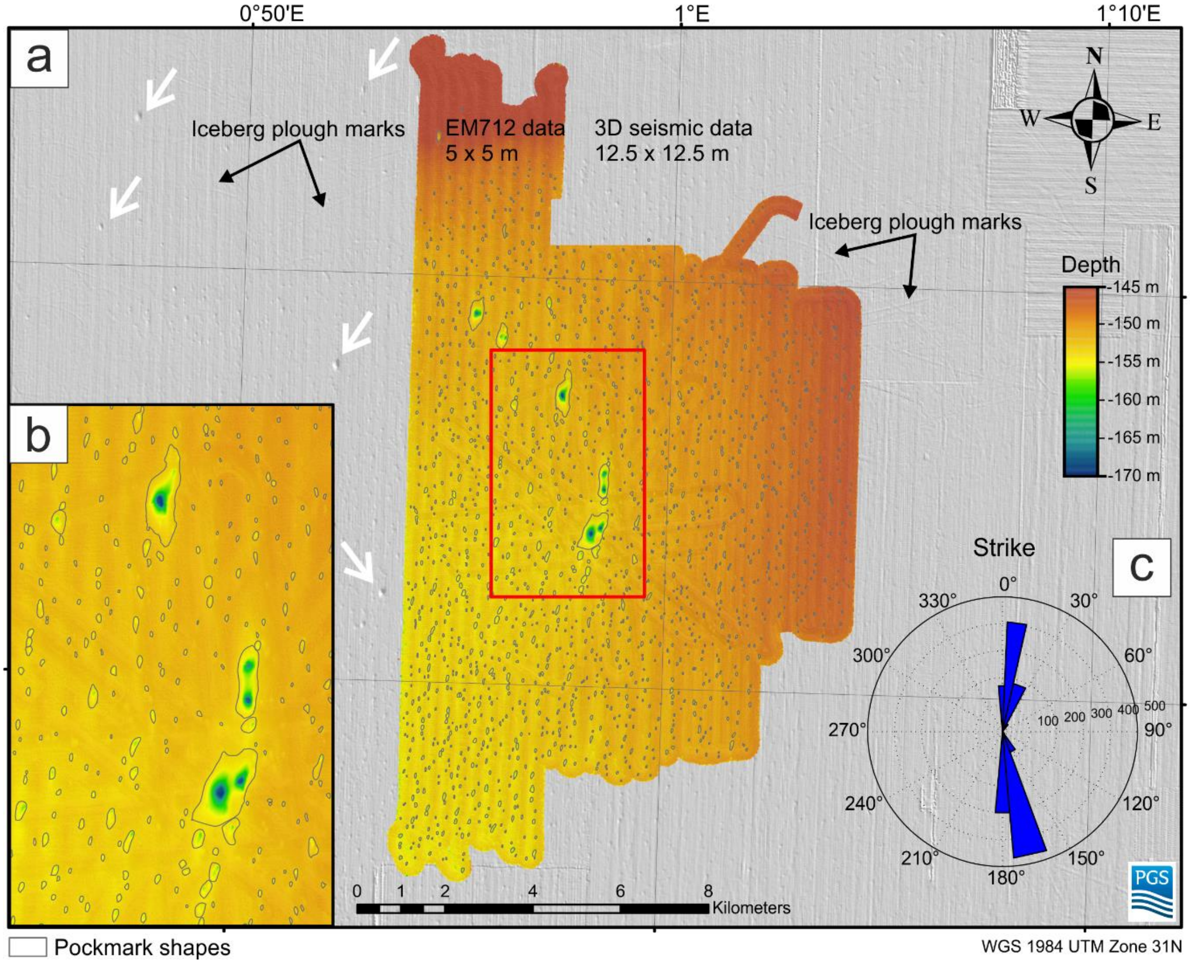

**Figure 2.3.** (**a**) Detailed bathymetric map with a compilation of high-resolution multibeam bathymetry (5 x 5 m lateral and up to 10 cm vertical resolution) and depth converted 3D seismic seafloor horizon in greyscale slope shader (12.5 x 12.5 lateral and ~20 m vertical resolution, converted with constant seismic velocity 1500 m/s). The semi-automatically picked pockmarks are outlined by black polygons. White arrows highlight class 1 pockmarks outside of the high-resolution bathymetry. (**b**) Zoom of Scanner, Scotia and Challenger pockmarks and numerous class 2 pockmarks. Semi-automatedly picked pockmarks are outlined by black polygons. (**c**) Rose-diagram of pockmark orientation (orientation of a-axis).

The pockmarks are usually elongated in one direction with a long axis orientation in NNE to SSW direction (Figure 2.3b). The predominant long axis orientations do not align with the orientation of the sail line (20° offset) and are therefore no acquisition artefacts. Based on their depths, widths and lengths, we separate the pockmarks into two classes: Class 1 pockmarks (n=9) include the Scanner, Scotia, Challenger and Alkor pockmark complexes, which are > 6 m deep, > 75 m wide and > 250 m long (Figure 2.3a); Class 2 pockmarks represent the vast majority of pockmarks with depths between 0.9-3.1 m, width between 14-57 m and length between 26-140 m (n=1670, Table 2.1).

### 2.6.2. Seismic stratigraphy

A 3D seismic profile shows the major seismostratigraphic units and is centered above the western part of the Scanner Pockmark (Figure 2.4c). Following the local seismostratigraphic framework, unit S1.1 shows laterally highly coherent and finely laminated seismic reflections, with an upper boundary defined by a distinct unconformity (R4), which is characterized by a zone of chaotic incoherent reflections (Figures 2.2b, 2.4c, and 2.5b). Unit S1.2 shows high lateral continuity of seismic reflections cut by numerous glacial tunnel valleys indicating different phases of erosion and deposition. The overlying unit S2 is discordant (erosional surface) and of chaotic to transparent seismic facies (Figures 2.4b and 2.5b). S2 varies in thickness between 0.015-0.050 s TWT corresponding to 10-40 m, and shows high amplitude patches (bright spots) with polarity reversals at stratigraphic highs in between adjacent tunnel valleys (Figure 2.4b, Figure 2.5b), indicating the presence of free gas in pore space (Løseth et al., 2009). In the 3D seismic data, unit S3 is characterized by a chaotic to transparent seismic facies at the bottom and laterally continuous, low reflective seismic reflections at the top (Figure 2.4c). Based on the echosounder and 2D seismic data we subdivide this unit into two subunits (S3.1 and S3.2, see Figure 2.4a, b). S3.2 shows a transparent to chaotic seismic facies at the bottom and a transition to laminated seismic reflections at the top (Figures 2.4a, b, and 2.5). This fine lamination of seismic reflections is also visible below 0.25 s TWT within the echosounder data (Figure 2.4a).

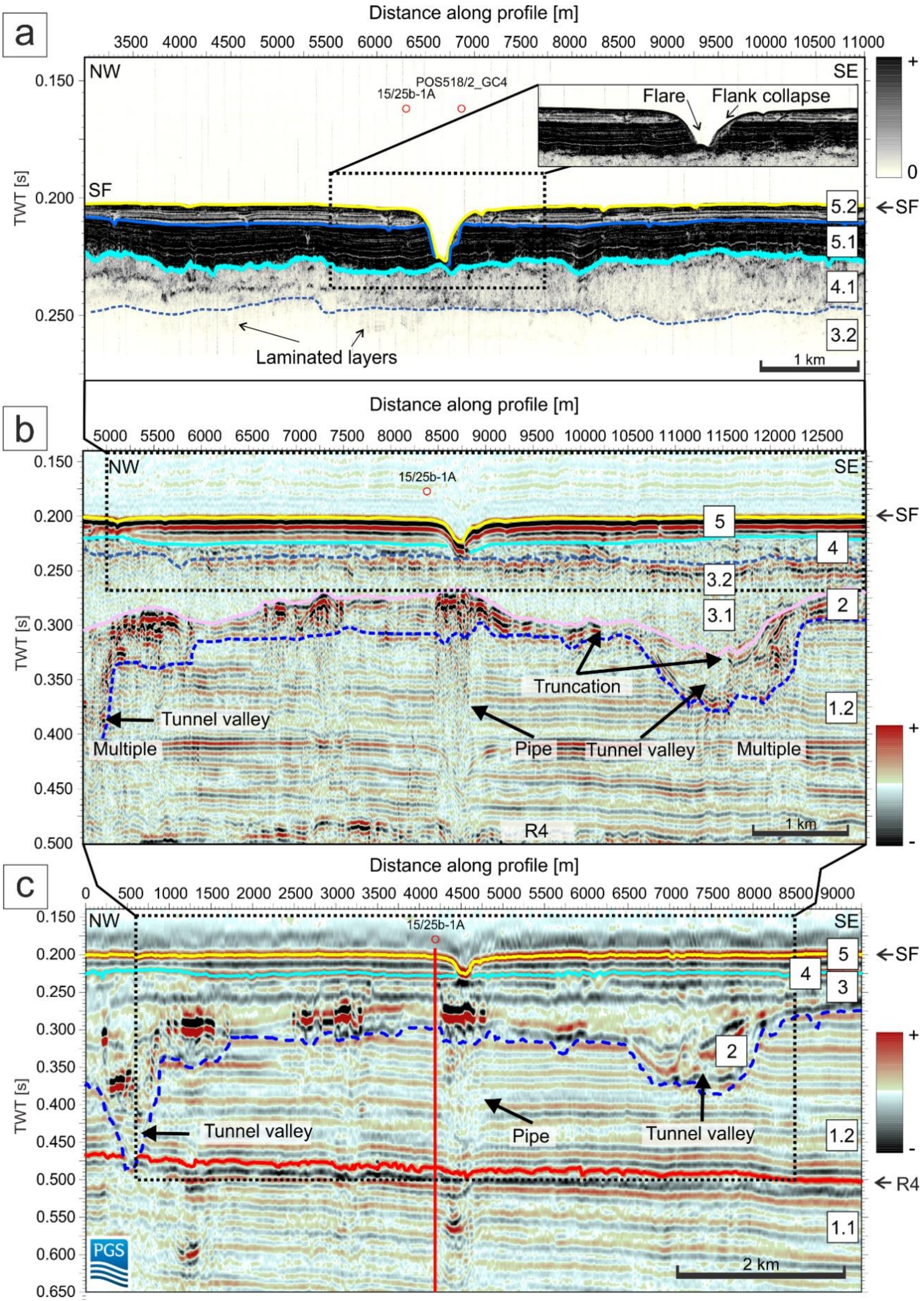

**Figure 2.4.** Combination of **(a)** echosounder data, **(b)** 2D seismic reflection data, and **(c)** 3D seismic reflection data extending from northwest to southeast across the Scanner pockmark showing interpreted horizons, interpreted seismic units S1 to S5 and unconformity R4. The dashed box in (c) shows location of (b), dashed box in (b) shows location of (a) and dashed box in (a) shows location of zoomed section in the right corner. Horizons are: red line = R4, dashed blue line = top S1.2, pink line = top S2, dashed slate blue line = top S3.2, bright blue line = top S4.1, blue line = top S5.1, yellow line = seafloor (SF). Vertical red bar in (c) shows the location of industry well 15/25b-1A. The location of the profile is given in Figure 2.1.

Figure 2.5 shows in further detail that unit S4 is discordant to S3.2, and characterized by a transparent to chaotic seismic facies and internal alternating dipping reflections separated by a distinct boundary (Figure 2.5a). Based on the echosounder data and the smeared boundary with high amplitude reflections (Figure 2.5a), we separate unit S4 into subunits S4.1 and S4.2. S4.1 varies in thickness (up to 0.033 s TWT corresponding to 25 m at 1500 m/s) and thins out eastward towards the Scanner pockmark (Figure 2.5a). Unit S5 shows well-stratified and laterally continuous seismic reflections, which overly the corrugated surfaces of S4.1 and S4.2 (Figure 2.5). Based on the echosounder and 2D seismic data, we subdivide S5 into two subunits (S5.1 and S5.2, Figure 2.5a, b), which will be described in detail below.

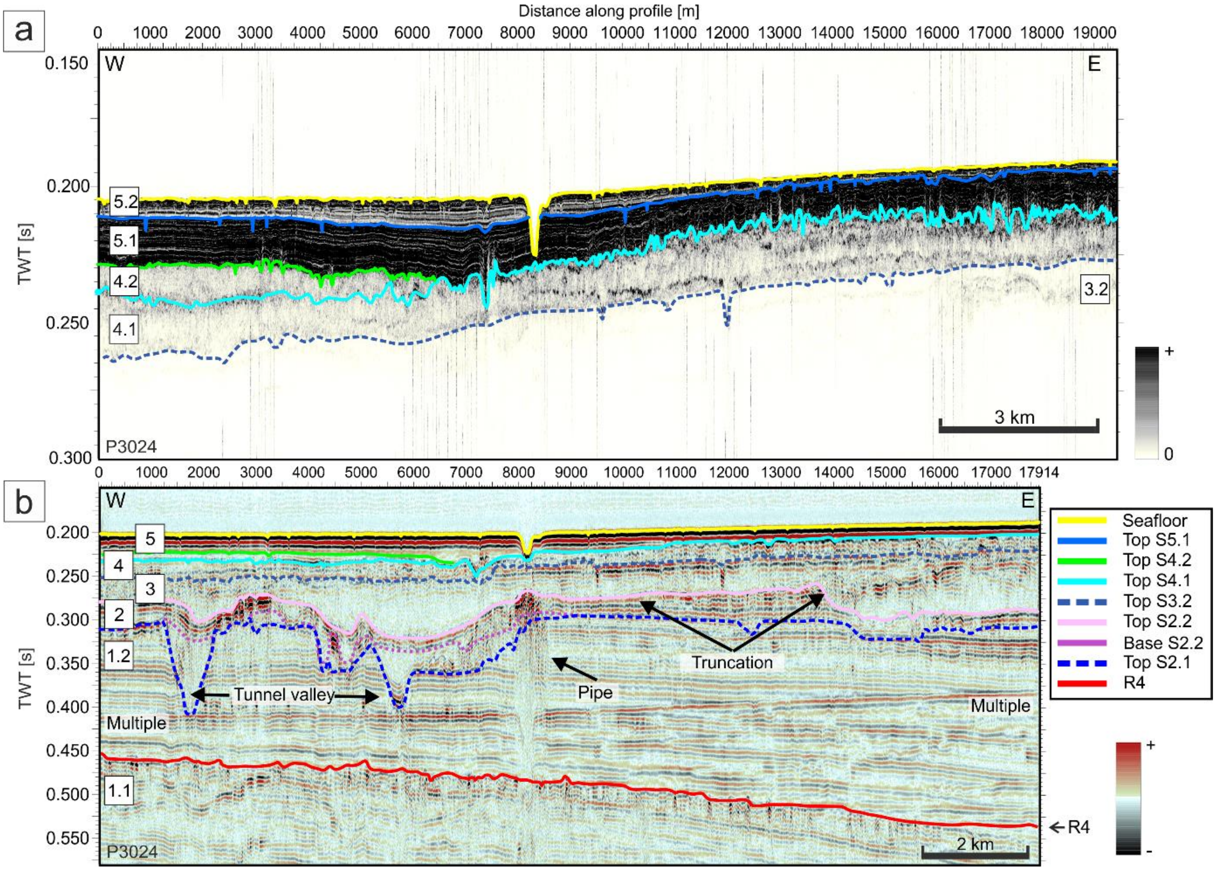

**Figure 2.5.** (**a**) ~20-km-long echosounder profile (perpendicular to the profiles shown in Figure 2.4) extending from west to east across the Scanner pockmark. Horizons are base S4.1 (dashed slate blue line), top S4.1 (turquoise line), top S4.2 (green line), top S5.1 (blue reflection) and seafloor (yellow line). (**INSET**) The inset shows a part of the echosounder profile for a detailed image of the lower/upper Witch Ground Formation (S5.1 respectively S5.2; yellow arrow indicates the seafloor, blue arrow top S5.2, and green arrow top 4.2) and to highlight class 2 pockmark formation at distinct stratigraphic horizons (I-IV). **(b)** Corresponding ~18-km-long 2D reflection seismic profile across the Scanner pockmark. Horizons are showing S1.1, R4 reflector (red line), top S1.2 (dashed blue line), base MIS 6 till/S2 (dashed purple line), top S2 (pink line), top S3.2 (dashed slate blue line), top S4.1 (turquoise line), top S4.2 (green line), and seafloor (yellow line). The location of the profile is given in Figure 2.1.

### 2.6.3. Shallow sedimentary succession and water column imaging

The high-resolution echosounder data image the very shallow sedimentary succession, including units S4 and S5 (Figure 2.6a). S4.1 is characterized by a chaotic to transparent facies with a highly corrugated surface and internal reflections that show alternating dipping directions. S4.1 is mostly present below 0.23 s TWT and surficially exposed at the center of the western Scanner pockmark (see also inset Figure 2.4a). S5.1 lies between 0.212-0.230 s TWT and consists of laterally continuous, very well laminated strata and high amplitude response (corresponding to dark colors in the echosounder profile). S5.1 also holds v-shaped amplitude anomalies at specific stratigraphic horizons terminating at two major stratigraphic boundaries (red boxes I, II in Figure 2.6a). On top, S5.2 (0.208-0.215 s TWT) shows lower amplitudes, but a well laminated and lateral coherent stratigraphy. This unit reveals as well v-shaped amplitude anomalies marked with red boxes III and IV. The v-shaped amplitude anomalies show very high amplitudes (black arrows in Figure 2.6a) at their center. They all terminate at the same stratigraphic horizon. Both, S5.1 and S5.2 show local vertical amplitude discontinuities, possibly indicating fractures in the subsurface (Figure 2.6a). The topmost part of unit S5.2 between the seafloor at 0.205-0.207 s TWT is characterized by a high amplitude chaotic seismic facies. Here, the class 2 pockmarks crop out at the seafloor and the unit comprises another set of v-shaped amplitude anomalies, which coincide with the pockmarks at the seafloor. This indicates that the v-shaped amplitude anomalies in the subsurface most probably correspond to previous phases of pockmark formation (further referred to as paleo-pockmarks, red boxes I-IV). If single seep sites would have been active over a long time, this activity would lead to stacked pockmarks (Andresen et al., 2011). However, paleo-pockmarks in the subsurface do not coincide with class 2 pockmarks at the seafloor. The echosounder data allows to determine the thickness of the sediment in unit S5.2, in which the vast majority of pockmarks and paleo-pockmarks are located (Figure 2.6a, Figure 2.7a, d).

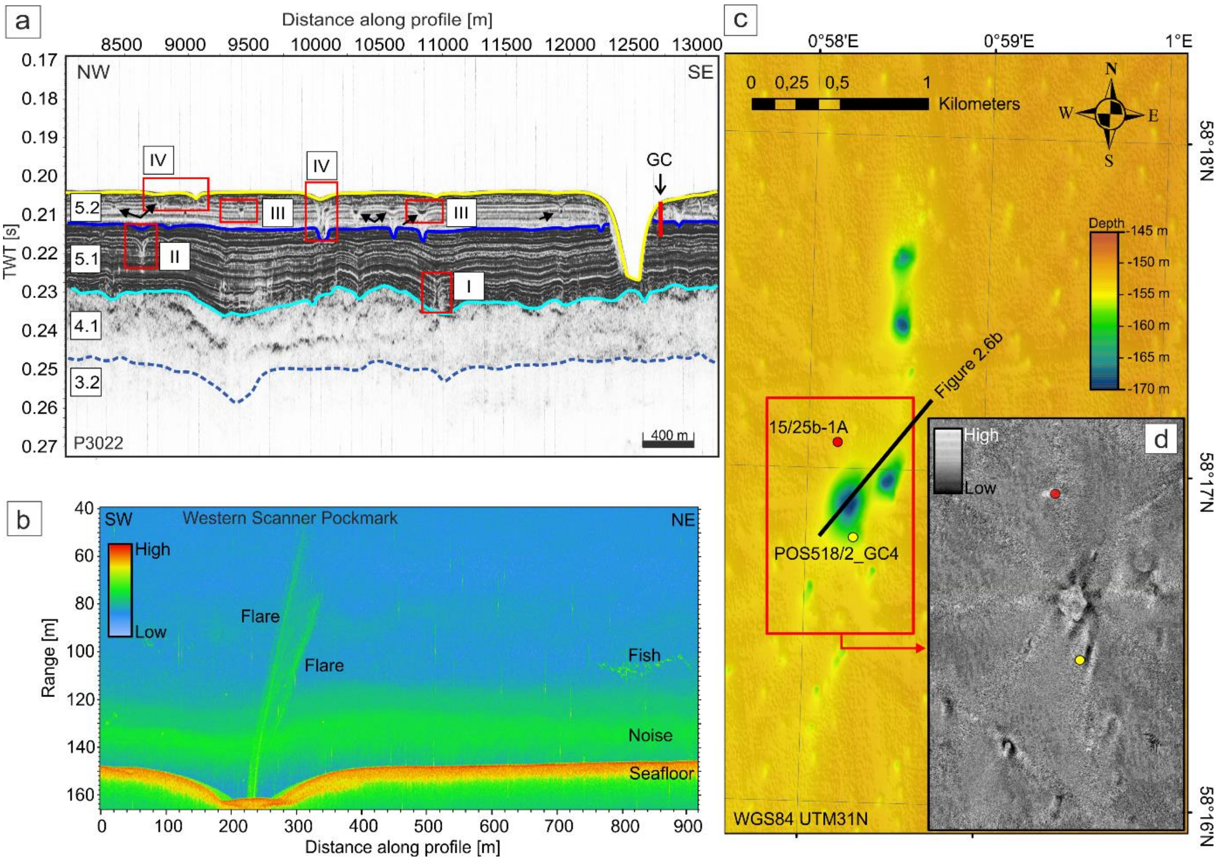

**Figure 2.6.** **(a)** ~4 km-long echosounder profile from northwest to southeast showing the shallow sedimentary succession in high-resolution. Horizons include the seafloor (yellow), base S5.2 (blue line), top S4.1 (turquoise line), and base S4.1/top S3.2 (dashed slate blue line). The red boxes highlight specific stratigraphic horizons where pockmarks/paleo-pockmarks occur in at least four phases (I-IV). Black arrows highlight examples of high-amplitude patches **(b)** 920-m-long EM712 water column imaging range stack perpendicular to (a) across the western part of the Scanner pockmark showing two flares emerging from the center into the water column (high backscatter = red). Location of the profile given in (c). **(c)** Bathymetric map showing the location of the Scanner and Scotia pockmark complexes (Class 1 pockmarks) and the location of gravity core POS518/2-GC4 (yellow dot) and industry well 15/25b-1A (red dot). (**d**) Zoom in bathymetric map within indicated extents (red box) showing backscatter derived from EM712 multibeam data. High backscatter is shown in white and low backscatter in black colors.

We observed no venting from class 2 pockmarks during MSM63 (April/May 2017). However, our backscatter images show high values for class 2 pockmarks around their center and their rim, of which the latter is most likely related to slope effects (Figure 2.6d). Active venting was limited to the class 1 pockmarks Scanner, Scotia, Challenger, and Alkor confirmed by water column imaging (Berndt et al., 2017). The western Scanner pockmark showed two adjacent flares (Figure 2.6b) that emerged from the center of the pockmark and extend ~100 m into the water column (water depth 180 m). Similar flare behavior has been observed at blowout site 22/4b further south, where released methane bubbles emerge in a spiral vortex (Schneider von Deimling et al., 2015). A high backscatter anomaly inside the western Scanner pockmark (Figure 2.6d) indicates a change in lithology probably related to previously identified authigenic carbonates. In areas where the Witch Ground Formation (S5) is absent and glacial deposits of unit S4.1 are surficial, class 1 pockmarks show a decrease in depth (from > 10 m to 6-10 m), width (> 300 m to ~ 100 m) and length (> 600 m to ~ 300 m) in areas where the Witch Ground Formation is absent (S5).

The pockmark density correlates with the sediment thickness of the uppermost sedimentary succession. Class 2 pockmarks predominantly occur in areas where seismic unit S5.2 is generally 2-8 m thick in the surrounding of the pockmarks, while a few pockmarks occur on gentle slopes where seismic unit S5.2 is between 1-2 m (Figure 2.7b, d). We calculated the surrounding sediment thickness by adding the maximum pockmark depth derived from bathymetric data to the echosounder horizon thickness converted with 1500 m/s (Figure 2.7a, blue lines P70/black lines SBP). The density of the pockmarks at the seafloor increases with increasing sediment thickness and water depth (1 pockmark per km² at 140 m to 25 per km² at 155 m water depth, see Figure 2.7c).

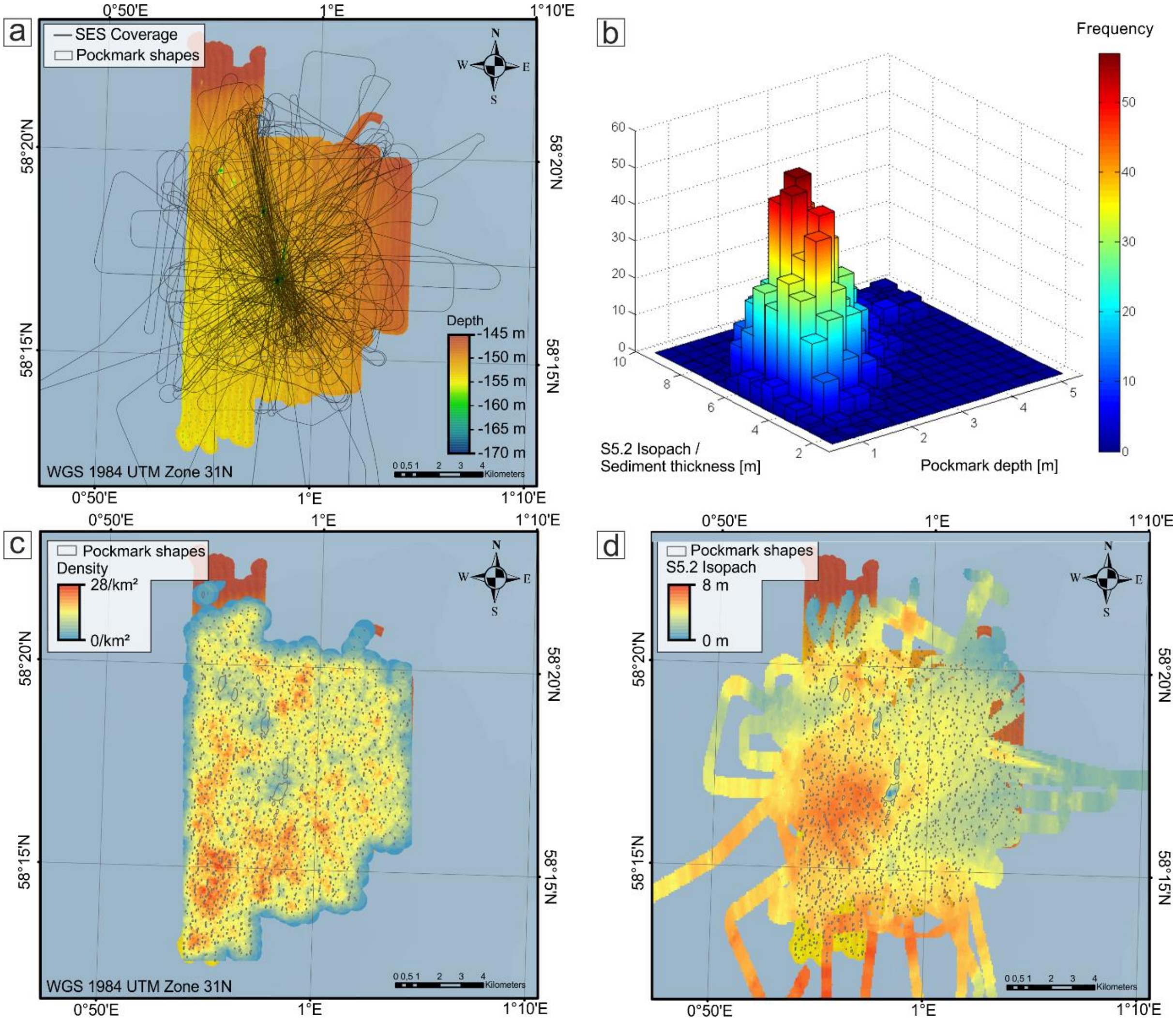

**Figure 2.7. (a)** Bathymetric map of the survey area showing echosounder profile coverage (Parasound = blue lines, SBP chirp = black lines). **(b)** 3D bar plot showing the density of pockmarks, depth versus sediment thickness around the corresponding pockmarks (S5.2 Isopach). **(c)** Density and semi-automated picked outlines (black polygons) of surface pockmarks derived from high-resolution bathymetric data. **(d)** Semi-automated picked outlines of surface pockmarks (black polygons) and sediment thickness of unit S5.2 (S5.2 Isopach) derived from echosounder profiles. For echosounder profile coverage see (**a**).

### 2.6.4. Sediment sampling

Gravity core POS518/2-GC4 shows three lithological units, which we can seismo-stratigraphically tie to the transition from S5.2 to S5.1 in our echosounder data (Figure 2.8): Unit 1 (3.4-6 m) comprises very well sorted clay to silty clay with wavy laminations of organic rich material (Figure 2.8). The matrix contains algal remains and shell fragments. The boundary between units 2 and 1 is gradational. Unit 2 (2.9-3.4 m) consists of well-sorted, faintly laminated silty clay with fragments of shale and shells (Figure 2.8). There is a sharp, possibly erosional boundary between units 3 and 2 that corresponds to an increase in density (> 2 g/cm$^3$), resistivity (0.6 Ohm-m), and magnetic susceptibility (50 x 10$^{-5}$). Here, p-wave velocity slightly decreases with a subtle increase in $CH_4$ (Figure 2.8). Furthermore, porewater analyses and ITRAX XRF shows a step increase in $SO_4$ and solid phase Fe with a step decrease in Cl. The

Zr/Rb, Ca/Ti and Ca/Fe ratios indicate shifts in sediment properties or provenance, also show step decreases between unit 2 and 3. Unit 3 (0-2.9 m) is well-sorted clayey silt to very fine sandy silt with wavy laminations or mottling but otherwise massive. The matrix contains algal remains with shell fragments and even whole shells are present. The lithic grains are sub-rounded and a dropstone was observed towards the base of the unit. The organic carbon content ($C_{org}$) is increases from 0.55 wt.% in unit 1 to about 1.5 wt.% in unit 3 (Figure 2.8). $CaCO_3$ shows low values (12 wt.%) in unit 1 with a sharp increase within unit 2 to high values (25 wt.%) in unit 3. $SO_4$ gradually increases over the whole core length (6 m) from ~10 mmol/l in unit 1 to seawater concentration of ~30 mmol/l in unit 3. $CH_4$ decreases above 4 m depth from ~10 µmol/l in unit 1 to 0-1 µmol/l in unit 3. Headspace gas analyses of all core segments show that the gas composition is almost purely methane (> 99%).

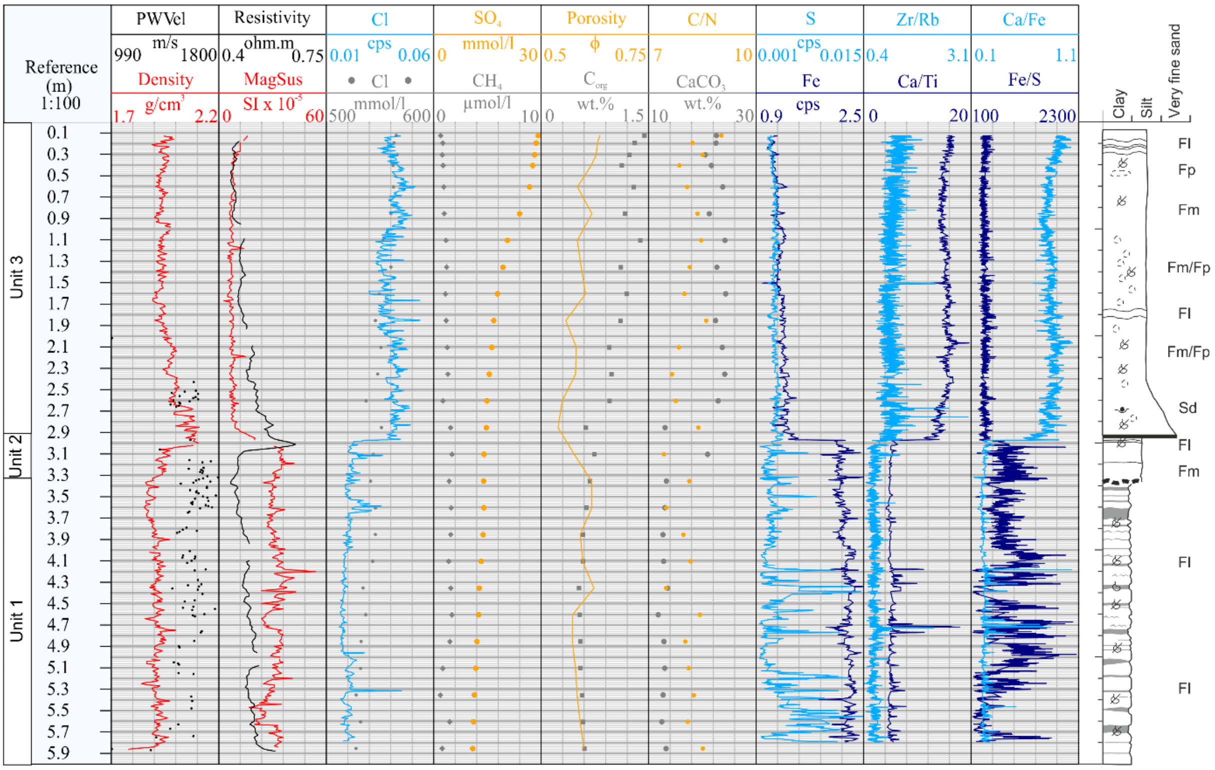

**Figure 2.8.** Gravity core POS518/2-GC4, subsequent sedimentary units from sedimentological description. The location of the core is given in Figure 2.6a The graphs show corresponding data retrieved from multi-sensor core logger data (MSCL, black and red lines), sediment and porewater analyses (PW, golden lines and grey dots), and ITRAX XRF data (bright and dark blue lines). ITRAX XRF data shows abundances of elements averaged over 1 cm normalized in counts per second (cps). Sedimentological record shows three units. Lithofacies code is given as Sd = Sand with dropstones, Fl = Silts & clays (laminated), Fm = Silts & clays (massive), Fp = Silts & clays (lenses/motling).

### 2.6.5. Subsurface fluid migration

In the Scanner pockmark area, the seismo-stratigraphic layering is disturbed by zones of dimmed reflections and the presence of bright spots at different depth levels (280 ms, 350 ms, 500 ms, 570 ms TWT, Figure 2.4c). This indicates the presence of interstitial fluids that cause a complex wave field propagation by significant changes in acoustic impedance (Domenico, 1977). These amplitude anomalies with bright spots and zones of dimmed amplitudes reach to at least the R4 reflector (Figure 2.4c). Here, we used the seismic symmetry attribute from 3D seismic amplitude data to identify the spatial extent of these amplitude anomalies and the subsurface expression (Figure 2.9c). The time slice of this attribute at 0.4 s TWT shows circular amplitude anomalies with constant diameters in depths ranging from 200-600 m beneath the unusually large pockmarks Scanner, Scotia, Challenger and Alkor (Figure 2.9c). Beneath the Scotia and Alkor pockmark complexes, there are two adjacent amplitude anomalies visible with a spacing of 50-100 m (Figure 2.9c, d, f).

The 3D seismic data show bright spots associated with unit S2 at ~0.3 s TWT in areas, where the tunnel valley erosion formed structural highs (Figure 2.9a, b). Previous surveys have interpreted these bright spots as free gas bearing layers within the uppermost sedimentary succession that cover the area in between two adjacent tunnel valleys (Judd et al., 1994).The pipe structures link the R4 reflector with the bright spots at the erosional unconformity by zones of dimmed seismic amplitudes. The 2D seismic data reveal that unit S2 is highly fractured where bright spots are visible (~0.3 s TWT; 5, 6.5, and 8.5 km distance along profile, Figure 2.4b).

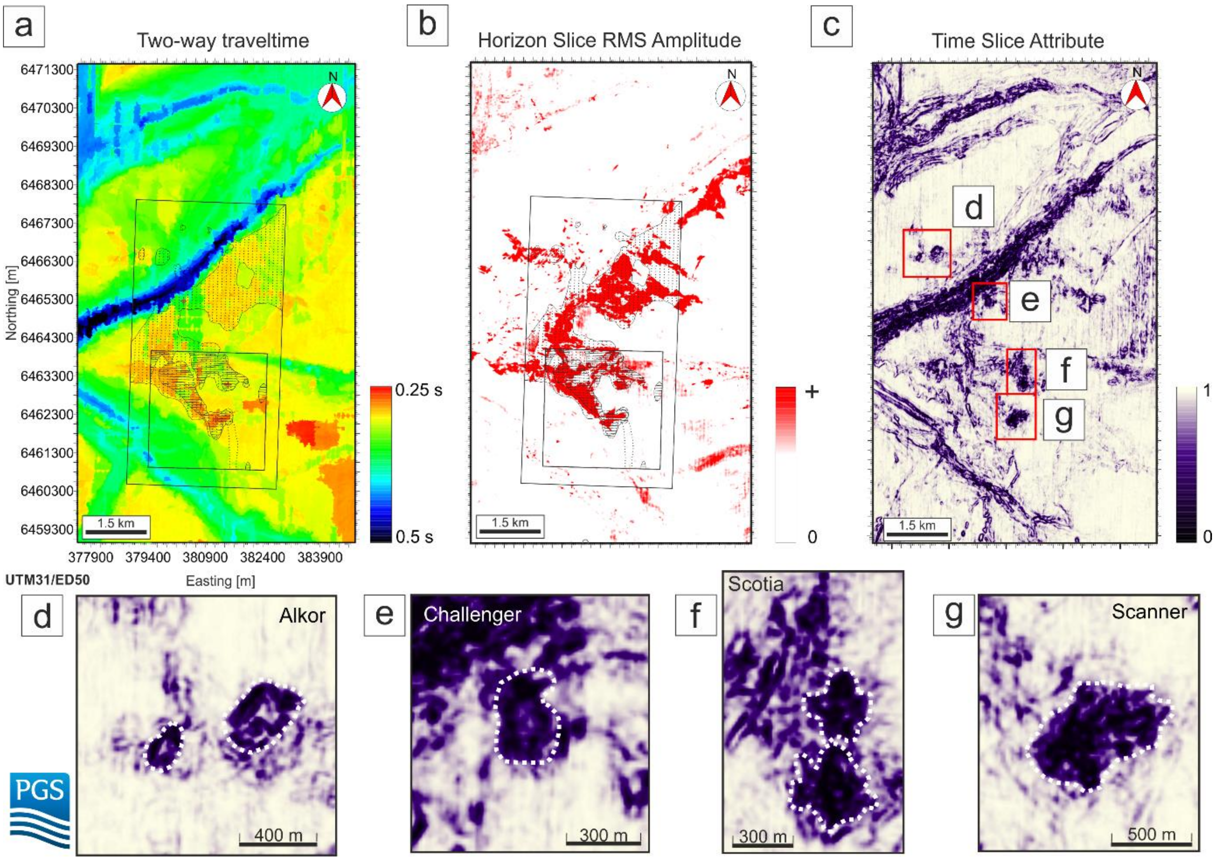

**Figure 2.9.** 3D seismic horizon top S1.2/bottom S2. The horizon is given in (**a**) two-way traveltime (TWT), (**b**) root mean square (RMS) amplitude horizon slice over a time window of ± 50 ms across the unconformity between units S1.2 and S2 to map the fluids and (**c**) symmetry attribute time slice. The slices show the gas accumulation within S2 across stratigraphic highs in between tunnel valleys in comparison to the previous analyses by Judd et al. (1994) (see map inset in a, b). Below are shown close-ups of the symmetry attribute for the (**d**) Alkor, (**d**) Challenger, (**f**) Scotia, (**g**) Scanner pockmark complexes (Class 1 pockmarks). White dashed lines outline the pipe structures in the subsurface. The locations of a, b and c are given in Figure 2.1.

## 2.7. Discussion

### 2.7.1. Fluid sources for pockmarks in the Witch Ground Basin

The morphometric analysis of the Witch Ground Basin bathymetry revealed 1679 individual pockmarks, which can be divided into class 1 and class 2 pockmarks. Pockmark formation and morphometry is highly dependent on the hosting sediments as well as the flux, flux variation and type of advected fluids (Orsi et al., 1995; Abegg & Anderson, 1996; Boudreau et al., 2001; Boudreau et al., 2005; Andrews et al., 2010; Mogollón et al., 2012). Predominant strike directions (NNE, SSE) derived from elongated elliptical shapes of the pockmarks may be attributed to local bottom currents shaping the seafloor (Gafeira et al., 2012). As the two types of pockmarks occur in the same sediments, the clear morphological separation between class 1 and 2 (see above) suggests that different fluids possibly sourced from different depth form the two types of pockmarks or that escape of the same fluids was controlled by different processes.

### 2.7.2. Source depth

The 2D and 3D seismic data show bright spots within S2, which corresponds to glacigenic sediments deposited during Mid Pleistocene (190-130 ka till from MIS 6; Reinardy et al., 2017). This till unit shows lateral changes in thickness and truncation of reflections to unit S3 indicating an erosional surface (Figure 2.5b). The free gas likely accumulates in the pore space of the glacigenic sediments of S2 rather than in the marine clays of the Aberdeen Ground Formation as previously suggested (Figure 2.4c, S1.2) (Andrews et al., 1990; Judd et al., 1994). While the glacial till S2 represents the shallow-most reservoir for the accumulation of free gas within the glacial till, unit 3.2 may act as a seal. S3.2 shows highly continuous reflections corresponding to glaciomarine sediments, which tend to have higher clay contents compared to subglacial sediments and can thus potentially act as a seal.

Horizon slices of RMS amplitudes show patches of bright spots within S2, where stratigraphic highs are present between adjacent tunnel valleys (Figures 2.4b, c, and 2.9a, b). Previous mapping of these high amplitude patterns (Judd et al., 1994) matches spatially our analysis. The high amplitude patterns are associated with gas in the shallow subsurface. It is likely that the small differences between the two mapping results are due to less complete seismic coverage of previous surveys (Judd et al., 1994) rather than temporal changes in gas distribution.

Below the gas-related bright spots in S2, we interpret the circular-shaped amplitude anomalies with zones of dimmed reflections and bright spots at different depth levels as seismic pipes (Figures 2.4c, 2.9c). Seismic pipes are strictly columnar anomalies with stacks of increased or dimmed amplitudes and are the seismic manifestation of vertical fluid conduits (Cartwright et al., 2007; Løseth et al., 2009; Karstens & Berndt, 2015). However, free gas in unit S2 can cause complex propagation of seismic waves and hence induces seismic artifacts, which may be misinterpreted as seismic pipes. While gas accumulations largely follow the morphology of the stratigraphic highs in between the adjacent tunnel valleys, seismic pipes are not related to any obvious subsurface structures or morphologic patterns. In addition, the circular shaped amplitude anomalies occupy only a small fraction of the area where free gas accumulates, indicating that the overlying gas induces only minor seismic artifacts (Figures 2.4, 2.9). The interpretation of circular-shaped amplitude anomalies as seismic pipes is also supported by the spatial correlation between seismic pipes in the subsurface and class 1 pockmarks at the seafloor (Figures 2.3a, 2.9c-g), which indicates their role as fluid migration pathways. We consider the interpretation of the seismic pipe structures robust down to the R4 reflector (Figure 2.4c). Below this reflector, the multiple reflection of the shallow gas bright spots within unit S2 increases interpretation ambiguity.

Unit S2 (intermediate reservoir for the fluids from deeper strata) may be hydraulically connected with the class 1 pockmarks either by a complex fracture network (likely below seismic data resolution), or by flow through unconsolidated sediments. Decompaction weakening may lead to fracture closure after gas bubble release, which would explain the weak seismic response of the fluid conduit beneath the Scanner pockmark complex (Figures 2.4, 2.5 and 2.6a; Räss et al., 2018).

Class 2 pockmark are significantly shallower and have shorter long axes than class 1 pockmarks (Figure 2.3a). Furthermore, our seismic and hydroacoustic data show no evidence for lateral gas migration from class 1 towards class 2 pockmarks identifying them as secondary fluid flow structures, nor for vertical gas migration from deeper strata (Figures 2.6, 2.7). The apparent differences in morphology and the lack of hydraulic connection suggest the presence of at least two independent sources of fluids in the area.

### 2.7.3. Class 1 pockmarks - Timing and controls of fluid venting

Class 1 pockmarks show vigorous venting (Figure 2.6b), indicating vertical fluid migration from deep strata through the pipe structures. Further, high amplitude reflections in echosounder and high backscatter anomalies in multibeam data indicate the precipitation of carbonates at the seafloor (Figure 2.6a, d). This is consistent with video observations during a previous survey showing MDACs in the central parts of the class 1 pockmarks (Dando et al., 1991; Clayton & Dando, 1996; Gafeira & Long, 2015). Previous geochemical analyses reported carbon isotope ratios ($\delta^{13}C$) of -79‰ in gas bubbles emanating from the western Scanner pockmark (Clayton & Dando, 1996) and -53 to -36‰ for the carbonate cements and the interstitial gas (Hovland & Irwin, 1989; Dando et al., 1991). Both indicate a biogenic gas origin possibly derived from microbial degradation of organic matter (Judd et al., 1994).

Our geochemical results match the biogenic character of the released methane at class 1 pockmarks (Figure 2.8). Biogenic methane is likely sourced from bright spots at Mid Pleistocene depth (R4) migrating through the pipe (Figure 2.4c). This horizon is primarily associated with biogenic methane (99.9% methane, $\delta^{13}CH_4$ -69‰; Rose et al., 2016). It may act as a trap focusing and mixing migrating microbial methane from the Quaternary succession with thermogenic methane from deeper sources. Thermogenic fluids may migrate through the overburden from deeper layers (Figure 2.2b), e.g. Kimmeridge clay (Judd et al., 1994), along faults (Chand et al., 2017), pipes or chimneys (Karstens & Berndt, 2015; Räss et al., 2018). This is, however, not corroborated by our geochemical results and the seismic data do not resolve the depth extent of the pipe structures underneath the class 1 pockmarks to the reservoir rocks (e.g. Montrose and Piper sands), but this may be due to imperfect imaging. We conclude that class 1 pockmarks are primarily sourced by biogenic methane from the upper 375 m of the Quaternary succession (corresponding to 500 ms TWT at constant velocity of 1500 m/s).

The timing of class 1 pockmark formation can be derived from the local stratigraphy. Class 1 pockmarks cut deep into the Witch Ground Formation (S5), truncating the stratigraphic layering of it and expose LGM deposits (S4.1) at their centers (Figure 2.6a, d). The Witch Ground Formation consists of two individual well-stratified stratigraphic units (S5.1 and S5.2; Figure 2.6a). S5.1 was deposited after 26,595 ± 387 cal. years BP when grounded ice retreated from the study area (Sejrup et al., 2014). The age of S5.2 is poorly constrained, but it was deposited during some period after 13,165 ± 55 cal. years BP (Sejrup et al., 2014). Furthermore, we observe a gentle shoaling of the Witch Ground Formation towards the class 1 pockmarks while S4.1 slightly dips down (Figure 2.6a), which may indicate sediment doming prior to pockmark formation (Barry et al., 2012; Koch et al., 2015). We therefore conclude that class 1 pockmarks formation initiated between 13,165 ± 55 and 26,595 ± 387 cal. years BP.

The formation of the class 1 pockmarks is related to seismic pipe structures in the subsurface. The formation of two very closely spaced pockmarks at the Scanner, Scotia and Alkor pockmark complexes are possibly due to two very closely spaced pipes ("twin pockmarks", Figure 2.9c, d, f). Seismic pipes or chimneys (and ultimately pockmarks) form, when (i) pore pressure exceeds the combined least principal stress and tensile strength of the sediment and induces hydrofracturing or, (ii) the pore pressure overcomes the capillary entry pressure and capillary failure occurs (Hubbert & Willis, 1957; Clayton & Hay, 1994). Bright spots at the R4 horizon indicate mobile fluids. We suggest that this R4 horizon, which comprises glacigenic sediments, therefore represents a reservoir. The upper Aberdeen Ground Formation (unit S1.2) with high clay content represents a low permeable seal/cap rock, which inhibits pore pressure release via diffusive flow. However, the buoyancy of the gas column itself may not be sufficient to breach through the overburden (Karstens & Berndt, 2015). To facilitate focused fluid flow through the overlying sediments the system may further need external forcing.

The documented seismic pipes postdate the deposition of the upper Aberdeen Ground Formation (S1.2, MIS 13-21: 474-866 ka). This suggests that they may relate to glacial isostatic and/or glacitectonic mechanisms (e.g. deformation by overriding ice). In glacial environments, overpressure can be generated by rapid sedimentation pulses (Hustoft et al., 2009) or cyclic loading and unloading by ice during the last glacial cycle (Karstens & Berndt, 2015). Gas hydrate dissociation similar to the Troll area further north also represents a possible scenario for gas release (Mazzini et al., 2017). However, the presence of sub-glacial gas hydrates during the LGM in the Witch Ground Basin remains speculative.

Evidence for class 1 pockmark activity is multifold. First, methane seepage is visible in water column images and second, the presence of methane derived authigenic carbonates (MDACs) indicate long-lasting seepage (Figure 2.6a, d). The gas supply is continuous through the co-located pipes. The pockmark activity and flow rates may have been relatively strong at the start with a gradual reduction due to decreasing overpressure in the subsurface. Similar to other seepage sites, current flow rates may also be dependent on tidal pressure changes (Römer et al., 2016).

Class 1 pockmark morphology is likely dependent on the properties of the host sediment (Boudreau et al., 2001; Boudreau et al., 2005; Andrews et al., 2010; Mogollón et al., 2012). We interpret the change in morphometry as a result of the different properties of the outcropping sediments, i.e. unit S4.1 comprises over-consolidated subglacial till with hard, muddy, pebbly sands or sandy muds instead of soft, fine-grained glaciomarine sediments of the Witch Ground Formation (unit S5; Andrews et al., 1990).

Class 1 pockmarks may easily form within the soft, fine-grained sediments of the Witch Ground Formation within the Witch Ground Basin. Elsewhere in the North Sea (e.g. Viking Graben), similar structural and geological conditions may also induce vertical fluid flow and methane seepage at the seafloor. However, coarser grained sediments, which are present over large areas of the central North Sea (Graham et al., 2010; Stoker et al., 2011; Sejrup et al., 2014; Reinardy et al., 2017), may hinder the formation of pockmarks. Budget calculations of natural geological sources based on pockmark numbers may therefore systematically underestimate the methane flux.

### 2.7.4. Class 2 pockmarks - Timing and controls of fluid venting

The timing of class 2 pockmark formation is constrained by the age of the Witch Ground Formation (S5). The Witch Ground Formation was deposited after 26,595 ± 387 cal. years BP. Initially during a transition from glaciomarine to marine environment, the sedimentation rates were very high, i.e. up to 50-100 cm/1000 years (unit S5, Figure 2.6a, 2.8; Erlenkeuser, 1979; Johnson & Elkins, 1979; Sejrup et al., 2014). Exposed iceberg plough marks at the seafloor indicate very limited input of sediment into the Witch Ground Basin later on during the Holocene (Figure 2.3a). Thus, we can constrain the time of formation of the class 2 pockmarks to between 26,595 ± 387 cal. years BP and the Holocene (8 ka). Class 2 pockmark formation was likely episodic as buried paleo-pockmarks occur at specific stratigraphic horizons within unit S5. If each of these horizons corresponds to their formation time, there have been at least four different phases of pockmark activity (Figure 2.6a). The density of pockmarks per tier is decreasing with increasing burial depth (Figures 2.5a, Figure 2.6a, Long 1992), which suggests that the late stages of pockmark formation had greater source strength and overpressure than the earlier ones. This is similar to what was proposed for the southern North Sea (Krämer et al., 2017).

Class 2 pockmark formation is likely dependent on the host sediments. They predominantly occur in areas where S5.2 exceeds 2 m thickness and there is a significant correlation of pockmark depth with sediment thickness (Figure 2.7). Neither the abundant iceberg plough marks nor the underlying tunnel valleys seem to play a role for pockmark distribution (Figures 2.3, 2.7). In this context, the distance between neighboring pockmarks (Table 2.1) and the similar appearance of class 2 pockmarks (Figure 2.3,Table 2.1) suggest homogeneous pre-conditions in the subsurface as well as an exclusion zone around each pockmark related to a drainage cell where no other pockmark may form (Maia et al., 2016).

The fluid source of class 2 pockmarks is more difficult to constrain. Similar pockmark occurrences in the North Sea have been associated with methane venting due to post-glacial gas hydrate dissociation (e.g. Troll; Mazzini et al., 2017). However, there are no observations of active gas venting or direct proof of MDACs associating class 2 pockmark formation in the

Witch Ground Basin with focused methane release. Furthermore, our results show low methane concentrations, low organic carbon content and porewater sulfate concentrations that decrease gently with depth indicating no upward migration of methane from below (Figure 2.8). At the same time, there are no direct indications for focused expulsion of porewater or biogenic activity, which may represent alternative formation processes (Judd and Hovland, 2007). Hence, we are not able to determine the fluids involved in the formation of class 2 pockmarks directly and need to constrain them based on the involved formation processes.

Mechanisms of pockmark formation in the Witch Ground Basin include (1) venting of interstitial biogenic or thermogenic gas (Judd & Hovland, 2007; Hovland et al., 2010; Kilian et al., 2017), (2) porewater escape during compaction (Harrington, 1985). Seepage of thermogenic hydrocarbons has often been proposed for the North Sea. However, we do neither see a hydraulic connection towards deeper strata nor any indication for gas venting into the water column or free gas in the shallow sedimentary successions (S5, Figure 2.6). The low methane concentrations and the downward decreasing sulfate concentrations indicate no upward transport of methane.

Biogenic methane from decomposition of organic material represents another possible source. Microbial methanogenesis may lead to accumulation of free gas due to the soft, cohesive, low permeable sediments of the Witch Ground Basin instead of migrating out of the sediments (Boudreau et al., 2001; Boudreau et al., 2005). Such a scenario has been proposed for organic-rich sediments in the Arkona Basin, Baltic Sea, (Orsi et al., 1995; Abegg & Anderson, 1996; Mogollón et al., 2012) and Belfast Bay, Maine, USA (Brothers et al., 2012). There, pockmark formation is dependent on the sediment thickness, flux of organic matter and sedimentation rates. The accumulation of free gas depends on the rate of degradation of organic matter and sediment properties, primarily permeability, and occurs where the sediment thickness exceeds 3 m (Boudreau et al., 2001; Boudreau et al., 2005; Mogollón et al., 2012). However, echosounder data for the Witch Ground Basin do not reveal any amplitude blanking indicating free gas within S5. Furthermore, the organic carbon content is not particularly high (~1%) and the methane concentrations too low to generate free gas in the subsurface. In combination, our results indicate that in-situ microbial methanogenesis and accumulation of free gas is unlikely the cause for pockmark formation.

Unrecognized sources such as gas hydrates or permafrost may provide other possible sources of fluids that may have formed the class 2 pockmarks. However, the presence of sub-glacial gas hydrates during the LGM remains speculative. The sedimentary succession of the Witch Ground Formation shows high lateral coherence indicating no disturbance due to the dissociation of gas hydrates. Permafrost in the Witch Ground Basin during deposition of the Witch Ground Formation (S5) was not possible as our results show that this unit was deposited in glaciomarine to marine environments (indicated by C/N, Ca/Ti, Zr/Rb, Ca/Fe and Fe/S ratios and dropstones in unit 1, Figure 2.8).

While pockmarks in the central North Sea are primarily associated with seepage of hydrocarbons, our aforementioned results show no conclusive evidence that class 2 pockmark formation was gas-driven. Therefore, we also consider purely sedimentological mechanisms (Paull et al., 2002). Such a mechanism may be compaction-related dewatering of fast accumulated sediments (disequilibrium compaction, Harrington, 1985). The accumulation rates during the deposition of the Witch Ground Formation are sufficiently high (0.5-1m/ka) to retain fluids at shallow depth (Mann & Mackenzie, 1990). In this case, the porewater would have been trapped within the soft cohesive sediments of the Witch Ground Formation (clays & silt) and pore pressure would have risen over time releasing fluids. Once vertical pathways are established, they laterally drain the surrounding sediments (Harrington, 1985).

This process broadly agrees with our observations. There is no acoustic turbidity within the Witch Ground Formation that would indicate free gas (Figures 2.4a, 2.5a, 2.6a). Instead a transition from glaciomarine to marine sediments is documented by the sediment core (Figure 2.8). The transition from glaciomarine to marine deposition represents a permeability inversion as less permeable distal marine sediments overlie proximal glaciomarine sediments. Because the glaciomarine sediments will continue to compact and dewater after the marine sediments have been emplaced the expelled porewater cannot escape easily, which causes overpressure and focusing of fluid migration. Fractures in the Witch Ground Formation may be the result of this compaction process (Figures 2.5a, 2.6a). Similar compaction-related dewatering and fractures at shallow depth below the seafloor are observed in the Hatton Basin in the northeast Atlantic Ocean (Berndt et al., 2012). The increase in pockmark density per tier with decreasing burial depth indicates an upward increase in source strength (Figure 2.5a). The random distribution instead of aggradation or stacking of pockmarks through time supports the diffusive source character (Figure 2.5a). Both observations match the process of compaction-related dewatering. Sediment compaction as genetic origin for the formation of class 2 pockmarks is further supported by a lower chlorinity at depth in the interstitial water (Figure 2.8). This is indicative for the upward migration of less saline water and would be expected because of the glaciomarine provenance of the lower Witch Ground Formation. Based on the considerations above we propose that class 2 pockmark formation in the Witch Ground Basin is at least partly related to compaction. However, it seems unlikely that this mechanism was dominating the formation of deep pockmarks (> 0.5 m) in areas where only 2 m of soft cohesive sediments exist unless there was additional forcing. We also note that the sediment properties are not well constrained.

All evoked models rely on external forcing to release the overpressure in the subsurface and cause pockmark formation, because the tiers of pockmarks and paleo-pockmarks in the subsurface indicate the intermittent nature of seepage events in the Witch Ground Basin. These external forces need to be basin-wide and must have induced sufficient overpressure by a change of subsurface temperature or pressure conditions. In the Witch Ground Basin, temperature conditions may have changed due to warm water inflow from the North Atlantic (e.g. Becker et al., 2018). Pressure conditions may have changed due to rapid sedimentation (Hustoft et al., 2009; Reinardy et al. 2017), disequilibrium compaction (Flemings et al., 2008, Talukder, 2012), tidal currents (Chen & Slater, 2016), large storms (Krämer et al., 2017), or earthquakes (Field & Jennings, 1987; Hasiotis et al., 1996), which may have ultimately led to episodic fluid escape from the shallow marine sediments in the Witch Ground Basin.

## 2.8. Conclusions

We document >1500 pockmarks over an area of 225 km² within the Witch Ground Basin, northern North Sea. Based on their morphologies we distinguish between two classes of pockmarks. Class 1 pockmarks are >6 m deep, >75 m wide and >250 m long. Class 2 pockmarks, which represent 99.5 % of the overall dataset, are much smaller and more uniformly distributed within the study area. Their maximum depth ranges between 0.9-3.1 m and their maximum widths and length are 14-57 m and 26-140 m respectively.

From the structural and morphological analyses, we draw the following conclusions:

- There is no evidence of hydraulic connection between class 1 and class 2 pockmarks. Class 2 pockmarks solely occur in the soft, fine-grained sediments of the Witch Ground Formation, while class 1 pockmarks are co-located with deep fluid accumulations and seismic pipe structures in the subsurface. Together with the lack of intermediate sized pockmarks between the two endmember classes (with respect to pockmark sizes), this indicates the presence of two different fluid sources within the sediments.
- Seismic pipe structures under most class 1 pockmarks, which hydraulically connect deeper strata with the surface, represent vertical conduits for the fluids that formed class 1 pockmarks.
- Class 1 pockmarks relate to biogenic methane sourced from Mid Pleistocene strata (upper 500 ms corresponding to 375 m of the sedimentary succession at 1500 m/s), which migrates through vertical fluid conduits. Mixing of biogenic fluids derived at shallow depths with thermogenic-derived fluids from deeper sources is, however, possible and may occur episodically
- The up-bending of Witch Ground Formation sediments towards the pockmark suggests that class 1 pockmarks formed between 13,165 ± 55 to 26,595 ± 387 cal. years BP and present-day activity suggests they may have been active since their formation. Active seepage imaged during the last three decades in combination with indications for long-lasting seepage from MDAC suggests that Class 1 pockmarks may be continuously active over long times.
- In contrast, class 2 pockmarks may only have been active during certain episodes corresponding to the distinct reflectors at which they cluster. During repeated campaign-based water column imaging over the last three decades no seep activity was documented for the class 2 pockmarks at the surface supporting that this type of pockmark is not continuously active. These pockmarks may be sourced by compaction-

related dewatering. As the pockmarks cluster on distinct stratigraphic levels their formation must have been triggered by externally induced pressure and temperature changes affecting the entire Witch Ground Basin.

## Acknowledgements

We thank the shipboard scientific party of Maria S. Merian cruise 63 and Poseidon cruise 518. The British Ocean Sediment Core Research Facility (BOSCORF) is thanked for the use of their facilities and IHS for providing the Kingdom interpretation software within the academic licensing program. We thank PGS for providing their 3D seismic data set "CNS MegaSurveyPlus". Access to 3D seismic data through PGS data library (https://www.pgs.com/data-library/europe/nw-europe/north-sea/cns). We thank the EMODnet Bathymetry Consortium (2016) for access to the EMODnet Digital Bathymetry (DTM) (http://doi.org/10.12770/c7b53704-999d-4721-b1a3-04ec60c87238). Access to 2D seismic, echosounder and MBES data through Pangaea data repository (https://doi.org/10.1594/PANGAEA.897523). This research is part of the STEMM-CCS project, which has received funding from the European Union's Horizon 2020 research and innovation program under grant agreement No 654462. We thank two anonymous reviewers for their careful reviews that helped us to clarify different aspects of this study.

## References

Abegg, F., & Anderson, A. L. (1997). The acoustic turbid layer in muddy sediments of Eckernfoerde Bay, Western Baltic: methane concentration, saturation and bubble characteristics. *Marine Geology*, 137(1-2), 137-147.

Andresen, K. J., & Huuse, M. (2011). 'Bulls-eye' pockmarks and polygonal faulting in the Lower Congo Basin: relative timing and implications for fluid expulsion during shallow burial. *Marine Geology*, 279(1-4), 111-127.

Andresen, K. J. (2012). Fluid flow features in hydrocarbon plumbing systems: What do they tell us about the basin evolution? *Marine Geology,* 332, 89-108.

Andrews, B. D., Brothers, L. L., & Barnhardt, W. A. (2010). Automated feature extraction and spatial organization of seafloor pockmarks, Belfast Bay, Maine, USA. *Geomorphology*, *124*(1-2), 55-64.

Andrews, I. J., Long, D., Richards, P. C., Thomson, A. R., Brown, S., Chesher, J. A., & McCormac, M. (1990). *The geology of the Moray Firth* (Vol. 3). HMSO.

Austen, M., Warwick, R., & Ryan, K. (1993). Astomonema southwardorum sp. nov., a gutless nematode dominant in a methane seep area in the North Sea. *Journal of the Marine Biological Association of the United Kingdom*, 73(3), 627-634. doi:10.1017/S0025315400033166

Barry, M. A., Boudreau, B. P., & Johnson, B. D. (2012). Gas domes in soft cohesive sediments. *Geology*, 40(4), 379-382.

Becker, L. W., Sejrup, H. P., Hjelstuen, B. O., Haflidason, H., & Dokken, T. M. (2018). Ocean-ice sheet interaction along the SE Nordic Seas margin from 35 to 15 ka BP. *Marine Geology*, *402*, 99-117.

Berndt, C. (2005). Focused fluid flow in passive continental margins. *Philosophical Transactions of the Royal Society of London A: Mathematical, Physical and Engineering Sciences*, 363(1837), 2855-2871.

Berndt, C., Elger, J., Böttner, C., Gehrmann, R., Karstens, J., Muff, S., ... & Völsch, A. (2017). RV MARIA S. MERIAN Fahrtbericht/Cruise Report MSM63-PERMO, Southampton–Southampton (UK) 29.04.-25.05. 2017.

Berndt, C., Jacobs, C., Evans, A., Gay, A., Elliott, G., Long, D., & Hitchen, K. (2012). Kilometre-scale polygonal seabed depressions in the Hatton Basin, NE Atlantic Ocean: Constraints on the origin of polygonal faulting. *Marine Geology*, *332*, 126-133.

Boudreau, B. P., Gardiner, B. S., & Johnson, B. D. (2001). Rate of growth of isolated bubbles in sediments with a diagenetic source of methane. *Limnology and Oceanography*, 46(3), 616-622.

Boudreau, B. P., Algar, C., Johnson, B. D., Croudace, I., Reed, A., Furukawa, Y., ... & Gardiner, B. S. (2005). Bubble growth and rise in soft sediments. *Geology*, 33(6), 517-520.

Brothers, L. L., Kelley, J. T., Belknap, D. F., Barnhardt, W. A., Andrews, B. D., Legere, C., & Clarke, J. E. H. (2012). Shallow stratigraphic control on pockmark distribution in north temperate estuaries. *Marine Geology*, 329, 34-45.

Buckley, F. A. (2012). An early Pleistocene grounded ice sheet in the Central North Sea. *Geological Society, London, Special Publications*, 368, SP368-8.

Buckley, F. A. (2016). A glaciogenic sequence from the Early Pleistocene of the Central North Sea. *Journal of Quaternary Science*, 32(2), 145-168.

Böttner, C., Gross, F., Geersen, J., Crutchley, G. J., Mountjoy, J. J., & Krastel, S. (2018). Marine Forearc Extension in the Hikurangi Margin: New Insights From High-Resolution 3-D Seismic Data. *Tectonics*.

Cartwright, J. (2007). The impact of 3D seismic data on the understanding of compaction, fluid flow and diagenesis in sedimentary basins. *Journal of the Geological Society*, 164(5), 881-893.

Chand, S., Crémière, A., Lepland, A., Thorsnes, T., Brunstad, H., & Stoddart, D. (2017). Long-term fluid expulsion revealed by carbonate crusts and pockmarks connected to subsurface gas anomalies and palaeo-channels in the central North Sea. *Geo-Marine Letters*, 37(3), 215-227.

Chen, X., & Slater, L. (2016). Methane emission through ebullition from an estuarine mudflat: 1. A conceptual model to explain tidal forcing based on effective stress changes. *Water Resources Research*, 52(6), 4469-4485.

Caress, D. W., and D. N. Chayes (2017), MB-System: Mapping the Seafloor, *https://www.mbari.org/products/research-software/mb-system*.

Ciais, P., Sabine, C., Bala, G., Bopp, L., Brovkin, V., Canadell, J., ... & Jones, C. (2013). Carbon and other biogeochemical cycles. In Climate change 2013: the physical science basis. Contribution of Working Group I to the *Fifth Assessment Report of the Intergovernmental Panel on Climate Change* (pp. 465-570). Cambridge University Press.

Clayton, C. J., & Dando, P. R. (1996). Comparison of seepage and seal leakage rates. In Schumacher, D., Abrams, M. A., eds., *Hydrocarbon migration and its near surface expression: AAPG Memoi*r 66, p. 169-171.

Clayton, C. J., & Hay, S. J. (1994). Gas migration mechanisms from accumulation to surface. *Bulletin of the Geological Society of Denmark*, 41(1), 12-23

Cole, D., Stewart, S. A., & Cartwright, J. A. (2000). Giant irregular pockmark craters in the Palaeogene of the outer Moray Firth basin, UK North Sea. *Marine and Petroleum Geology*, 17(5), 563-577.

Croudace, I. W., Rindby, A., & Rothwell, R. G. (2006). ITRAX: description and evaluation of a new multi-function X-ray core scanner. *Geological Society, London, Special Publications*, *267*(1), 51-63.

Dando, P. R., Austen, M. C., Burke Jr, R. A., Kendall, M. A., Kennicutt, M. C., Judd, A. G., ... & Southward, A. J. (1991). Ecology of a North Sea pockmark with an active methane seep. *Marine Ecology Progress Series*, 49-63.

Dean, J. F., Middelburg, J. J., Röckmann, T., Aerts, R., Blauw, L. G., Egger, M., ... & Slomp, C. P. (2018). Methane feedbacks to the global climate system in a warmer world. *Reviews of Geophysics*.

Dickens, G. R. (2011). Down the rabbit hole: Toward appropriate discussion of methane release from gas hydrate systems during the Paleocene-Eocene thermal maximum and other past hyperthermal events. *Climate of the Past*, *7*(3), 831-846.

Domenico, S. N. (1977). Elastic properties of unconsolidated porous sand reservoirs. *Geophysics*, 42(7), 1339-1368.

Erlenkeuser, H. (1979). Environmental effects on radiocarbon in coastal marine sediments. *University of California Press*.

Etiope, G., Lassey, K. R., Klusman, R. W., & Boschi, E. (2008). Reappraisal of the fossil methane budget and related emission from geologic sources. *Geophysical Research Letters*, 35(9).

Field, M. E., & Jennings, A. E. (1987). Seafloor gas seeps triggered by a northern California earthquake. *Marine Geology*, 77(1-2), 39-51.

Flemings, P. B., Long, H., Dugan, B., Germaine, J., John, C. M., Behrmann, J. H., ... & Expedition, I. O. D. P. (2008). Pore pressure penetrometers document high overpressure near the seafloor where multiple submarine landslides have occurred on the continental slope, offshore Louisiana, Gulf of Mexico. *Earth and Planetary Science Letters*, 269(3), 309-325.

Gafeira, J., Dolan, M., & Monteys, X. (2018). Geomorphometric characterization of pockmarks by using a GIS-based semi-automated toolbox. *Geosciences*, 8(5).

Gafeira, J., & Long, D. (2015). Geological investigation of pockmarks in the Scanner Pockmark SCI area. *JNCC Report*, (570).

Gafeira, J., Long, D., & Diaz-Doce, D. (2012). Semi-automated characterisation of seabed pockmarks in the central North Sea. Near Surface Geophysics, 10(4), 303-314.

Gay, A., Lopez, M., Berndt, C., & Seranne, M. (2007). Geological controls on focused fluid flow associated with seafloor seeps in the Lower Congo Basin. *Marine Geology*, 244(1-4), 68-92.

Graham, A. G., Lonergan, L., & Stoker, M. S. (2010). Depositional environments and chronology of Late Weichselian glaciation and deglaciation in the central North Sea. *Boreas*, 39(3), 471-491.

Harrington, P. K. (1985). Formation of pockmarks by pore-water escape. *Geo-Marine Letters*, *5*(3), 193-197.

Hasiotis, T., Papatheodorou, G., Kastanos, N., & Ferentinos, G. (1996). A pockmark field in the Patras Gulf (Greece) and its activation during the 14/7/93 seismic event. Marine *Geology*, 130(3-4), 333-344.

Holmes, R. (1977). The quaternary geology of the UK sector of the North Sea between 56N and 58N. *Report of the Institute of Geological Sciences*, *77*(14), 50-51.

Hovland, M., & Irwin, H. (1989). Hydrocarbon leakage, biodegradation and the occurrence of shallow gas and carbonate cement. In Norwegian Petroleum Society Conf. *Shallow Gas and Leaky Reservoirs, Stavanger, Norway*. Apr (pp. 10-11).

Hovland, M., & Judd, A. (1988). Seabed pockmarks and seepages: impact on geology, biology, and the marine environment. *Springer*.

Hovland, M., & Sommerville, J. H. (1985). Characteristics of two natural gas seepages in the North Sea. *Marine and Petroleum Geology*, 2(4), 319-326.

Hovland, M., Heggland, R., De Vries, M. H., & Tjelta, T. I. (2010). Unit-pockmarks and their potential significance for predicting fluid flow. *Marine and Petroleum Geology*, 27(6), 1190-1199.

Hubbert, M.K., Willis, D.G., 1957. Mechanic of hydraulic fracturing. *Trans. Soc. Pet. Eng*. AIME1957, 153–168.

Hustoft, S., Dugan, B., & Mienert, J. (2009). Effects of rapid sedimentation on developing the Nyegga pockmark field: Constraints from hydrological modeling and 3-D seismic data, offshore mid-Norway. *Geochemistry, Geophysics, Geosystems*, 10(6).

Johnson, T. C., & Elkins, S. R. (1979). Holocene deposits of the northern North Sea evidence for dynamic control of their mineral and chemical composition. *Geologie en Mijnbouw*, 58(3), 353-366.

Judd, A., & Hovland, M. (2007). Seabed fluid flow: the impact on geology, biology and the marine environment. *Cambridge University Press*.

Judd, A. G., Hovland, M., Dimitrov, L. I., Garcia Gil, S., & Jukes, V. (2002). The geological methane budget at continental margins and its influence on climate change. *Geofluids*, 2(2), 109-126.

Judd, A. G., Long, D., & Sankey, M. (1994). Pockmark formation and activity, UK block 15/25, North Sea. *Bulletin of the Geological Society of Denmark*, 41(1), 34-49.

Karstens, J., & Berndt, C. (2015). Seismic chimneys in the Southern Viking Graben–Implications for palaeo fluid migration and overpressure evolution. *Earth and Planetary Science Letters*, 412, 88-100.

Karstens, J., Haflidason, H., Becker, L. W., Berndt, C., Rüpke, L., Planke, S., ... & Mienert, J. (2018). Glacigenic sedimentation pulses triggered post-glacial gas hydrate dissociation. *Nature communications*, 9(1), 635.

Kilian, R., Breuer, S., Behrmann, J. H., Baeza, O., Diaz-Michelena, M., Mutschke, E., ... & Lamy, F. (2017). The Seno Otway pockmark field and its relationship to thermogenic gas occurrence at the western margin of the Magallanes Basin (Chile). *Geo-Marine Letters*, 1-14.

King, L. H., & MacLean, B. (1970). Pockmarks on the Scotian shelf. *Geological Society of America Bulletin*, *81*(10), 3141-3148.

Koch, S., Berndt, C., Bialas, J., Haeckel, M., Crutchley, G., Papenberg, C., ... & Greinert, J. (2015). Gas-controlled seafloor doming. *Geology*, 43(7), 571-574.

Krämer, K., Holler, P., Herbst, G., Bratek, A., Ahmerkamp, S., Neumann, A., ... & Winter, C. (2017). Abrupt emergence of a large pockmark field in the German Bight, southeastern North Sea. *Scientific reports*, 7(1), 5150.

Lafuerza, S., Sultan, N., Canals, M., Frigola, J., Berne, S., Jouet, G., ... & Sierro, F. J. (2009). Overpressure within upper continental slope sediments from CPTU data, Gulf of Lion, NW Mediterranean Sea. *International Journal of Earth Sciences*, 98(4), 751-768.

Linke, P., Haeckel, M. (2018) Baseline Study for the Environmental Monitoring of Subseafloor CO2 Storage Operations. RV POSEIDON Fahrtbericht / Cruise Report POS518: GEOMAR Report, N. Ser. 040. GEOMAR Helmholtz-Zentrum für Ozeanforschung, Kiel, 84 pp. DOI 10.3289/GEOMAR_REP_NS_40_2018.

Long, D. (1992). Devensian late-glacial gas escape in the central North Sea. *Continental Shelf Research*, 12(10), 1097-1110.

Long, D., Bent, A., Harland, R., Gregory, D. M., Graham, D. K., & Morton, A. C. (1986). Late Quaternary palaeontology, sedimentology and geochemistry of a vibrocore from the Witch Ground Basin, central North Sea. *Marine Geology*, 73(1-2), 109-123.

Løseth, H., Gading, M., & Wensaas, L. (2009). Hydrocarbon leakage interpreted on seismic data. *Marine and Petroleum Geology*, 26(7), 1304-1319.

Løseth, H., Wensaas, L., Arntsen, B., Hanken, N. M., Basire, C., & Graue, K. (2011). 1000 m long gas blow-out pipes. *Marine and Petroleum Geology*, 28(5), 1047-1060.

Maeck, A., DelSontro, T., McGinnis, D. F., Fischer, H., Flury, S., Schmidt, M., ... & Lorke, A. (2013). Sediment trapping by dams creates methane emission hot spots. *Environmental science & technology*, 47(15), 8130-8137.

Maia, A. R., Cartwright, J., & Andersen, E. (2016). Shallow plumbing systems inferred from spatial analysis of pockmark arrays. *Marine and Petroleum Geology*, *77*, 865-881.

Mann, D. M., & Mackenzie, A. S. (1990). Prediction of pore fluid pressures in sedimentary basins. *Marine and Petroleum Geology*, *7*(1), 55-65.

Mazzini, A., Svensen, H. H., Forsberg, C. F., Linge, H., Lauritzen, S. E., Haflidason, H., ... & Tjelta, T. I. (2017). A climatic trigger for the giant Troll pockmark field in the northern North Sea. *Earth and Planetary Science Letters*, 464, 24-34.

Mogollón, J. M., Dale, A. W., Fossing, H., & Regnier, P. (2012). Timescales for the development of methanogenesis and free gas layers in recently-deposited sediments of Arkona Basin (Baltic Sea). *Biogeosciences*, 9(5), 1915-1933.

Moss, J. L., Cartwright, J., Cartwright, A., & Moore, R. (2012). The spatial pattern and drainage cell characteristics of a pockmark field, Nile Deep Sea Fan. *Marine and Petroleum Geology*, 35(1), 321-336.

Niemann, H., Elvert, M., Hovland, M., Orcutt, B., Judd, A., Suck, I., ... & Boetius, A. (2005). Methane emission and consumption at a North Sea gas seep (Tommeliten area). *Biogeosciences Discussions*, 2(4), 1197-1241.

Orsi, T. H., Werner, F., Milkert, D., Anderson, A. L., & Bryant, W. R. (1996). Environmental overview of Eckernförde bay, northern Germany. *Geo-Marine Letters*, 16(3), 140-147.

Osborne, M. J., & Swarbrick, R. E. (1997). Mechanisms for generating overpressure in sedimentary basins: A reevaluation. *AAPG bulletin*, *81*(6), 1023-1041.

Ottesen, D., Dowdeswell, J. A., & Bugge, T. (2014). Morphology, sedimentary infill and depositional environments of the Early Quaternary North Sea Basin (56–62 N). *Marine and Petroleum Geology*, 56, 123-146.

Paull, C., Ussler Iii, W., Maher, N., Greene, H. G., Rehder, G., Lorenson, T., & Lee, H. (2002). Pockmarks off Big Sur, California. *Marine Geology*, *181*(4), 323-335.

Petrenko, V. V., Smith, A. M., Schaefer, H., Riedel, K., Brook, E., Baggenstos, D., ... & Fain, X. (2017). Minimal geological methane emissions during the Younger Dryas–Preboreal abrupt warming event. *Nature*, 548(7668), 443.

Pfannkuche, O. (2005). Cruise Report ALKOR 259: Methane Cycle at Shallow Gaseous Sediments in the Central North Sea. GEOMAR, Kiel, 42pp.

Pfannkuche, O. (2006). Preliminary Report ALKOR 290: Gas seeps in the central and northern North Sea, GEOMAR, Kiel, 8pp.

Plaza-Faverola, A., Bünz, S., & Mienert, J. (2011). Repeated fluid expulsion through sub-seabed chimneys offshore Norway in response to glacial cycles. *Earth and Planetary Science Letters*, 305(3-4), 297-308.

Plaza-Faverola, A., Vadakkepuliyambatta, S., Hong, W. L., Mienert, J., Bünz, S., Chand, S., & Greinert, J. (2017). Bottom-simulating reflector dynamics at Arctic thermogenic gas provinces: An example from Vestnesa Ridge, offshore west Svalbard. *Journal of Geophysical Research: Solid Earth*, 122(6), 4089-4105.

Rea, B. R., Newton, A. M., Lamb, R. M., Harding, R., Bigg, G. R., Rose, P., ... & Buckley, F. (2018). Extensive marine-terminating ice sheets in Europe from 2.5 million years ago. *Science advances*, 4(6), eaar8327.

Reinardy, B. T., Hjelstuen, B. O., Sejrup, H. P., Augedal, H., & Jørstad, A. (2017). Late Pliocene-Pleistocene environments and glacial history of the northern North Sea. *Quaternary Science Reviews*, 158, 107-126.

Rose, P., Byerley, G., Vaughan, O., Cater, J., Rea, B. R., Spagnolo, M., & Archer, S. (2016). Aviat: a Lower Pleistocene shallow gas hazard developed as a fuel gas supply for the Forties Field. In Geological Society, London, Petroleum Geology Conference series (Vol. 8, pp. PGC8-16). *Geological Society of London*.

Römer, M., Riedel, M., Scherwath, M., Heesemann, M., & Spence, G. D. (2016). Tidally controlled gas bubble emissions: A comprehensive study using long-term monitoring data from the NEPTUNE cabled observatory offshore Vancouver Island. *Geochemistry, Geophysics, Geosystems*, *17*(9), 3797-3814.

Saunois, M., Bousquet, P., Poulter, B., Peregon, A., Ciais, P., Canadell, J. G., ... & Janssens-Maenhout, G. (2016). The global methane budget 2000–2012. *Earth System Science Data (Online)*, 8(2).

Schneider von Deimling, J. , Linke, P., Schmidt, M., & Rehder, G. (2015). Ongoing methane discharge at well site 22/4b (North Sea) and discovery of a spiral vortex bubble plume motion. *Marine and Petroleum Geology*, *68*, 718-730.

Sejrup, H. P., Aarseth, I., Ellingsen, K. L., Reither, E., Jansen, E., Løvlie, R., ... & Stoker, M. (1987). Quaternary stratigraphy of the Fladen area, central North Sea: a multidisciplinary study. *Journal of Quaternary science*, 2(1), 35-58.

Sejrup, H. P., Haflidason, H., Aarseth, I., King, E., Forsberg, C. F., Long, D., & Rokoengen, K. (1994). Late Weichselian glaciation history of the northern North Sea. *Boreas*, 23(1), 1-13.

Sommer, S., Linke, P., Pfannkuche, O., Schleicher, T., Schneider, J., Reitz, A., Haeckel, M., Flögel, S., Hensen, C. (2009) Seabed methane emissions and the habitat of frenulate tubeworms on the Captain Arutyunov mud volcano (Gulf of Cadiz). *Marine Ecology Progress Series 382*, 69-86. DOI 10.3354/meps07956

Stewart, M. A., & Lonergan, L. (2011). Seven glacial cycles in the middle-late Pleistocene of northwest Europe: Geomorphic evidence from buried tunnel valleys. *Geology*, 39(3), 283-286.

Stoker, M. S., Balson, P. S., Long, D., & Tappin, D. R. (2011). An overview of the lithostratigraphical framework for the Quaternary deposits on the United Kingdom continental shelf.

Stoker, M. S., & Bent, A. J. (1987). Lower Pleistocene deltaic and marine sediments in boreholes from the central North Sea. *Journal of Quaternary Science*, 2(2), 87-96.

Stoker, M. S., & Long, D. (1984). A relict ice-scoured erosion surface in the central North Sea. *Marine Geology*, 61(1), 85-93.

Svensen, H., Planke, S., Malthe-Sørenssen, A., Jamtveit, B., Myklebust, R., Eidem, T. R., & Rey, S. S. (2004). Release of methane from a volcanic basin as a mechanism for initial Eocene global warming. *Nature*, *429*(6991), 542.

Talukder, A. R. (2012). Review of submarine cold seep plumbing systems: leakage to seepage and venting. *Terra Nova*, 24(4), 255-272.

White, J. E. (1975). Computed seismic speeds and attenuation in rocks with partial gas saturation. *Geophysics*, 40(2), 224-232.

Whiticar, M. J. (2000). Can stable isotopes and global budgets be used to constrain atmospheric methane budgets?. In *Atmospheric methane* (pp. 63-85). Springer, Berlin, Heidelberg.

Wegener, G., Shovitri, M., Knittel, K., Niemann, H., Hovland, M., & Boetius, A. (2008). Biogeochemical processes and microbial diversity of the Gullfaks and Tommeliten methane seeps (Northern North Sea*). Biogeosciences Discussions*, 5(1), 971-1015.

Yu, Y., Kelley, C. L., & Mardanova, I. M. (2015). U.S. patent no. 9,105,075. Washington, DC: U.S. patent and Trademark Office.

# 3. Greenhouse gas emissions from marine decommissioned hydrocarbon wells: Leakage detection, monitoring and mitigation strategies

Christoph Böttner, Matthias Haeckel, Mark Schmidt, Christian Berndt, Lisa Vielstädte, Jens Karstens, Tim Weiß

In review at International Journal of Greenhouse Gas Control.

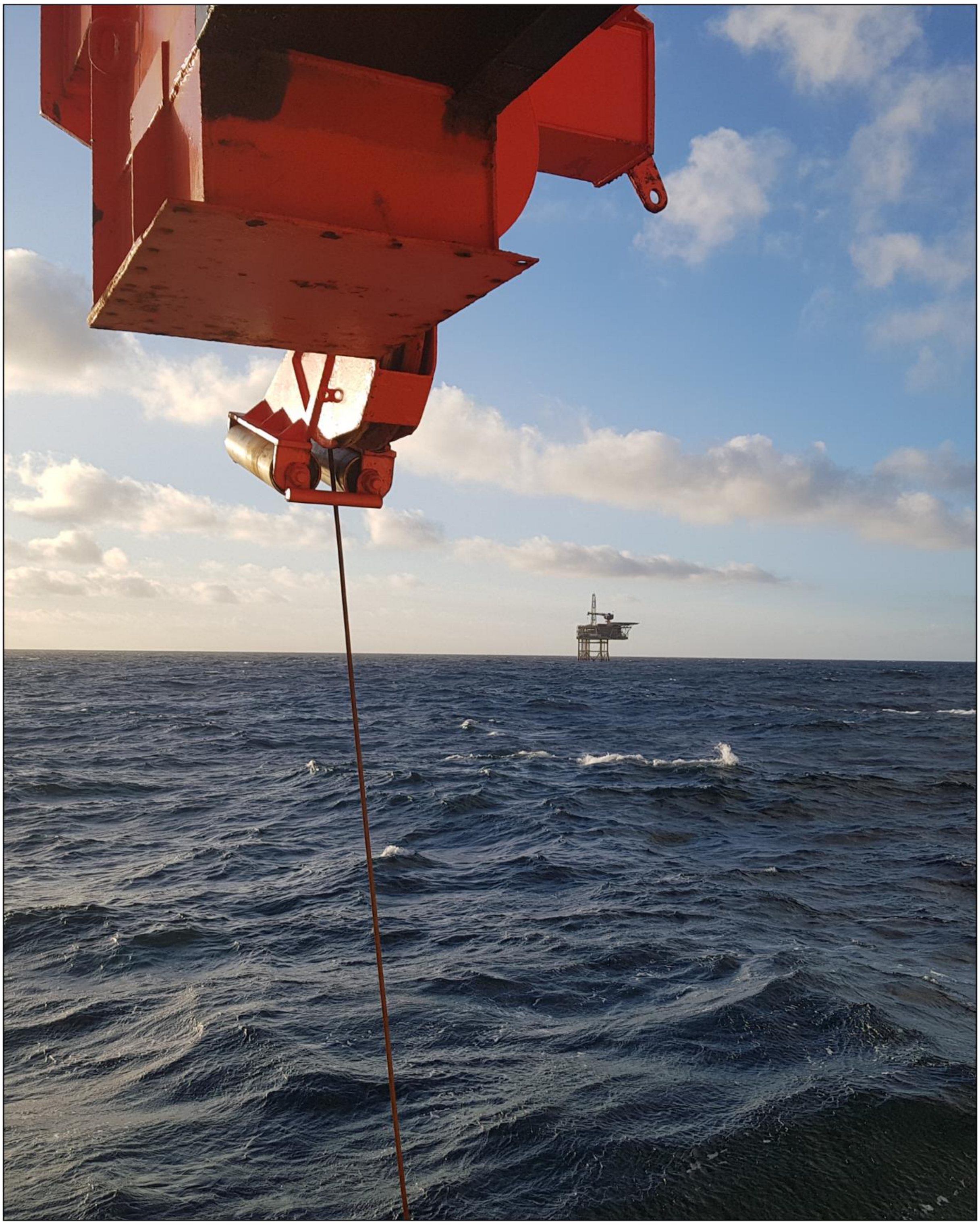

The Goldeneye platform during sundown at cruise POS518 to the Central North Sea.

## Highlights

1. Gas release from wells may counteract efforts to mitigate greenhouse gas emissions
2. An approach for assessing methane release from marine decommissioned wells
3. This gas release largely depends on the presence of shallow gas accumulations
4. Methane release from hydrocarbon wells represents a major source in the North Sea

## 3.1. Abstract

Hydrocarbons gas emissions from decommissioned hydrocarbon wells may counteract efforts to mitigate greenhouse gas emissions from fossil fuel infrastructure. We have developed an approach for assessing methane leakage from marine decommissioned wells based on a combination of existing regional industrial seismic and newly acquired hydroacoustic water column imaging data from the Central North Sea. There is evidence that 28 out of 43 investigated wells release gas from the seafloor into the water column. This gas release largely depends on the presence of shallow gas accumulations and their distance to the wells. In the upper 1000 m below the seabed, gas migration is likely focused along drilling-induced fractures around the borehole. Combining available direct measurements for methane release from marine decommissioned wells with our leakage analysis suggests that gas release from investigated decommissioned hydrocarbon wells are a major source of methane (0.9-3.8 kt of methane per year from 1,794 wells) in the North Sea. This means inadvertent gas release from hydrocarbon wells has to be considered when compiling regional gas budgets.

## 3.2. Introduction

Inadvertent hydrocarbon gas emissions from offshore wells have to be considered when compiling regional gas budgets, particularly for methane ($CH_4$), which is the second most important greenhouse gas after carbon dioxide (Ciais et al., 2013; Saunois et al., 2016). The impact of anthropogenic methane emissions on climate change receives increasing attention (Saunois et al., 2016) as societies attempt to transit from coal as primary energy source to gas and further on to renewables. While our understanding of carbon dioxide ($CO_2$) sources and sinks is well established (Global emissions 2008-2017: 9.4 ± 0.5 Gt C $yr^{-1}$; Le Quéré et al., 2018), estimates for the global methane budget still show large uncertainties both with attributing and quantifying methane emissions, as evidenced by the large discrepancies between top-down and bottom-up estimates of global sources and sinks (Global emissions 2003-2012 top-down: 0.558 [0.540-0.568] Gt $CH_4$ $yr^{-1}$, bottom-up: 0.736 [0.596-0.884] Gt $CH_4$ $yr^{-1}$; Saunois et al., 2016). Methane emissions from the up- and down-stream natural oil and gas sectors are estimated to reach 0.079 [0.069-0.088] Gt $CH_4$ $yr^{-1}$ representing about 65% of total fossil $CH_4$ emissions for the decade 2003-2012 (Saunois et al., 2016). Emissions of methane and other hydrocarbon gases from abandoned wells add to this part of the budget and counteract efforts to mitigate greenhouse gas emissions from fossil fuel infrastructure (Vielstädte et al., 2017). There is also another societal context in which greenhouse gas emissions from offshores may become important. To slow down global warming due to the injection of CO2 and into the atmosphere, it has been proposed to store large amounts of CO2 in geological formations. Wells that penetrate these storage formations may represent potential leakage pathways to shallower strata (Gasda et al., 2004; Nordbotten et al., 2005). Prolonged leakage from numerous wells may thus counteract the effort to store CO2 in the long term (Vielstädte et al., 2019).

Measured methane emissions from decommissioned wells span two orders of magnitude with higher releases for marine wells in proximity of shallow gas accumulations, i.e. 1-19 t yr$^{-1}$ of $CH_4$ (Vielstädte et al., 2015) and lower releases for unplugged onshore wells in the proximity of coal areas, i.e. 0.5 t yr$^{-1}$ of $CH_4$ (Kang et al., 2016). Well attributes, such as geographic location, age, drilling data (spud date), production and abandonment, may be used as proxies to assess the leakage propensity of wells (Vielstädte et al., 2015; Kang et al., 2016; Townsend-Small et al., 2016). As onshore wells show a correlation of leakage with well attributes, i.e. geographic location, age, and proximity to shallow gas accumulations (Kang et al., 2016) it is likely that similar attributes may be identified for offshore boreholes (i.e. Vielstädte et al., 2015). In offshore areas seismic data have been used to identify shallow gas accumulations in the subsurface and help defining areas, where leakage is more likely (White, 1975; Anstey, 1977; Karstens & Berndt, 2015; Marfurt & Alves, 2015). In combination with information on the status of wells and their spatial distribution, this should allow to constrain leakage propensity and flow of hydrocarbon gases from drilled wells. However, basic information, such as the number of wells or their location, even in regions with a long history of oil and gas exploration and production, are often poorly documented (e.g. Kang et al., 2016; Townsend-Small et al., 2016).

Inadvertent release of hydrocarbon gases from offshore wells occurs through two main processes controlling vertical fluid migration. First, leakage may occur through faulty well casings and/or annuli (Celia & Bachu, 2003; Gasda et al., 2004) commonly referred to as "well integrity issues". Such migration pathways may open in the micro annulus between casing and annular cement, micro annulus between cement plug and casing, cracks or channels in cement plugs, rupture or pits in casing resulting in connection between annular cement and wellbore, cracks or channels in annular cement resulting in connections between formation and casing, or through the micro annulus between annular cement and formation (Gasda et al., 2004). Second, fluid migration may occur along the outside of the well through drilling-induced fractures surrounding the well path (Harrison et al., 1954; Gurevich et al., 1993; Aadnøy & Bell, 1998; Brudy & Zoback, 1999; Gasda et al., 2004; Vielstädte et al., 2015). The induced fracture networks may act as a fluid migration pathway bypassing permeability barriers in the subsurface, thus connecting deeper strata hydraulically with the seabed (Aydin, 2000; Cartwright et al., 2007; Løseth et al., 2011). The process of focused vertical fluid migration is up to ten times more efficient in areas, where pre-existing natural high-permeability pathways, such as seismic chimneys or pipe structures, exist in the subsurface (Vielstädte et al., 2015).

However, currently no quantitative data exist for leakage through the fractured surroundings of well paths.

Here, we present an approach for assessing the propensity of leakage from boreholes based on existing regional three-dimensional seismic data. For this purpose, we analyze the conditions for gas leakage from hydrocarbon wells in the Central North Sea. We constrain the amount of methane that is escaping from specific decommissioned hydrocarbon wells into the North Sea based on hydroacoustic water column imaging. We combine these constraints to approximate the total methane release from wells covered by seismic data in the Central North Sea. Furthermore, we formulate recommendations for future borehole placements and best practice for drilling and decommissioning of wells to avoid inadvertent gas release after abandonment. In addition, we provide the basis for recommendations for prolonged leakage monitoring after abandonment.

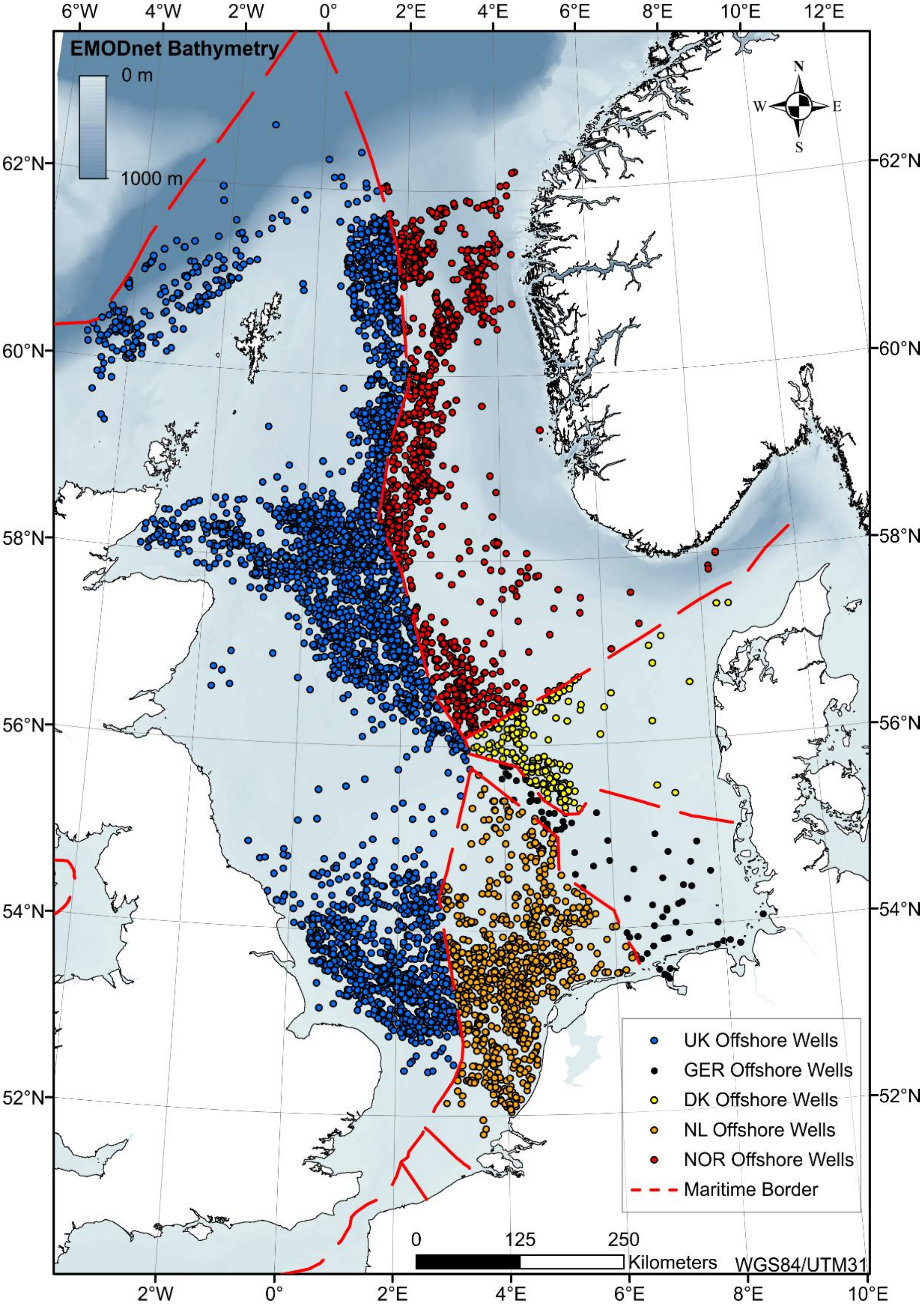

**Figure 3.1.** The North Sea comprises of 20507 documented offshore wells (draped on EMODnet bathymetric data). The wells cumulate in areas where prolific hydrocarbon provinces exist in the subsurface. The well data set comprises of 11672 UK (UK, blue dots), 6254 Norwegian (NOR, red dots), 269 Danish (DK, yellow dots), 204 German (GER, black dots) and 2108 Dutch (NL, orange) offshore wells in the North Sea separated by the maritime border (red dashed line). The available information with respect to these offshore wells is highly variable, however, for all of them at least geographic information, well intent, drilling date and drilling depth exist. See sources for North Sea well inventory in supplement tables S1 & S2.

## 3.3. Gas leakage

### 3.3.1. Gas migration through the overburden

The transport of fluids through marine sediments is primarily governed by pressure and permeability contrasts (Berndt, 2005). In general, Darcy's law, a specific solution of the Navier-Stokes-equation, describes fluid flow through sedimentary basins (Whitaker, 1986). More specific, Darcy's law describes the more effective transport of fluid phases through permeable beds from deeper strata towards the surface dependent on the permeability of rocks and the hydraulic head (Whitaker, 1986). In other words, Darcy's law describes the volume of fluid flowing through a solid matrix dependent on its ability to conduct fluids (permeability) and the driving pressure gradient. Permeability is a rock property that describes how easily fluids may move through them. Three-dimensional (3D) seismic data show that subsurface permeability barriers often correlate with a wide range of anomalies, which can be related to focused fluid migration. Focused fluid flow is primarily directed upwards and occurs, when pore pressure exceeds the combined least principal stress and tensile strength of the sediment and induces hydrofracturing (Hubbert & Willis, 1957). Alternatively, fluids may start to move if the pore pressure overcomes the capillary entry pressure and capillary failure occurs (Clayton & Hay, 1994). Both types of seal bypass commonly occur in areas, where the pressure is increased by e.g. compaction, rapid loading, hydrothermal activity, or diagenetic processes.

In seismic data, direct hydrocarbon indicators (DHI) highlight areas in the subsurface, where a hydrocarbon phase exists. Hydrocarbon accumulations are often manifesting as seismic amplitude anomalies. These amplitude anomalies include seismic attenuation, velocity pushdown, bright spots, seismic chimneys or pipes and flat spots (White, 1975; Anstey, 1977; Karstens & Berndt, 2015; Marfurt & Alves, 2015). Seismic attenuation describes the energy absorption of a seismic wave due to the presence of free gas and the subsequent amplitude dimming of underlying reflectors. Velocity pushdown is an apparent depression of seismic reflectors (in the time domain) due to the decrease of seismic velocities in the accumulated gas phase above the reflectors. Bright spots are high amplitude seismic reflections with reversed polarity (with respect to the seafloor) that indicate a change in pore space filling (White, 1975). Seismic chimneys or pipes are the seismic expression of vertical fluid conduits attributed to localized release of overpressure in the subsurface and manifest themselves in seismic data as circular, often chaotic amplitude anomalies with dimmed reflections and bright spots at different stratigraphic levels (Cartwright et al., 2007; Løseth et al., 2009; Andresen, 2012; Karstens & Berndt, 2015). Flat spots indicate a fluid contact (oil/gas, gas/water, oil/water) and manifest themselves in seismic data as horizontal (high-amplitude) reflections that cut dipping strata.

In the North Sea, vertical gas migration is typically attributed to (I) structure-controlled flow, i.e. along faults or fracture zones (Gurevich et al., 1993; Berndt et al., 2003; Cartwright et al., 2007), (II) vertical fluid conduits (Karstens & Berndt, 2015; Böttner et al., 2019) or (III) well paths, including the well path itself and the fractured surrounding (Gurevich et al., 1993;

Nordbotten et al., 2004; Vielstädte et al., 2015; 2017). Once migration pathways have formed, they may remain conductive for further gas migration from deeper strata towards the surface for millions of years (Dumke et al., 2014).

### 3.3.2. Regulations and guidelines for well abandonment in the North Sea

Procedures for well decommissioning, including plugging and abandonment (P&A), largely depend on the geographic location of the wells (e.g. national/international jurisdiction, onshore/offshore environment) and the operator. The procedures for well plugging and abandonment are similar for both onshore and offshore wells. The operator is normally required to remove the completion hardware and install cement plugs at specific depths across permeable layers, such as water-bearing zones or reservoirs (Abshire et al., 2012). Such cement plugs protect the permeable layer against out- and inflow, but also shields a formation from pressure differences from above and below. While the precise regulations depend on the operator and national/international jurisdiction, these plugs are generally tested in a pressure test to ensure their functionality. Today, regulators require operators to remove all well casing and to cement the sections continuously along the entire borehole, which is referred to as rock-to-rock method (Abshire et al., 2012). Although the principles are the same for onshore and offshore wells, it is far costlier to abandon wells offshore as they are less accessible and have larger diameters. Decommissioning (incl. all offshore installations) in the U.K. was expected to cost several hundred billion British pounds (GBP), and although recent developments in plugging material and well barrier establishment (e.g. PWC- Perforate, Wash and Cement) have reduced the expected costs significantly, the overall estimated cost for decommissioning all wells in the U.K. offshore areas is still likely to cost about 60 billion GBP (Abshire et al., 2012; UKCS Decommissioning Cost Report, 2017). The largest proportion (45%) of decommissioning costs in the U.K. offshore areas will be run up in the Central North Sea with the largest single item being well abandonment, which amounts to 48% of the total costs and adds up to 28.8 billion GBP (UKCS Decommissioning Cost Report, 2017).

Plugging practices across the North Sea depend on the national regulations. Regulations differ little between the countries and concern mainly the plug testing method (weight or pressure tests) and the required length of permanent barriers at the level of the deepest casing shoe (NOR: NORSOK D-010, 2013; DK: Guide to Hydrocarbon Licences in Denmark, 2009; UK: Well Decommissioning Guidelines, 2018; GER: BVOT, 1981; LEBG, 1998; BVEG, 2017; NL: Mining Regulations of the Netherlands, 2014). For example, the U.K. regulations require operators to install a permanent cement barrier with a minimum column of ~30 m (i.e. 100 feet) measured depth (MD) in the case of two barriers (internal/annular) and of a cumulative ~60 m (i.e. 200 feet) MD in the case of a combination barrier of good cement to constitute a permanent barrier. The integrity of barriers must be tested with weight tests in open holes and via pressure or inflow tests in cased holes. The number of barriers required should be determined by risk assessment and all permanent barriers should consider the (bore-)hole conditions, inclination, fluid density hierarchy, stinger geometry, verification method and offset experience, but typically one to three barriers are required (Well Decommissioning Guidelines, 2018). The U.K. defines three phases of well decommissioning. In phase 1 (AB1) the reservoir is permanently isolated with permanent barrier material. At this stage the tubing may be left in place or is partly or fully retrieved. During Phase 2 (AB2) all intermediate zones with flow potential are permanently isolated with cement or permanent barriers and tubing as well as casing have to be retrieved or milled. The phase is completed when no further permanent barriers are required. In phase 3 (AB3) the wellhead and conductor are removed and if deemed necessary environmental plugs are put in place. Subsequently, the well is considered fully decommissioned never to be used or re-entered again.

Norway, Denmark, Germany and The Netherlands require at least 100 m-long cement plugs with 50 m above and below potential reservoirs, sources of inflow, or leakage (NOR: NORSOK D-010, 2013; DK: Guide to Hydrocarbon Licenses in Denmark, 2009; GER: BVOT, 1981; LEBG, 1998; NL: Mining Regulations of the Netherlands, 2014). In Germany, the regulations require testing the well barrier integrity via pressure-, weight- or flow tests within three months of plugging and abandonment. In Norway, NORSOK-D010 regulations require pressure tests of the barriers. The regulations in The Netherlands and Denmark do not specify testing methods, but Denmark requires daily reports on performed plugging operations including testing results (DK: Guide to Hydrocarbon Licenses in Denmark, 2009; NL: Mining Regulations of the Netherlands, 2014).

None of the above stated regulations in any country require monitoring of the well after plugging and permanent abandonment. While Norwegian regulations recommend excluding zones for drilling activities around shallow gas accumulation, the UK shallow gas accumulations are considered to occur everywhere and do not necessarily indicate permanent barrier failure (Well Decommissioning Guidelines, 2018). In Norway the costs for well abandonment are significantly higher to meet the self-imposed standards of the operators and official regulations. Furthermore, Norway is the only country that requires monitoring of temporarily suspended wells in form of fluid level and pressure measurements above the shallowest plug when access to the well exists (NORSOK D-010, 2013).

## 3.4. Methods

### 3.4.1. 3D seismic imaging

We used an extensive industry 3-D seismic dataset (“PGS MegaSurveyPlus”) that is a merger of a large number of individual 3-D seismic surveys and covers more than 22,000 km$^2$ of the central and northern North Sea from the seafloor down to 1.5 s two-way travel time (TWT, Figure 3.1). The 3-D dataset was pre-stack time-migrated and the seismic amplitude data (full offset) extend approximately 200 km from north to south and 140 km from east to west. The vertical resolution is approximately 20 m with a spatial resolution of approximately 12.5 m. The data quality varies between the individual datasets depending on acquisition and processing. However, such conventional 3-D reflection seismic datasets have been shown to be useful to identify fluid flow systems, including their geometry, permeability barriers and fluid accumulations, as these manifest themselves in seismic data as amplitude anomalies (Cartwright et al., 2007).

The investigated 3D seismic data cover 1794 of a total of 8969 non-sidetracked wells in the UK sector of the North Sea (i.e. 300 appraisal, 980 development, and 514 exploration wells). We excluded 3071 sidetracked and multilateral wells from our analysis because of limited information about their exact well paths and because no sidetracks exist in the upper 1000 m below the seafloor. Gas release from abandoned wells likely depends on the occurrence of shallow gas in the sedimentary succession. Shallow gas is a generic term to describe gas accumulations in the upper 1000 m below the sea floor and can be identified using direct hydrocarbon indicators, e.g. amplitude anomalies such as bright spots with polarity reversals. We mapped these amplitude anomalies for interpreted seismic horizons with root-mean-square (RMS) amplitude maps.

### 3.4.2. Water column imaging

During the cruise POS518 in October 2017, we acquired bathymetric and water column imaging data with the ELAC SEABEAM3050 MKII system, which is designed for very high-resolution imaging of the water column and is mounted to the hull of R/V Poseidon. The system has a 1.5° x 2° transducer, works at a frequency of 50 kHz, and has 191 equi-angle or 386 equi-distant beams. In addition, we used the Imagenex 837B Delta T multibeam for shallow water (260 kHz) to widen the range of frequencies and acquire very high-resolution images of the upper 100 m of the water column. It has a transducer beam width of 120°x 3° and uses 120 beams.

For water column imaging, we used the ELAC WCI Viewer (version 3.21) to process and display data. Water column imaging uses the scattered energy of acoustic signals in the water column and calculates the backscatter intensity (Schneider von Deimling et al., 2007). The system is highly sensitive to any changes in the temperature and density of the water column. We used this system to identify ascending gas bubbles (flares), which originate at the seafloor and align vertically in the water column indicating leakage (Schneider von Deimling et al., 2007). The surveys were planned as intersecting sail lines above known locations of decommissioned hydrocarbon wells to provide high-resolution images of the water column and identify potential gas flares. The water column sound velocity profiles for multibeam processing were measured at the start of every sub-survey using a CTD (conductivity, temperature, depth/pressure) sensor.

Additional water column imaging data were acquired with a newly designed KM SIMRAD ADCP/Echosounder combination (Schmidt et al., 2019), mounted in the moon-pool of R/V Poseidon during cruise POS534 in May 2019. The build-in single-beam echosounder (ES70-18) operates at 70 kHz with a beam angle of 18°. SIMRAD EK80 software controls both, the echosounder and the 170 kHz ADCP and images the water column in high-resolution. The system enables the detection of gas bubbles released at the seafloor, which are visible as a high backscatter anomaly also known as “flares”. The lateral drift of the gas bubble plumes can be correlated with simultaneously measured acoustic Doppler current profiles of the water column.

## 3.5. Results

### 3.5.1. Distribution of shallow gas at different stratigraphic levels in the study area with respect to well location

A ~70 km-long seismic profile across the Central Graben of the Central North Sea shows the sedimentary succession down to 1.2 s two-way travel time (TWT) (Figure 3.2). Numerous high amplitude anomalies with polarity reversals (bright spots) are present at ~5-15 km distance along the profile and at ~0.7-0.8 s TWT. They indicate the presence of shallow free gas at about 700 m below the sea level (0.8 s TWT correspond to 640 m at 1600 m/s seismic velocity). The corresponding seismic horizon can be traced throughout the entire seismic data set and forms a NE-SW oriented trough (Figure 3.2). Seismo-stratigraphic correlation of the seismic horizon with literature and well information ties this reflector to the Early Pleistocene (EP, Figure 3.2) (Ottesen et al., 2014; Rose et al., 2016). This seismic horizon is characterized by a regional unconformity, which manifests as a zone of chaotic, incoherent reflectors with a corrugated surface and is dissected by a large number of linear erosional features. The second prominent horizon is located between 0-50 km distance along profile and at ~ 0.5 s TWT. The seismic horizon shows prominent bright spots with polarity reversals at ~0.55 s TWT and at 2.5 km, between 15-40 km and 45 km distance along profile (Figure 3.2). Seismo-stratigraphic correlation ties this reflector to the Mid Pleistocene (MP) (Ottesen et al., 2014; Rose et al., 2016; Reinardy et al., 2017). The seismic facies of the MP horizon is characterized by zones of chaotic, incoherent reflectors with a corrugated surface and is dissected by a large number of tunnel valleys, indicating a regional unconformity (Figure 3.2). From the MP horizon upwards to the seafloor (~0.1-0.5 s TWT) numerous bright spots in the sedimentary succession indicate the upward migration of free gas (e.g. at 40 km distance along profile and ~0.3 s TWT). The shallow sedimentary succession is dissected by a large number of tunnel valleys. The seafloor horizon (SF) is a good measure of the data quality. The displayed seismic profile consists of four different 3D seismic data sets (0-13 km, 13-25 km, 25-49 km and 49-72.5 km) with different data qualities shown in this seismic section.

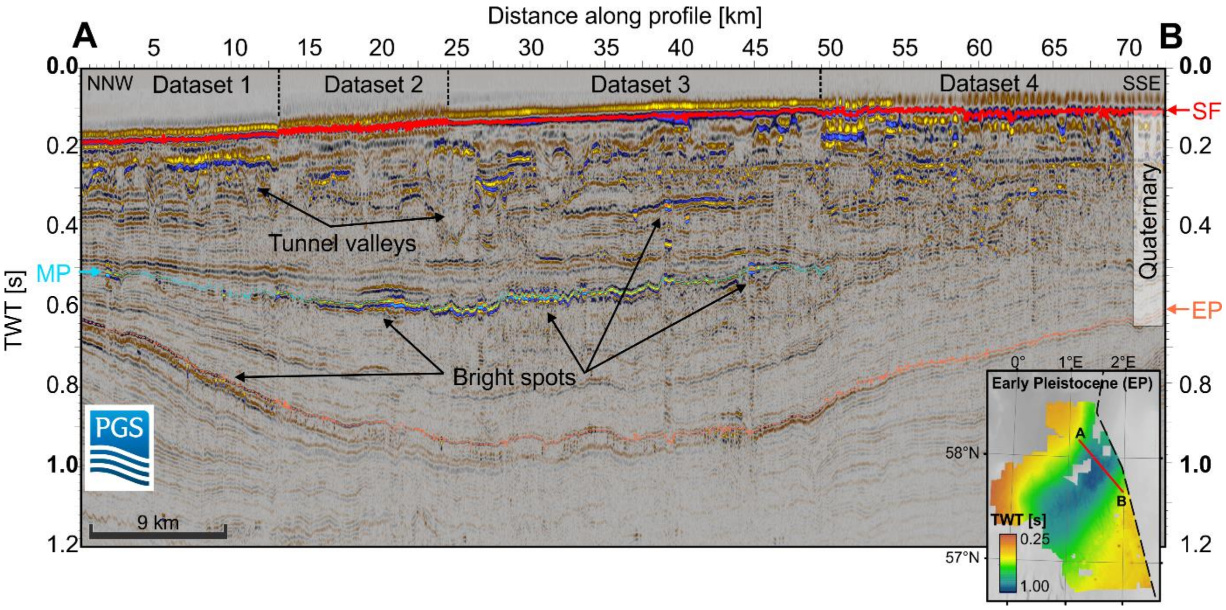

**Figure 3.2.** ~70-km long seismic profile across the Central Graben in the Central North Sea showing the sedimentary succession down to 1.2 s two-way travel time (TWT). Beneath the seafloor (SF, the Mid-Pleistocene Basin Sands (MP, turquoise line) and the Early Pleistocene Crenulate Marker (EP) are visible as high amplitude anomalies within the Quaternary sedimentary succession (white box indicates the extent of the Quaternary succession). The profile shows distance along the profile in kilometers [km] on the x-axis and the vertical penetration of the seismic energy in seconds [s] of two-way travel time (TWT) on the y-axis. The location of the profile is shown in the inset. **(INSET)** Map of the seismic Early Pleistocene Crenulate Marker horizon outlining the 3D seismic data set. The red line indicates the location of the seismic profile. The depth of the horizon is given in seconds [s] two-way travel time (TWT). The map is projected in UTM31/WGS84.

Figure 3.3 shows the derived seismic horizons (time structure maps) and RMS amplitude calculations (RMS amplitude maps) and the location of the 3D seismic data set in the North Sea (see Figure 3.3a). Imaging of the seafloor morphology is highly dependent on the quality of the seismic data and the applied processing (Figure 3.3b). Nevertheless, the seafloor time structure map shows the smooth morphology of the North Sea and water depth ranging between 0.1 and 0.2 s TWT. The EP horizon was traced semi-automated across the 3D seismic data set and follows the depression formed by the Central Graben over most of the data and some elevated areas, where the strata is bent upwards (Figure 3.3c). Figure 3.3d shows RMS amplitudes calculated for the interval between the seafloor plus 50 ms to avoid processing-induced artifacts of the seafloor (SF) reflection and the Early Pleistocene horizon (EP) plus 50 ms. In this way we were able to map all amplitude anomalies within the Quaternary succession, which indicate either a change in lithology or pore space filling, i.e. accumulations of free gas in the upper 1000 m (shallow gas) (Figure 3.2, Figure 3.3). There are two prominent provinces, where bright spots occur (Figure 3.3d). The first is the central Graben, which dominates the central to northern parts of the seismic data. Here, bright spots are predominantly associated to the two prominent seismic horizons tied to EP and MP (Figure 3.2, Figure 3.3). The second is the southern part of the survey area, where bright spots are primarily associated with upward-bent sedimentary strata indicating the doming of salt layers from beneath. Above these salt domes, steep-dipping faults dissect the sedimentary succession. Numerous bright spots accompany these geological features at different depth/stratigraphic levels (Figure 3.3c-d).

We investigated if gas can be released from the seafloor along any type of well (appraisal, development, exploration) and independently of its status (decommissioned, active). We assumed that shallow gas would have to be present in the vicinity (up to 1 km) of the well, and an increased permeability induced by the drilling operation and a driving force for gas movement (buoyancy or excess pore pressure). Consequently, we correlated the well paths of 1794 wells located within the 3D seismic data set with bright spots with polarity reversals indicating shallow gas pockets in the subsurface (Figure 3.3b, d). More than 700 of the 1794 wells are located in close proximity to bright spots and/or show elevated RMS amplitude values and thus are potentially sites for gas release from the seafloor.

The quality differences of the individual 3D seismic data sets included in the PGS “MegaSurveyPlus” compilation are clearly visible. Some areas show very high amplitude response in comparison to others and complicate the analysis (see highlighted area in Figure 3.3d).

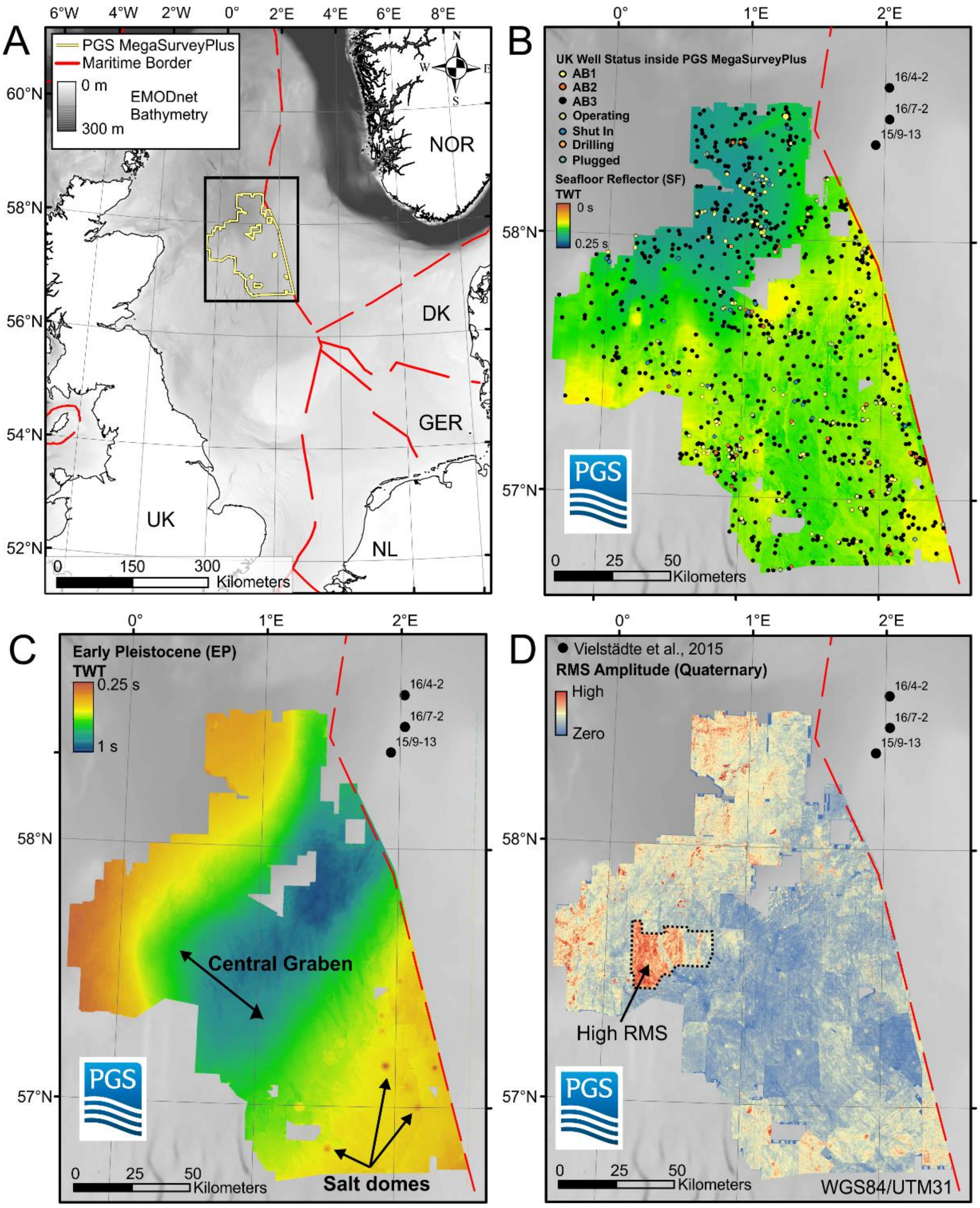

**Figure 3.3**. **(A)** EMODnet bathymetric map of the North Sea indicating the extent of the 3D seismic data set (yellow line) and the maritime border (dashed red line) separating the UK, Norwegian, Danish, German and Dutch Exclusive Economic Zones (EEZs). The black box indicates the extent of maps B, C, and D. **(B)** Seismic seafloor horizon showing the location and current status of wells within the 3D seismic data set. AB1-3 = Abandonment phases 1, 2, and 3. **(C**) Map of the seismic Early Pleistocene (EP) horizon in the 3D seismic data set showing the Central Graben and salt domes in the southern part. Depth is given in seconds [s] TWT. **(C)** RMS-amplitude map of the Quaternary succession showing the spatial distribution of bright spots identified in the 3D seismic data set. Red colors indicate areas with high-amplitude anomalies whereas blue colors indicate low amplitudes. The RMS-amplitude is calculated over the time-window from 50 ms beneath the seafloor to 50 ms beneath the EP horizon as indicated in **Figure 3.2**a for the Quaternary succession. Black dots indicate the wells analyzed by Vielstädte et al. (2015). The dashed line indicates an area where the seismic subset shows high RMS-amplitude values due to different acquisition and processing procedures resulting in different data quality. In maps B, C, and D the red dashed line indicates the maritime border separating the UK and the Norwegian EEZs.

### 3.5.2. Mapping of gas flares

We collected water column imaging data along intersecting profiles above selected well with high seismic RMS amplitude values in close proximity (Figure 3.3d). This survey design was chosen to avoid misinterpretation of shoals of fish as flares. Based on the seismic RMS amplitude map we picked arbitrarily 20 wells for detailed surveying of the water column during POS518 using the ELAC SB3050 MKII system (Figure 3.4, Figure 3.5) and 23 wells during POS534 using a SIMRAD EK80 system (Figure 3.5). Figure 3.4 shows three examples of flares identified during cruise POS518, which are associated with gas release from the seafloor. Figure 3.4a displays the fan views of the backscatter intensity in the water column above wells 16/26-3, 16/27a-6 and 16/27b-5. All three fan views show bright anomalies above the wells indicating gas release at the respective seafloor locations (Figure 3.4a). Figure 3.4b displays fan views that are stacked along the part of the survey profile close to the well to image the entire flare. This shows that the flares emerge from the seafloor above the well locations and ascend into the water column but that the gas bubbles do not reach the sea surface (Figure 3.4).

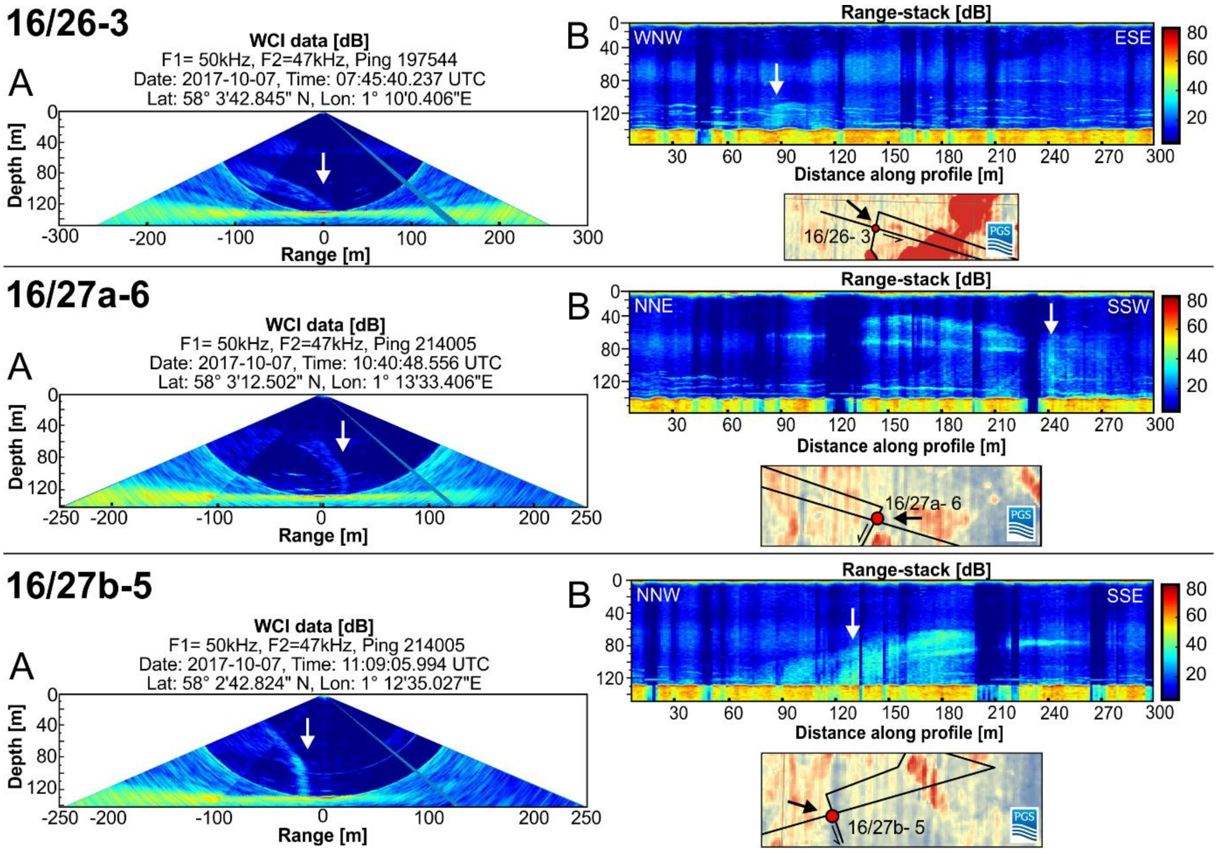

**Figure 3.4.** Water column images acquired with the ELAC SB3050 MKII during POS518 at three decommissioned hydrocarbon well locations (well IDs 16/26-3, 16/27a-6, and 16/27b-5). (**A**) Fan view at the well locations and (**B**) the range-stack view along the sailed survey lines as seen in the RMS-amplitude maps below (for details see Figure 3.5). White arrows indicate the location of the respective wells. Flares at the well locations indicate the leakage of gas from the well head location. The stacked view shows the behavior of the ascending gas bubbles in the water column, which are diverted laterally.

Figure 3.5 shows the survey lines and the investigated wells draped on top of the 3D seismic data RMS-amplitude map. Red dots indicate wells, where we observed gas flares in the water column while white dots indicate those where no anomalies were found in the water column. In total, we observed gas flares at 28 of the investigated 43 well locations during the two cruises (POS518: 15 of 20 wells, POS534: 13 of 23 wells, see table S3). 3D seismic data is available for 41 of the investigated 43 wells (Figure 3.5). Distances to bright spots with polarity reversals, indicating free gas in the subsurface, vary between 0 and 3300 m. All investigated wells with a distance to the next bright spot of less than 300 m show flares in the water column above the well location, indicating gas release from the well (Figure 3.6).

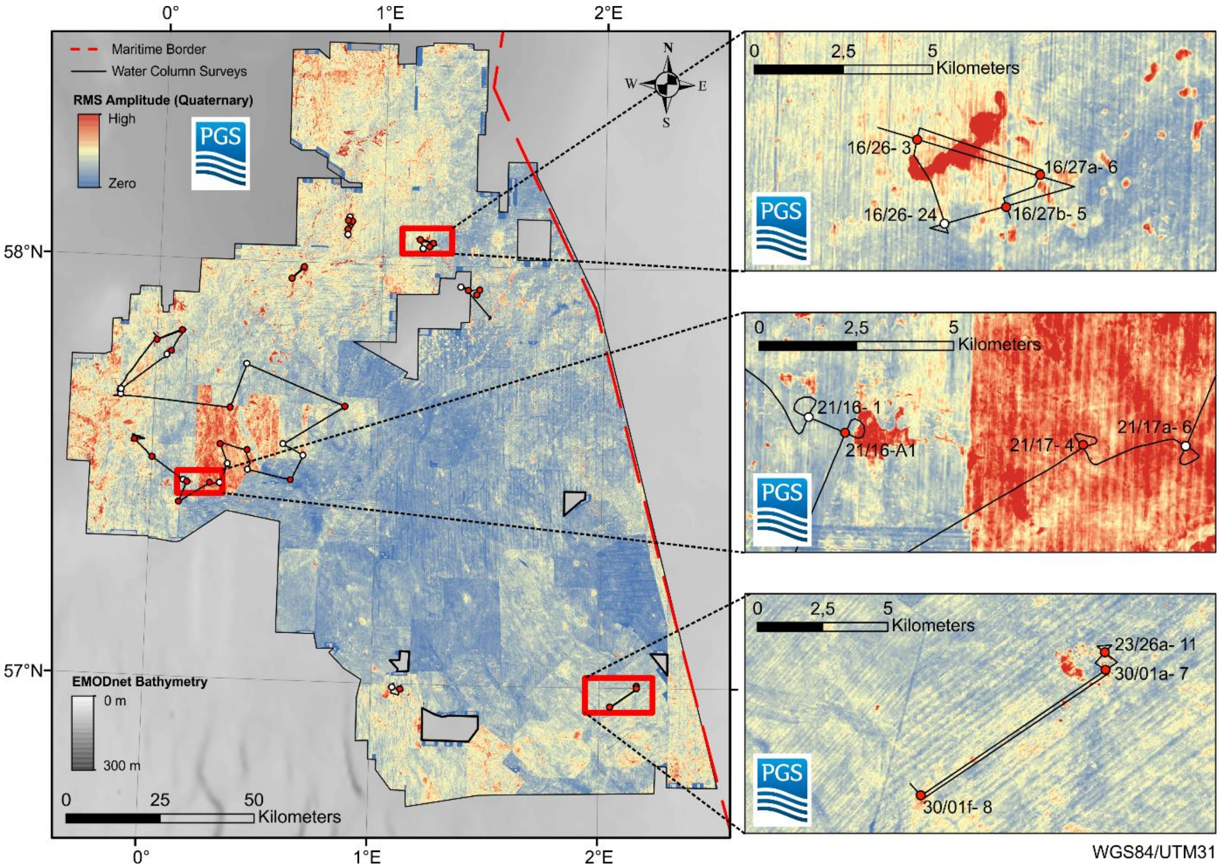

**Figure 3.5.** RMS-amplitude map showing the water column imaging surveys (black lines) during POS518 and well leakage identification through flare detection (flares = red dots, no flares = white dots). The red dashed line indicates the maritime border (red dashed line) between the UK and Norway in the Central North Sea. The black dots indicate the locations of wells in the Norwegian sector analyzed by Vielstädte et al. (2015). Further information on well investigation see supplementary material S3.

For all 43 investigated wells activity data including geographic location, spud date (age), deviation type, well intent, abandonment status, drilling depth, water depth is available. The 43 wells comprise 33 exploration wells, 9 appraisal wells, and 1 development well. All 43 wells are in abandonment phase 3 (AB3), i.e. wells that are plugged and abandoned permanently. Figure 3.6 shows the distribution of spud dates (start of drilling) versus the leakage-occurrence-rates for the 43 investigated wells. Older wells from the 1970’s show high leakage-occurrence-rates with a decreasing trend towards wells drilled during the most recent decade (2010-2019) where no leakage is observed (Figure 3.6).

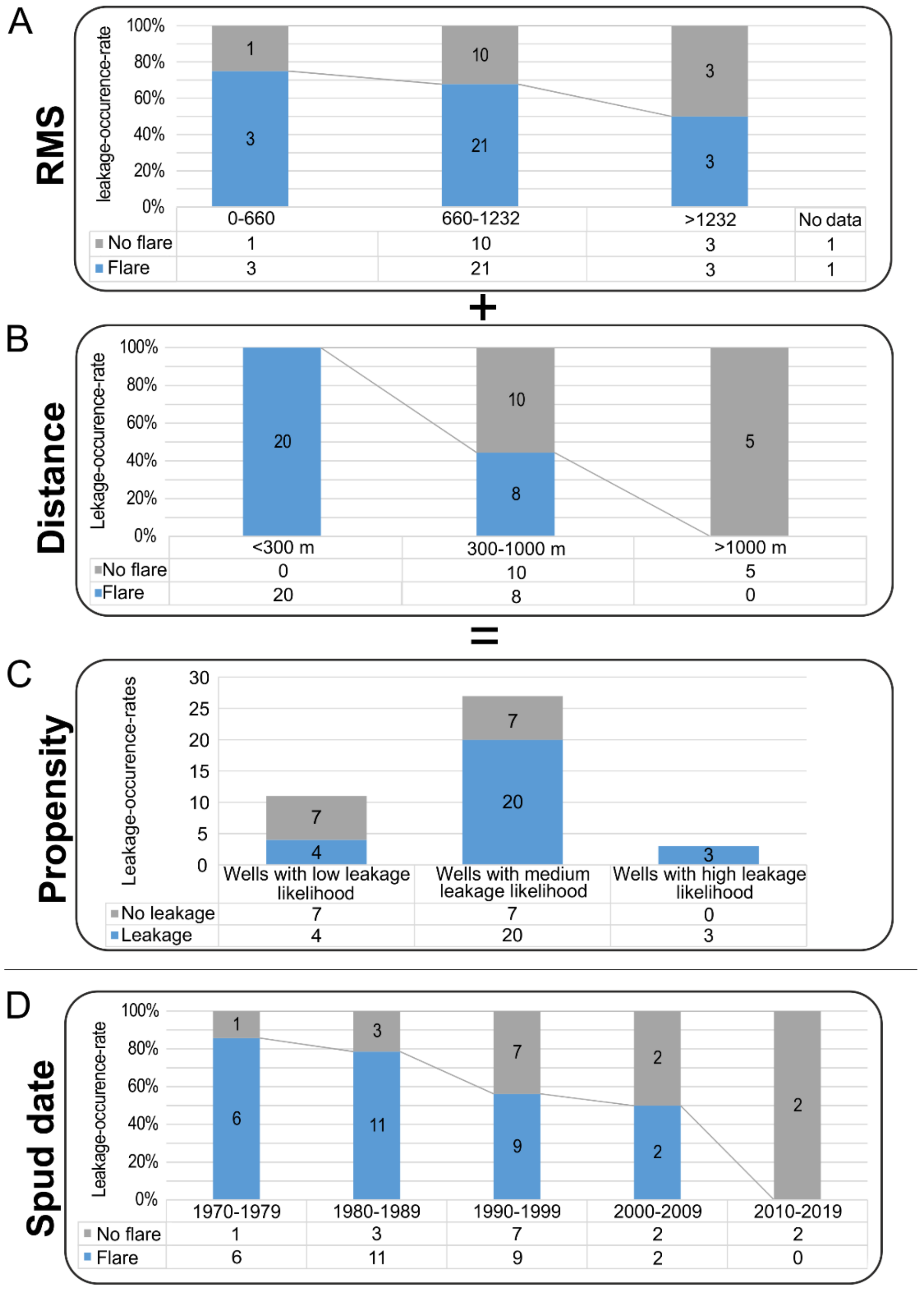

Figure 3.6: 43 investigated wells showing results based on the flare detection during POS518 and POS534 (see also supplementary material S3). Bar charts from top to bottom showing leakage-occurrence-rates for: (**A**) RMS-amplitude ranges for low (<660), medium (660-1232) and high (>1232) leakage probabilities versus gas release indicated by flare anomalies in the water column. (**B**) Distance to next bright spot with polarity reversal indicating free gas in the subsurface versus gas release indicated by flare anomalies in the water column. (**C**) Combination of RMS-amplitude analysis and distance to most proximate bright spot with polarity reversal to define groups of low, medium and high leakage probabilities testes against direct measurements from the water column acquired during POS518 and POS534. (**D**) Spud (drilling start) dates per decade versus gas release indicated by flare anomalies in the water column.

### 3.5.3. Leakage propensity and sensitivity analyses for free gas identification

Figure 3.7a shows a 5-km long seismic section across a typical bright spot in the subsurface located at 0.5 s TWT and lateral extent of ~ 3000 m. This bright spot is associated with the Mid-Pleistocene strata and is in close proximity to wells 16/26-3 and 16/26-24 (see Fig. 6c). The RMS-Amplitude map indicates one single large bright spot and several smaller bright spots in the surrounding (red color) that suggest possible accumulations of free gas in the Quaternary sediments (see Figure 3.7c). However, a high amplitude response of the subsurface in form of bright spots alone is not a direct hydrocarbon indicator (DHI). It can also be caused by a change in acoustic impedance due to a change in lithology. In the low frequency 3D seismic data used in this study bright spots associated with shallow gas in the subsurface should also exhibit reversed polarity in comparison to the seafloor, i.e. a phase shift of 180° (Figure 3.7b). Figure 3.7b shows the apparent polarity attribute for the same area as the RMS-Amplitude map (Figure 3.7c), indicating the phase of the reflections seen on the vertical seismic display. Bright pink colors indicate areas with polarity reversals and thereby validate that the formerly identified bright spots are indeed caused by accumulations of free gas in the subsurface. We measured the distance between the wells and the closest bright spot with polarity reversal for all investigated wells. Furthermore, we calculated the mean RMS-amplitudes for a buffer radius of 300 m around the well paths as this is the minimum distance, where the leakage-occurrence-rate is not 100%, Figure 3.6).

Based on these parameters, we define three groups of leakage probability for the seismic data set: To wells at short distance to bright spots with polarity reversals (< 300 m) and high RMS-amplitudes (> 1232 for our data set) we assigned a high leakage probability, to wells with medium RMS-amplitudes (660-1232) and medium distances (300-1000 m) we assigned a medium leakage probability and to wells with low RMS-amplitude (< 660) and long distance (>1000 m) we assigned a low leakage probability (Figure 3.6). Wells with less than 300 m distance from the next gas accumulation show gas release (leakage-occurrence-rate 100% = 20 of 20 wells, Figure 3.6), whereas those with a distance of more than 1000 m show no gas release (leakage-occurrence-rate 0% = 0 of 5 wells, Figure 3.6). The maximum distance between a well showing gas release at the seafloor and a bright spot with polarity reversal is 1000 m (Figure 3.6). Thus, the potential of a well to leak can be identified by a combination of (1) bright spots in RMS-Amplitude maps, (2) an associated apparent polarity reversal, and (3) the wells proximity to such seismic attributes.

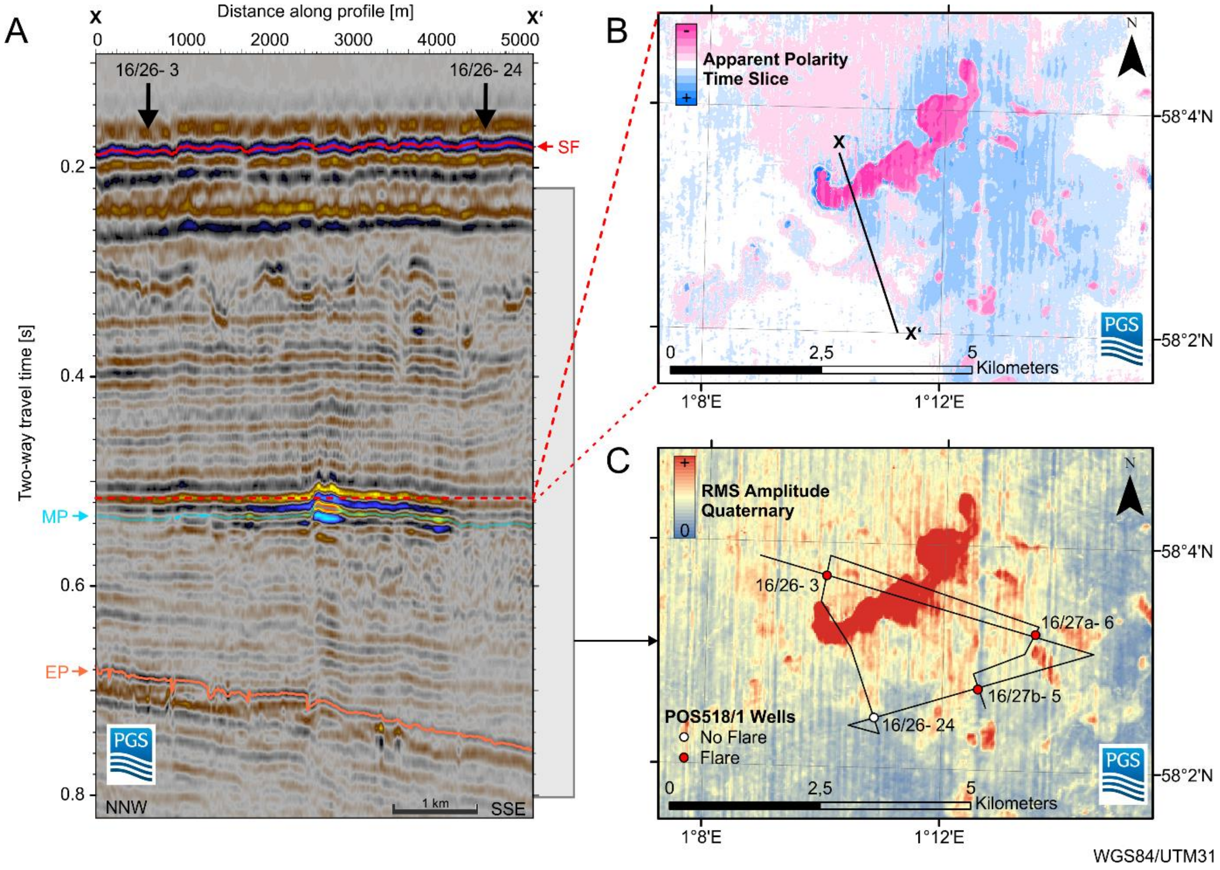

**Figure 3.7.** Sensitivity analysis of the 3D seismic data for bright spots indicating free gas accumulations in the subsurface. Bright spots with polarity reversals indicate gas accumulations whereas other bright spots are predominantly associated to changes in lithology. Exemplarily we show (**A**) a seismic profile of the 3D seismic data across wells 16/26-3 and 16/26-24 showing the seafloor (SF), Mid-Pleistocene Basin Sands (MP) and the Early Pleistocene Crenulate Marker (EP). (**B**) 3D seismic attribute analysis using apparent polarity to identify areas with polarity reversal (pink areas). The black line indicates the location of the seismic profile shown in (A). (**C**) RMS-Amplitude map of the Quaternary succession showing in red colors bright spots in the subsurface. The black line indicates the sailed survey lines for water column imaging. The RMS-amplitude map shows hydrocarbon wells investigated during POS518 showing gas leakage (red dots) and no gas leakage (white dot).

## 3.6. Discussion

### 3.6.1. Correlation of subsurface gas accumulations and gas flares in the water column

Potential leakage from the investigated decommissioned hydrocarbon wells primarily depends on the occurrence of gas accumulations in the upper 1000 m of the sedimentary succession penetrated by the wells, but also on the local geology, hydraulic connectivity, and rock type (Vielstädte et al., 2015). The analysis of seismic and water column imaging data presented in this study further refines our previous findings by correlating the gas release from abandoned wells with the distance from gas accumulations in the shallow subsurface: Wells that are in close proximity, i.e. less than 300 m away from the well, to bright spots with polarity reversals are likely to leak, whereas wells drilled more than 1000 m away from such shallow gas accumulations do not tend to leak (Figure 3.6). For a proper assessment of a well's propensity to leak, however, it is important to further analyze the distribution of gas in the upper 1000 m of the seabed.

### 3.6.2. Sources and character of shallow gas in the Central North Sea

The accumulation and migration of free gas and subsequently leakage along the well path is favored in the shallow Quaternary sediments in less than 1000 m below the seafloor as, here, the necessary conditions, i.e. overpressure and local rock strength and tensile strength of unconsolidated sediments are matched (Clayton & Hay, 1994). Potential gas sources include both upward migrated thermogenic gas from mature source rocks and biogenic gas from geologically young, organic-rich sediments (Judd et al., 1997). Shallow gas in the Central North Sea is primarily associated with two prominent, laterally extensive horizons within the Early to Mid-Pleistocene sediments of the Quaternary succession (Figure 3.2). These horizons are known as (1) the Crenulate Marker horizon (Top Unit Z, Ottesen et al., 2014; Rose et al., 2016) and (2) Mid Pleistocene sands (URU-equivalent in Ottesen et al., 2014; R4 in Reinardy et al., 2017). The accumulation of shallow gas, however, is not limited to the Central North Sea. Similar shallow gas accumulations of biogenic origin are documented for many areas across the North Sea, e.g. for the Dutch sector (Schroot & Schüttenhelm, 2003; Kuhlmann & Wong, 2008), the German sector (Müller et al., 2018), and the Norwegian sector (Vielstädte et al., 2015; Crémière et al., 2016).

The Crenulate Marker is an Early Pleistocene horizon close to the base of the Quaternary and upper Pleistocene sediments, i.e. the base of the Aberdeen Ground Formation. These sediments have been deposited under subglacial, glaciomarine to marine conditions (Sejrup et al., 1987; Stoker & Bent, 1987; Buckley, 2012, 2016; Rose et al., 2016; Reinardy et al., 2017; Rea et al., 2018). The Crenulate Marker is found across the Central North Sea Basin and forms a NE-SW oriented trough (Central Graben) representing a permeable layer, with hydraulic barriers due to deformation by overriding of ice (Rose et al., 2016). At this seismic horizon, shallow gas manifests as bright spots with polarity reversals which that are caused by water-bearing reservoirs with free gas saturations of 0-10% (Rose et al., 2016). The Mid Pleistocene basin sands underlie a regional glacial unconformity, which manifests itself in the seismic data by a zone of chaotic, incoherent reflectors with a corrugated surface and is dissected by a large number of tunnel valleys. In the center of the Central Graben, numerous bright spots with polarity reversals accompany this unconformity, which are most likely caused by sand bodies deposited during the advance of grounded ice into the North Sea Basin dating to the Mid Pleistocene Transition (~1.2-0.5 Ma BP, Reinardy et al., 2017). These sand bodies show increased gas saturations of up to 65% in some areas, e.g. the Aviat Member directly above the Crenulate Member in the central North Sea Basin (Rose et al., 2016). There, the gas in composed mostly of methane (99.9% $CH_4$) that is isotopically light (average $\delta^{13}$-CH4 of -69‰ VPDB and average $\delta D$-$CH_4$ of -195‰ VSMOW) indicating a biogenic origin (metabolic $CO_2$ reduction pathway typical for marine environments) with no thermogenic admixture (Rose et al., 2016).

In the southern part of the survey area, shallow gas accumulations are primarily associated with salt domes (Figure 3.5). The salt domes push the overlying sedimentary strata upward and salt migration leads to salt withdrawal basins in between the salt domes. This creates structural traps (i.e. southern North Sea: Ward et al., 2016). Above the salt domes, normal faults form as a result of the gravitational collapse of the overburden sediments that often represent efficient fluid migration pathways (i.e. Tommeliten, Judd & Hovland, 2009). Within these structural traps, biogenic and thermogenic gas may accumulate and possibly mix. Higher order hydrocarbons may be microbially degraded and thus, complicate identifying their origin (Clayton et al., 1997; Nuzzo et al., 2009; Pape et al., 2010; Haffert et al., 2013).

### 3.6.3. Migration through the overburden along wells in the Central North Sea

Upward gas migration along well paths from shallow gas accumulations (within the upper 1000 m) may initiate through fractures in the surrounding of the well induced by the drilling procedure (Vielstädte et al., 2015). These amount of drilling-induced fractures varies depending on the surrounding lithology, tectonic stress magnitude and orientation, pressure and temperature (Harrison et al., 1954; Aadnøy & Bell, 1998; Brudy & Zoback, 1999). The induced fractures may extend outward from the borehole to about the same diameter of the drill bit but can reach up to three times the diameter of the drill bit into the surrounding rocks at high pressure and temperature (Brudy & Zoback, 1999). If present, these fractures are forming pathways through natural/lithological permeability barriers (Gurevich et al., 1993; Gasda et al., 2004; Vielstädte et al., 2015). For shallow sediments (less than 2-3 km), these fractures mechanically weaken the sediment and increase the permeability with regard to the surrounding. Thus, they provide fluid migration pathways except for situations in which the mechanical compaction of sediments closes the fractures after drilling (Bjørlykke & Høeg, 1997; Bjørlykke, 1999). For well paths connecting the seafloor with deep reservoirs, mechanical and chemical compaction that involves the dissolution and precipitation of minerals may lead to closure of drilling-induced fractures in deep layers (> 1000 m) within a short time span, while the upper sedimentary succession may remain hydraulically connected with the seafloor (Bjørlykke & Høeg, 1997).

Geological pre-conditions play a key role in the well's propensity to leak. Our results show that if the distance between the well and the most proximal bright spot with polarity reversal is shorter than 300 m, leakage is highly likely (100%, 20/20 wells) and for a distance of more than 1000 m not likely (0/5 wells). For distances in between 300 and 1000 m, our data show that only 44% (8 of 18) show gas release from the seafloor. Two geological boundary conditions may explain the increase in leakage probability with decreasing distance. First, lateral gas migration may be favored by dipping beds (up to 1.2-1.4 km; Landrø, 2011). Without dipping strata, lateral gas migration for more than 300 m towards the well is unlikely to occur. Second, pre-existing fracture networks may favor the vertical migration of fluids through the overburden (Karstens & Berndt, 2015; Vielstädte et al., 2015). Such fracture networks manifest in seismic data as amplitude anomalies known as seismic chimneys or pipes (Cartwright et al., 2007; Løseth et al., 2009; Andresen, 2012; Karstens & Berndt, 2015). Measurements at well 16/7-2, which was drilled through such a seismic chimney structure, show ten times higher release rates of up to 19 t of $CH_4$ per year (Vielstädte et al., 2017). Leakage of shallow gas accumulations along wells thus largely depends on the local lithology and lateral hydraulic connectivity of the subsurface strata. If no pre-existing natural fracture networks exist, the wells connect hydraulically shallow gas accumulations in the subsurface with the seafloor, thereby draining the gas, that otherwise would stay in place over geological times.

### 3.6.4. Seismic data limitation and other proxies for leakage from wells

Seismic data can be used to identify areas where gas release from the seafloor is more likely than in other areas. However, their suitability is limited by the quality of the data and homogeneity of the compiled data sets used (see Figure 3.2). In our case, areas with systematically elevated (biased) amplitudes limit the quantitative assessment of the well leakage propensity based on RMS amplitudes. For this reason, we could not include the seismic data set used in Vielstädte et al. (2015, 2017) as the differences in seismic data processing and data quality are too large.

Bright spots identified in RMS-Amplitude maps do not necessarily indicate free gas in the subsurface. As we show, it is necessary to identify polarity reversals in combination with the bright spots to ascertain the presence of gas and exclude any false positives. Also, gas mobility depends on its saturation in the pore space (Buckley & Leverett, 1942; Ham & Eilerts, 1967, Gregory; 1976). However, post-stack seismic data alone cannot distinguish between large connected gas bodies and dispersed free gas as all gas occurrences with concentrations above 4 vol. % show as bright spots with reversed polarity (White, 1975; Domenico; 1976; Anstey, 1977). Nevertheless, the correlation between mapped gas and seepage suggest that our approach is permissible. Either because some of the gas occurs at high saturation or because also gas at low saturation is mobile enough to reach the wells if the sediment properties are conducive. Subsequent seismic data evaluation can be used to help in estimating methane emission budgets for the central North Sea as it indicates where high probabilities of gas release from the seafloor are to be expected, i.e. where RMS amplitudes are high and bright spots with polarity reversals are in close proximity.

Other factors, such as the age of wells (Figure 3.6) may also be of importance (Kang et al., 2016). The age reflects the employed techniques for abandonment. Improved drilling and abandonment practices in the past two decades may also decrease the propensity of wells to leak (i.e. Abshire et al., 2012; King & Valencia, 2014). But, lateral gas migration towards the well and subsequently along the fractured surrounding of the well is also a matter of time. And, our data analysis shows that younger wells from the decade 2000-2009 still show a 50% leakage-occurrence-rate. Hence, the current 0% leakage-occurrence-rate after 2010 may eventually simply reflect the fact that the gas has not yet reached the seafloor.

### 3.6.5. Leakage propensity analyses based on seismic data for wells in the North Sea

Our analysis indicates that leakage from decommissioned hydrocarbon wells is elevated in areas where seismic amplitude anomalies in the sedimentary succession indicate the presence of shallow gas (Figure 3.2, Figure 3.4, and Figure 3.5). The sensitivity analysis reveals a strong correlation between bright spots with polarity reversals and elevated leakage rates from wells (Figure 3.7). Therefore, the analysis of shallow gas in the subsurface in seismic data (Figure 3.5) can be used to predict the probability of leakage from abandoned wells. The potential for leakage of shallow gas along wells is not only a local phenomenon but occurs across the entire North Sea.

An identification of shallow gas in correlation with drilled wells is needed on a global scale to update the estimates of methane emissions from fossil fuels. This is particularly important for onshore as drilling-induced leakage along wells in this setting emits the methane directly into the atmosphere, because the mitigating water column is absent.

### 3.6.6. Assessing the rate of methane release

Gas release from abandoned hydrocarbon wells in the Central North Sea is primarily associated with biogenic hydrocarbon gas (Vielstädte et al., 2017). Water column imaging identifies leakage at 28 out of the investigated 43 wells (Figure 3.4 and Figure 3.5). In combination with the RMS-amplitude maps, we were able to determine probabilities (low, medium, high) for leakage from single wells. This allows calculation of the approximate inadvertent greenhouse gas emission from abandoned hydrocarbon wells in the Central North Sea (Figure 3.8). We calculated the probability of leakage and tested our leakage propensity estimates against the direct measurements using water column imaging (Figure 3.4, Figure 3.5). Based on the findings from the investigated wells, we predicted that 11 wells have a low, 27 wells have a medium, and 3 wells have a high leakage probability.

The assigned leakage probability groups are:

- high leakage probability wells with a leakage-occurrence-rate of 100% (3 of 3)
- medium leakage probability wells with a leakage-occurrence-rate of 74,1% (20 of 27)
- low leakage probability wells with a leakage-occurrence-rate of 36,4% (4 of 11)
- wells not covered by seismic data having a leakage-occurrence-rate of 50% (1 of 2)

Our analysis reveals that there is a strong correlation between the predicted leakage propensities based on the combination of distance to the most proximal bright spots with polarity reversal and increased RMS-amplitudes and the observed gas flare in the water column. However, our estimations are derived from only 43 investigated wells and are thus likely prone associated with large uncertainties (Table 1). Additional information on well leakage is scarce and little is known about inadvertent greenhouse gas release from decommissioned offshore hydrocarbon wells and in particular in the North Sea. Independent and open access data on inadvertent greenhouse gas emissions from decommissioned hydrocarbon wells would help to constrain the leakage rates from fossil fuel infrastructure and thus help to derive quantitative conclusions on future well abandonment practices.

The 20,000 km² of the PGS "Mega Survey Plus" data set comprise 1,794 wells. From our small test group, we derived the necessary seismic RMS amplitudes and found that within our seismic data set 1,024 wells show low leakage probability, 754 wells show medium leakage probability and 14 wells show high leakage probability (Figure 3.8). We utilize the gas release rate quantified by Vielstädte et al. (2015) at leaky wells 16/4-2 and 15/9-13 in the Norwegian sector of the Central North Sea (location shown in Figure 3.3b), which ranges between 1 and 4 t of $CH_4$ per year. We exclude the high leakage rate of 19 t of $CH_4$ per year determined at well 16/7-2 in the regional emission budget, because this well was drilled in a seismic chimney structure that likely provides a non-representative and highly permeable leakage pathway.

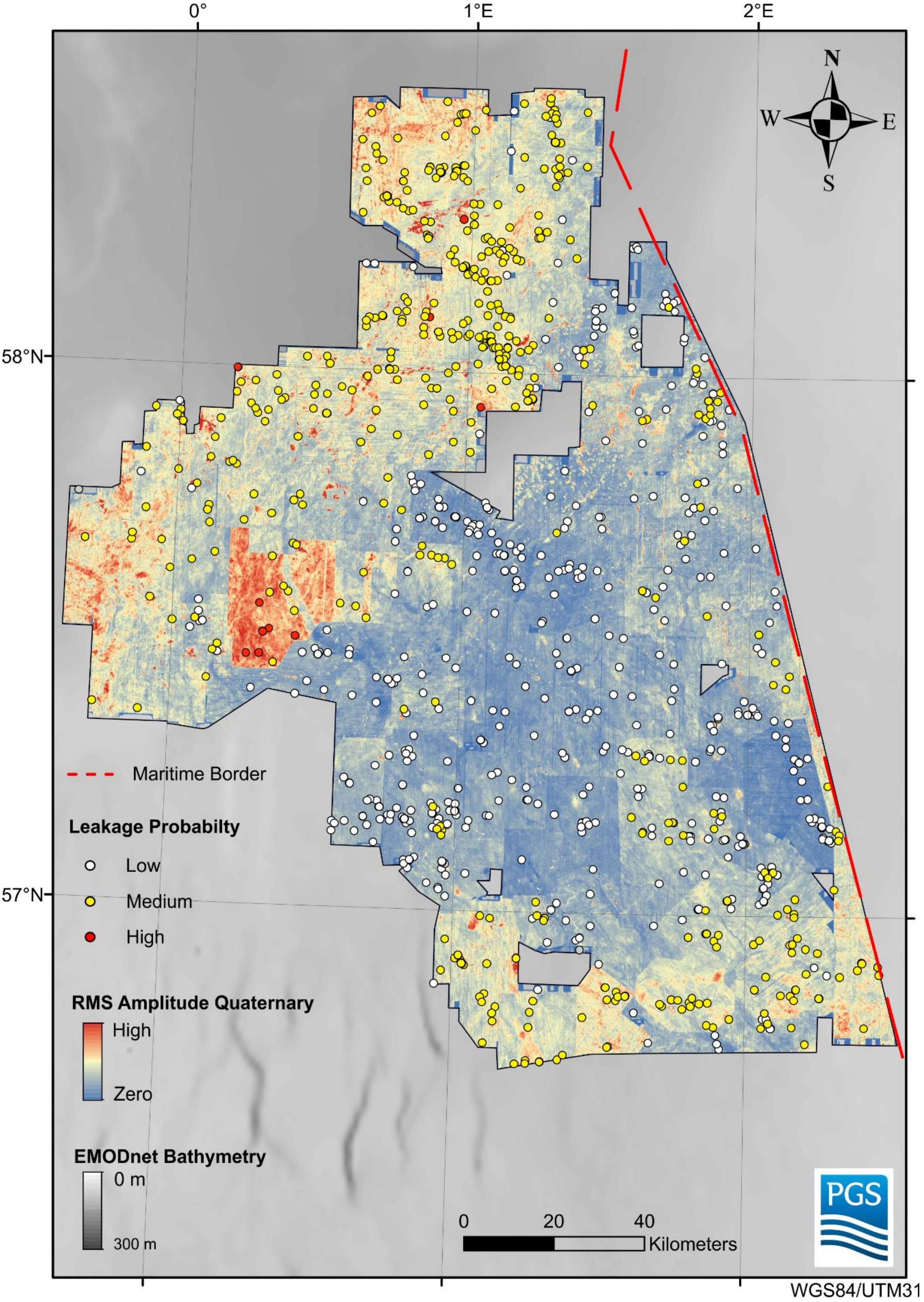

**Figure 3.8.** Overview EMODnet bathymetric map of the North Sea indicating the location and extent of the seismic data set within the North Sea. The RMS-amplitude map of the 3D seismic data is draped on top of the bathymetry map and shows leakage probabilities of the 1794 wells as color-scaled dots (low leakage probability shown in white, medium leakage probability shown in yellow and high leakage probability shown in red).

Combining these constraints in our analysis, we can approximate the amount of methane that leaks from wells to 0.9-3.8 kt yr$^{-1}$ of $CH_4$ for 1,794 wells spread over 20,000 km² of the UK sector in the Central North Sea. However, more direct measurements of gas release from boreholes through remote operated vehicles are necessary to further improve the results. Despite the uncertainty of this estimate, it is in good agreement with our previously estimated regional leakage rate of 3-17 kt yr$^{-1}$ of $CH_4$ for the total of 11,122 wells in the entire North Sea (Vielstädte et al., 2017). Numerical modelling shows that ~58% of this $CH_4$ will dissolve in the deep water below the surface mixed layer (< 50 m; Thomas et al., 2005) of the North Sea while ~42% will reach the atmosphere via venting of dissolved $CH_4$ from the surface mixed layer and direct bubble transport, resulting in ~ 10 % of the total CH4 flow from the North Sea (Vielstädte et al., 2017). Inadvertent methane emissions from decommissioned hydrocarbon wells are thus a major source of methane into the North Sea. Globally, decommissioned wells may play a key role in methane gas emissions from hydrocarbon provinces, particularly on land, and consequently should be monitored.

**Table 1.** Leakage probabilities derived from RMS-amplitude maps of the 3D seismic data and subsequent well classification (n= 1794) into three groups of wells with low, medium and high leakage probability. Based on our water column imaging and the fluxes derived by Vielstädte et al. (2015) (leakage rate of 1-4 t of $CH_4$ per year), we estimate the total amount of methane leakage from decommissioned hydrocarbon wells within the 3D seismic data set.

| Analysis | Well count | Percentage of all wells | RMS-amplitude | Percentage of leaking wells | Minimum $CH_4$ release [t/yr] | Maximum $CH_4$ release [t/yr] |
|---|---|---|---|---|---|---|
| Wells with low leakage likelihood | 1024 | 57.1% | 0-660 | 36.4% | 372.4 | 1489.5 |
| Wells with medium leakage likelihood | 754 | 42.0% | 660-1232 | 74.1% | 558.5 | 2234.1 |
| Wells with high leakage likelihood | 14 | 0.8% | 1232-1432 | 100% | 14 | 56 |
| No value | 2 | 0.1% | N/A | 50% | 0 | 0 |
| **SUM** | **1794** | **100.0%** | | | **944.9** | **3779.5** |

### 3.6.7. Suggestions for improved drilling and abandonment practice

We show that leakage from decommissioned hydrocarbon wells is primarily associated with gas accumulations in the upper 1000 m of the sedimentary succession. Here, both biogenic and thermogenic gases may rise along vertical, permeable fluid migration pathways such as wells, chimneys and pipes or faults and the associated fractures. We propose that drilling practice should consider shallow gas accumulations not only as a drilling hazard, but also take into consideration their potential for drilling-induced inadvertent hydrocarbon gas release. Ideally, drilling operations should avoid gas accumulations by a distance of at least one kilometer to minimize the risk of leakage. This distance will depend on the local lithology and permeability of hydraulically conductive layers in the sedimentary record and should be analyzed carefully based on local/regional geological information prior to starting any drilling operations.

In global perspective, the North Sea has a relatively short history of drilling for hydrocarbons with the first commercial well drilled in 1950 (German well CUXH 1001, see table S1). Plugging and abandonment practices have improved significantly over the past decades and likely retain fluids within their respective reservoir (Figure 3.6). In contrast, California has a more than 150 years-long record of oil and gas development since the first commercial well in 1865, and old wells tend to be poorly documented and abandoned, which likely makes these wells unrecognized emitters of thermogenic gas from the deep reservoir. However, in the North Sea, there have been no indications for hydrocarbon emission from the deep-seated reservoir so far. Instead, in this and our previous studies (Vielstädte et al., 2015, 2017) we have documented that wells pose a high risk for leakage of biogenic methane from gas accumulations in the upper 1000 m, if drilled through or in close proximity to those shallow gas pockets. Therefore, monitoring of wells (e.g. through acoustic water column imaging and water/gas sampling in case of leakage identification) should not end after their abandonment. This would not only help to constrain the methane emissions from fossil fuel infrastructure, but also to understand if and how quickly well barriers degrade (in the case of leakage from the deep reservoirs). This should be used to improve plugging and abandonment standards.

### 3.7. Conclusions

We document inadvertent gas release from decommissioned hydrocarbon wells by using water column imaging in combination with 3D seismic data. We show that 28 out of 43 investigated wells show indications for gas release from the seafloor into the water column. We assess their propensity to leak and define three classes of low, medium and high leakage probability based on their RMS-amplitudes and distance to the most proximate bright spots (high amplitude anomalies with polarity reversals). This work flow is a suitable tool to predict leakage of hydrocarbon gases from abandoned wells with a high probability and without further data acquisition.

Gas release from wells in the North Sea largely depends on the presence of shallow gas accumulations (i.e. in the upper 1000 m below the seabed) and their proximity to the wells (i.e. less than 1000 m distance). These shallow, biogenic gas accumulations are sourced primarily from geologically young, organic-rich Neogene sediments. Gas from deeper, thermogenic reservoirs may also contribute to the formation of these shallow gas accumulations, e.g. if hydraulic connections to the shallow subsurface exist. Leakage is highly variable depending on the local lithology as well as the lateral hydraulic connection to deeper strata, e.g. dipping beds may deviate the gas flow in the subsurface. As a leakage mitigation measure, wells should be drilled in sufficient distance from such shallow gas accumulations.

In the upper 1000 m below the seafloor, gas migration is likely focused along the fractures induced by the drilling procedure around the well path. Below 1000 m sediment depth, the plugging and abandonment practices and the protective measures stipulated by local regulations and guidelines have improved over the past decades. This likely prevents the ascent of deep reservoir fluids. However, none of the guidelines and protective measures include monitoring of the wells, neither directly after permanent abandonment nor in the long term, but this would help to improve not only the estimates of methane released from decommissioned hydrocarbon wells but it would also help to improve the plugging and abandonment standards. We therefore recommend not only to monitor wells during the initial period after plugging and abandonment, but also to have repeated long-term monitoring surveys in the water column.

Here, we show that small emissions from single hydrocarbon wells in UK sector of the central North Sea may accumulate to a significant contribution of 0.9-3.8 kt $CH_4$ $yr^{-1}$ (from 1,794 wells in an area of 20,000 $km^2$). Considering the more than 20,507 hydrocarbon wells (currently 6689 decommissioned, not considering the multi-lateral wells drilled in > 1 km sediment depth) in the entire North Sea, the large number of wells likely constitute a major source of methane in the North Sea. In the context of geological storage of $CO_2$ in the North Sea, the cumulative effect of leaking wells may lead to a loss in efficiency of storage sites over longer timescales. However, information on methane emissions from fossil fuel infrastructure almost always originates from the oil and gas industry itself. Independent emission estimates are scarce. In the U.S., for example, studies have shown that the numbers provided by the industry are too low (Allen et al., 2013; Miller et al., 2013). Further independent emission measurements are needed for the development of guidelines and legally binding regulations.

## Acknowledgements

We thank the captains, crews and shipboard scientific parties of Poseidon cruises 518 and 534. The DFG is thanked for funding these two cruises through DFG grant no. STG 23-17. We thank PGS for providing their 3-D seismic data set “CNS Mega-Survey Plus” and the EMODnet Bathymetry Consortium (2016) for access to the EMODnet Bathymetry (DTM) (http://doi.org/10.12770/c7b53704-999d-4721-b1a3-04ec60c87238). Funding of work through Horizon 2020 Framework Programme of the European Commission project STEMM-CCS (grant no. 654462).

## References

Aadnøy, B. S., & Bell, J. S. (1998). Classification of drilling-induced fractures and their relationship to in-situ stress directions. *The Log Analyst*, 39(06).

Abshire, L. W., Desai, P., Mueller, D., Paulsen, W. B., Robertson, R. D., & Solheim, T. (2012). Offshore permanent well abandonment. Oilfield Review, 24(1), 42-50.

Allen, D. T., Torres, V. M., Thomas, J., Sullivan, D. W., Harrison, M., Hendler, A., ... & Lamb, B. K. (2013). Measurements of methane emissions at natural gas production sites in the United States. *Proceedings of the National Academy of Sciences*, *110*(44), 17768-17773.

Andresen, K. J. (2012). Fluid flow features in hydrocarbon plumbing systems: What do they tell us about the basin evolution?. *Marine Geology*, *332*, 89-108.

Anstey, N. A. (2013). *Seismic interpretation: the physical aspects*. Springer Science & Business Media.

Aydin, A. (2000). Fractures, faults, and hydrocarbon entrapment, migration and flow. *Marine and petroleum geology*, *17*(7), 797-814.

Berndt, C., Bünz, S., & Mienert, J. (2003). Polygonal fault systems on the mid-Norwegian margin: a long-term source for fluid flow. *Geological Society, London, Special Publications*, *216*(1), 283-290.

Berndt, C. (2005). Focused fluid flow in passive continental margins. *Philosophical Transactions of the Royal Society A: Mathematical, Physical and Engineering Sciences*, *363*(1837), 2855-2871.

Bjørlykke, K., & Høeg, K. (1997). Effects of burial diagenesis on stresses, compaction and fluid flow in sedimentary basins. *Marine and Petroleum Geology*, *14*(3), 267-276.

Bjørlykke, K. (1999). Principal aspects of compaction and fluid flow in mudstones. *Geological Society, London, Special Publications*, *158*(1), 73-78.

Böttner, C., Berndt, C., Reinardy, B. T., Geersen, J., Karstens, J., Bull, J. M., ... & Schramm, B. (2019). Pockmarks in the Witch Ground Basin, Central North Sea. Geochemistry, Geophysics, Geosystems, 20(4), 1698-1719.

Brandt, A. R., Heath, G. A., Kort, E. A., O'sullivan, F., Pétron, G., Jordaan, S. M., ... & Wofsy, S. (2014). Methane leaks from North American natural gas systems. *Science*, *343*(6172), 733-735.

Brudy, M., & Zoback, M. (1999). Drilling-induced tensile wall-fractures: implications for determination of in-situ stress orientation and magnitude. *International Journal of Rock Mechanics and Mining Sciences*, *36*(2), 191-215.

Buckley, S. E., & Leverett, M. (1942). Mechanism of fluid displacement in sands. *Transactions of the AIME*, *146*(01), 107-116.

Buckley, F. A. (2012). An early Pleistocene grounded ice sheet in the Central North Sea. *Geological Society, London, Special Publications*, *368*, SP368–8(1), 185–209. https://doi.org/10.1144/SP368.8

Buckley, F. A. (2016). A glaciogenic sequence from the Early Pleistocene of the Central North Sea. *Journal of Quaternary Science*, *32*(2),145–168.

BVEG, Bundesverband Erdgas, Erdöl und Geoenergie e.V. Technische Regel Bohrungsintegrität (2017). Bundesverband Erdgas, Erdöl und Geoenergie e.V., Hannover, Deutschland.

BVOT, Landesverordnung –Bergverordnung über Tiefbohrungen, Tiefspeicher und die Gewinnung von Bodenschätzen durch Bohrungen im Lande Schleswig-Holstein (Tiefbohrverordnung – BVOT), GVOBl. Schl.-H. S. 264 (1981). Oberbergamt für das Land Schleswig-Holstein, Clausthal-Zellerfeld, Deutschland.

Cartwright, J. (2007). The impact of 3D seismic data on the understanding of compaction, fluid flow and diagenesis in sedimentary basins. *Journal of the Geological Society*, *164*(5), 881–893. https://doi.org/10.1144/0016-76492006-143

Celia, M. A., & Bachu, S. (2003, January). Geological sequestration of CO2: is leakage unavoidable and acceptable?. In *Greenhouse Gas Control Technologies-6th International Conference* (pp. 477-482). Pergamon.

Ciais, P., Sabine, C., Bala, G., Bopp, L., Brovkin, V., Canadell, J., et al. (2013). Carbon and other biogeochemical cycles. In *Climate change 2013: The physical science basis. Contribution of Working Group I to the Fifth Assessment Report of the Intergovernmental Panel on Climate Change*, (pp. 465–570). United Kingdom and New York, NY, USA: Cambridge University Press.

Clayton, C. J., & Hay, S. J. (1994). Gas migration mechanisms from accumulation to surface. *Bulletin of the Geological Society of Denmark*, *41*(1), 12-23.

Clayton, C. J., Hay, S. J., Baylis, S. A., & Dipper, B. (1997). Alteration of natural gas during leakage from a North Sea salt diapir field. *Marine Geology*, *137*(1-2), 69-80.

Crémière, A., Lepland, A., Chand, S., Sahy, D., Kirsimäe, K., Bau, M., ... & Brunstad, H. (2016). Fluid source and methane-related diagenetic processes recorded in cold seep carbonates from the Alvheim channel, central North Sea. *Chemical Geology*, *432*, 16-33.

Domenico, S. N. (1976). Effect of brine-gas mixture on velocity in an unconsolidated sand reservoir. *Geophysics*, *41*(5), 882-894.

Dumke, I., Berndt, C., Crutchley, G. J., Krause, S., Liebetrau, V., Gay, A., & Couillard, M. (2014). Seal bypass at the Giant Gjallar Vent (Norwegian Sea): Indications for a new phase of fluid venting at a 56-Ma-old fluid migration system. *Marine Geology*, 351, 38-52.

Gasda, S. E., Bachu, S., & Celia, M. A. (2004). Spatial characterization of the location of potentially leaky wells penetrating a deep saline aquifer in a mature sedimentary basin. *Environmental geology*, *46*(6-7), 707-720.

Gregory, A. R. "Fluid saturation effects on dynamic elastic properties of sedimentary rocks." *Geophysics* 41.5 (1976): 895-921.

Guide to Hydrocarbon Licences in Denmark, General Legislation and Information Exploration and Drilling Activities, Subchapter Guidelines for Drilling p.228 (2009). Danish Energy Agency, Copenhagen, Denmark.

Gurevich, A. E., Endres, B. L., Robertson Jr, J. O., & Chilingar, G. V. (1993). Gas migration from oil and gas fields and associated hazards. *Journal of Petroleum Science and Engineering*, *9*(3), 223-238.

Haffert, L., Haeckel, M., Liebetrau, V., Berndt, C., Hensen, C., Nuzzo, M., ... & Weise, S. M. (2013). Fluid evolution and authigenic mineral paragenesis related to salt diapirism–The Mercator mud volcano in the Gulf of Cadiz. *Geochimica et Cosmochimica Acta*, *106*, 261-286.

Ham, J. D., & Eilerts, C. K. (1967). Effect of saturation on mobility of low liquid-vapor ratio fluids. *Society of Petroleum Engineers Journal*, *7*(01), 11-19.

Harrison, E., Kieschnick, W. F., & McGuire, W. J. (1954). The Mechanics of Fracture Induction and Extension. *AIME Petroleum Transactions*, *201*, 252-263.

Hubbert, M.K., Willis, D.G., 1957. Mechanic of hydraulic fracturing. *Trans. Soc. Pet. Eng. AIME 1957*, 153–168.

Judd, A., Davies, G., Wilson, J., Holmes, R., Baron, G., & Bryden, I. (1997). Contributions to atmospheric methane by natural seepages on the UK continental shelf. Marine Geology, 137(1-2), 165-189.

Judd, A., & Hovland, M. (2009). *Seabed fluid flow: the impact on geology, biology and the marine environment*. Cambridge University Press.

Kang, M., Christian, S., Celia, M. A., Mauzerall, D. L., Bill, M., Miller, A. R., ... & Jackson, R. B. (2016). Identification and characterization of high methane-emitting abandoned oil and gas wells. *Proceedings of the National Academy of Sciences*, *113*(48), 13636-13641.

Karstens, J., & Berndt, C. (2015). Seismic chimneys in the Southern Viking Graben–Implications for palaeo fluid migration and overpressure evolution. *Earth and Planetary Science Letters*, *412*, 88-100.

King, G. E., & Valencia, R. L. (2014). Environmental risk and well integrity of plugged and abandoned wells. In *SPE Annual Technical Conference and Exhibition*. Society of Petroleum Engineers, Amsterdam.

Kuhlmann, G., & Wong, T. E. (2008). Pliocene paleoenvironment evolution as interpreted from 3D-seismic data in the southern North Sea, Dutch offshore sector. *Marine and Petroleum Geology*, *25*(2), 173-189.

Landrø, M. (2011). Seismic monitoring of an old underground blowout–20 years later. *First Break*, *29*(6), 39-48.

Le Quéré, C., Andrew, R. M., Friedlingstein, P., Sitch, S., Hauck, J., Pongratz, J., ... & Arneth, A. (2018). Global carbon budget 2018. *Earth System Science Data (Online)*, *10*(4).

LEBG, Richtlinie des Oberbergamtes in Clausthal-Zellerfeld über das Verfüllen auflässiger Bohrungen (1998). Oberbergamt, Clausthal-Zellerfeld, Deutschland.

Løseth, H., Gading, M., & Wensaas, L. (2009). Hydrocarbon leakage interpreted on seismic data. *Marine and Petroleum Geology*, *26*(7), 1304-1319.

Løseth, H., Wensaas, L., Arntsen, B., Hanken, N. M., Basire, C., & Graue, K. (2011). 1000 m long gas blow-out pipes. *Marine and Petroleum Geology*, *28*(5), 1047-1060.

Marfurt, K. J., & Alves, T. M. (2015). Pitfalls and limitations in seismic attribute interpretation of tectonic features. *Interpretation*, *3*(1), SB5-SB15.

Miller, S. M., Wofsy, S. C., Michalak, A. M., Kort, E. A., Andrews, A. E., Biraud, S. C., ... & Miller, B. R. (2013). Anthropogenic emissions of methane in the United States. *Proceedings of the National Academy of Sciences*, *110*(50), 20018-20022.

Mining Regulations of the Netherlands, Regulations of the Staatssecretaris of Economic Affairs of 16 December 2002/nr WJZ 02063603 regulating the implementation of the Mijnbouwbesluit (2003, updated 2014). Dorhout Advocaten N.V, Groningen, Netherlands.

Müller, S., Reinhardt, L., Franke, D., Gaedicke, C., & Winsemann, J. (2018). Shallow gas accumulations in the German North Sea. *Marine and Petroleum Geology*, *91*, 139-151.

Nordbotten, J. M., Celia, M. A., & Bachu, S. (2004). Analytical solutions for leakage rates through abandoned wells. *Water Resources Research*, *40*(4).

Nordbotten, J. M., Celia, M. A., Bachu, S., & Dahle, H. K. (2005). Semianalytical solution for CO2 leakage through an abandoned well. *Environmental science & technology*, *39*(2), 602-611.

NORSOK D-010, Well integrity in drilling and well operations, NORSOK Standard D-010 (Rev. 4, 2013). Standards Norway, Lysaker, Norway.

Nuzzo, M., Hornibrook, E. R., Gill, F., Hensen, C., Pancost, R. D., Haeckel, M., ... & Pinheiro, L. M. (2009). Origin of light volatile hydrocarbon gases in mud volcano fluids, Gulf of Cadiz—evidence for multiple sources and transport mechanisms in active sedimentary wedges. *Chemical Geology*, *266*(3-4), 350-363.

Ottesen, D., Dowdeswell, J. A., & Bugge, T. (2014). Morphology, sedimentary infill and depositional environments of the Early Quaternary North Sea Basin (56–62 N). *Marine and Petroleum Geology*, *56*, 123-146.

Pape, T., Bahr, A., Rethemeyer, J., Kessler, J. D., Sahling, H., Hinrichs, K. U., ... & Bohrmann, G. (2010). Molecular and isotopic partitioning of low-molecular-weight hydrocarbons during migration and gas hydrate precipitation in deposits of a high-flux seepage site. *Chemical Geology*, *269*(3-4), 350-363.

Rea, B. R., Newton, A. M., Lamb, R. M., Harding, R., Bigg, G. R., Rose, P., et al. (2018). Extensive marine-terminating ice sheets in Europe from 2.5 million years ago. *Science Advances*, *4*(6), eaar8327). https://doi.org/10.1126/sciadv.aar8327

Reinardy, B. T., Hjelstuen, B. O., Sejrup, H. P., Augedal, H., & Jørstad, A. (2017). Late Pliocene-Pleistocene environments and glacial history of the northern North Sea. *Quaternary Science Reviews*, *158*, 107–126. https://doi.org/10.1016/j.quascirev.2016.12.022

Rose, P., Byerley, G., Vaughan, O., Cater, J., Rea, B. R., Spagnolo, M., & Archer, S. (2016). Aviat: A Lower Pleistocene shallow gas hazard developed as a fuel gas supply for the Forties Field. In *Geological society, London, petroleum geology conference series*, (Vol. 8, pp. PGC8–PGC16). London: Geological Society of London.

Saunois, M., Bousquet, P., Poulter, B., Peregon, A., Ciais, P., Canadell, J. G., et al. (2016). The global methane budget 2000–2012. *Earth System Science Data (Online)*, *8*(2), 697–751. https://doi.org/10.5194/essd-8-697-2016

Schmidt, M., et al. (2019). RV POSEIDON Fahrtbericht/Cruise Report POS534: STEMM-CCS Study of the Environmental Monitoring of Subseafloor CO2 Storage Operations. Bremerhaven-Kiel (Germany) 01.05.-29.05.2019.

Schneider von Deimling, J., Brockhoff, J., & Greinert, J. (2007). Flare imaging with multibeam systems: Data processing for bubble detection at seeps. *Geochemistry, Geophysics, Geosystems*, *8*(6).

Schroot, B. M., & Schüttenhelm, R. T. E. (2003). Expressions of shallow gas in the Netherlands North Sea. *Netherlands Journal of Geosciences*, *82*(1), 91-105.

Sejrup, H. P., Aarseth, I., Ellingsen, K. L., Reither, E., Jansen, E., Løvlie, R., et al. (1987). Quaternary stratigraphy of the Fladen area, central North Sea: A multidisciplinary study. *Journal of Quaternary science*, *2*(1), 35–58. https://doi.org/10.1002/jqs.3390020105

Stoker, M. S., & Bent, A. J. (1987). Lower Pleistocene deltaic and marine sediments in boreholes from the central North Sea. *Journal of Quaternary Science*, *2*(2), 87–96. https://doi.org/10.1002/jqs.3390020202

Thomas, H., Bozec, Y., De Baar, H. J., Elkalay, K., Frankignoulle, M., Schiettecatte, L. S., ... & Borges, A. V. (2005). The carbon budget of the North Sea. *Biogeosciences*, *2*(1), 87-96.

Townsend‐Small, A., Ferrara, T. W., Lyon, D. R., Fries, A. E., & Lamb, B. K. (2016). Emissions of coalbed and natural gas methane from abandoned oil and gas wells in the United States. *Geophysical Research Letters*, *43*(5), 2283-2290.

UKCS Decommissioning Cost Report, Oil & Gas Authority UKCS Decommissioning, 2017 Cost Estimate Report (2017). Oil & Gas Authority, London, United Kingdom.

Vielstädte, L., Karstens, J., Haeckel, M., Schmidt, M., Linke, P., Reimann, S., ... & Wallmann, K. (2015). Quantification of methane emissions at abandoned gas wells in the Central North Sea. *Marine and Petroleum Geology*, *68*, 848-860.

Vielstädte, L., Haeckel, M., Karstens, J., Linke, P., Schmidt, M., Steinle, L., & Wallmann, K. (2017). Shallow gas migration along hydrocarbon wells–An unconsidered, anthropogenic source of biogenic methane in the North Sea. *Environmental science & technology*, *51*(17), 10262-10268.

Vielstädte, L., Linke, P., Schmidt, M., Sommer, S., Haeckel, M., Braack, M., & Wallmann, K. (2019). Footprint and detectability of a well leaking CO2 in the Central North Sea: Implications from a field experiment and numerical modelling. *International Journal of Greenhouse Gas Control*, *84*, 190-203.

Ward, N. I., Alves, T. M., & Blenkinsop, T. G. (2016). Reservoir leakage along concentric faults in the Southern North Sea: Implications for the deployment of CCS and EOR techniques. *Tectonophysics*, *690*, 97-116.

Well Decommissioning Guidelines, The UK Oil and Gas Industry Association Limited trading as Oil & Gas UK Guidelines for Well Decommissioning (Issue 6, 2018). Oil & Gas UK, Aberdeen, United Kingdom. ISBN: 903 004 92 6.

Whitaker, S. (1986). Flow in porous media I: A theoretical derivation of Darcy's law. *Transport in porous media*, *1*(1), 3-25.

White, J. E. (1975). Computed seismic speeds and attenuation in rocks with partial gas saturation. *Geophysics*, *40*(2), 224–232. https://doi.org/10.1190/1.1440520

# 4. Marine forearc extension in the Hikurangi margin: New insights from high-resolution 3D seismic data

Christoph Böttner, Felix Gross, Jacob Geersen, Gareth Crutchley, Joshu Mountjoy and Sebastian Krastel

Published in 2018 Tectonics, 37(5), 1472-1491.

The Poverty Bay at the Hikurangi Margin, New Zealand.

## Key Points

1. High-resolution 3D seismic data indicate widespread normal faulting on the upper slope of the northeastern Hikurangi margin.
2. The normal faults show two major strike directions, primarily landward dip, low vertical displacements and steep dip angles.
3. Extension may be controlled by regional uplift or/and extensional strain due to rotation of tectonic blocks around nearby poles.

## 4.1. Abstract

Upper-plate normal faults are a widespread structural element in erosive plate margins. Increasing coverage of marine geophysical data has proven that similar features also exist in accretionary margins where horizontal compression usually results in folding and thrust-faulting. There is a general lack of understanding of the role and importance of normal faulting for the structural and tectonic evolution of accretionary margins. Here, we use high-resolution 2D and 3D seismic reflection data and derived seismic attributes to map and analyze upper-plate normal faulting in the marine forearc of the accretionary Hikurangi margin, New Zealand. We document extension of the marine forearc over a wide area along the upper continental slope. The seismically imaged normal faults show low vertical displacements, high dip angles, a preference for landward dip and often en echelon patterns. We evaluate different processes, which may cause the observed extension, including (1) stress change during the earthquake cycle, (2) regional or local uplift and decoupling of shallow strata from compression at depth, as well as (3) rotation of crustal blocks and resulting differential stresses at the block boundaries. The results suggest that normal faults play an important role in the structural and tectonic evolution of accretionary margins, including the northern Hikurangi forearc.

## 4.2. Introduction

In subduction zones, upper-plate normal faults have long been considered a tectonic feature primarily associated with erosive margins. However, increasing coverage of marine seismic data has proven that similar features also exist in accretionary margins, such as Cascadia (McNeill et al., 1997), Makran (Grando and McClay, 2007), Nankai (Gulick et al., 2010; Moore et al., 2013) or Central Chile (Geersen et al., 2011, 2016), where kinematics are dominated by compression. In addition, extensional aftershocks in the overriding-plate have been documented in the wake of recent large megathrust earthquakes, including the 2010 Chile (Mw. 8.8) and 2011 Japan (Mw. 9.0) events (Asano et al., 2011; Farías et al., 2011; Ide et al., 2011). After being recognized in many accretionary subduction zones, there is currently much debate about the role and importance of normal faults and zones of extension in these settings. This not only includes their role for the seismo-tectonic evolution of an accretionary margin, but also the seismic and tsunami hazard they pose, as well as their impact on fluid flow and fluid seepage.

Different models have been evoked to explain extension in accretionary margins. These models include (1) regional uplift due to basal underplating of subducted sediment or shortening across upper-plate thrust faults (e.g. Gulick et al., 2010); (2) local uplift due to subduction of excess topography on the oceanic plate (Masson et al., 1990; Ranero and von Huene, 2000); (3) mechanical decoupling of the shallow forearc strata from the underlying compressional subduction regime along a crustal décollement (Buck and Sokoutis, 1994; McNeill et al., 1997; Moore et al., 2013; Zoback et al., 1981); (4) dominance and prevalence of extensional strain during the co-seismic or early post-seismic phase of a megathrust earthquake (Aron et al., 2013; Cubas et al., 2013a, 2013b).

For the Hikurangi margin off the North Island of New Zealand (Fig. 4.1), geodetic data and structural investigations have revealed normal faulting in parts of the terrestrial forearc (Cashman and Kelsey, 1990; Mazengarb, 1984; Walcott, 1978, 1987). In the offshore forearc, normal faults have been imaged locally around the crests of slope-parallel ridges by means of seismic reflection and multibeam bathymetric data (Kukowski et al., 2010; Plaza-Faverola et al., 2014). However, little is known about how large-scale upper-plate extension in the terrestrial forearc continues offshore into the marine forearc. Here, we combine regional 2D seismic reflection lines and a high-resolution 3D seismic volume from the upper slope of the northern Hikurangi margin in the area of Tuaheni Slope (off the coast from Gisborne) to map and analyze normal faulting in the marine forearc. Based on the structural investigations, we consider the mechanisms that control upper-plate extension.

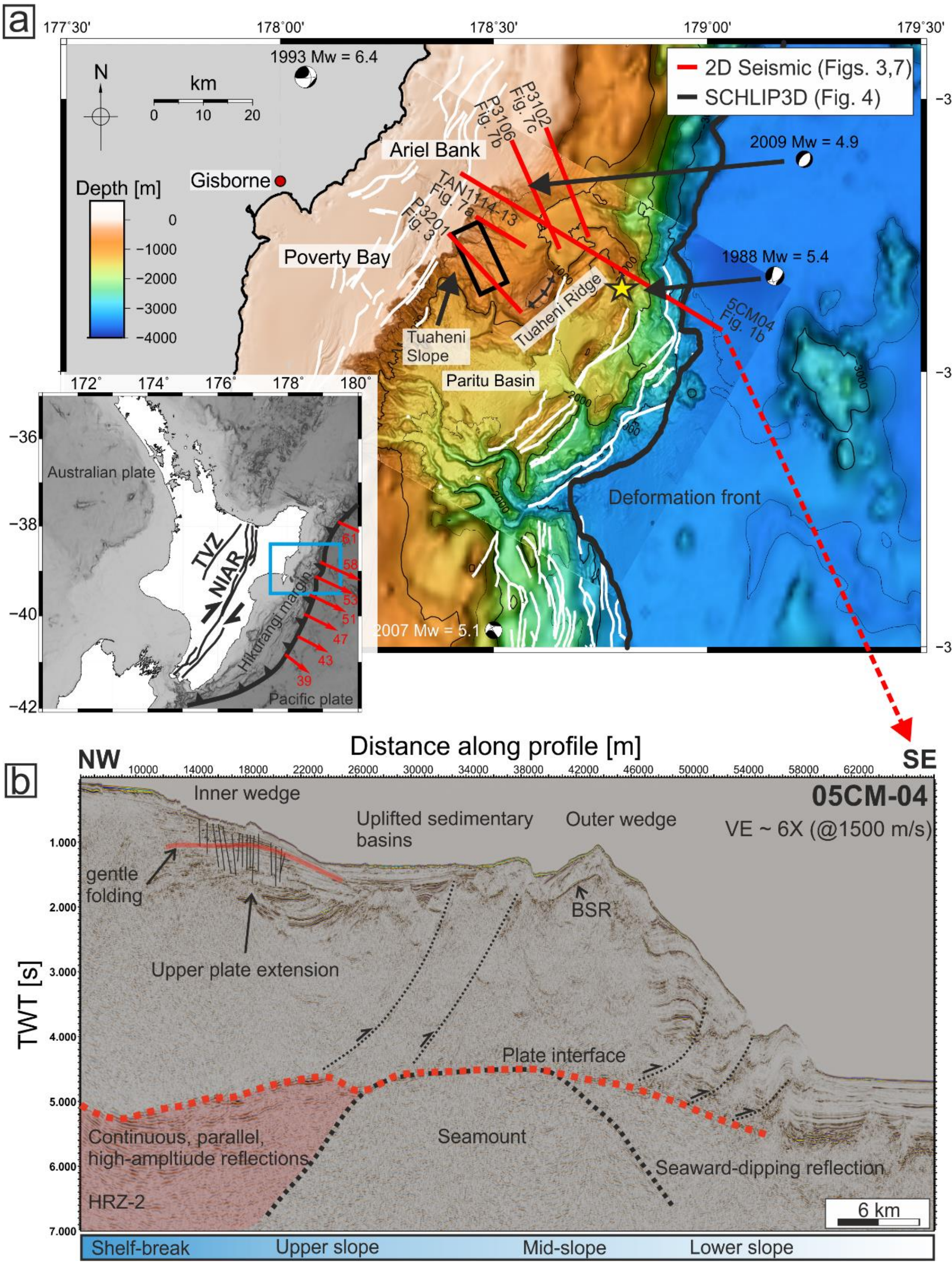

**Figure 4.1.** (a) Map of the northern Hikurangi margin composed of GEBCO and high-resolution bathymetry (100 m grid, source: NIWA). Focal mechanisms are taken from the global CMT catalog (Dziewonski et al., 1981; Ekström et al., 2012) and the location of the 1947 Poverty Bay earthquake is indicated with a yellow star (after Bell et al., 2014). The small inset shows location of the area of study within respect to the Australian and Pacific plates. Red vectors show long-term convergence at the Hikurangi trench in mm/yr (modified after Wallace et al., 2004 and Wallace et al., 2009). White lines image active faults within the region (source: NIWA). TVZ = Taupo volcanic zone; NIAR = North Island axial ranges. (b) Interpreted seismic reflection profile 05CM-04 located at the northern Hikurangi Margin off Gisborne, New Zealand with seismic interpretations after Bell et al. (2010) (HRZ-2 = high-amplitude reflectivity zone 2). Red line highlights gentle folding of upper-plate strata. The location of the profile is shown in (a) and vertical exaggeration is ~ 6X at 1500 m/s.

### 4.2.1. Geological setting of the Hikurangi margin

The Hikurangi margin, located off the East Coast of the North Island of New Zealand, is shaped by the subduction of the Pacific Plate beneath the Australian Plate (Fig. 4.1). It represents the transition from Tonga-Kermandec subduction to the north to continental collision and the strike-slip Alpine fault farther south (Nicol et al., 2007). The rate of plate convergence decreases from 60 mm/a in the North to 30 mm/a in the South (Beavan et al., 2002, Wallace et al., 2004). Convergence occurs oblique towards the SW (Beavan et al., 2002). The oblique convergence separates into a margin-normal component, accommodated in the subduction thrust, and a margin-parallel component, mainly accommodated across the North Island Axial Ranges (dextral shear zone) and by clockwise rotation of the eastern North Island (Beanland and Haines, 1998; Nicol and Wallace, 2007; Wallace et al., 2004; Webb and Anderson, 1998). Geodetic measurements indicate a segmentation of the Australian Plate in the region of the North Island into individual tectonic blocks (Nicol and Wallace, 2007; Wallace et al., 2004). The southward decrease in convergence along the margin results in clockwise rotation of the tectonic blocks around poles located to the west of the North Island (Mumme et al., 1989; Walcott, 1984; Wallace et al., 2004). The stresses that result from rotation of the individual blocks are mainly accommodated along interconnected faults along the block boundaries (McCaffrey, 2002; McCaffrey et al., 2000; McClusky et al., 2001; Wallace et al., 2004). Intra-arc extension occurs within the Taupo volcanic zone as a result of rapid rotation of the North Island forearc (Nicol and Wallace, 2007; Wallace et al., 2004).

The structure and geometry of the Hikurangi margin, including the nature of the plate-boundary, vary along the margin (Barker et al., 2009; Bell et al., 2010; Reyners, 1998; Wallace et al., 2004). Crustal thickness of the Pacific Plate along the trench increases from 10 – 15 km in the North to 20-25 km at the Chatham Rise (Davy and Wood, 1994). Frontal accretion of trench sediments results in the formation of an active accretionary prism with predominantly landward-dipping prism thrust faults. The frontal part of the accretionary prism takes up about 90% of the margin normal component of plate convergence (Pedley et al., 2010). In addition to horizontal shortening and thrust faulting, the geomorphology and structural evolution of the Hikurangi margin is further influenced by the subduction of several seamounts on the oceanic plate as well as gravitationally driven sediment transport processes and resulting mass transport deposits (Bell et al., 2010; Mountjoy et al., 2009, 2014; Mountjoy and Barnes, 2011; Pedley et al., 2010).

### 4.2.2. Local geological setting

This study is located in the area of Tuaheni Slope (Fig. 4.1a). The tectonic setting and margin geometry has been described and analyzed by Barker et al. (2009) and Bell et al. (2010) based on margin orthogonal 2D seismic reflection data such as line 05CM-04 (compare Fig. 4.1b). Line 05CM-04 images the plate interface to 50 km landward of the deformation front. The outermost accretionary wedge shows high slope angles (up to 10°) suggesting over-steepening (Barker et al., 2009). The margin is locally modified by the subduction of a seamount (Fig.

4.1b). At depth, the landward section of the subducting seamount shows continuous, parallel, high amplitude reflections, which Bell et al. (2010) defined as high-amplitude reflectivity zone 2 (HRZ-2). The seismic section reveals a bottom-simulating reflection (BSR), which is visible from the upper slope to lower slope (Fig. 4.1b). At the upper continental slope, Tuaheni Ridge forms the lower boundary of an upper slope basin. In this area the upper slope basins are uplifted, possibly due to upper plate contractional faulting (Berryman et al., 1989; Ota and Yamaguchi, 2004), underplating (Reyners and McGinty, 1999; Walcott, 1987) and/or seamount subduction during the last 2 Ma (Bell et al., 2010; Pedley et al., 2010). The continental shelf is dominated by Ariel Bank fault, which shows vertical slip rates of up to 3-5 mm/yr (Mountjoy and Barnes, 2011). However, the activity of upper-plate faults underlying the middle and upper continental slope is usually not well constrained (Bell et al., 2010; Mountjoy and Barnes, 2011).

Two major geological units make up the sedimentary succession at Tuaheni Slope. The lower unit consists of Miocene to Pliocene rock, partly exposed by erosion and tectonic uplift, e.g. Tuaheni ridge, with possible Cretaceous and Paleogene sedimentary rocks at depth (Barnes et al., 2002, 2010; Field and Uruski, 1997; Mountjoy and Barnes, 2011; Pedley et al., 2010). The upper unit consists of Quaternary shelf-edge low-stand clinoform sequences from the outer shelf to the upper slope. These clinoform sequences developed during a eustatic low of the sea level due to glacial cycles (Catuneanu et al., 2009; Van Wagoner et al., 1988). Holocene sedimentation formed fine-grained clinoform sequences southwest of Tuaheni Slope, with intercalated sand fractions (Alexander et al., 2010; Barnes et al., 1991). A similar sedimentary succession is likely present at Tuaheni Slope (Mountjoy et al., 2014). The upper slope shows indications for upper plate extension within the first 0.5 s two-way travel time (TWT) of the sedimentary succession (Fig. 4.1b).

Most earthquakes of the offshore northern Hikurangi margin are associated with thrust faulting. Peak ground acceleration of 0.4-0.5 g is expected at a recurrence rate of about 250 years, according to the New Zealand National Seismic Hazard Model (Stirling et al., 2012). Over the past century, the margin experienced a series of tsunamogenic earthquakes (Fraser, 1998) including one in 1931 (Mw ~7.9) near Napier/Hawke Bay (Conly, 1980; De Lange and Healy, 1986) and two in 1947 (Mw 7.0-7.1, yellow star in Fig. 4.1a, and Mw 6.9–7.1) off Gisborne (Bell et al., 2014; De Lange and Healy, 1986). These events caused 6-10 m run-up heights, damage to shore-based structures, damage and loss of floating objects and flooding of coastal regions (De Lange and Healy, 1986). During the last ~30 years, four earthquakes (1988, 1993, 2007, and 2009) occurred at depths less than 20 km indicating that they likely originated in the upper-plate (Dziewonski et al., 1981; Ekström et al., 2012). The four earthquakes had magnitudes ranging from 4.9 to 6.4 Mw, and were of normal to strike-slip character (Fig. 4.1a).

## 4.3. Materials and Methods

### 4.3.1. Seismic data – SCHLIP3D and 2D

In this study we use a combination of high-resolution 2D and 3D seismic reflection data. Most of the seismic data were acquired during RV Tangaroa cruise TAN1404 in April 2014.

During survey TAN1404, the 2D seismic system consisted of a 0.7 l GI Gun and a 150 m long streamer with 96 channels; channel spacing was 1.5625 m. Processing included crooked line common midpoint (CMP) binning at a spacing of 1.5 m, a Butterworth-type frequency filter (10/35-150/200 Hz), normal move-out (NMO) correction with constant velocity of 1500 m/s, stacking and a 2D Stolt time migration with a constant velocity of 1500 m/s. From the TAN1404 dataset, we use seismic lines P3106, P3406, and P3102 (Fig. 4.1a). In addition, we use seismic line TAN1114-13 which was acquired during RV Tangaroa cruise TAN1114 (2011) using a 600 m long streamer with 48 channels at 12.5 m spacing and 2x 0.7 l/1.7 l GI guns (Barnes et al., 2011; Mountjoy et al., 2014).

3D seismic data were also collected during cruise TAN1404 using the 3D P-cable system. The system consists of a cross-cable towed behind the ship in between two paravanes. The cross cable approximately forms the shape of a catenary as it is towed through the water, with the end points (at the paravanes) spanning a distance of ~150 m. The catenary form enables a predictive calculation of receiver array positions given the known end points (the paravanes equipped with GPS), the length of the cable, and the ship's azimuth. These predicted receiver positions were refined using the direct wave arrival times at each streamer channel. During cruise TAN1404, the P-cable system consisted of 15 streamer segments, each ~12.5 m long, with 8 channels at a spacing of 1.5625 m. The 0.7 l GI Gun was towed ~30 m behind the ship, shot every 3 seconds and had frequencies between 15 to 400 Hz. This small shot interval (equating to ~5 m at 3.5 knots sailing speed) enabled dense CMP binning onto a grid with a 3.125 m CMP spacing. Processing included bandpass filtering (40/70-350/500 Hz), CMP-stacking, stacking of successive inlines to reduce data gaps (resulting in a 6.25 m inline spacing while maintaining the 3.125 m crossline spacing), NMO-correction with a constant velocity (1500 m/s) and despiking. We ran a 2D trace interpolation, first in the crossline direction, then in the inline direction, to fill small data gaps in the 3D seismic volume. Finally, we migrated the volume with a 3D post-stack Kirchhoff time migration using a constant velocity of 1500 m/s and an aperture of 500 m. The resulting seismic volume is ~13.5 km long and ~5.9 km wide. We hereafter refer to the 3D seismic volume as SCHLIP3D (the acronym of the project named 'Submarine Clathrate Hydrate Landslide Imaging Project in 3D' under which the data were acquired).

### 4.3.2. Seismic attribute analyses

#### 4.3.2.1. Fault detection with attributes

Bahorich and Farmer (1995) introduced the use of attributes (coherence) to seismic interpretation to enhance the interpretation of seismic sections. Faults are visible in seismic data as a clear displacement of adjacent reflections. Seismic attributes make use of this discontinuity and therefore provide a powerful and reliable tool for fault detection within 3D seismic volumes (e.g. Moore et al., 2013; Neves et al., 2004). Crucial to a proper analysis are well-interpreted seismic horizons, which avoid the issue of discontinuities induced by the intersection of time slices with stratigraphic layering. Common attributes use either physical or geometrical properties of the complex seismic trace (Taner et al., 1979), e.g. Similarity (Bahorich and Farmer, 1995). Here we favor and apply visual attributes (Symmetry and derivative I3D volumes) introduced by IHS Kingdom. These attributes provide a clear image of deformation patterns and fault planes, offer high resolution and show a good signal-to-noise ratio at all depth levels and horizons (Yu et al., 2015).

#### 4.3.2.2. Symmetry (I3D attributes)

Symmetry is a newly designed post-stack, post migration structural feature detection tool (e.g. fault detection) based on a 3D log-Gabor filter array (Yu et al., 2015) introduced by IHS within their Kingdom software. It represents a new type of seismic attribute for 3D data analysis, which is referred to as visual attributes. Symmetry is inspired by neuronal mechanisms of visual perception for orientation patterns. The attribute is sensitive to seismic amplitude variations and hence correlates with discontinuities and curvatures associated with geological surfaces. Its strength is to identify faults, fractures, channels and other discontinuous events.

We used the SCHLIP3D seismic volume for our Symmetry I3D Energy attribute, a derivative volume of the Symmetry attribute (Yu et al., 2015). The algorithm ran with a 100 ms vertical filter window to obtain a better image, resolve only relatively long faults (i.e. longer than 100 ms), and to diminish the influence of noise, e.g. from diffraction hyperbolas (Yu et al., 2015; IHS Kingdom 2017 manual).

### 4.3.3. Estimation of fault dip and vertical displacement

We derived the fault dip from fault planes visible in vertical seismic displays (2D) and attribute horizon slices (3D). To obtain accurate measurements we took the topmost and lowermost point to which we could trace the coherent displacement of adjacent traces and measured the vertical and horizontal lengths (Fig. 4.2). With these length measurements perpendicular to the fault strike and basic trigonometric calculations, we were able to estimate the true fault dip. We calculated the vertical displacement from measurements at the top, center, and bottom of the visible fault plane (Fig. 4.2). With these two parameters, we calculated the total horizontal displacement with trigonometric calculations. The resulting estimates give us a good approximation of the extension per unit length without considering the rock parameters.

All these measurements and calculations depend on the applied seismic velocity model. For our analysis, we use a constant velocity of 1600 m/s, which is a good approximation for water-saturated sediments. The in-situ displacements will increase slightly with depth due to higher velocities in deeper strata. An increase to a velocity of 2000 m/s, which may be representative for sandy interbeds inside the clinoforms (Press, 1966), would result in 25% higher displacement values. Similarly, the dip angle calculations are dependent on the velocities through the tangent function (Fig. 4.2). However, as the velocities only influence the numerator of the calculation the deviations possible from the actual dip angles are relatively small. For example, a fault with a dip angle of 88.4° would change in dip from 88.4° at 1600 m/s to 88.7° at 2000 m/s. Increasing velocities with depth are expected in the subsurface, which would cause similar or higher increase in fault angle (e.g. Yielding et al., 1991).

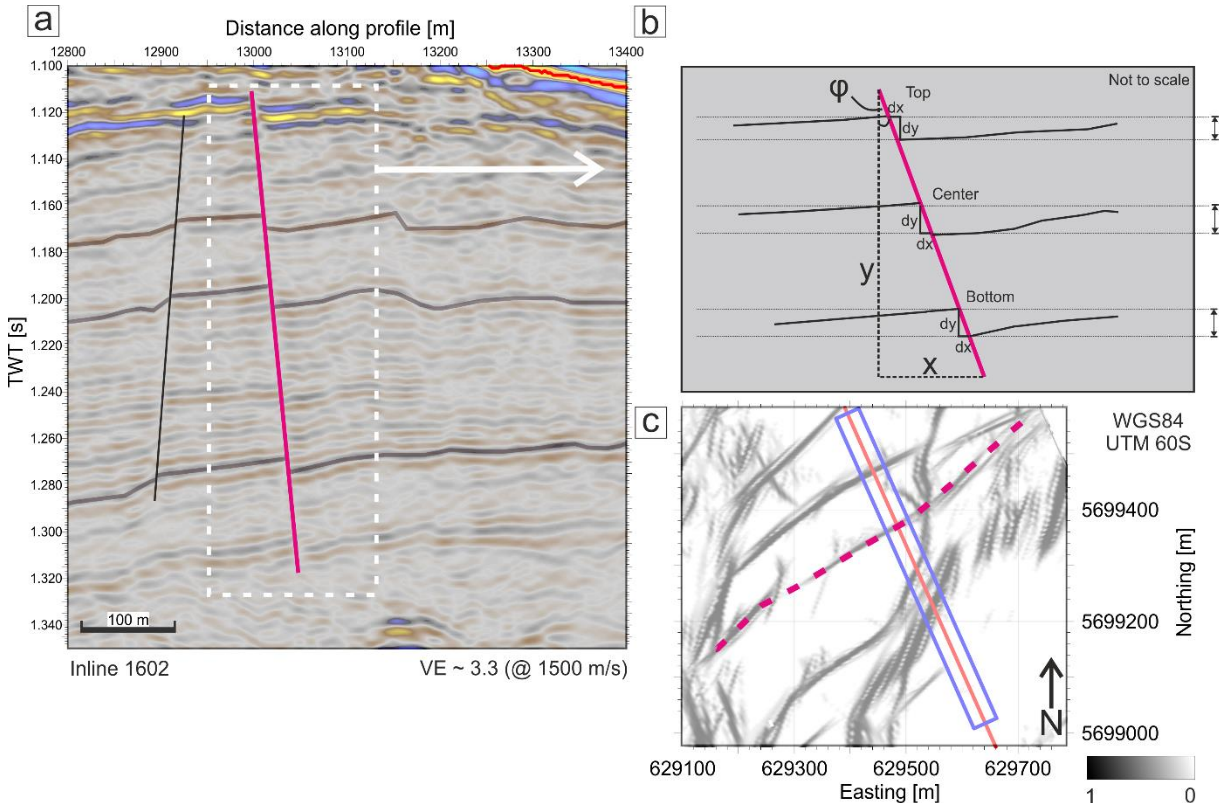

**Figure 4.2**. (a) Example arbitrary line from the 3D seismic volume, highlighting normal faults and the offset reflections. (b) Schematic Sketch of the methods applied to determine fault characteristics: Total vertical (x) and horizontal (y) fault extents for dip calculation (phi), and three measurements at different depth levels (Top, Center, Bottom) of horizontal (dx) and vertical (dy) displacement. This sketch is not to scale, in order to emphasize dx/dy measurements. (c) Location within the seismic attribute map (I3D Energy) of the seismic profile displayed in (a).

## 4.4. Results

### 4.4.1. Results from 2D seismic data

High-resolution 2D seismic line P3201 (Fig. 4.3) extends over 21 km from the shelf-break, which represents the transition from Ariel Bank to the headwall of the Tuaheni Landslide Complex (Mountjoy et al., 2009), to the Tuaheni Ridge (Fig. 4.1a). The latter forms the distal boundary of the upper slope (Fig. 4.1a). The western part of the seismic line (3-13.5 km along profile) overlaps with inline 1664 of the 3D seismic volume shown in Figure 4.4 and discussed subsequently.

Quaternary clinoforms dominate the seismic image in the western part of line P3201 (Fig. 4.3). The base of gas hydrate stability is manifested in this section as an alignment of truncated high-amplitude reflections – i.e. a discontinuous BSR (white arrows in Fig. 4.3b). Between 9-18 km along profile, the clinoforms are pervasively intersected by steeply dipping normal faults (> 65°), which have vertical offsets in the range of 1 - 19 ms TWT (~1 - 15 m, assuming a representative velocity of 1600 m/s). A decreasing signal-to-noise ratio with increasing depth below seafloor prohibits the analysis of these faults below ~1.4 s TWT (10-17 km along profile). The presence of Tuaheni Ridge modifies the sedimentary succession eastward of 14 km along profile. Folded strata that crop out at the seafloor from 19-21 km along profile characterize the ridge (Fig. 4.3).

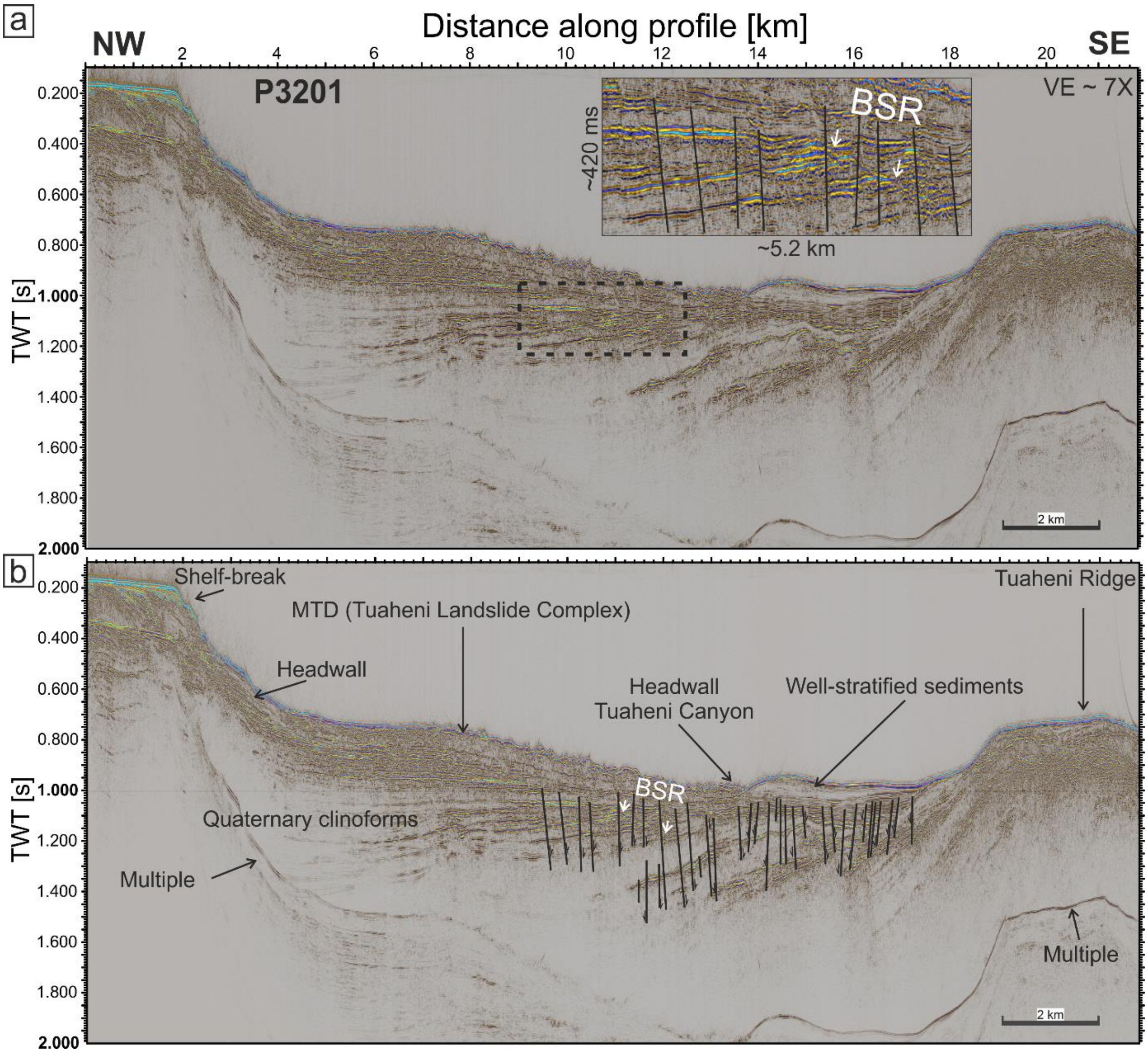

**Figure 4.3.** (a) Uninterpreted and (b) interpreted seismic reflection profile P3201 (see Fig. 4.1a for location) showing major geological units. Interpretation of the mass transport deposit (MTD) is after Mountjoy et al. (2009, 2014). Black lines are normal faults; “BSR” marks the location of a bottom simulating reflection, marking the base of gas hydrate stability, on this profile. The inset shows a zoom around the BSR. The dashed box on the interpreted seismic profile marks the exact location of this zoom extraction. The vertical exaggeration is ~ 7X at 1500 m/s.

### 4.4.2. Results from 3D seismic data

The SCHLIP3D seismic volume extends from the shelf-break to Tuaheni Canyon (Fig. 4.1a). It images the upper-slope in the area of the southern lobe of the Tuaheni Landslide Complex down to the acoustic basement at 1.5 s TWT. Figure 4.4 shows inline 1664, which is located adjacent to 2D line P3201 (3-13.5 km along profile, Fig. 4.3). From 3 to 13.5 km along profile, in the area of the Tuaheni Landslide Complex, the upper 300 ms TWT of the sub-seafloor show two different seismic units with chaotic seismic facies, commonly interpreted as mass transport deposits (see Fig. 4.4).

Low-stand clinoforms dominate inline 1664 between 2.2-13 km along profile and at TWTs greater than 0.7 s (Fig. 4.4). We pick two characteristic clinoform surfaces (Clinoform A and Clinoform B, Fig 4.4b) due to their seismic significance with high amplitudes and good lateral continuity. Thereby, we separate the sediments below the MTDs of the Tuaheni Landslide Complex into seismic units A and B. The BSR crosscuts the sedimentary succession from ~10 to 13.5 km along profile (Fig. 4.4).

Between 9-13.2 km along profile and below the MTDs, the reflections are dissected by the previously described normal faults (compare Fig. 4.3). The normal faults cause small (< 0.019 s TWT; 15 m) vertical displacements of the reflections. About 70% of the normal faults dip landwards towards the NW (Fig. 4.4). Some of the normal faults exhibit high-amplitude fault plane reflections. In the upward direction within the region where MTD1 is absent, most normal faults can be traced to MTD 2, the shallowest of the Tuaheni Landslide Complex deposits. The chaotic facies of the mass transport deposit and the rugged seafloor morphology inside the 3D seismic volume complicate fault identification at shallow depths and at the seafloor (Fig. 4.4).

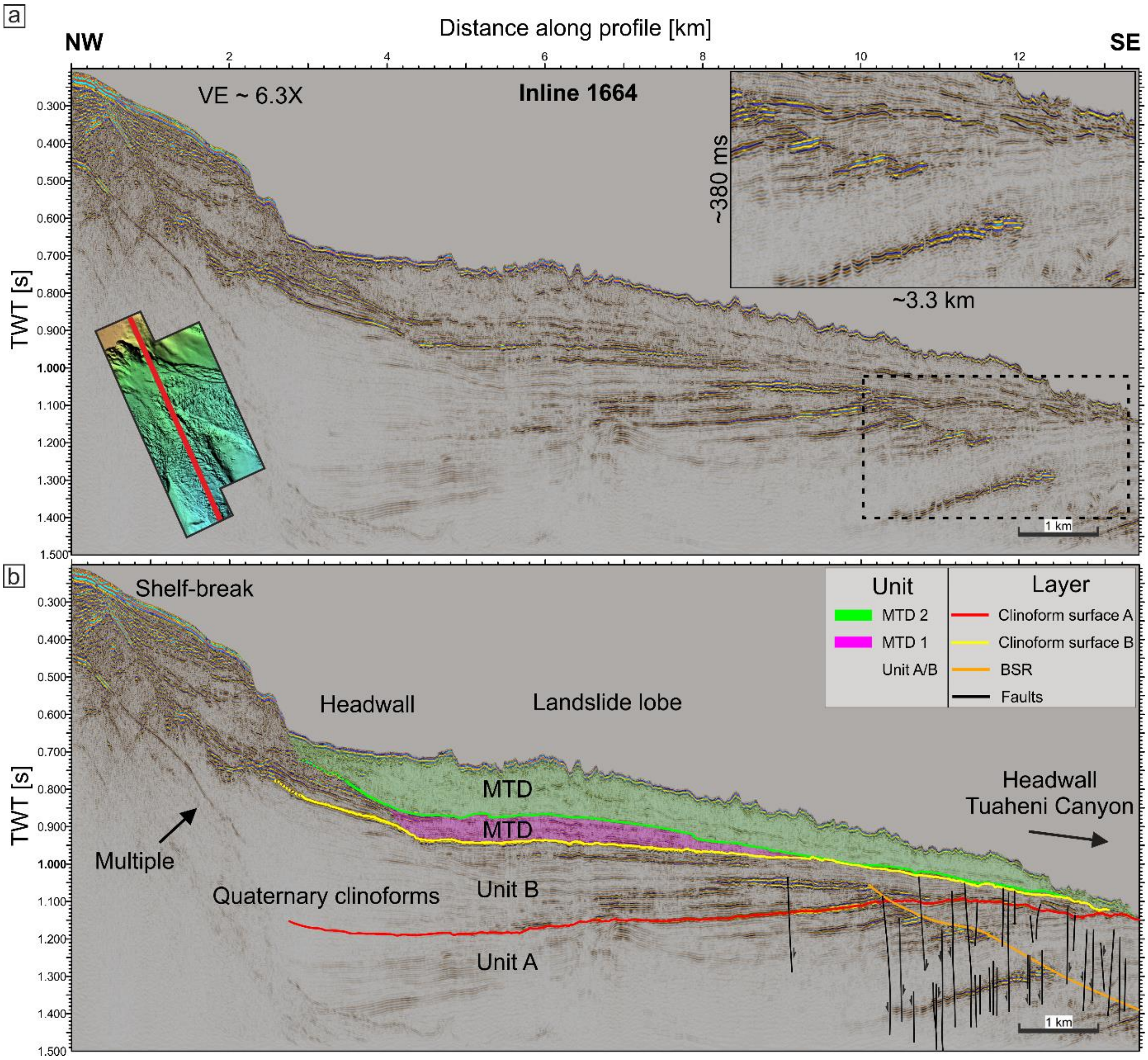

**Figure 4.4.** (a) Uninterpreted and (b) interpreted seismic reflection inline 1664 from the high-resolution 3D seismic volume SCHLIP3D. The left inset in (a) shows the location of the profile (red line) within the extent of 3D seismic coverage (note: the black box in Figure 4.1a shows the regional location of the 3D seismic survey). The right inset in (a) shows a zoom of the normal faults (from the region enclosed by the dashed box). The vertical exaggeration is ~6.3X at 1500 m/s.

### 4.4.3. Characteristics of the normal faults

We used the Symmetry I3D Energy seismic attribute and applied it to four horizons: the seafloor, the base of the most recent mass transport MTD 2, and clinoform surfaces A and B (Fig. 4.5). Consequently, we are able to derive fault parameters at different stratigraphic levels. The fault parameters include spatial distribution, strike direction, true dip angles, dip direction, vertical displacement and vertical extent of traceable fault planes. Our attribute analyses reveal sail-line induced seismic artifacts (Fig. 4.5). As the sail lines strike at a different angle than the normal faults, they do not interfere with our analysis.

Clinoforms A and B display a wide network of linear anomalies in the Symmetry I3D Energy with coherent low attribute values, which indicate amplitude variations attributed to faults or noise (Fig. 4.5). Because linear attribute anomalies can also be caused by noise in amplitude data, we cross-checked their locations with the locations of the low-displacement faults on vertical seismic displays (2D profiles) between 10-15 km along profile and 1.2-1.5 s TWT (Fig. 4.4). The comparison confirms that the linear attribute anomalies are all caused by vertical displacement along the faults. The faults exist within the 3D seismic volume from the southwestern to the northeastern edge over an area of about 30 km$^2$.

The base of MTD 2 shows fewer linear attribute anomalies with predominantly north and northeastern strike directions (Fig. 4.5). Cross-checking the seismic attributes with amplitude data on vertical displays confirms a decrease of traceable faults to this horizon (Fig. 4.4). At the seafloor, no linear attribute anomalies with the characteristic azimuth angles are observed (Fig. 4.5). We can conclude that either (a) the faults do not extend all the way to the seafloor, or (b) surficial deformation fabrics of the landslide system have overprinted any structural signal from active faulting.

The vast majority of the normal faults is interconnected and forms a network with arcuate (in plan view) fault plane shapes (Fig. 4.5). A minor group of faults is connected through small-scale fault triplets perpendicular to their planes (Fig. 4.5). Fault triplets are three en echelon faults with fault planes that intersect / connect at depth. Throughout the whole fault network, fault planes in juxtaposition show rhombic shaped subsided sections in between (Fig. 4.5). The normal faults occur at high angles with 75% of all mapped faults dipping greater than 80°. In combination, these observations indicate that normal faulting may include a transtensional component, since transtensional movement is typically accommodated on multiple steeply-dipping faults that intersect at depth (Woodcock and Fischer, 1986).

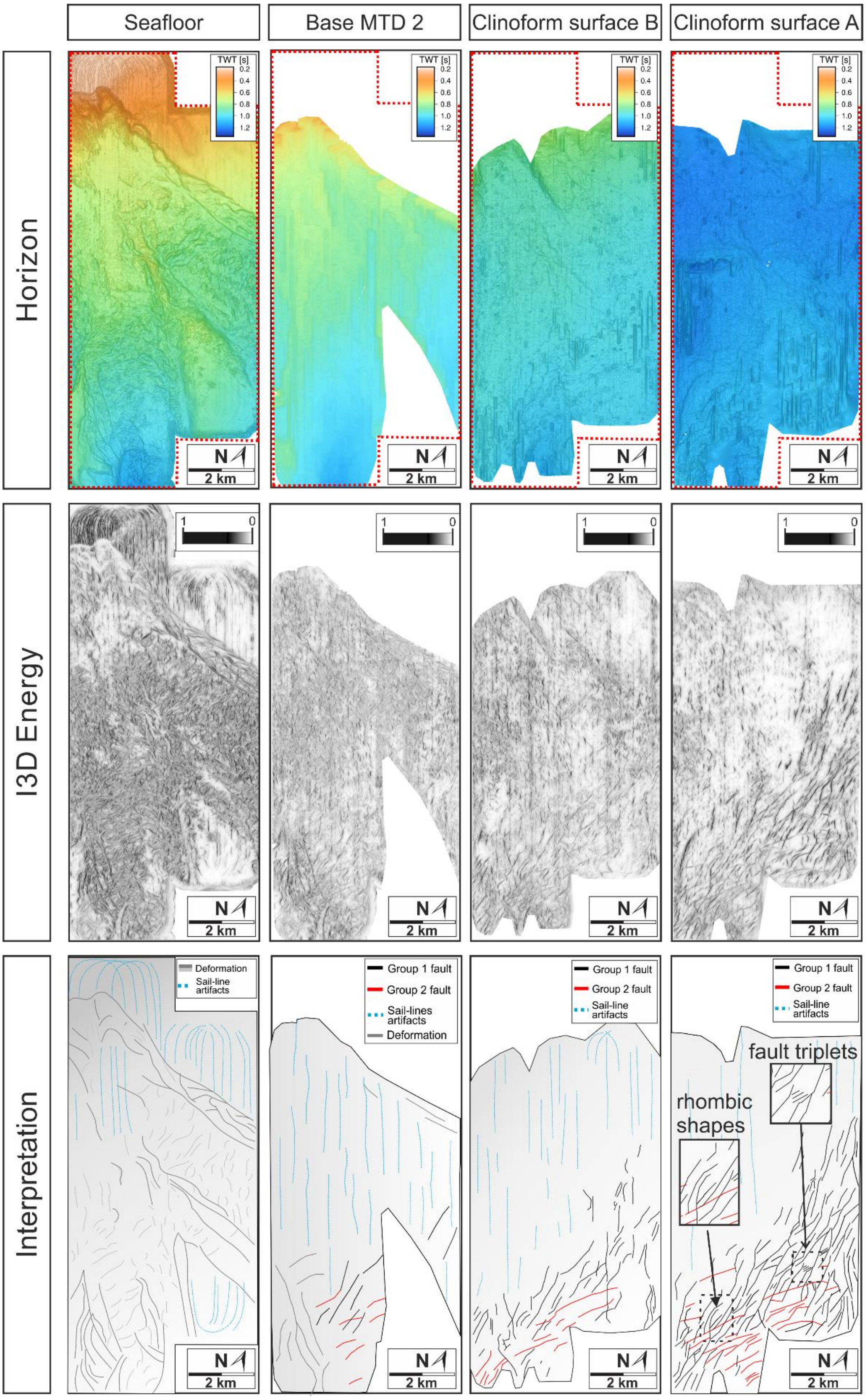

**Figure 4.5.** (Top) This row shows seismic horizons at stratigraphic surfaces (surfaces as labeled in Fig. 4.4b). The regional location of the seismic volume is shown in Fig. 4.1a. (Center) This row shows seismic horizon analysis with the I3D (Illuminator 3D) Energy attribute. (Bottom) Interpretation of seismic attribute maps on aforementioned horizons.

In total, we characterized 195 faults in terms of their spatial distribution, strike direction, dip angles, dip direction, vertical displacement and vertical extent of traceable fault planes (Fig. 4.6). The strike directions of the normal faults can be categorized into two groups. About 80% of the faults strike 350-15° and ~10% show an azimuth of 40-60°. The remaining 10% of the normal faults lie outside of the two major strike directions (Fig. 4.6). By extending the results from the 3D data onto 2D profiles, we observe a decrease in fault dip angle with decreasing distance from Tuaheni Ridge.

The decreasing seismic resolution of the 3D seismic volume towards the acoustic basement limits the measurable vertical fault length to a maximum of 0.15 s TWT (~120 m at 1600 m/s, Fig. 4.4). Vertical displacements are in the range of 4 - 15 m (Fig. 4.4) and derived horizontal displacements per unit length in the range of 0 - 3 m (Fig. 4.2). The analysis of fault dip direction shows that 70% of all faults dip landward, 20% dip seaward and 10% are near vertical (Fig. 4.6).

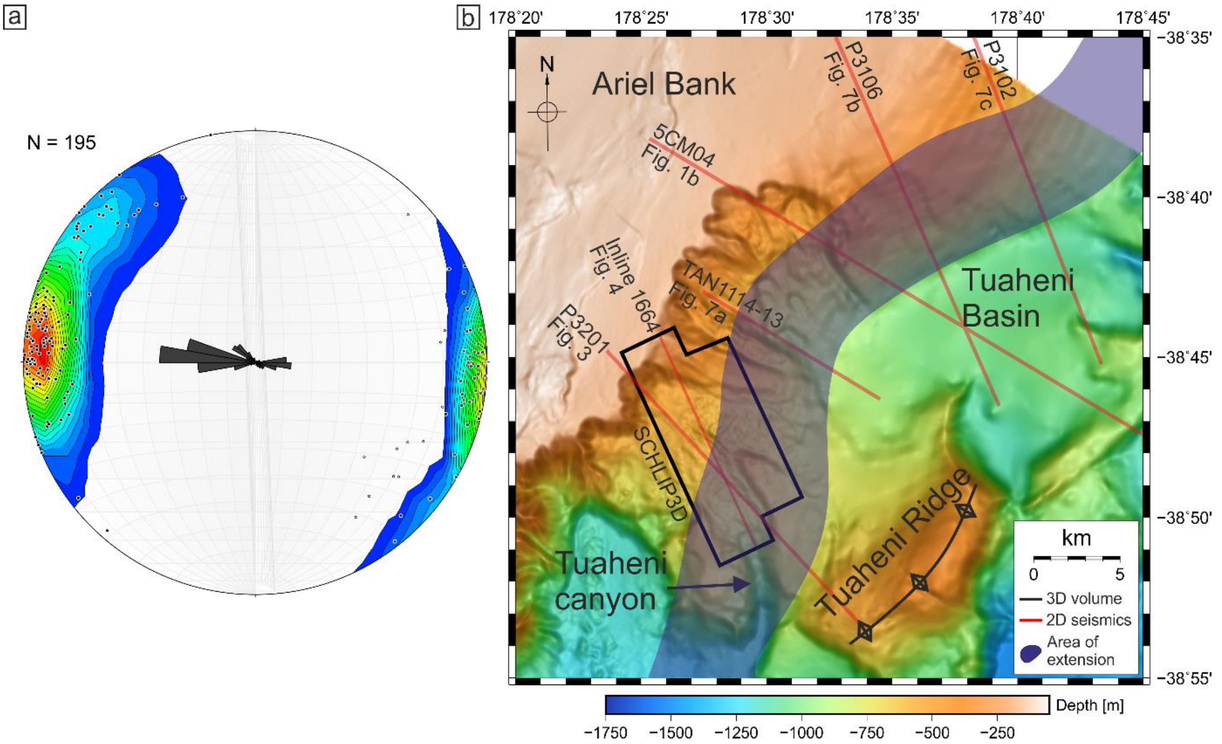

**Figure 4.6.** (a) Distribution of mapped normal faults on a stereographic projection (plotted with Stereonet software (Allmendinger et al., 2011; Cardozo & Allmendinger, 2013)). Rose diagram gives distribution of faults within a 10° range. The colored contour is an indicator for distribution over dip and azimuth. Two major strike directions are evident in the rose diagram: (40-60°) and (350-10°) – the latter being parallel to the deformation front and other active faults on the lower trench slope (Fig. 4.1). The majority of faults are dipping landward at very high angles (> 65°). (b) Bathymetric map showing locations of 2D (red lines) and 3D (black polygon) seismic data and the distribution of normal faults across the upper slope (semi-transparent blue region). The normal faults are confined between the shelf-break and the upper slope of Tuaheni Basin.

### 4.4.4. Regional extent of normal faulting

Upper-plate normal faults within the NE Hikurangi margin are not limited to the 3D seismic volume, but occur over a large area. 2D seismic profiles across the upper slope show widespread normal faulting within the upper 500 m of the sub-seafloor (Fig. 4.7). The presence of seafloor scarps overlying the seismically imaged fault planes (Fig. 4.7) indicates that, if not masked by mass-transport deposits (like in the area of the SCHLIP3D data), extensional deformation continues to the seafloor. With our spatially limited 2D seismic data, we are able to map normal faulting along the upper continental slope between 38°55’ S - 38°35’S (Fig. 4.6). In this area, the normal faults are abundant across the slope in between the shelf-break and the upper slope basins, confined to 500-1000 m water depth. These latitudes, however, only represent the minimum spatial extent of upper plate extension, and normal faulting may well continue farther along the margin.

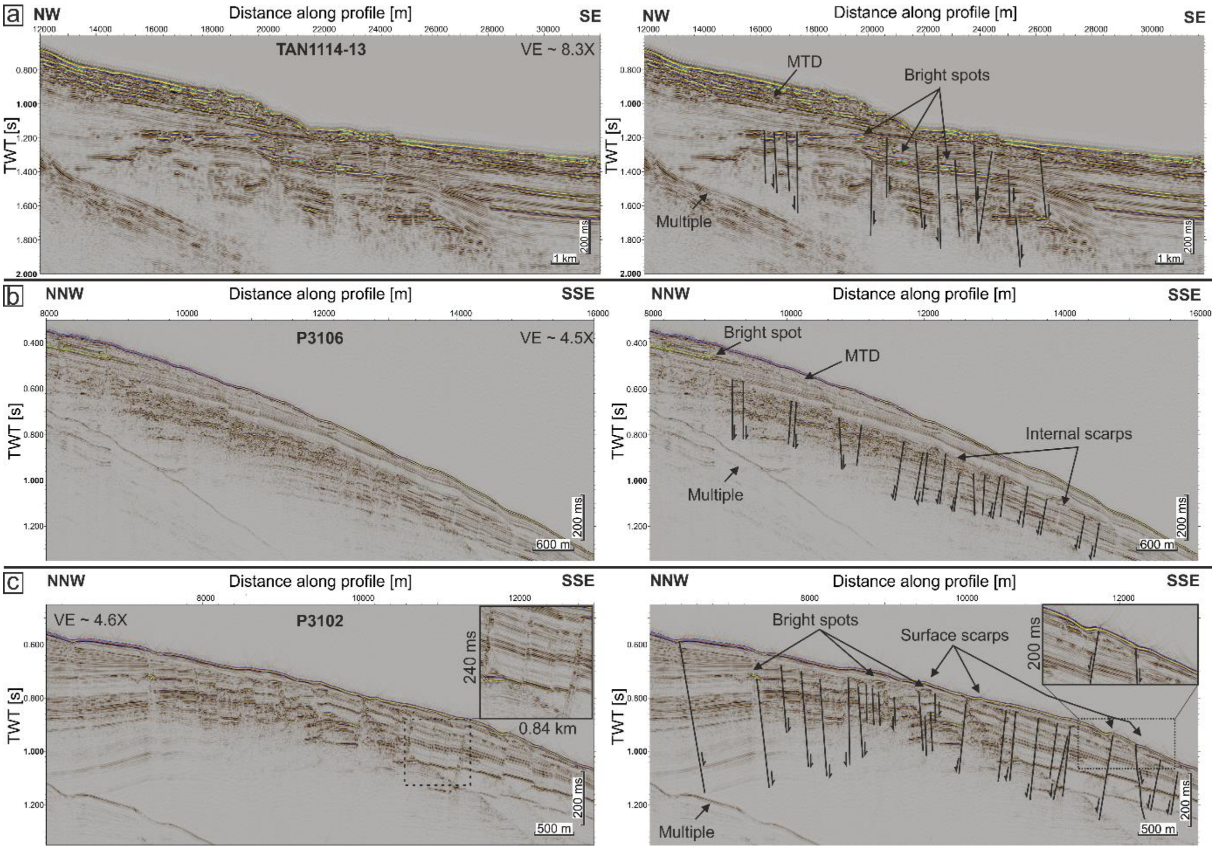

**Figure 4.7.** Uninterpreted and interpreted seismic profiles (a) TAN1114-13, (b) P3106 and (c) P3102 (locations on Figs. 4.1a, 4.6b). (a) Seismic profile TAN114-13 shows a mass transport deposit (MTD), normal faults and bright spots associated with the normal faults indicating the presence of fluids inside pore space. The vertical exaggeration is 8.3X at 1500 m/s. (b) Seismic profile P3106 showing a MTD and bright spots indicating fluid flow inside the sedimentary succession (after Micallef et al., 2016). The abundant normal faults show vertical displacement resulting in internal scarps. These scarps are overprinted by down-slope sedimentary processes. The vertical exaggeration is 4.5X at 1500 m/s. (c) Seismic profile P3102 showing prolonged normal faults with associated bright spots and high amplitude reflection fault planes (inset uninterpreted profile). Many normal faults cut the seafloor and form scarps. The inset on the interpreted profile emphasizes these surface scarps that indicate that there is recent/active normal faulting across the marine forearc of Hikurangi margin. The vertical exaggeration is 4.6X at 1500 m/s.

## 4.5. Discussion

Geodetic measurements (Wallace et al., 2004, 2012), the analysis of regional seismicity (Reyners and McGinty, 1999), and structural investigations (Cashman and Kelsey, 1990) have provided evidence for upper-plate extension within the terrestrial parts of the Central Hikurangi and Raukumara tectonic blocks of the North Island (Fig. 4.8). Our study area is located at the boundary between these two blocks and we are able to extend the analysis of upper-plate extension into the marine forearc.

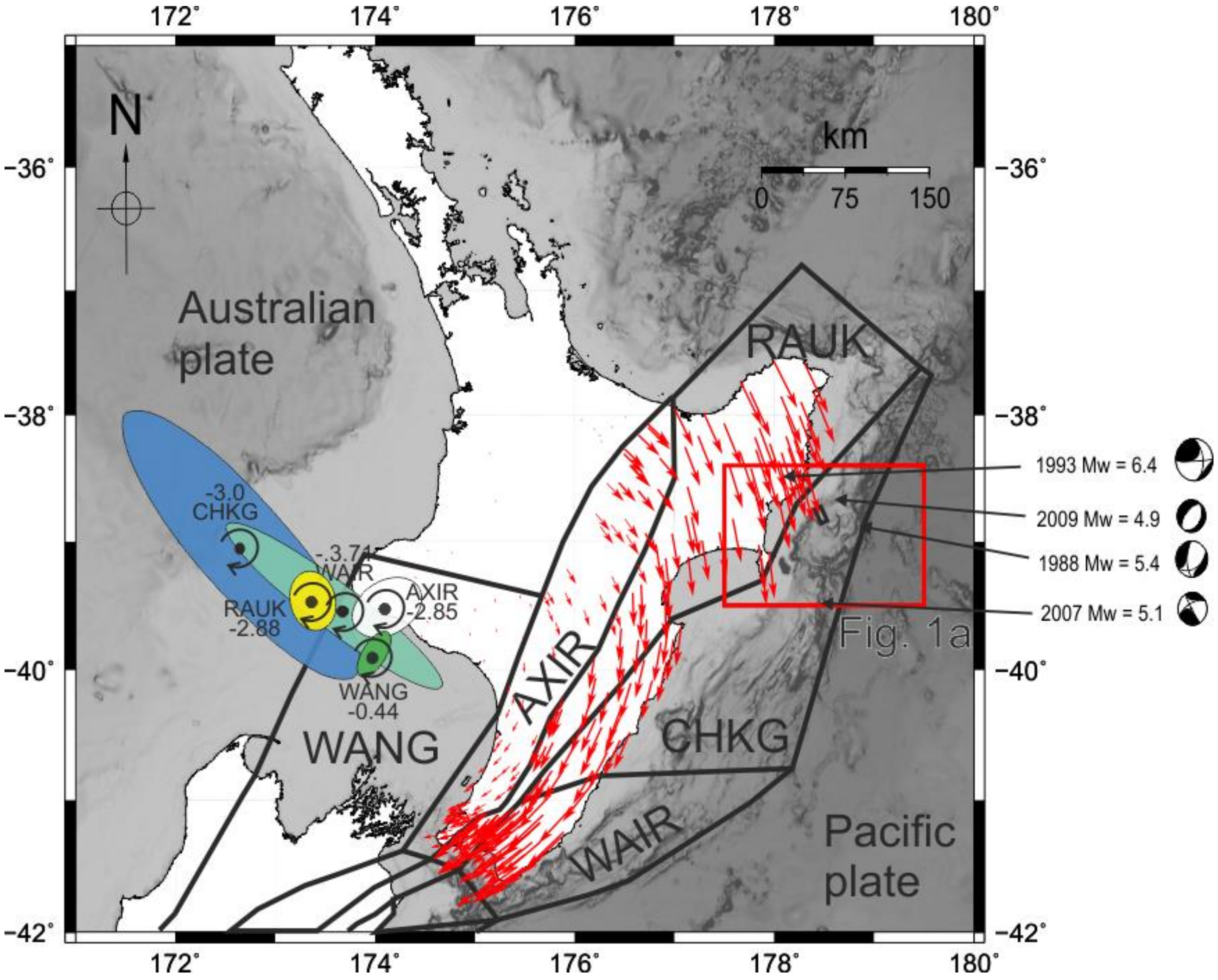

**Figure 4.8.** Bathymetric (GEBCO) map of the North Island and northwestern South Island of New Zealand with GPS velocity field (red arrows) and block model introduced by Wallace et al. (2004) with tectonic micro-blocks that rotate clockwise around nearby poles (modified after Nicol and Wallace, 2007; Wallace et al., 2004). All velocities are shown relative to the Australian Plate. Error ellipses are at 68% confidence level. The rotation rates are given in °/Myr with negative values for clockwise rotation. WAIR = Wairarapa block; AXIR = Axial Ranges block; RAUK = Raukumara block; CHKG = Central Hikurangi block; WANG = Wanganui block. Red square marks the bounds of our survey area (Fig. 4.1a). Focal mechanisms are taken from the global CMT catalog (Dziewonski et al., 1981; Ekström et al., 2012).

### 4.5.1. Decoupling and gravitational collapse of shallow strata

For other accretionary margins such as Cascadia and Nankai, upper-slope normal faulting has been suggested to result from decoupling of shallow strata from the underlying compressional wedge (Gulick et al., 2010; Moore et al., 2013; Sacks et al., 2013; McNeill et al., 1997). We compare the normal faults identified in our Hikurangi margin study area to the normal fault systems at Cascadia and Nankai.

Off Cascadia, listric normal faults occur in less than 1000 m water depth, detach to a relatively shallow crustal décollement, and dip seaward with hundreds of meters vertical displacements (McNeill et al., 1997). Normal faults at Cascadia margin may be associated with contemporaneous gravity sliding on mid-crustal layers or décollement surfaces (Buck and Sokoutis, 1994; Zoback et al., 1981) and suggest a decoupling of the shelf and upper slope from the subduction thrust (McNeill et al., 1997). Generally, the normal fault system, which we observe on this part of the Hikurangi margin, differs from what has been observed at the Cascadia margin offshore Grays Harbor, Washington, USA. We do not observe a predominantly seaward-dip for the faults, nor the large offsets, nor a listric character and shallow detachment.

The normal fault system in Nankai resembles many characteristics of the normal faults we observe in this study. In the Kumano Basin, Nankai Trough (Japan), normal faults show high dip angles, preferred landward dip, distinct groups of strike, and many of the faults cut the seafloor indicating recent activity (Gulick et al., 2010; Moore et al., 2013; Sacks et al., 2013). There, the normal faults have been mapped with a similar attribute-based seismic interpretation, and extension of the Kumano forearc basin is attributed to decoupling of shallow strata from the underlying thrust (Moore et al., 2013). Despite the structural similarities between the normal fault systems in the Hikurangi and the Nankai margins, there remain some arguments against a similar genetic origin. First, landward dipping thrust faulting in our study area continues to shallow strata (Figs. 4.1a, 4.3). This contradicts a possible decoupling of the latter from the underlying compressional wedge (Mountjoy and Barnes, 2011). Second, the normal faults form at the lower boundary of the upper slope, in regions of shallow inclined seafloor (Figs. 4.1a, 4.6). If these faults were an effect of compensatory movement due to uplift, we would expect them to occur predominantly in steeper areas farther downslope, where normal faults are absent (Figs. 4.1b, 4.3, 4.7). Such compensatory movement and subsequent extensional deformation have been observed at distinct anticlinal ridges farther South on the margin, where normal faults and fractures developed in response to flexural extension around the apex of folding (Barnes et al., 2010; Wang et al., 2017). Third, the normal faults in our study area show a clear landward dipping preference and no change in dip angle with depth (see Figs. 4.1b, 4.3, 4.4).

In summary, the seismic data from Hikurangi do not reveal any mid-crustal detachment, listric fault behavior or large displacement normal faults. We therefore conclude that decoupling of shallow strata from the underlying compressional wedge and related gravitational collapse of the upper plate is an unlikely mechanism for upper-plate extension on the northern Hikurangi margin.

### 4.5.2. Extension as a result of uplift

Active faults on the onshore Raukumara Peninsula are predominantly extensional structures that are responding to rapid landscape uplift and are not thought to play a significant role in crustal deformation (Berryman et al., 2009). Active extension is also mapped onshore in Hawke's Bay to the south of our study area (Cashman and Kelsey 1990). Uplift has been related to sediment underplating beneath the Raukumara range (Walcott, 1987; Eberhart-Phillips and Chadwick, 2002) and either margin tectonic deformation or underplating in the south. Bell et al. (2010) found a high-amplitude reflectivity zone (HRZ-2) in several multichannel seismic profiles beneath the offshore northern Hikurangi forearc. The location of this anomalous reflectivity results in an ambiguous interpretation of the plate interface thrust (Figs. 4.1b, 4.9b). One possible interpretation of HRZ-2 is that it represents sedimentary material that is underplated at the base of the upper plate (Fig. 4.9b). Pecher et al. (2014, 2017) invoke substantial uplift in the northern region of normal faulting as forming a pronounced double BSR at the base of gas hydrate stability. No clear indication of sediment underplating has been found for the offshore forearc.

A somewhat different driving mechanism for uplift may be the subduction of excess topography (Fig. 4.9b). There is ample evidence that the subduction of seamounts or basement ridges increase the structural complexity of a margin (Bangs et al., 2006; Geersen et al., 2015; Gulick et al., 2004; Kodaira et al. 2000; Park et al., 2003; Ranero and von Huene, 2000; Wang and Bilek, 2011). Usually, the process of seamount subduction results in severe fracturing of the overriding plate above and around the subducting seamount (Dominguez et al., 1998; Wang and Bilek, 2011). The track of the subducting seamount is recorded in the deformation pattern of the upper plate (Dominguez et al., 1998). Above the seamount, arcuate thrust faults, sub-vertical fan-shaped fracture networks, and strike-slip faults develop which usually crosscut each other. In addition, normal faults, which show no consistent strike direction, form due to collapse of the upper-plate in the wake of the subducting seamount (Dominguez et al., 1998; Wang and Bilek, 2011).

At multiple locations within the Hikurangi margin, subducting seamounts are known to have caused localized uplift, out of sequence faulting and large-scale mass failure (Barnes et al., 2010; Pedley et al., 2010). These deformation patterns are for example observed at the Poverty Bay indentation, which is located ~25 km southwest of our study area. Here, seamount subduction initiated during the past ~ 2 Ma leads to a gravitational collapse of the upper plate in the wake of the seamount (Pedley et al., 2010; Wang and Bilek, 2011). In the area of our study, a subducting seamount is interpreted under the mid-slope area between 18 – 54 km along seismic line 05CM-04 (Fig. 4.1b) (Bell et al., 2010) which may lead to uplift and hence cause extension of the upper plate (Fig. 4.9b). The documented normal fault system is, however, located between 450 – 1200 m water depths on the landward side of the subducting seamount.

It further shows a clear preference for landward dip and the majority of faults have a margin parallel strike (Figs. 4.4, 4.5, 4.6, 4.7). As such, our structural observations do not completely agree with observed and modeled deformation patterns caused by subducting seamounts at accretionary margins elsewhere (Dominguez et al. 1998; Ranero and von Huene, 2000; Ruh et al., 2016). This does not rule out the possibility that seamount subduction induces regional uplift inducing extensional deformation at the upper slope. However, the structural discrepancies indicate that other processes that could also drive upper-plate extension may be active at the same time.

Regardless of a driving mechanism for uplift (underplating and seamount subduction are two possible mechanisms), a manifestation of upper-plate folding in the vicinity of the normal faults can be observed on Line 05CM-04, where subtle bending of upper-plate strata is seen (Fig. 4.1b). As such, we consider flexural extension near the apex of folding (Fig. 4.9b) as a mechanism that could lead to the extension in the areas where we have mapped the normal faults (Fig. 4.6b). Flexural extension and normal faulting around the apex of folding is well known from other parts of the Hikurangi margin (Barnes et al., 2010; Wang et al., 2017), as well as on other convergent margins (e.g. López et al., 2010).

### 4.5.3. Extension as a result of positive Coulomb stress increase

The 2010 Chile (Mw. 8.8) and 2011 Japan (Mw. 9.0) earthquakes where accompanied by large-magnitude (~Mw=7.0) extensional aftershocks that nucleated on upper-plate normal faults above the seismogenic zone (Farías et al., 2011; Toda et al., 2011). In both cases, subsequent studies confirmed that the extensional aftershocks, which first took the scientific community by surprise, were related to the subduction process and the regional earthquake cycle (compare Fig. 4.9a). For the 2010 Maule earthquake, different authors suggested that a positive Coulomb stress change induced into the upper-plate by rupture of the underlying plate-boundary triggered normal faulting in some parts of the marine forearc (Fig. 4.9a) (Aron et al., 2013; Farias et al., 2011; Geersen et al., 2016). The same process was likely responsible for upper-plate normal faulting in the wake of the 2011 Japan earthquake (Toda et al., 2011). In both cases, upper-plate normal faulting was possibly driven by dynamic weakening of the plate-boundary, which moved the forearc into a critical extensional stress-regime during the co-seismic phase, likely further contributing to upper-plate normal faulting (Cubas et al., 2013a, 2013b).

To evaluate our mapped normal faults in the context of seismic rupture during a large megathrust earthquake we need to consider the subduction interface in terms of fault behavior. The normal faults are located on the upper slope above a region of low interseismic coupling (ϕic < 0.5) of the plate-interface (Wallace et al., 2009). The region has hosted two moderate magnitude tsunami earthquakes (Mw ~7.0) in 1947 as well as a series of slow-slip events in recent years (Doser and Webb, 2003; Wallace et al., 2016). However, no large (> Mw 8) plate-boundary earthquake which may have caused permanent extensional deformation of the upper-plate, as it happened during the 2010 Chile and 2011 Japan events, has yet been recorded in the area of the normal faults (Doser and Webb, 2003). While the potential for large megathrust earthquakes in the region remains an outstanding research question, our current knowledge on the seismo-tectonic setting makes it questionable whether the mapped pervasive extensional deformation of the upper-plate solely relates to large plate-boundary earthquakes.

### 4.5.4. Extension as a result of clockwise rotation of the Hikurangi forearc

Our analysis shows that aspects of the structural character of the normal fault system in the Hikurangi margin differs from forearc normal fault systems reported from other accretionary margins such as Nankai or Cascadia. In combination with differences in the large scale tectonic setting of the upper-plate (e.g. continuation of thrust faulting to shallow strata), we conclude that the origin of the normal faults in the Hikurangi margin may require a new explanation. Below, we consider whether stress and strain domains identified in geodetic modelling may contribute to normal faulting at the northeastern Hikurangi margin.

#### 4.5.4.1. Tectonic block rotation as an alternative model to explain upper-plate extension

Oblique convergence, as it is the case in most active margins, usually results in strain partitioning within the forearc and/or the volcanic arc (Fitch, 1972; Teyssier et al., 1995). In some subduction zones, the oblique component is accommodated along prominent crustal-scale strike-slip faults, which extend parallel to the trench and the coastline over hundreds to thousands of kilometers. Prominent examples for such faults are the Liquiñe-Ofqui fault in Central and Southern Chile (Hervé, 1994;) or the Mentawai Fault Zone off Sumatra (Diament et al., 1992). In other subduction settings, oblique convergence causes the development of individual tectonic blocks, which rotate around nearby poles (e.g. Cascadia, Marianas, Vanuatu, and Papua New Guinea) (Calmant et al., 2003; McCaffrey et al., 2000; Kato et al., 2003; Wallace et al., 2004).

Off northeastern New Zealand, oblique convergence of the Pacific Plate in combination with an overall decrease in convergence rate towards the south results in clockwise rotation of North Island crustal blocks around poles lying to the west of the North Island (Fig. 4.8) (Mumme et al., 1989; Walcott, 1984; Wallace et al., 2004). Geodetic measurements, earthquake slip vectors, and geological fault slip rates have been used to estimate the angular velocities of the tectonic blocks and the degree of coupling along the faults, which separate the different blocks (Wallace et al., 2004). In some parts of the marine forearc, block rotation is expected to result in extensional differential stresses. Although most of the extensional budget resulting from the rotation can be explained by slip on normal faults within the Taupo volcanic zone, minor positive residual strain ($1\text{-}35 * 10^{-9}$) is calculated for the eastern North Island forearc blocks (Wallace et al., 2004). For scale, a strain rate of $20 * 10^{-9}$ for the Wairarapa block (50 km wide) causes 1 mm $yr^{-1}$ differential slip rate. Wallace et al. (2004) suggest that the residual strain might be released by slip on previously unrecognized extensional faults along the block boundaries. However, widespread upper-plate extension had not been observed previously for the northeastern and central marine forearc of the Hikurangi margin.

The upper-plate normal faults we have identified in the study area beneath the upper continental slope may represent a fault system that accommodates such residual strain. From their location and spatial distribution, the normal faults would accommodate extensional stresses between the Raukumara and the Central Hikurangi blocks (Figs. 4.8, 4.9c).

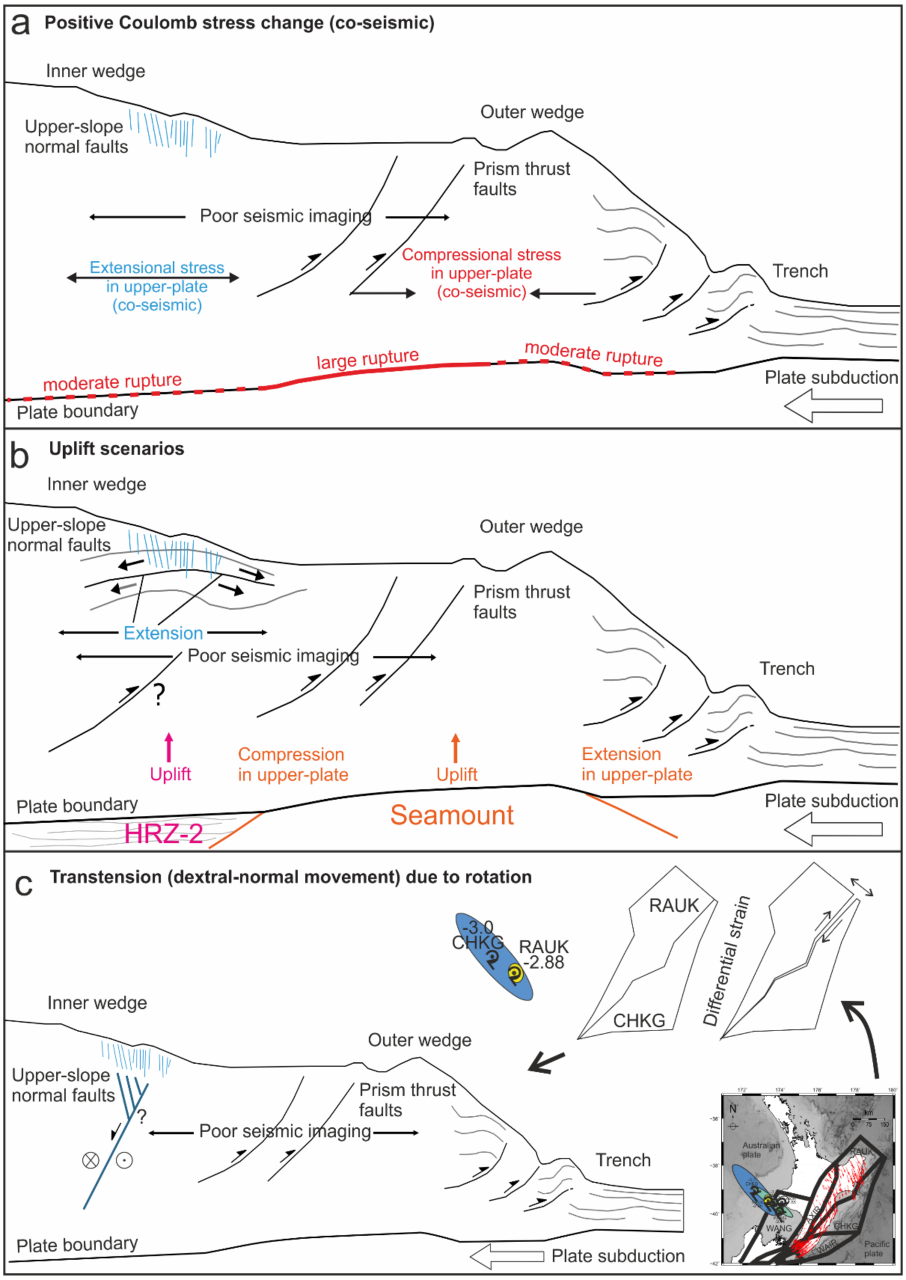

**Figure 4.9.** Conceptual models of the Hikurangi margin and mechanisms for marine forearc extension: (a) Positive Coulomb stress increase induced into the upper plate during the co-seismic phase of earthquakes (after Aron et al., 2013; Farías et al., 2011; Geersen et al., 2016; Toda et al., 2011). (b) Regional uplift due to underplating (magenta arrow) (Cashman and Kelsey, 1990; Bell et al., 2010) or seamount subduction (orange arrow) (after Dominguez et al., 1998; Wang and Bilek, 2011). Also shown is flexural extension around the apex of long-wavelength folding within the upper part of the wedge. (c) Transtension (dextral-normal movement) accommodated in the upper-plate, induced into the marine forearc by residual extensional strain by differential clockwise rotation of Raukumara and Central Hikurangi micro-tectonic blocks around nearby poles (modified after Nicol and Wallace, 2007; Wallace et al., 2004).

### 4.5.4.2. Application to the northeastern Hikurangi margin

Mountjoy et al. (2009) describe the shallow sedimentary succession in the study area as Quaternary low-stand clinoforms with Holocene sediments above (Figs. 4.1b, 4.3, 4.4). Profile 05CM04 (Fig. 4.1b) suggests that the normal faults are confined to this section. Assuming a maximum age for the quaternary clinoforms of 0.4 Ma or younger (Mountjoy and Barnes, 2011) in combination with the minor positive residual strain of 1-35*$10^{-9}$ (Wallace et al., 2004), the maximum dilatation of the crustal block would cumulate to ~400 m of extension. The 195 faults within the 3D seismic volume cumulate to a total horizontal displacement of approximately 120 m. However, the 3D seismic volume does not cover the full spatial extent of the normal faults in the across slope direction. Based on 2D seismic line P3201, we estimate that our 3D seismic volume covers approximately two thirds of the whole fault network and use this line (Line P3201) to extrapolate the total horizontal displacement. We estimate that the fault network could account for about 180 m of total horizontal displacement. The normal fault network thus covers bulk extension within the same order of magnitude as proposed by the modelled block-rotation (Wallace et al., 2004).

In 2009, an extensional earthquake (Mw 4.9) with a minor strike-slip component took place within the upper-plate in the area of this study (Fig. 4.1a, 4.8). The en echelon normal faults we image in this study enclose rhombic shaped subsided areas, show high dip angles (75% > 80°) and are interconnected by small-scale fault triplets (Figs. 4.5, 4.6). These observations indicate duplex structures in the subsurface and hence a transtensional (dextral-normal) character of the fault network (Woodcock and Fischer, 1986). Together with the 2009 earthquake, this lends support to the hypothesis that the differential stresses between the Central Hikurangi and the Raukumara tectonic blocks may have contributed to development of normal faults in the marine forearc of the northeastern Hikurangi margin (Figs. 4.8, 4.9c).

These indications are consistent with observations in Crete, Greece, where transtension in the Hellenic forearc forms sinistral-normal faults with distinct azimuth groups because of rotation (Ten Veen and Kleinspehn, 2003). Similar to our indications for transtension (though dextral in our case), the sinistral-normal deformation in Crete is inferred from en echelon rhombic depressions and ridges (Huchon et al., 1982; Huguen et al., 2001). This proposed model (Fig. 4.9c) agrees with local observations farther south within the Central Hikurangi block, where shear structures form in combination with proto-thrusts and extensional faults at Omakere Ridge (Plaza-Faverola et al., 2014).

## 4.6. Conclusions and outlook

Our study documents extension within the marine forearc of the Hikurangi margin based on 2D and 3D seismic data. We map and analyze normal faults with low vertical displacements over an along-margin distance of at least 50 km. These faults occur between the shelf-break and the upper slope basins, and are confined to 500-1000 m water depth. We draw the following main conclusions:

(1) The normal faults at the upper slope of the Hikurangi margin show two major strike directions, primarily landward dip, and steep fault angles. Where mass transport deposits are absent, seafloor scarps indicate recent fault activity. The normal faults are interconnected, e.g. by small-scale fault triplets, enclose rhombic-shaped subsided sections and the majority dips at angles > 80 deg. These observations suggest transtensional deformation.

(2) Mechanisms that may have contributed to the development of the normal faults in the Hikurangi margin include uplift and gravitational collapse and/or flexural bending of the upper-plate and residual extensional strain, which is induced into the marine forearc by rotation of tectonic blocks around nearby poles.

The block rotation model agrees with the transtensional character of the normal faults. However, the limited spatial (and depth) extent of our seismic data does not allow us to ultimately resolve the dominant tectonic process behind the generation of the normal faults. As in any complex geologic system, the interplay of different processes may be responsible for causing marine forearc extension in the northeastern Hikurangi margin.

Our work adds another piece of evidence that normal faults play an important role in the seismo-tectonic evolution of accretionary margins. However, a better understanding of the mechanisms that cause upper-plate extension in the different place remains a research challenge. Large-scale 3D seismic experiments and scientific drilling may provide critical data to further investigate the driving mechanisms behind forearc normal faulting.

**Acknowledgments and Data**

The collection and processing of the P-Cable 3D volume and 2D data was jointly funded by the New Zealand Ministry for Business Innovation and Employment (MBIE), NIWA and GNS Science Core funding and the Deutsche Forschungsgemeinschaft (DFG-Grant BI 404/7 | KR 2222/18). Jacob Geersen was funded by a grant (CP1404) of the Cluster of Excellence 80 “The Future Ocean”. The Future Ocean is funded within the framework of the Excellence Initiative by the Deutsche Forschungsgemeinschaft (DFG) on behalf of the German federal and state governments. We thank the officers and crew of RV Tangaroa and all the shipboard participants who made the data collection possible. Line TAN114-13 was collected on voyage TAN1114 led by Philip Barnes and funded by MBIE through OS2020 and NIWA and GNS Science SSIF funding. Stuart Henrys processed the TAN1114 seismic data on board. Line 05CM-04 was collected by Crown Minerals for the New Zealand Government (https://www.nzpam.govt.nz/maps-geoscience/). Access to the bathymetric and seismic data is through NIWA marine data repository (https://marinedata.niwa.co.nz/project-map-sam/). The corresponding author would like to thank Christian Berndt for his support during the process of writing this manuscript. We thank IHS for providing the Kingdom software through their University Grant Program.

## References

Allmendinger, R. W., Cardozo, N., & Fisher, D. M. (2011). Structural geology algorithms: Vectors and tensors. Cambridge University Press.

Alexander, C. R., J. P. Walsh, and A. R. Orpin (2010). Modern sediment dispersal and accumulation on the outer Poverty continental margin, *Marine Geology*, 270(1-4), 213–226, doi:10.1016/j.margeo.2009.10.015.

Aron, F., Allmendinger, R. W., Cembrano, J., González, G., and Yáñez, G. (2013). Permanent fore-arc extension and seismic segmentation: Insights from the 2010 Maule earthquake, Chile. *Journal of Geophysical Research: Solid Earth*, 118(2), 724-739.

Asano, Y., Saito, T., Ito, Y., Shiomi, K., Hirose, H., Matsumoto, T., ... and Sekiguchi, S. (2011). Spatial distribution and focal mechanisms of aftershocks of the 2011 off the Pacific coast of Tohoku Earthquake. *Earth, planets and space*, 63(7), 29.

Bahorich, M., and Farmer, S. (1995). 3-D seismic discontinuity for faults and stratigraphic features: The coherence cube. *The leading edge*, 14(10), 1053-1058.

Bangs, N. L., Gulick, S. P., and Shipley, T. H. (2006). Seamount subduction erosion in the Nankai Trough and its potential impact on the seismogenic zone. *Geology*, 34(8), 701-704.

Barker, D. H., Sutherland, R., Henrys, S., and Bannister, S. (2009). Geometry of the Hikurangi subduction thrust and upper plate, North Island, New Zealand. *Geochemistry, Geophysics, Geosystems*, 10(2).

Barnes, P. M., Cheung, K. C., Smits, A. P., Almagor, G., Read, S. A., Barker, P. R., & Froggatt, P. (1991). Geotechnical analysis of the Kidnappers Slide, upper continental slope, New Zealand. *Marine Georesources & Geotechnology*, *10*(1-2), 159-188.

Barnes, P. M., et al. (2011). National Institute of Water and Atmospheric Research (NIWA) Voyage Report, Ocean 2020 Northern Hikurangi Margin Geohazards, RV Tangaroa Rep. Tan1114, NIWA, Wellington, New Zealand.

Barnes, P. M., Lamarche, G., Bialas, J., Henrys, S., Pecher, I., Netzeband, G. L., ... and Crutchley, G. (2010). Tectonic and geological framework for gas hydrates and cold seeps on the Hikurangi subduction margin, New Zealand. *Marine Geology*, 272(1), 26-48.

Barnes, P. M., Nicol, A., and Harrison, T. (2002). Late Cenozoic evolution and earthquake potential of an active listric thrust complex above the Hikurangi subduction zone, New Zealand. *Geological Society of America Bulletin*, 114(11), 1379-1405.

Beanland, S., and Haines, J. (1998). The kinematics of active deformation in the North Island, New Zealand, determined from geological strain rates. *New Zealand Journal of Geology and Geophysics*, 41(4), 311-323.

Beavan, J., Tregoning, P., Bevis, M., Kato, T., and Meertens, C. (2002). Motion and rigidity of the Pacific Plate and implications for plate boundary deformation. *Journal of Geophysical Research: Solid Earth*, 107(B10).

Bell, R., Holden, C., Power, W., Wang, X., and Downes, G. (2014). Hikurangi margin tsunami earthquake generated by slow seismic rupture over a subducted seamount. *Earth and Planetary Science Letters*, *397*, 1-9.

Bell, R., Sutherland, R., Barker, D. H., Henrys, S., Bannister, S., Wallace, L., and Beavan, J. (2010). Seismic reflection character of the Hikurangi subduction interface, New Zealand, in the region of repeated Gisborne slow slip events. *Geophysical Journal International*, 180(1), 34-48.

Berryman, K., Marden, M., Palmer, A., & Litchfield, N. (2009). Holocene rupture of the Repongaere Fault, Gisborne: implications for Raukumara Peninsula deformation and impact on the Waipaoa Sedimentary System. *New Zealand Journal of Geology and Geophysics*, *52*(4), 335-347.

Berryman, K. R., Ota, Y., and Hull, A. G. (1989). Holocene paleoseismicity in the fold and thrust belt of the Hikurangi subduction zone, eastern North Island, New Zealand. *Tectonophysics*, *163*(3-4), 185-195.

Buck, W. R., and Sokoutis, D. (1994). Analogue model of gravitational collapse and surface extension during continental convergence. *Nature*, *369*(6483), 737-740.

Calmant, S., Pelletier, B., Lebellegard, P., Bevis, M., Taylor, F. W., and Phillips, D. A. (2003). New insights on the tectonics along the New Hebrides subduction zone based on GPS results. *Journal of Geophysical Research: Solid Earth*, *108*(B6).

Cardozo, N., & Allmendinger, R. W. (2013). Spherical projections with OSXStereonet. Computers & Geosciences, 51, 193-205.

Cashman, S. M., and Kelsey, H. M. (1990). Forearc uplift and extension, southern Hawke's Bay, New Zealand: Mid-Pleistocene to present. *Tectonics*, *9*(1), 23-44.

Catuneanu, O., Abreu, V., Bhattacharya, J. P., Blum, M. D., Dalrymple, R. W., Eriksson, P. G., ... & Giles, K. A. (2009). Towards the standardization of sequence stratigraphy. Earth-Science Reviews, 92(1-2), 1-33.

Conly, G. (1980). *The Shock of'31: The Hawke's Bay Earthquake*. Wellington. A.H. and A.W. Reed Ltd.

Cubas, N., Avouac, J. P., Leroy, Y. M., and Pons, A. (2013a). Low friction along the high slip patch of the 2011 Mw 9.0 Tohoku-Oki earthquake required from the wedge structure and extensional splay faults. *Geophysical Research Letters*, *40*(16), 4231-4237.

Cubas, N., Avouac, J. P., Souloumiac, P., & Leroy, Y. (2013b). Megathrust friction determined from mechanical analysis of the forearc in the Maule earthquake area. Earth and Planetary Science Letters, 381, 92-103.

Davy, B., and Wood, R. (1994). Gravity and magnetic modelling of the Hikurangi Plateau. *Marine geology*, *118*(1-2), 139-151.

De Lange, W. P., and Healy, T. R. (1986). New Zealand tsunamis 1840–1982. *New Zealand Journal of Geology and Geophysics*, *29*(1), 115-134.

Diament, M., Harjono, H., Karta, K., Deplus, C., Dahrin, D., Zen, M. T., ... and Malod, J. (1992). Mentawai fault zone off Sumatra: A new key to the geodynamics of western Indonesia. *Geology*, *20*(3), 259-262.

Dominguez, S., Lallemand, S. E., Malavieille, J., and von Huene, R. (1998). Upper plate deformation associated with seamount subduction. *Tectonophysics*, *293*(3), 207-224.

Doser, D. I., & Webb, T. H. (2003). Source parameters of large historical (1917–1961) earthquakes, North Island, New Zealand. *Geophysical Journal International*, *152*(3), 795-832.

Dziewonski, A. M., Chou, T. A., and Woodhouse, J. H. (1981). Determination of earthquake source parameters from waveform data for studies of global and regional seismicity. *Journal of Geophysical Research: Solid Earth*, 86(B4), 2825-2852.

Eberhart-Phillips, D., and Chadwick, M. (2002). Three-dimensional attenuation model of the shallow Hikurangi subduction zone in the Raukumara Peninsula, New Zealand. *Journal of Geophysical Research: Solid Earth*, *107*(B2).

Ekström, G., Nettles, M., and Dziewoński, A. M. (2012). The global CMT project 2004–2010: Centroid-moment tensors for 13,017 earthquakes. *Physics of the Earth and Planetary Interiors*, 200, 1-9.

Farías, M., Comte, D., Roecker, S., Carrizo, D., and Pardo, M. (2011). Crustal extensional faulting triggered by the 2010 Chilean earthquake: The Pichilemu Seismic Sequence. *Tectonics*, *30*(6).

Field, B. D., and Uruski, C. I. (1997). *Cretaceous-Cenozoic geology and petroleum systems of the East Coast region, New Zealand* (Vol. 1). Institute of Geological and Nuclear Sciences.

Fitch, T. J. (1972). Plate convergence, transcurrent faults, and internal deformation adjacent to southeast Asia and the western Pacific. *Journal of Geophysical research*, *77*(23), 4432-4460.

Fraser, R. J. (1998). *Historical tsunami database for New Zealand* (Doctoral dissertation, University of Waikato).

Geersen, J., Behrmann, J. H., Völker, D., Krastel, S., Ranero, C. R., Diaz-Naveas, J., and Weinrebe, W. (2011). Active tectonics of the South Chilean marine fore arc (35 S–40 S). *Tectonics*, *30*(3).

Geersen, J., Ranero, C. R., Barckhausen, U., and Reichert, C. (2015). Subducting seamounts control interplate coupling and seismic rupture in the 2014 Iquique earthquake area. *Nature communications*, *6*.

Geersen, J., Scholz, F., Linke, P., Schmidt, M., Lange, D., Behrmann, J. H., ... & Hensen, C. (2016). Fault zone controlled seafloor methane seepage in the rupture area of the 2010 Maule earthquake, Central Chile. Geochemistry, Geophysics, Geosystems, 17(11), 4802-4813.

Grando, G., and McClay, K. (2007). Morphotectonics domains and structural styles in the Makran accretionary prism, offshore Iran. *Sedimentary Geology*, *196*(1), 157-179.

Gulick, S. P. S., Bangs, N. L. B., Shipley, T. H., Nakamura, Y., Moore, G., and Kuramoto, S. (2004). Three-dimensional architecture of the Nankai accretionary prism's imbricate thrust zone off Cape Muroto, Japan: Prism reconstruction via en echelon thrust propagation. *Journal of Geophysical Research: Solid Earth*, *109*(B2).

Gulick, S. P., Bangs, N. L., Moore, G. F., Ashi, J., Martin, K. M., Sawyer, D. S., ... and Taira, A. (2010). Rapid forearc basin uplift and megasplay fault development from 3D seismic images of Nankai Margin off Kii Peninsula, Japan. *Earth and Planetary Science Letters*, *300*(1), 55-62.

Hervé, F. (1994). The southern Andes between 39 and 44 S latitude: the geological signature of a transpressive tectonic regime related to a magmatic arc. In *Tectonics of the Southern Central Andes* (pp. 243-248). Springer Berlin Heidelberg.

Huchon, P., Lybéris, N., Angelier, J., Le Pichon, X., and Renard, V. (1982). Tectonics of the Hellenic Trench: a synthesis of Sea-Beam and submersible observations. *Tectonophysics*, *86*(1-3), 69767880828486889092949698100102-74112.

Huguen, C., Mascle, J., Chaumillon, E., Woodside, J. M., Benkhelil, J., Kopf, A., and Volkonskaïa, A. (2001). Deformational styles of the eastern Mediterranean Ridge and surroundings from combined swath mapping and seismic reflection profiling. *Tectonophysics*, *343*(1), 21-47.

Ide, S., Baltay, A., and Beroza, G. C. (2011). Shallow dynamic overshoot and energetic deep rupture in the 2011 Mw 9.0 Tohoku-Oki earthquake. *Science*, *332*(6036), 1426-1429.

Kato, T., Beavan, J., Matsushima, T., Kotake, Y., Camacho, J. T., and Nakao, S. (2003). Geodetic evidence of back-arc spreading in the Mariana Trough. *Geophysical Research Letters*, *30*(12).

Kukowski, N., Greinert, J., & Henrys, S. (2010). Morphometric and critical taper analysis of the Rock Garden region, Hikurangi Margin, New Zealand: Implications for slope stability and potential tsunami generation. Marine Geology, 272(1), 141-153.

Kodaira, S., Takahashi, N., Nakanishi, A., Miura, S., and Kaneda, Y. (2000). Subducted seamount imaged in the rupture zone of the 1946 Nankaido earthquake. *Science*, *289*(5476), 104-106.

López, C., Spence, G., Hyndman, R., & Kelley, D. (2010). Frontal ridge slope failure at the northern Cascadia margin: Margin-normal fault and gas hydrate control. Geology, 38(11), 967-970.

Masson, D. G., Parson, L. M., Milsom, J., Nichols, G., Sikumbang, N., Dwiyanto, B., and Kallagher, H. (1990). Subduction of seamounts at the Java Trench: a view with long-range sidescan sonar. *Tectonophysics*, *185*(1-2), 51-65.

Mazengarb, C. (1984). The Fernside Fault: an active normal fault, Raukumara Peninsula, New Zealand. *New Zealand Geological Survey Record*, *3*, 98-103.

McCaffrey, R. (2002). Crustal block rotations and plate coupling. *Plate boundary zones*, 101-122.

McCaffrey, R., Long, M. D., Goldfinger, C., Zwick, P. C., Nabelek, J. L., Johnson, C. K., and Smith, C. (2000). Rotation and plate locking at the southern Cascadia subduction zone. *Geophysical Research Letters*, *27*(19), 3117-3120.

McClusky, S. C., Bjornstad, S. C., Hager, B. H., King, R. W., Meade, B. J., Miller, M. M., ... and Souter, B. J. (2001). Present day kinematics of the eastern California shear zone from a geodetically constrained block model. *Geophysical Research Letters*, *28*(17), 3369-3372.

McNeill, L. C., Piper, K. A., Goldfinger, C., Kulm, L. D., and Yeats, R. S. (1997). Listric normal faulting on the Cascadia continental margin. *Journal of Geophysical Research: Solid Earth*, *102*(B6), 12123-12138.

Micallef, A., Mountjoy, J. J., Krastel, S., Crutchley, G., & Koch, S. (2016). Shallow gas and the development of a weak layer in submarine spreading, Hikurangi margin (New Zealand). In Submarine Mass Movements and their Consequences (pp. 419-426). Springer International Publishing.

Moore, G. F., Boston, B. B., Sacks, A. F., and Saffer, D. M. (2013). Analysis of normal fault populations in the Kumano Forearc Basin, Nankai Trough, Japan: 1. Multiple orientations and generations of faults from 3-D coherency mapping. *Geochemistry, Geophysics, Geosystems*, *14*(6), 1989-2002.

Mountjoy, J. J., and Barnes,P. M. (2011). Active upper plate thrust faulting in regions of low plate interface coupling, repeated slow slip events, and coastal uplift: Example from the Hikurangi Margin, New Zealand. *Geochemistry, Geophysics, Geosystems*, *12*(1).

Mountjoy, J. J., McKean, J., Barnes, P. M., and Pettinga, J. R. (2009). Terrestrial-style slow-moving earthflow kinematics in a submarine landslide complex. *Marine geology*, *267*(3), 114-127.

Mountjoy, J. J., Pecher, I., Henrys, S., Crutchley, G., Barnes, P. M., and Plaza-Faverola, A. (2014). Shallow methane hydrate system controls ongoing, downslope sediment transport in a low-velocity active submarine landslide complex, Hikurangi Margin, New Zealand. *Geochemistry, Geophysics, Geosystems*, *15*(11), 4137-4156.

Mumme, T. C., Lamb, S. H., and Walcott, R. I. (1989). The Raukumara paleomagnetic domain: Constraints on the tectonic rotation of the east coast, North Island, New Zealand, from paleomagnetic data. *New Zealand journal of geology and geophysics*, *32*(3), 317-326.

Neves, F. A., Zahrani, M. S., & Bremkamp, S. W. (2004). Detection of potential fractures and small faults using seismic attributes. The Leading Edge, 23(9), 903-906.

Nicol, A., and Wallace, L. M. (2007). Temporal stability of deformation rates: Comparison of geological and geodetic observations, Hikurangi subduction margin, New Zealand. *Earth and Planetary Science Letters*, *258*(3), 397-413.

Nicol, A., Mazengarb, C., Chanier, F., Rait, G., Uruski, C., and Wallace, L. (2007). Tectonic evolution of the active Hikurangi subduction margin, New Zealand, since the Oligocene. *Tectonics*, *26*(4).

Ota, Y., and Yamaguchi, M. (2004). Holocene coastal uplift in the western Pacific Rim in the context of late Quaternary uplift. *Quaternary International*, *120*(1), 105-117.

Park, J. O., Moore, G. F., Tsuru, T., Kodaira, S., and Kaneda, Y. (2004). A subducted oceanic ridge influencing the Nankai megathrust earthquake rupture. *Earth and Planetary Science Letters*, *217*(1), 77-84.

Pecher, I., Crutchley, G., Mountjoy, J., Gorman, A., Fraser, D., & Henrys, S. (2014). Double BSRs on the Hikurangi Margin, New Zealand—Possible implications for gas hydrate stability and composition. In *8th International Conference on Gas Hydrates*.

Pecher, I. A., Villinger, H., Kaul, N., Crutchley, G. J., Mountjoy, J. J., Huhn, K., ... & Coffin, R. C. (2017). A fluid pulse on the Hikurangi subduction margin–evidence from a heat flux transect across the upper limit of gas hydrate stability. *Geophysical Research Letters*.

Pedley, K. L., Barnes, P. M., Pettinga, J. R., and Lewis, K. B. (2010). Seafloor structural geomorphic evolution of the accretionary frontal wedge in response to seamount subduction, Poverty Indentation, New Zealand. *Marine Geology*, *270*(1), 119-138.

Plaza-Faverola, A., Pecher, I., Crutchley, G., Barnes, P. M., Bünz, S., Golding, T., ... and Bialas, J. (2014). Submarine gas seepage in a mixed contractional and shear deformation regime: Cases from the Hikurangi oblique-subduction margin. *Geochemistry, Geophysics, Geosystems*, *15*(2), 416-433.

Press, F. (1966). Section 9: Seismic velocities. *Geological Society of America Memoirs*, *97*, 195-218.

Ranero, C. R., and von Huene, R. (2000). Subduction erosion along the Middle America convergent margin. *Nature*, *404*(6779), 748.

Reyners, M. (1998). Plate coupling and the hazard of large subduction thrust earthquakes at the Hikurangi subduction zone, New Zealand. *New Zealand Journal of Geology and Geophysics*, *41*(4), 343-354.

Reyners, M., and McGinty, P. (1999). Shallow subduction tectonics in the Raukumara Peninsula, New Zealand, as illuminated by earthquake focal mechanisms. *Journal of Geophysical Research: Solid Earth*, *104*(B2), 3025-3034.

Ruh, J. B., Sallarès, V., Ranero, C. R., & Gerya, T. (2016). Crustal deformation dynamics and stress evolution during seamount subduction: High-resolution 3-D numerical modeling. Journal of Geophysical Research: Solid Earth, 121(9), 6880-6902.

Sacks, A., Saffer, D. M., & Fisher, D. (2013). Analysis of normal fault populations in the Kumano forearc basin, Nankai Trough, Japan: 2. Principal axes of stress and strain from inversion of fault orientations. Geochemistry, Geophysics, Geosystems, 14(6), 1973-1988.

Stirling, M., McVerry, G., Gerstenberger, M., Litchfield, N., Van Dissen, R., Berryman, K., ... and Lamarche, G. (2012). National seismic hazard model for New Zealand: 2010 update. *Bulletin of the Seismological Society of America*, *102*(4), 1514-1542.

Taner, M. T., Koehler, F., and Sheriff, R. E. (1979). Complex seismic trace analysis. *Geophysics*, *44*(6), 1041-1063.

Ten Veen, J. H., and Kleinspehn, K. L. (2003). Incipient continental collision and plate-boundary curvature: Late Pliocene-Holocene transtensional Hellenic forearc, Crete, Greece. *Journal of the Geological Society*, *160*, 161.

Teyssier, C., Tikoff, B., and Markley, M. (1995). Oblique plate motion and continental tectonics. *Geology*, *23*(5), 447-450.

Toda, S., Stein, R. S., & Lin, J. (2011). Widespread seismicity excitation throughout central Japan following the 2011 M= 9.0 Tohoku earthquake and its interpretation by Coulomb stress transfer. Geophysical Research Letters, 38(7).

Van Wagoner, J. C., Posamentier, H. W., Mitchum, R. M. J., Vail, P. R., Sarg, J. F., Loutit, T. S., and Hardenbol, J. (1988). An overview of the fundamentals of sequence stratigraphy and key definitions. *Soc. of Econ. Paleontol. and Miner. Spec. Publ.*, *Sea-Level Changes: An Integrated Approach*, *42*, pp. 39–44, Special Publications of SEPM.

Walcott, R. I. (1978). Geodetic strains and large earthquakes in the axial tectonic belt of North Island, New Zealand. *Journal of Geophysical Research: Solid Earth*, *83*(B9), 4419-4429.

Walcott, R. I. (1984). The kinematics of the plate boundary zone through New Zealand: A comparison of short- and long-term deformations. *Geophys. J. R. Astron. Soc*., 79, 613–633.

Walcott, R. I. (1987). Geodetic strain and the deformational history of the North Island of New Zealand during the late Cainozoic. *Philosophical Transactions for the Royal Society of London. Series A, Mathematical and Physical Sciences*, 163-181.

Wallace, L. M., Barnes, P., Beavan, J., Van Dissen, R., Litchfield, N., Mountjoy, J., ... and Pondard, N. (2012). The kinematics of a transition from subduction to strike-slip: An example from the central New Zealand plate boundary. *Journal of Geophysical Research: Solid Earth*, *117*(B2).

Wallace, L. M., Beavan, J., McCaffrey, R., and Darby, D. (2004). Subduction zone coupling and tectonic block rotations in the North Island, New Zealand. *Journal of Geophysical Research: Solid Earth*, *109*(B12).

Wallace, L. M., Reyners, M., Cochran, U., Bannister, S., Barnes, P. M., Berryman, K., ... & Nicol, A. (2009). Characterizing the seismogenic zone of a major plate boundary subduction thrust: Hikurangi Margin, New Zealand. Geochemistry, Geophysics, Geosystems, 10(10).

Wallace, L. M., Webb, S. C., Ito, Y., Mochizuki, K., Hino, R., Henrys, S., ... & Sheehan, A. F. (2016). Slow slip near the trench at the Hikurangi subduction zone, New Zealand. Science, 352(6286), 701-704.

Wang, K., and Bilek, S. L. (2011). Do subducting seamounts generate or stop large earthquakes?. *Geology*, *39*(9), 819-822.

Wang, H., Crutchley, G. J., & Stern, T. (2017). Gas hydrate formation in compressional, extensional and un-faulted structural settings–Examples from New Zealand's Hikurangi margin. Marine and Petroleum Geology, 88, 69-80.

Webb, T. H., and Anderson, H. (1998). Focal mechanisms of large earthquakes in the North Island of New Zealand: slip partitioning at an oblique active margin. *Geophysical journal international*, *134*(1), 40-86.

Woodcock, N. H., and Fischer, M. (1986). Strike-slip duplexes. *Journal of structural geology*, *8*(7), 725-735.

Yielding, G., Badley, M. E., & Freeman, B. (1991). Seismic reflections from normal faults in the northern North Sea. Geological Society, London, Special Publications, 56(1), 79-89.

Yu, Y., Kelley, C. L., and Mardanova, I. M. (2015). *U.S. Patent No. 9,105,075*. Washington, DC: U.S. Patent and Trademark Office.

Zoback, M. L., Anderson, R. E., and Thompson, G. A. (1981). Cainozoic evolution of the state of stress and style of tectonism of the Basin and Range province of the western United States. Philosophical Transactions of the Royal Society of London. Series A, Mathematical and Physical Sciences, 407-434.

# 5. Free gas distribution and basal shear zone development in a subaqueous landslide – Insight from 3D seismic imaging of the Tuaheni Landslide Complex, New Zealand

Felix Gross, Joshu J. Mountjoy, Gareth Crutchley, Christoph Böttner, Stephanie Koch, Jörg Bialas, Ingo Pecher, Susi Woelz, Anke Dannowski, Aaron Micallef, Katrin Huhn, Sebastian Krastel

Published in 2018 Earth and Planetary Science Letters, 502, 231-243.

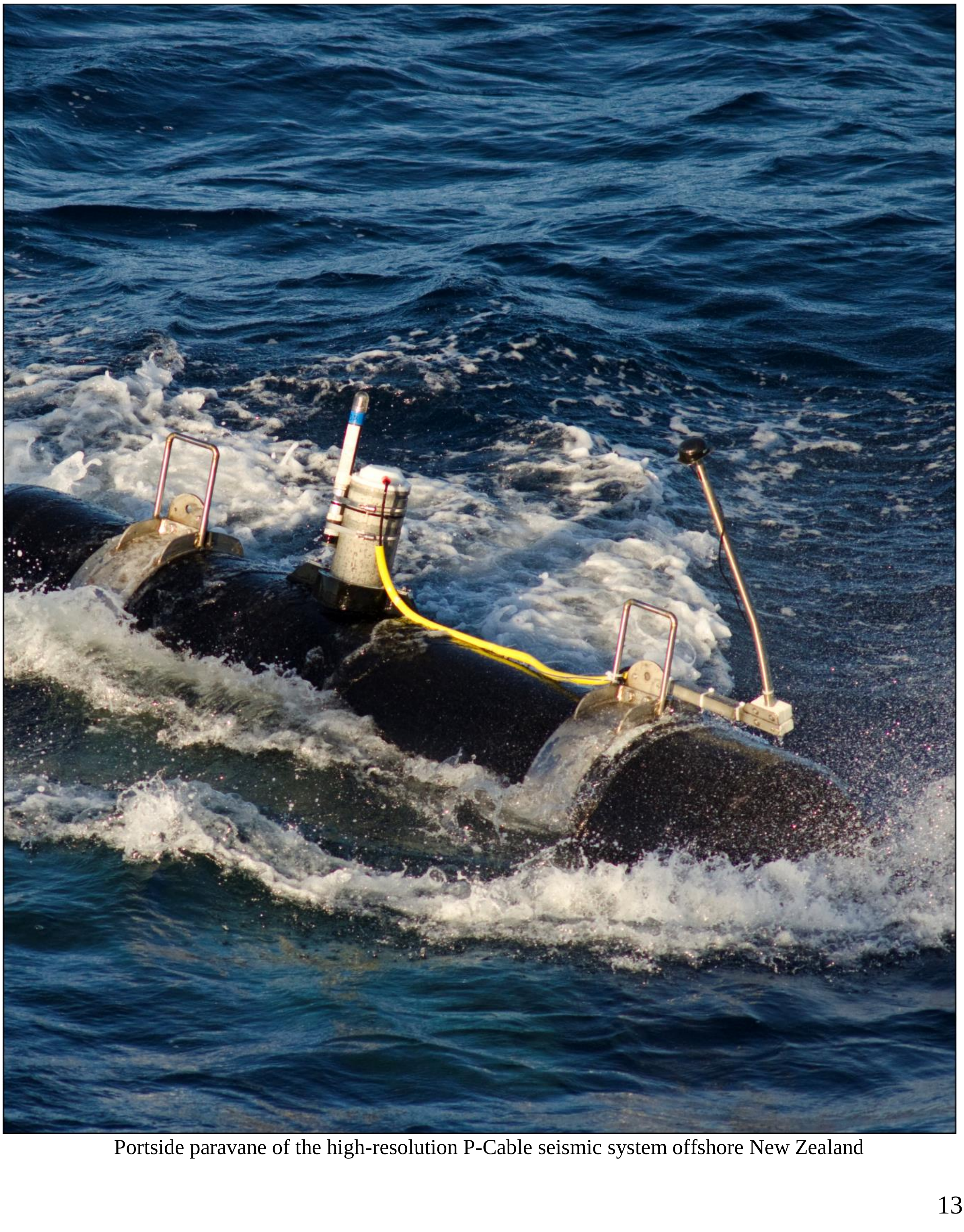

Portside paravane of the high-resolution P-Cable seismic system offshore New Zealand

**Key Points**

1. 3D seismic imaging of an entire landslide complex
2. Shallow gas accumulation within and underneath Tuaheni Landslide Complex
3. Imaging of a basal shear zone within a subaqueous landslide complex

## 5.1. Abstract

The Hikurangi margin is an active continental margin east of New Zealand’s North Island. It is well recognized as a seismically active zone and is known for the occurrence of free gas and gas hydrates within the shallow sediments. A variety of subaqueous landslides can be observed at the margin, including the Tuaheni Landslide Complex off Poverty Bay. This slide complex has been interpreted previously as a slowly creeping landform, as its morphology and internal deformation is comparable to terrestrial earthflows and rock glaciers. In 2014, we acquired a high-resolution 3D seismic volume covering major parts of the Tuaheni South landslide. The 3D data show a variety of fluid migration indicators, free gas accumulations and manifestations of the base of gas hydrate stability in the pre-slide sedimentary units and the lower unit of the landslide system. The data also show that the landslide system is composed of an upper and lower unit that are separated by an intra-debris negative-polarity reflection. Free gas accumulations directly beneath the landslide units suggest that the debris acts as a boundary for rising fluids and only few migration pathways to the intra-debris reflector are observed in the distal parts of the landslide. Deformation within the landslide’s debris is focused in the upper landslide unit, and we interpret the intra-debris reflector as a basal shear zone or ‘glide plane’ upon which the debris has been remobilized. The origin of the intra-debris reflector is unclear, but we suggest it could be a relatively coarse-grained horizon that would be prone to fluid flow focusing and the development of excess fluid pressure. Our seismic study provides one of the most detailed examples of a subaqueous landslide system and reveals insights into the fluid flow system and potential basal shear zone development of the Tuaheni Landslide Complex.

## 5.2. Introduction

Classification schemes for subaqueous landslides include a large number of components and processes similar to terrestrial landslides, including translational slides, slumps, as well as debris and earth flows (Hampton et al. 1996; Bull et al. 2009; Hungr et al. 2014). Multi-beam bathymetry and seismic reflection datasets can resolve surface morphology, depositional character and large-scale structure of landslides that are preserved in the marine sedimentary record (Locat & Lee 2002; Joanne et al. 2013; Clarke et al. 2014). However, the fine scale details of internal deformation, which are observable in landslides exposed on land, are rarely imaged for subaqueous landslides. Much of what we know about macro- to meso scale deformation processes and the control of the mechanical movement of large subaqueous landslides comes from analysis of uplifted mass transport complexes (MTCs) exposed in outcrops onshore (Ogata et al. 2014a; Ogata et al. 2014b) and numerical modelling (Urlaub et al., 2015). Basal shear zones are readily observable in these exhumed MTCs and occur as discrete lithologically mixed intervals that are thin with respect to slide thickness. As with active terrestrial landslides, kinematic indictors show that deformation in subaqueous landslides is primarily focused within/along these shear zones (Festa et al. 2010; Ogata et al. 2012.

Basal failure surfaces in the marine sedimentary record are variably referred to as slip surfaces or glide planes, and can be imaged in seismic reflection data as a contact between chaotic/transparent seismic character representing the MTD and coherent/stratified reflectivity below. The origin of slip surfaces may be correlated to specific horizons in the intact sedimentary sequence either laterally or upslope of the landslide. These horizons are often referred to as weak layers. Due to the complexity of submarine sampling, like deep sea drilling, only a few examples in shallow successions of shallow seated subaqueous landslides have been imaged and sampled (e.g. Beaten et al. 2014). Localized shear zones are well-documented features observed in terrestrial active landslide complexes (Vulliet & Hutter 1988). They are present at the interface between different moving masses/blocks, and are therefore a major internal element of rock glaciers and slow-moving landslides (Haeberli et al. 2006). The most intensive deformation of active slow-moving landslides occurs along these shear zones in terms of repeated shearing over prolonged periods as these zones act as a basal decollement (Haeberli et al. 2006; Kawamura et al. 2007). While the analogue between terrestrial and subaquous landslide shear zones is informative, observations from outcrop MTCs are sparse and subject to post-deposition deformation. Therefore, internal shear zones preserved in the subaquous environment warrant further research.

Gas and gas hydrates are common within marine sediments in the world’s continental margins (Klauda & Sandler 2005), and are often cited as playing an important role in sediment strength and even contributing to subaqueous landsides (e.g. Field & Barber 1993; Paull et al. 1996; Sultan et al. 2004). It is important to consider the flow of both water and free gas in this context, since permeability changes can result in partial trapping of fluid flow, which can lead to the development of excess fluid pressure. Particularly in the shallow sub-seafloor, where differential stresses are low, trapping of fluids could have a significant influence on overpressure development and the associated reduction of sediment strength (Ellis et al. 2010). 3D seismic data provide excellent insights into shallow fluid flow systems, and have been used previously to highlight the role of gas migration and accumulation in slope destabilization (Berndt et al. 2012).

In this study we use high-resolution P-Cable seismic reflection data to analyze the Tuaheni Landslide Complex (TLC) off the East Coast of New Zealand’s North Island (Fig. 5.1). We use seismic imaging to analyze internal features of the landslide complex including a prominent intra-debris reflector and the distribution of free gas. We investigate the mechanisms proposed to be influencing landslide reactivation based on 3D analysis of the spatial relationship of landslide elements to free gas and faulting.

## 5.3. Tectonic and Geologic setting

Our study area is located on an active subducting margin, the Hikurangi Margin off New Zealand’s East Coast (Fig. 5.1c). Convergence between the Pacific and Australian plates in this region is orthogonal to the NE-SW strike of the margin, with the inter-plate motion approximately 46 mm $yr^{-1}$ (Beavan et al. 2002). Active upper plate faults in the offshore region of the northern Hikurangi Margin are dominated by thrusts (Barker et al. 2009; Barnes et al. 2010; Mountjoy & Barnes 2011), but recent work has also shown evidence for upper-plate normal faulting (Böttner et al. 2018). The TLC occurs on the upper slope in an area that is locally relatively un-deformed by major faulting or folding. However, the Ariel Bank Fault (Fig. 5.1a), an active splay fault with a vertical slip rate of 4.1 +/- 0.9 mm $yr^{-1}$ , is expressed as uplifted reefs 2 km inboard of the landward limit of the head scarp (Mountjoy & Barnes 2011). Tuaheni Ridge bounds the distal limit of the landslide deposit and is the result of uplift and folding above a splay fault (Fig. 5.1a). Based on all known earthquake sources, probabilistic seismic hazard modelling indicates peak ground acceleration (PGA) of 0.4–0.5 g at a 250 year return period across the upper slope (Stirling et al. 2012).

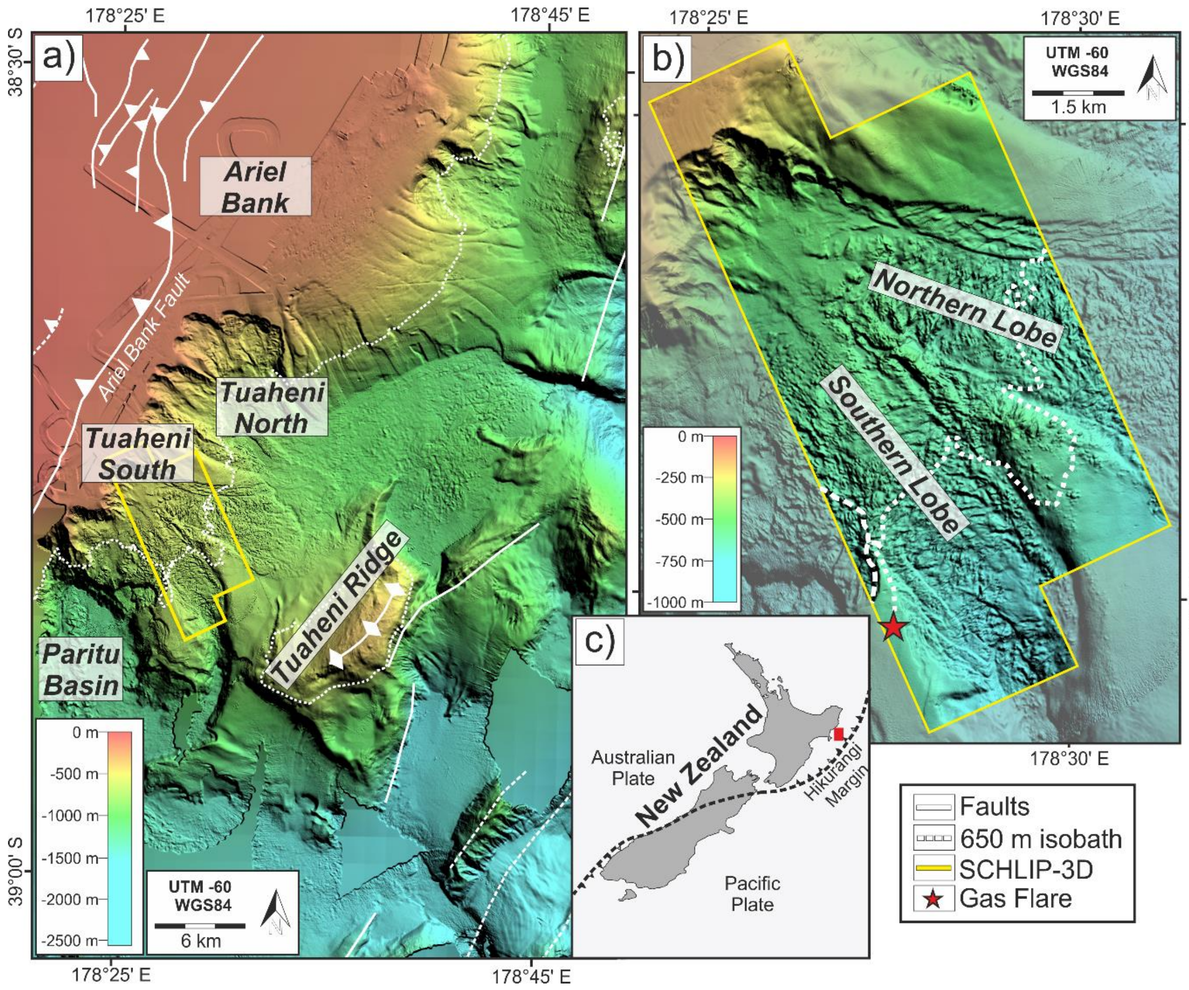

**Figure 5.1.** The Tuaheni Landslide Complex (TLC) is located east off the North Island of New Zealand. a) Bathymetric map of the Tuaheni North and Tuaheni South landslides. Regional faults after Mountjoy & Barnes (2011) and Böttner et al. (2018) b) Bathymetric map of the new SCHLIP-3D dataset. The TLC is divided into the Northern Lobe and Southern Lobe of Tuaheni South. The SCHLIP-3D seismic volume (outlined in yellow) was acquired at the northern and southern lobes of Tuaheni South. The white dotted line shows the 650 m contour; the approximate upper limit of gas hydrate stability. c) Overview map of New Zealand showing the location of the enlarged map in (a).

The TLC has formed in Quaternary shelf-edge clinoform sequences that are widely recognized on the outer shelf and upper slope on this margin (Paquet et al. 2010; Pedley et al. 2010). The clinothemes are wedge shaped, gently dipping and parallel-bedded sedimentary packages characteristic of sea-level-cycle controlled progradational deposits. Sediments are fine-grained at the surface, reflecting modern sedimentation rates of 1.7 mm yr$^{-1}$ (Alexander et al. 2010), but likely contain a significant sand fraction at depth as documented for equivalent clinoform sequences nearby (Barnes et al. 1991).

The debris of TLC is deposited in water depths between ~500 m and ~900 m b.s.l and it is intersected by the upper limit of the gas hydrate stability zone at ~650 m b.s.l (Mountjoy et al. 2014). The TLC was first described by Mountjoy et al. (2009) and is divided into Tuaheni North and Tuaheni South (Fig. 5.1b). Tuaheni South can be sub-divided into two different lobes of debris (Fig. 5.1c). In contrast to many other subaqueous landslides, which evacuate from continental margins, the debris is still located on the margin within the sloping landslide scar and has not been fully emplaced into a depositional system like an intra-slope basin or the trench of the Hikurangi Margin. Nearly 50% of the entire landslide complex is located within the gas hydrate stability zone (GHSZ). The base of gas hydrate stability (BGHS) manifests itself mainly as clear truncations of anomalous high-amplitude reflections that arise from free gas within strata beneath the BGHS (Fig. 5.2). Classic bottom simulating reflections (BSRs) are also present in places. Based on the upper limit of the BGHS at ~650 m b.s.l., which was inferred by Mountjoy et al. (2014), the BGHS can be traced from the central to distal parts of the debris (Fig. 5.1c).

Based on the deformation character of the TLC from surface morphology analogous to active terrestrial landslides, including lateral bounding scarps and stepped landslide track deflation (indicating multiple periods of material removal) and upslope compression vs downslope extension (the opposite from that expected for single movement landslides), Mountjoy et al. (2009) postulated a post-slide remobilization and ongoing movement of the slide debris. They inferred this movement to be taking place at timeframes less than the recurrence interval of strong, earthquake-generated ground motion. By observing a spatial correlation between the inferred BGHS and the landslide debris, Mountjoy et al. (2014) subsequently proposed three different hypotheses for how the presence of gas hydrates could explain a potential activity of TLC. Their first hypothesis considers gas hydrate dissociation and subsequent excess fluid pressure generation as a driving mechanism. This mechanism has been described and invoked elsewhere since the 1980s (e.g. McIver 1982). Due to the considerable depth of the BGHS beneath most of the slide mass, Mountjoy et al. (2014) deemed this mechanism unlikely. Second, they invoked the contribution of excess fluid pressure in the absence of hydrate dissociation, but rather as a result of focused upward gas-charged fluid flow becoming partially trapped beneath gas hydrate-bearing sediments (e.g. Crutchley et al. 2010; Ellis et al. 2010). Third, they presented a new failure mechanism whereby gas hydrate within the sediment could constitute a rheology that enables the landslide debris to behave in a similar way to a terrestrial rock glacier that slowly creeps downslope (Mountjoy et al. 2014). Despite this focus on the possible role of gas hydrates, the potential has always remained that reactivation of the TLC could be a co-seismic phenomenon. The relatively frequent high-frequency ground motion experienced in this subduction zone setting, and the low rates of surface geomorphic modification in some deep marine environments, make this a valid interpretation.

## 5.4. Methods

### 5.4.1. 3D seismic data acquisition and processing of the SCHLIP-3D volume

During RV Tangaroa cruise TAN1404, we acquired a high-resolution 3D seismic volume covering an area of ~69 km$^2$, at Tuaheni South. The seismic volume was acquired as two sub-volumes adjacent to each other; the first sub-volume (covering an area of ~41 km$^2$) was collected over the southwestern lobe of the landslides, while the second sub-volume (area of

~28 km$^2$) was collected over the northeastern lobe. The sub-volumes were merged during the stacking stage of the processing flow. We used GEOMAR's P-Cable system for high-resolution 3D seismic acquisition (Fig. 5.1c). The P-Cable system is characterized by a "cross cable" towed behind the vessel between two paravanes (e.g. Petersen et al. 2010). At the cross cable, a number of short streamer segments are attached. During TAN1404 we used 12 parallel 12.5 m long steamers with 8 channels and 3 25 m long streamers with 16 channels. The channel spacing of the GEOMETRICS® GeoEel digital streamers is 1.5625 m. To ensure adequate coverage, the distance between neighboring sail lines was set to ~55 m. For seismic signal generation we used a GI gun with a reduced chamber volume (0.7 l primary volume), which was shot in harmonic mode. The shot interval was set to 3 s, resulting in a shot point interval of ~5 m at 3.5 knots. The data were recorded with a sampling rate of 0.5 ms.

We filtered the data by using a bandpass filter with corner frequencies of 40, 70, 350, and 500 Hz. We removed persistent noise in traces from channels closest to the cross cable from the processing flow. We sorted the data into common midpoint (CMP) bins on a 3.125 x 3.125 m grid and applied a normal move-out (NMO) correction to the CMP gathers using a constant velocity of 1500 m s$^{-1}$. The combination of slow acquisition speed and short shot intervals ensured good coverage in the sail line direction on the 3.125 m grid. To reduce the number of data gaps in the crossline direction on the 3.125 m grid, we stacked successive inlines, which resulted in a stacked dataset with 3.125 m trace spacing in the inline direction and 6.25 m spacing in the crossline direction. We applied an automatic de-spiking routine in the post-stack domain to remove rare spurious noise bursts. This routine only muted short segments (20 ms) of traces if the peak amplitude in a given 20 ms window exceeded a value 5 times that of a peak amplitude in aligned 20 ms windows on neighboring traces. A 2D trace interpolation, run first in the crossline direction, then in the inline direction, was used to fill small data gaps that persisted in the stacked volume. Finally, we migrated the dataset with GLOBE Claritas' 3D Kirchhoff time migration, using a constant velocity of 1500 m s$^{-1}$ and a migration aperture width of 500 m. The resulting 3D seismic volume spans an inline range of 478-2378 (increment 2) and crossline range of 3376-7705 (increment 1). The inlines are ~13500 m long and the crosslines are ~5900 m long.

We used the Kingdom Suite 2017 software for attribute analysis. In this work, we present seismic attributes, which were calculated on horizons indicating major stratigraphic changes and cross cutting features like the inferred BGHS. For fault and deformation fabric identification, we used the poststack, postmigration structural feature detection tool, which is based on a 3-D log-Gabor filter array (Yu et al. 2015). Symmetry is classified as a visual attribute, as it is inspired by neuronal mechanisms of visual perception for orientation patterns. The attribute's sensitivity to amplitude variations makes it to a reliable tool for the identification of discontinuities and curvatures of geological surfaces. We used the SCHLIP-3D seismic volume for our Symmetry I3D Energy attribute, a derivative volume of the Symmetry attribute (Yu et al., 2015). We used an analysis window of 100 ms and a 5x5 cylindrical filter as line versus trace parameter. In the following, we refer to the Symmetry I3D attribute as “Fault Attribute”. Dip-steering was applied as part of this Fault Attribute. We inspected numerous vertical seismic sections throughout the volume to confirm that the fault network derived from the attribute analysis does indeed correlate to faults that can be observed in vertical seismic sections. The reader is also referred to Böttner et al. (2018)–a detailed analysis of faulting in this dataset–for more information on this attribute.

In our interpretation of the data we focused on four horizons, including the seafloor, the base of gas hydrate stability, the base of debris, and an internal reflector between debris units. These four horizons are the spatially coherent surfaces that give insight into the recent mass wasting processes at the TLC.

### 5.4.2. Multi-beam and sediment echo-sounder data acquisition and processing

For bathymetric data acquisition, a Kongsberg EM302 swath multi-beam echo-sounder was used during RV Tangaroa cruise TAN1404. Data were quality controlled and processed with the commercial software Caris HIPS™ and SIPS™. The multi-beam data were processed with a bin size of 8 m within water depths of 115 – 1180 m in the region of the SCHLIP-3D seismic volume. During TAN1508, high-resolution parametric sediment echo-sounder data were acquired by using RV Tangaroa’s hull mounted TOPAS PS 18. A linear chirp with frequencies from 2.0 to 6.0 kHz and a chirp length of 25 ms was set as transmission waveform.

## 5.5. Results

Tuaheni South has a distinct surface morphology that stands out clearly from the surrounding seafloor morphology (Fig. 5.1). The hummocky topography characterizes an area of ~74 km$^2$, and is related to the debris evacuated during a medium-scale landslide in this region. The head scarp of Tuaheni South is characterized by steep slope angles of up to 30° and cuts distinctively into the shelf sediments off Poverty Bay. As the landslide’s seafloor morphology has been described previously by Mountjoy et al. (2009; 2014), we concentrate on the landslide’s subsurface features. The subsurface seismic stratigraphy of the TLC can be described in terms of three major stratigraphic units (Fig. 5.2). These are 1) the pre-slide Quaternary clinoforms defining the intact sedimentary sequence and bounded on their upper surface by either the seafloor or the base of the slide debris, 2) a lower landslide unit, and 3) an upper landslide unit. A regional intra-debris reflector separates the two landslide units. The inferred BGHS is marked by the truncation of dipping high-amplitude reflections, which mimics the seafloor beneath the medial and distal parts of the landslide complex (Fig. 5.2).

### 5.5.1. Pre-slide Quaternary clinoforms

Quaternary clinoform sequences previously identified on the shelf off Poverty Bay (Paquet et al. 2010; Pedley et al. 2010) are observable beneath the landslide debris of Tuaheni South (Fig. 5.2). The sequence beneath the landslides is characterised by gently dipping, laterally continuous reflectivity. Reflection character alternates between high amplitude horizons that can be tracked widely throughout the volume (Boettner et al. 2018) and tens of metres-thick packages of opaque chaotic reflectivity. Strata dips are flat to gentle beneath the up-slope portion of the slide and steepen to the southeast, progressively increasing in dip back into the slope. The southeastern region of the 3D volume images a zone of closely-spaced, steeply-dipping normal faults (Fig. 5.2) with vertical displacements of up to ~15 m (20 ms TWT). This network of faults is exceptionally well imaged with the Fault Attribute, which reveals a family of N-S to NE-SW striking structures (Fig. 5.3c) that were investigated in detail by Böttner et al. (2018). The faults are 0.5-2 km long and in places terminate against each other as well as showing some cross cutting relationships. The chaotic to transparent seismic facies of the landslide debris hinders tracing these faults towards the seafloor. Low-amplitude, sub-vertical features are also observed throughout the volume, disrupting the otherwise coherent and continuous clinoform sequences (Fig. 5.2).

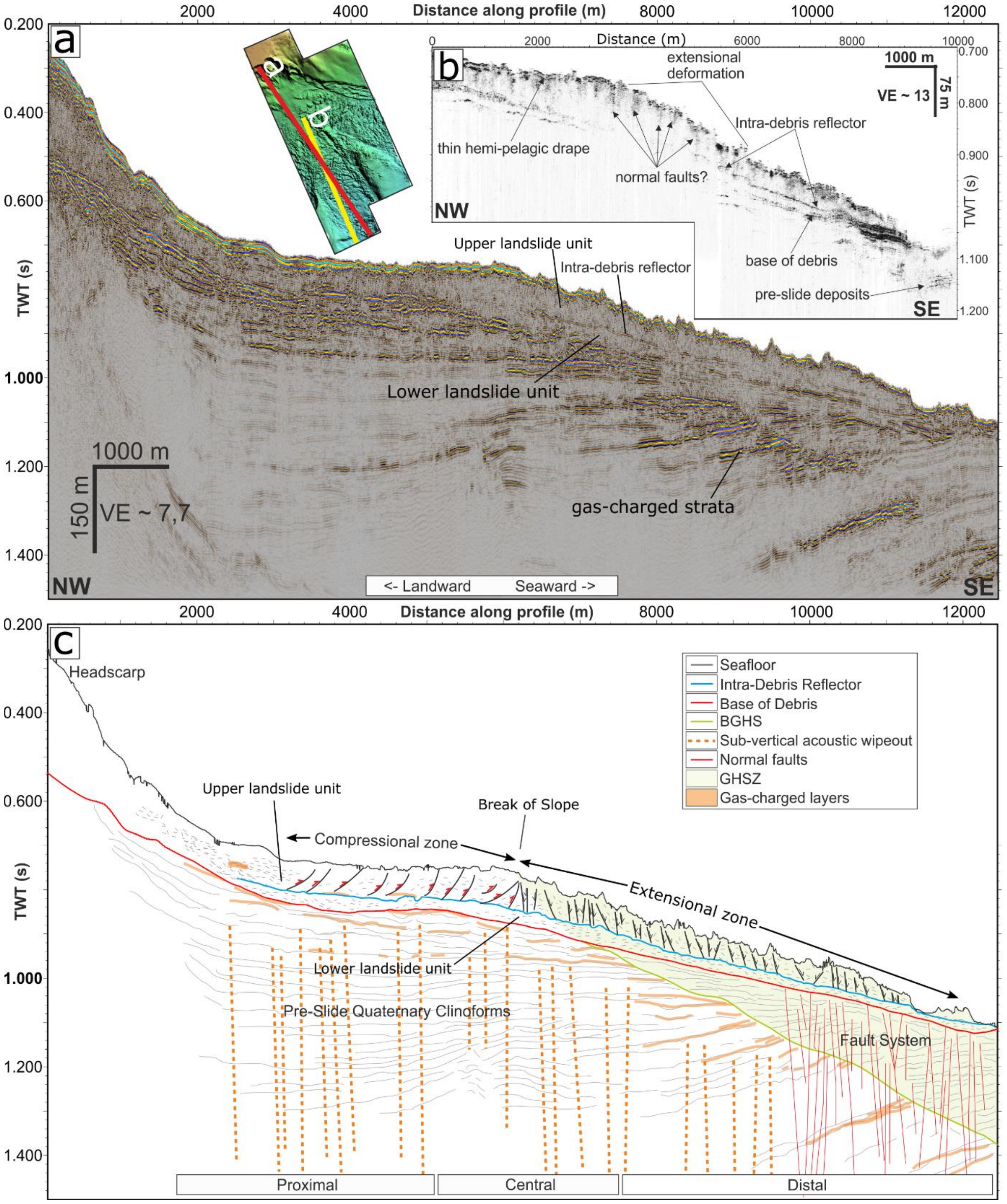

**Figure 5.2.** a) Representative seismic profile from the SCHLIP-3D volume through the Southern Lobe (see small inset map for location). b) TAN1508-TOPAS-152 Sub-bottom profiler line through the Southern Lobe (see small inset map for location). c) Interpretation of the main components of the TLC. A break in slope angle is observed at ~6000 m (distance along profile), where the transition between compression (upslope) and extension (downslope) has been interpreted (Mountjoy et al. 2014). The TLC is separated into upper and lower units that are divided by an intra-debris reflector that can be seen in both the 3D seismic data and the sub-bottom profiler data. Other interpretations are as labeled in the legend.

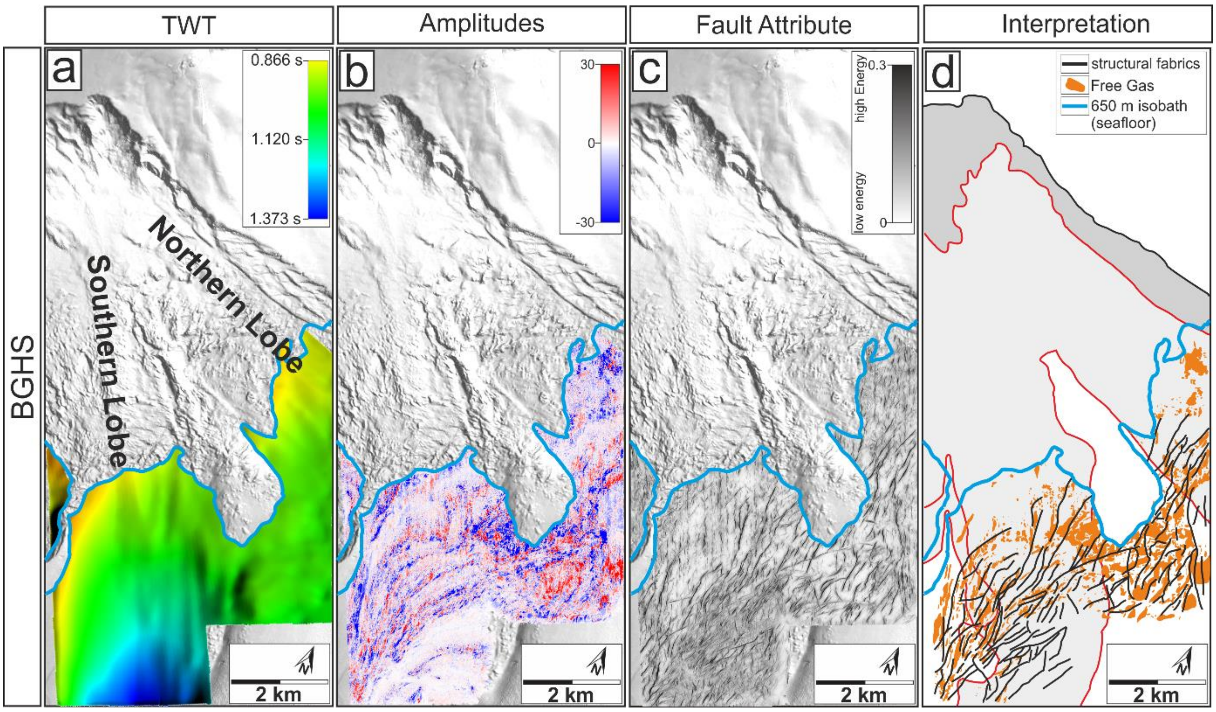

**Figure 5.3.** a) Picked and interpolated horizon map of the BGHS in two-way time (TWT). Note that the upper limit of this horizon (0.87 s TWT) is equivalent to the 650 m isobath shown in Fig. 5.1b) Amplitude map calculated on the BGHS. c) Fault Attribute extracted on the BGHS. Structural fabrics (faults) appear as dark grey. d) Interpretation is based on features observed by assessing the amplitude and Fault Attribute maps. The red line indicates the outlines of the TLC lobes. The attribute mapping reveals a complex fault system in the distal part of TLC and anomalously-high amplitudes at the BGHS are interpreted as patches of free gas.

### 5.5.2. Landslide debris units

We recognize two distinct landslide debris units from seismic character that are broadly characterized by chaotic seismic facies in multichannel and high frequency seismic reflection images, and are separated by a clear but discontinuous through going reflector (Fig. 5.2). The upper landslide unit is almost entirely characterised by a chaotic to transparent seismic facies (e.g. Fig. 5.4) with only localized areas of laterally discontinuous, high amplitude reflectivity in the up-slope region of the unit (Fig. 5.2a). In contrast, the lower landslide unit includes both chaotic and continuous high amplitude reflectivity that is present throughout the unit (e.g. Fig. 5.4b). High amplitude regions of the lower landslide debris unit include laterally continuous reflections separating discrete packages of chaotic facies. The two units are separated by a semi-coherent intra-debris reflector, which is further described in section 5.5.3.

Throughout most of the landslide complex the base of the lower landslide unit can be traced in the 3D volume as the contact between chaotic reflectivity above and mostly stratified sediments of the clinoform sequence below (e.g Fig. 5.4a). In other regions, like below the northern lobe, older landslide deposits occur beneath the base of the lower landslide unit (Fig. 5.4d). We have interpreted the contact at the base of debris (broken red line in Fig. 5.4) throughout the data and then extracted attributes on this horizon, as shown in Fig. 5.5.

The morphology at the base of landslide debris shows elongated depressions, oriented downslope (Fig. 5.5a). The reflectivity at this level is highly variable throughout the data (Fig. 5.5b), with most of the anomalously-high reflectivity occurring in the up-slope region of the landslide, and in the northern lobe. Anomalously-high reflectivity patches at the base of the debris are rare in the distal parts of the southern lobe – i.e. downslope of the 650 m contour, in the region where gas hydrates are stable beneath the seafloor. Our data do not cover as much of the distal extent of the northern lobe to be able to make similar observations about anomalously-high reflectivity distribution in that lobe.

The broadly chaotic nature of the debris means we do not observe clear deformation fabrics with the fault attribute on the base of debris horizon (Fig. 5.5c). The only clear fabrics at this depth in the data are in the distal parts of the landslide, and they relate to the distinct fault network that we also observe at the BGHS deeper in the sedimentary section (Fig. 5.3d).

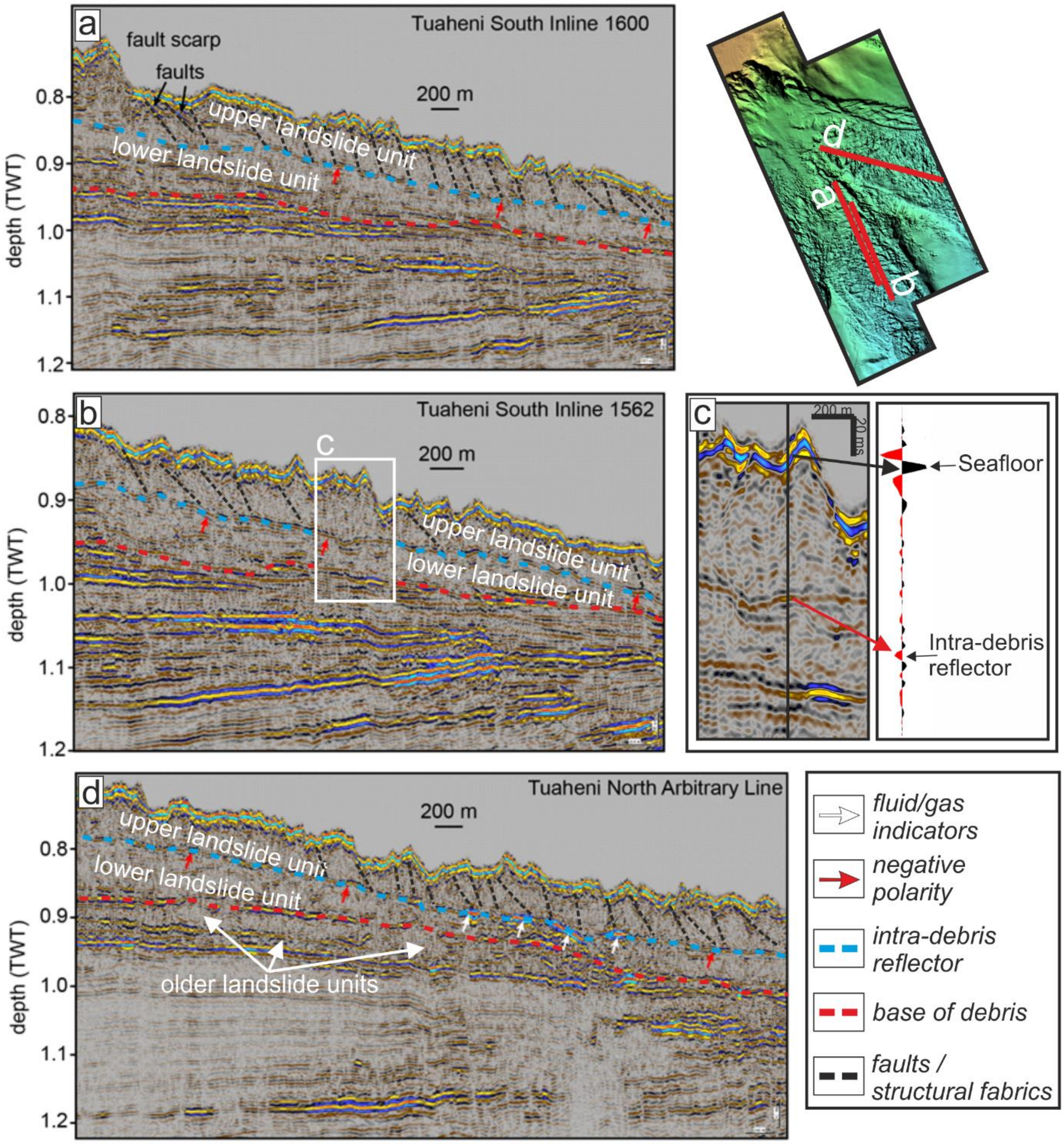

**Figure 5.4.** Seismic reflection profiles from the 3D seismic volume illustrating the continuity and nature of the intra-debris reflector mapped in Fig. 5.6. The location of the reflector is indicated by arrows. a) Extensional faulting soling onto the reflector in Tuaheni South. b) Continuous expression of the reflector through Tuaheni South. c) left: Zoom-in of B, illustrating a section of the intra-debris reflector. Right: wavelet character of a trace from the zoom-in - the seafloor shows positive polarity, whereas the intra-debris reflector exhibits negative polarity. d) Strong reverse-polarity reflection segments (≥ seafloor amplitude) on the intra-debris reflector in Tuaheni North (small white arrows).

### 5.5.3. Intra-debris reflector

The intra-debris reflector separating the upper and lower landslide units (Figs. 5.2 and 5.5) is characterized by negative polarity with respect to the seafloor and is only imaged within the debris deposits of TLC (Fig. 5.6). The reflector is best imaged with good continuity far downslope at the debris front of the southern lobe. In the central segment of TLC, the reflector is less pronounced and disappears towards the proximal segments close to the headscarp.

In contrast to the hummocky seafloor morphology, the intra-debris reflector is regionally smooth and reveals a steady dip in the direction of the debris' runout (Figs. 5.5a, 5.6). The character of the intra-debris reflector is resolved in both echo-sounder profiles and the 3D seismic volume (Figs. 5.2, 5.4).

In TOPAS data, the intra-debris reflector is imaged as a high amplitude boundary between the two landslide units. In multichannel seismic data the reflector is consistently a single wavelet and does not occur as a package of reflectivity (e.g. Fig. 5.4a, 5.4d). In places, deformation structures such as fault plane reflectors merge or strike off onto the intra-debris reflector (Fig. 5.4d). The reflector is also an angular unconformity to some reflections within the lower landslide unit. In some locations, patches of anomalously-high amplitudes (negative polarity)occur on the intra-debris reflector (Fig. 5.5d, 5.6b).

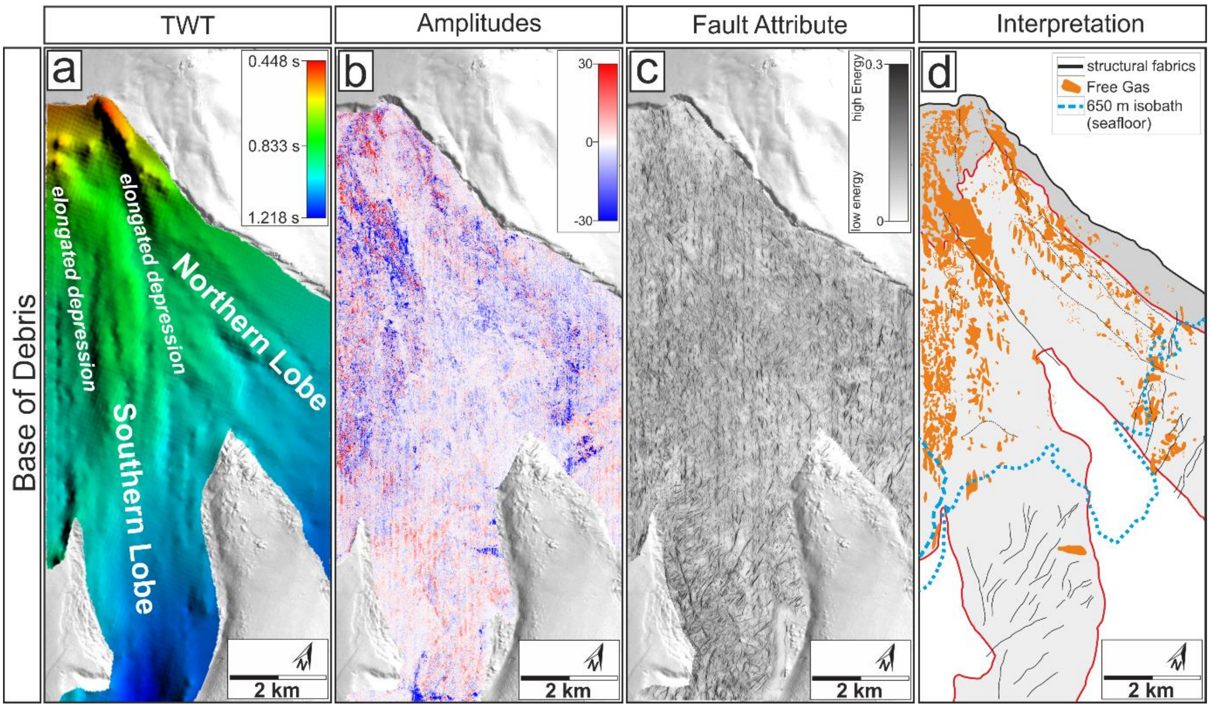

**Figure 5.5.** a) Morphology of the base of debris in TWT, as mapped throughout the 3D seismic data. b) Seismic amplitudes from the horizon mapped in (a). c) Fault Attribute extracted on the horizon in (a). Structural fabrics (faults) appear in dark grey. d) Interpretation of free gas distribution and structural fabrics based on the maps in (b) and (c).

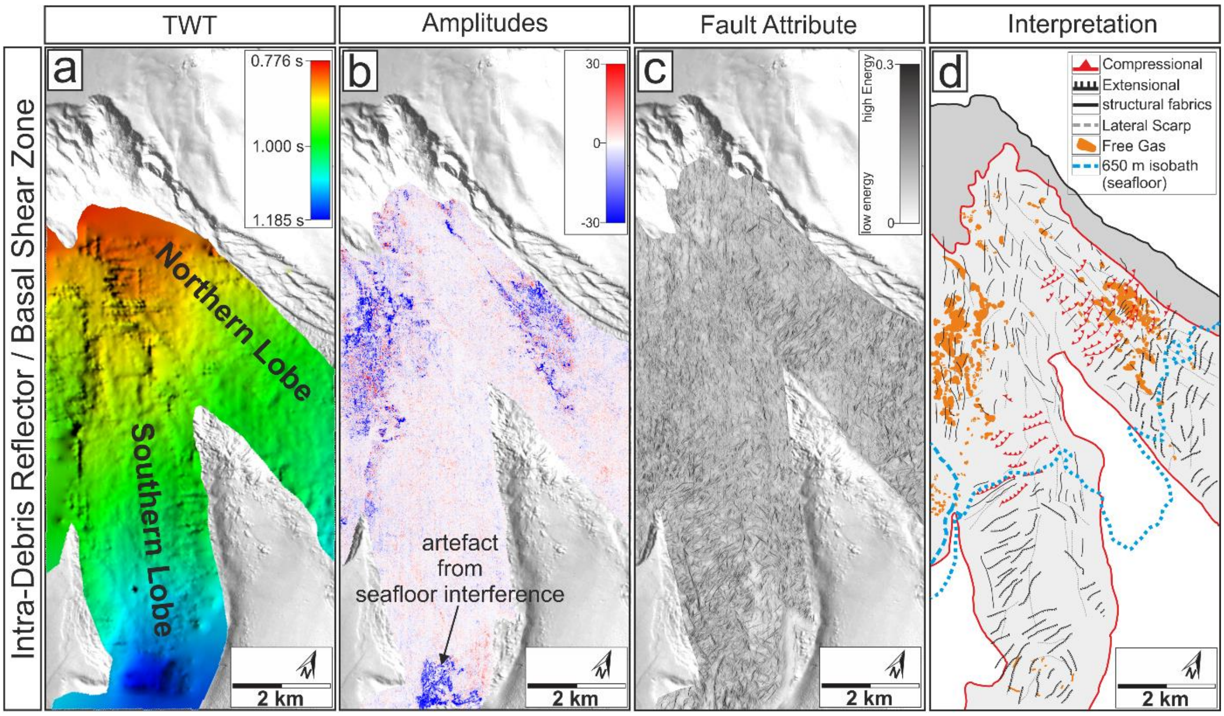

**Figure 5.6.** a) Morphology of the intra-debris reflector (TWT), as mapped throughout the 3D seismic data. The intra-debris reflector is less-continuous in the proximal segments (Fig. 5.2) and was interpolated to obtain a consistent grid throughout the 3D volume. b) Seismic amplitudes from the horizon mapped in (a). c) Fault Attribute extracted on the horizon in (a) - structural fabrics (faults) appear in dark grey. d) Interpretation of free gas distribution at the reflector and structural fabrics based on the maps in (b) and (c).

### 5.5.4. Distribution of free gas and gas hydrates within TLC

2D seismic data indicate that free gas is accumulating at the BGHS within the lower region (deeper than 650 m water depth) of the landslides (Mountjoy et al. 2014; Figs. 5.2, 5.3). Our 3D dataset provides more insight into the distribution of free gas and the gas hydrate system from high-amplitude reflectivity and polarity reversals (Fig. 5.2, 5.7). We have mapped the BGHS throughout the 3D volume and derived associated attribute maps (Fig. 5.3). Few true BSRs occur in the dataset and we have picked the BGHS from truncations of high-amplitude, gas-charged reflections for the bulk of the volume (see Fig. 5.7a). Such reflectivity character at the BGHS is common (particularly in high-frequency datasets) and is sometimes referred to as a discontinuous BSR (e.g. Shedd et al. 2012). Although we observe the BGHS projecting to shallow depths beneath the landslide (Fig. 5.7c) we cannot confidently map any BSR pinch-outs at the seafloor or indications of the BGHS within the landslide debris itself. We did observe free gas escaping into the water column near a lateral shear zone of the landslide (Fig. 5.8a). Free gas in sediments within the GHSZ is not common, but where it does occur it appears to be associated with high-angle normal faults that act as fluid migration pathways (Fig. 5.8b).

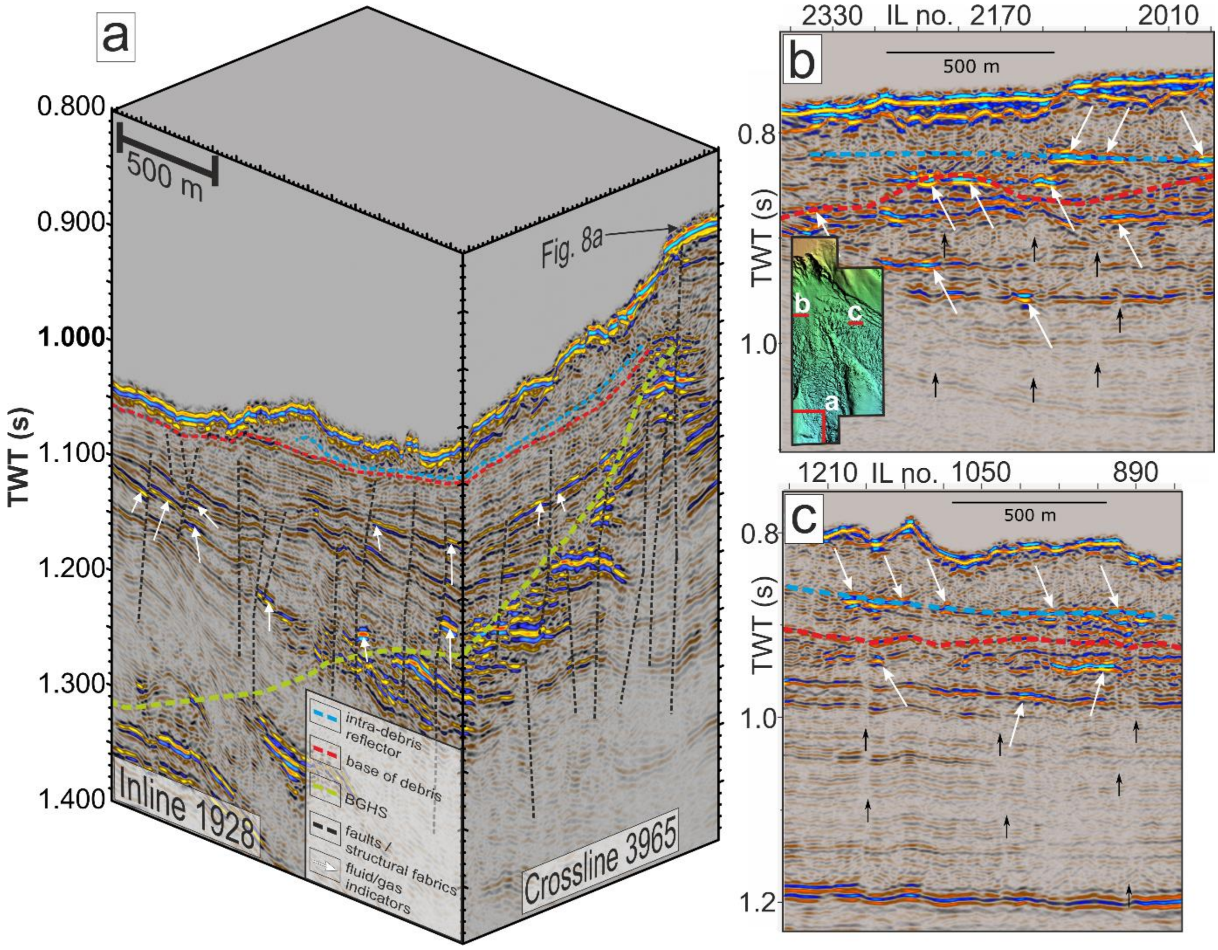

**Figure 5.7**. Examples of fluid migration pathways and gas accumulation beneath and within the landslide debris from SCHLIP-3D. See inset in (b) for the location of each sub-section. a) 3D perspective view in the distal region of the landslide. Free gas escapes from a lateral shear on the western sidewall of TLC, close to where the BGHS is expected to ‘pinch-out’ at the seafloor (see Fig. 5.8a for water column data). Free gas within the GHSZ (highly-reflective, negative-polarity patches; white arrows) occurs on the margins of normal faults, which appear to act as fluid migration pathways. b) Example from the proximal region of the landslide’s southern lobe, where localized free gas patches (white arrows) exist at the intra-debris reflector and deeper in the succession. c) Proximal region of the landslide’s northern lobe. Free gas (white arrows) is more widely distributed at shallower depths, and exists around the intra-debris reflector.

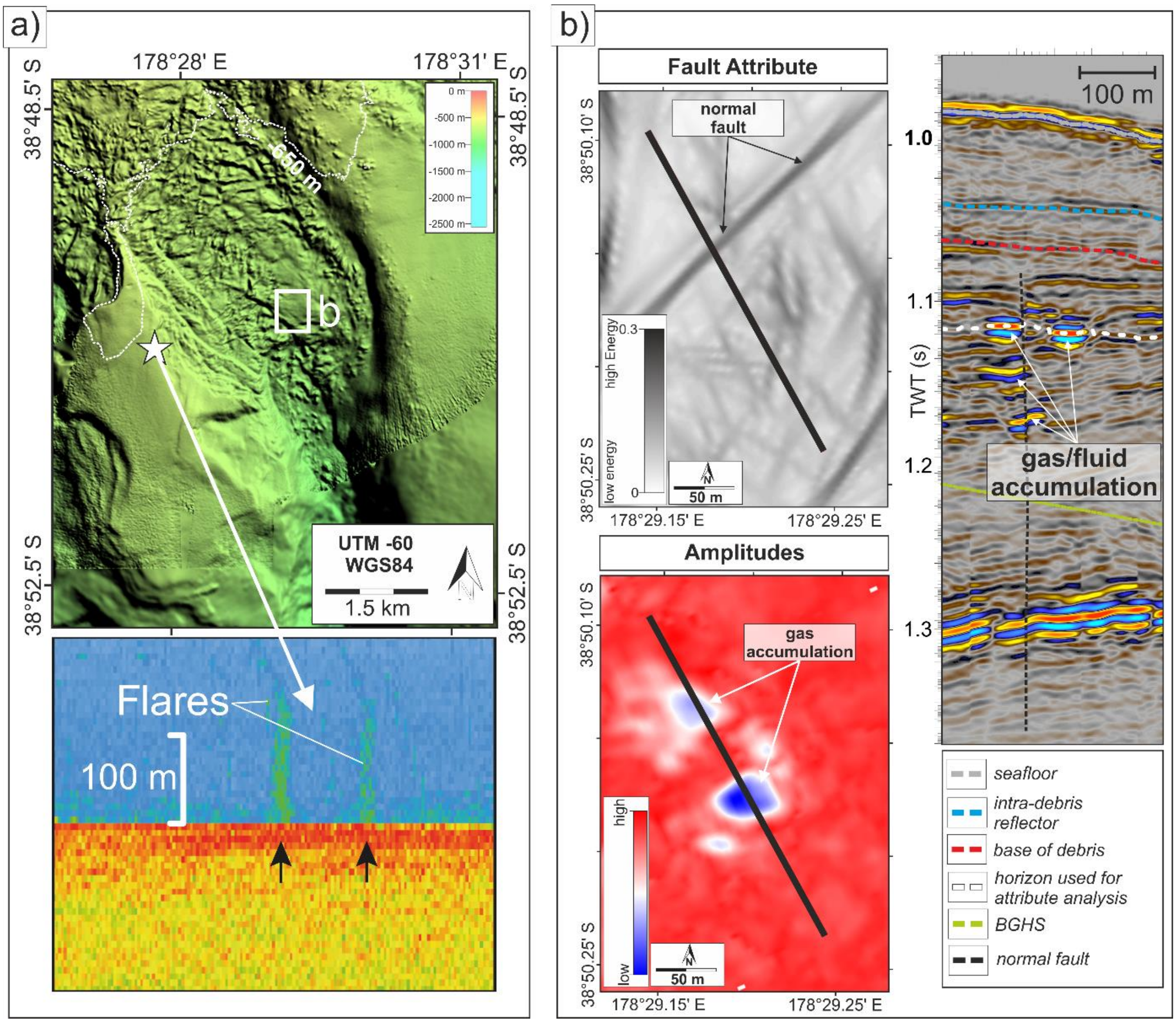

**Figure 5.8.** a) Water column imaging of gas seepage at the southwestern edge of TLC. Two flares were imaged at this location during TAN1404. b) an example of fluid migration indicators along a fault above the BGHS within the extensional regime of TLC (see a for location). The two maps (upper and lower) show the Fault Attribute and amplitude, respectively, extracted along the dotted white line in the seismic section to the right. The seismic section (on the right) is an arbitrary extraction along the orientation of the black lines shown in the Fault Attribute and Amplitude maps. Such gas migration along faults in the dataset is relatively rare (not a widespread feature of all faults mapped).

## 5.6. Discussion

Analysis of the P-Cable data has revealed several significant aspects of this landslide complex that were not previously apparent. We have mapped two distinct units in the landslide complex. The upper unit is a relatively continuous-thickness debris body with no evidence for internal partitioning in terms of continuous reflectivity, indicating that it is behaving mechanically as a single landslide body. The lower unit however is a composite body made up of multiple poorly-defined MTD's characterized by chaotic reflectivity separated by coherent reflectors. The two landslide units are separated by a prominent reflector (the internal reflector) that we will subsequently discuss as a critical component of the mechanical behavior of the TLC. The morphology of the basal surface of the lower landslide unit shows elongate depressions in the direction of debris movement and we interpret these as pre-existing topographic features (e.g. channels or landslide scars) that the landslide debris is infilling. It is unlikely that the multiple small scale MTD's that make up this unit would be capable of eroding the seafloor in such a significant way. We have used the 3D seismic data to map the variable distribution of gas within and beneath the landslide. The spatial distribution of these features within the TLC enables a better understanding of the deformation behavior and potential role of free gas migration and accumulation in subaqueous slope instability.

### 5.6.1. Intra-debris reflectivity

The intra-debris reflector is represented by one wavelet that is present as a mostly continuous feature through most of the landslide debris within the seismic volume. It has negative polarity with respect to the seafloor reflector (Figs. 5.5c, d). The surface picked on the reflector has a relatively linear dip in the direction of landslide movement without much topographic expression (Fig. 5.6). Based on sub-bottom profiler data it is apparent that the reflector does not mimic the seabed (Fig. 5.2b).

We consider three possibilities for the reflector. 1) It is an artifact in the data. 2) It is an intact hemipelagic sediment drape or a tephra deposit between two MTDs. 3) It is neither hemiplegic sediments nor a tephra deposit, but rather marks a distinct material contrast (boundary) between successive MTDs. Mountjoy et al. (2009; 2014) postulated a reactivation of the landslide complex. By assessing scenarios 2 and 3, we will have investigate how the upper landslide unit could have been reactivated in a post-failure stage.

#### 5.6.1.1. Is this reflector an artifact?

Mountjoy et al (2014) observed this reflector approximately mimicking the seafloor in 2D seismic data and concluded that it represents a geophysical artifact. Our 3D seismic data show that this feature does not mimic the seafloor everywhere and has an independent topography (Fig. 5.2). The reflector is imaged in both the 3D seismic data and the sub-bottom profiling data, indicating this is not a source or processing artifact. Hence, we rule out the possibility that this reflector is a geophysical artifact.

#### 5.6.1.2. Intra-debris reflector caused by lithological boundary

The internal reflector could represent a lithological boundary or thin layer dividing the upper and the lower MTDs. Either a fine or coarse grained horizon draped over unit 2 could induce a geophysical response in seismic reflection data. Previous studies (e.g. Harders et al., 2010; Kuhlman et al. 2015) have showed that tephra layers might influence translational sliding during seismic loading. Coarse grained volcanic tephra are widely recognized across the margin (e.g. Orpin 20014) and may be a widespread tephra layer could be one explanation for the observed geophysical response (Fig. 5.9C).

Alternatively, the geophysical response could be due to a thin sequence of fine grained sediments such as a hemipelagic drape or a regional fine grained event bed. Development of a hemipelagic drape would require prolonged sediment accumulation to form a seismically-imageable reflector in between the two mass transport events.

For either fine or coarse grained sediment drape between the upper and lower debris units, the sedimentation process would lead to local build-up of sediment within topographic lows on the surface of the lower MTD (Fig. 5.9b). Localised sediment accumulation would manifest itself in seismic data as small packages of multiple-wavelet coherent reflectivity, which we do not observe. Furthermore, the high resolution TOPAS profile in Fig. 5.2 characterizes the intra-debris reflector as a boundary between two acoustic units and does not indicate a "package" of material at any location. Based on the lack of evidence for a package of sediment we conclude that the intra debris reflector is unlikely to represent a discrete package of either coarse or fine grained sediments.

In the absence of sedimentation between the upper and lower debris units it is possible that the base of the upper MTD has a higher acoustic impedance than the top of the lower MTD, resulting in a negative polarity reflection. However, given that we expect the same source region and therefore lithological composition for both MTDs, a difference in density and/or velocity between the two would require significant differences in compaction to develop either in-situ or related to the landslide processes. In Fig. 5.9c we show how the base of the upper MTD, which would have to be more compacted than the top of the immediately underlying MTD, could generate a negative polarity reflection. We deem this scenario rather unlikely, as deposition of the younger MTD would itself cause increased compaction of the lower MTD.

#### 5.6.1.3. Intra-debris reflector caused by pore fluids / pore pressure

As a pure lithological boundary is not likely to explain the reversed polarity intra-debris reflector, we now consider the role of pore fluids and pore pressure in our analysis. Reverse polarity can be caused by either a distinct physical properties contrast (as discussed above), by free gas (e.g. MacKay et al. 1994) or excess fluid pressure (e.g. Moore et al. 2001). In contrast to the gassy horizons beneath the BGHS (Fig. 5.2), the reflector has relatively weak reflectivity. Given the lower amplitudes we consider gas unlikely to be the cause of polarity reversal, but the presence of pressurized fluid cannot be discounted (Fig. 5.9D).

The underlying intact sequence reveals a dense fault network in the lower slide region with an anastomosing network of NNE-SSW striking structures (Figs. 5.2, 5.3). Faults propagate upwards to the base of debris but do not penetrate the slide base, indicating that no displacement has occurred on these faults since the slide last moved. Faults are spatially coincident with the gas hydrate stability zone and their strike approximately follows the orientation of the upper limit of gas hydrate stability (Fig. 5.3). The lack of polygonal structures in the 3D data indicates that the faults are more likely to be tectonic in nature than having a genesis related to fluid flow and overpressure (Böttner et al. 2018).

These faults may act as fluid migration pathways and focus fluid flow from lower strata to the intra-debris reflector. Leakage may occur localized to regions where the faults are most likely to slip and fault slip promotes fault-parallel flow. Once this mechanism ruptures the sediments, the permeability increases and high pore pressure is dissipated (Wiprut and Zoback, 2000). This steady state or episodic mechanism might hinder the development of gas chimneys or pipe structures (Plaza-Faverola et al., 2014).

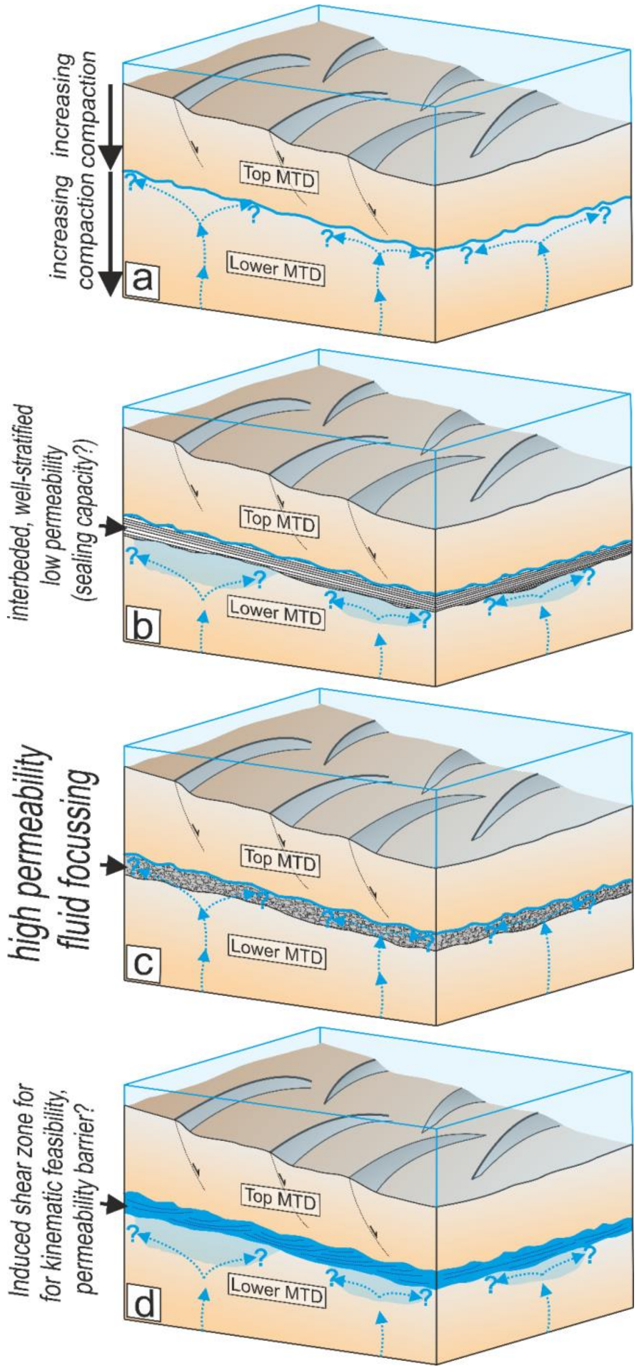

**Figure 5.9**. Conceptual model of geological features that could result in the observed geophysical imaging of the intra-debris reflector.

### 5.6.2. Intra-debris reflector as indicator for internal deformation and slide remobilisation

Landslide movement and deformation is controlled by gravitational forces and primarily takes place along surfaces or zones of reduced friction thus leading to reduced shear strength. In the terrestrial realm and especially at rock glaciers, these zones show a high water or ice/water content, which reduces the shear strength significantly (Haeberli et al., 2006; Ikeda and Matsuoka, 2006). In the marine realm, it is assumed that near surface sedimentary systems are water saturated. To reduce shear strength of sediments in these environments, processes such as focused fluid migration and seismic (earthquake) excitation can increase pore fluid pressure, leading to a reduction of shear strength and possibly liquefaction.

TLC's deformation is partitioned between compression in the proximal and extension in distal part of the landslide (Fig. 5.2). The transition between these kinematic domains is marked by a prominent break in slope (Fig. 5.2). The intra-debris reflector does not entirely mimic this slope break and 3D seismic as well as TOPAS data show that it is relatively planar in long section (Fig. 5.2). Mountjoy et al. (2014) suggested repeated slide movements, in the distal extensional zone. Our 3D seismic data reveal a more continuous reflector in the distal extensional zone. This observation supports the idea of repeated movements if repeated shear deformation modifies the physical properties of the sediments, leading to a well-developed and continuous seismic horizon.

In addition to these along-slope changes there is a disconnection between deformation in the landslide units above and below the intra-debris reflector (Fig. 5.2). This suggests that post-emplacement deformation in the upper slide terminates at the intra-debris reflector. Our 3D seismic analysis reveals a significant amount of structural information that was previously not known from 2D seismic data presented by Mountjoy et al. (2009; 2014). Structural deformation occurs throughout the upper landslide unit, corroborating the compression versus extension observations made by Mountjoy et al (2014) (Fig. 5.2). Faults within this upper unit sole down to the intra-debris reflector, but do not penetrate through it. This restriction of deformation to the upper landslide unit is a key observation in our data. We hence interpret that a remobilization of the TLC has taken place wholly within this upper landslide unit and is utilizing the intra-debris reflector as a basal shear surface. This is analogous to shear zones observed in terrestrial slowly creeping landslide complexes. Marine and subaerial exposed subaqueous landslides rarely show indications for such a basal shear zone (e.g. Frey-Martinez et al. 2006; Lee & Stow 2007) and the nature of subaqueous landslide basal shear zones is poorly known.

### 5.6.3. Free gas beneath and within the landslide: an agent in slope destabilization?

There are several important observations about the distribution of free gas both beneath and within the TLC. Extensive free gas accumulations occur in dipping layers beneath the BGHS (Figs. 5.2, 5.7a). There is local evidence for gas that migrated from that reservoir into the GHSZ, e.g. through sub-vertical features like faults (e.g. Fig. 5.8b). We also observe one place where gas is actively migrating out of the seafloor near the up-dip limit of hydrate stability, at a transverse shear on the western margin of the landslide (Fig. 5.8a). These observations are typical for many other places on the Hikurangi margin (e.g. Crutchley et al. 2010; Netzeband et al. 2010; Plaza-Faverola et al. 2014) and elsewhere around the world (e.g. Gorman et a. 2002; Flemings et al. 2003; Petersen et al. 2010), where high local fluid flux through sub-vertical structures means that gas co-exists with gas hydrate within the GHSZ.

Despite the widespread indications of free gas beneath the BGHS and the localized examples of gas migration through the GHSZ, there is a general lack of gas on the intra-debris reflector in the central to distal parts of the slide (Fig. 5.6). If the intra-debris reflector represents the modern glide plane (basal shear zone) for extensional deformation, the question arises: What role, if any, does gas play in destabilizing the landslide?

It could be argued that periodic movement of the slide mass causes extensional structures to dilate and thereby release gas from the basal shear zone through the overlying landslide mass into the water column. If this were the case, it would indicate that we surveyed the landslide during a phase where the gas has been released from the basal shear zone. However, such an explanation is probably unnecessarily complicated, and we deem it unlikely that a movement phase would release all gas from the basal shear zone. A simpler and preferable explanation would be that the lack of free gas on the basal shear zone indicates that gas at that level in the landslide system is not playing a key role in landslide movement.

As landslide debris is often over-consolidated and of low bulk density, it is likely that there is a significant permeability contrast at the basal shear zone (Dugan 2012). In this case, it would be feasible that fluid flowing into this basal shear zone from below becomes trapped by the overlying low-permeability mass and thereby accumulates excess fluid pressure. Upward-migrating fluid could comprise both gas and water, and given the scarcity of free gas indicators on the basal shear zone in the landslide's extensional domain, water may be the primary agent for excess pressure accumulation. Here, the dense network of faults within the GHSZ would provide suitable migration pathways for ascending liquids. Excess fluid pressure accumulating at the BGHS, a process that has been observed elsewhere (Flemings et al. 2003), could cause dilation of the faults and a dramatic increase in structural permeability to allow rapid upward fluid flow (Sibson 1990; Hornbach et al. 2004).

We interpret the intra-debris reflector as the basal shear surface/zone of TLC's upper landslide unit. We recognize that free gas is widespread beneath the landslide, and that it does migrate into the basal shear zone in some (albeit few) places. However, we do not observe migration pathways throughout the landslide. This has implications for our understanding of other subaqueous landslides in similar settings. Micallef et al. (2016) document a high amplitude reflector in the intact sedimentary sequence beneath Tuaheni North (Fig. 5.1) that they interpret to be gas charged. This reflector becomes the glide plane for a subaqueous landslide and at that point the amplitudes decrease significantly, indicating that the gas has "bled' from the horizon. The observation of low amplitude basal reflectivity for subaqueous landslides has been made in other places where fluid migration is interpreted to be linked to landslide occurrence (Berndt et al. 2012). We consider that increased fluid pressure may have contributed to reduced frictional properties and facilitated slope failure, but once a failure has occurred the pressure has been reduced.

### 5.6.4. Driving mechanisms of reactivation in the TLC

Our analysis has shown that any reactivation in the TLC is taking place within an upper debris unit with a potential basal detachment surface that was not recognised by previous studies (e.g. Mountjoy et al. 2009; 2014). Previous hypotheses for landslide reactivation proposed by Mountjoy et al. (2014) were (1) Gas hydrate dissociation could result in excess pore pressure within the upper reaches of the landslide. (2) Overpressure below low-permeability gas hydrate-bearing sediments could cause hydrofracturing in the gas hydrate zone valving excess pore pressure into the landslide body. (3) Gas hydrate-bearing sediment could exhibit time-dependent plastic deformation enabling glacial-style deformation. These were proposed on top of the potential destabilising factors suggested by Mountjoy et al. (2009) which included earthquake ground shaking and rapid sediment loading in the up-slope region.

From our detailed 3D analysis of the distribution of gas and gas hydrate indicators we do not see evidence for gas hydrates (from localised amplitude anomalies, c.f. Paganoni et al. 2017) within the upper landslide unit anywhere within the data. For gas hydrates to form this shallow in the section (i.e. well above the base of hydrate stability) there would need to be high gas flux along focused flow pathways. Although there is evidence for such focused flow in some places (e.g. Fig. 5.7), we do not expect significant gas hydrate occurrences within the upper (reactivated) landslide unit. This means that hypotheses 1 and 3 of Mountjoy et al. (2014) are not supported by our data. We do map widespread free gas deeper within the system and observe several locations where gas pockets occur along faults, indicating gas migration related to subvertical structures and localised gas accumulation within the landslide itself (Fig. 5.7 and Fig. 5.8). These observations support a form of hypothesis 2 of Mountjoy et al. (2014) that gas is migrating into the critical mechanical zone at the base of the landslide and building up overpressure leading to reactivation of movement. Similar mechanisms to this have been proposed by other workers (e.g. Berndt et al., 2012; Li et al., 2016; Elger et al., 2018) implying this could be a wide-spread process.

Distinctive differences between the TLC and many other landslides, such as the amount of debris remaining in the landslide scar, the surface morphology analogous to regularly active terrestrial landslides, and the distribution of kinematic indicators (upslope compression vs downslope extension and the presence of an internal basal shear surface) have driven the search for perturbations on similar timeframes to that provided by rainfall induced excess pore pressure on land. We cannot however discount the potential role of earthquake-generated ground shaking in landslide reactivation in the TLC. Although the recurrence time for high magnitude ground motion is hundreds of years, the low rate of geomorphic change in deep water seafloor environments can preserve sharply defined geomorphic features for long periods of time. The lack of significant undeformed hemipelagic drape across the surface of the TLC, despite high sedimentation rates (Alexander et al 2010; Kuhlman et al., 2018; this study), indicates that this landslide is not a relict feature. To the contrary, the Tuaheni Landslide Complex has been subject to ongoing reactivation through time and remains one of the best global study sites for understanding subaqueous landslide reactivation processes.

## 5.7. Conclusions

We observe an intra-debris reflector within the Tuaheni Landslide Complex, which we interpret as a critical mechanical component of the reactivated subaqueous landslide. We cannot conclude a unique solution for the physical nature/sedimentology of this geophysical feature from the 3D seismic data analysed here, but note that it has to represent a distinct contrast in physical properties. We interpret this intra-debris reflector as a basal shear feature for this landslide, and based on our findings suggest that many other subaqueous landslides will exhibit similar mechanical elements.

We map free gas throughout the slope sediments within which the landslide complex occurs. Gas is migrating up from beneath the landslide and in places it is focused into the basal shear feature. However, this gas accumulation at the base of the landslide is not widespread. We envisage two scenarios that explain this observation. 1) Gas is not accumulating regionally on the basal shear and therefore does not play any role in landslide mobility or 2) gas builds up on the basal shear until movement takes place, releasing the gas and removing any evidence for its prior existence at that point evidence for it is removed. Based on our data, we do not rule out focused water flow and accumulation at the basal shear surface, as this mechanism could also lead to excess fluid pressure and slope destabilization.

Our 3D characterization of the internal horizon within the Tuaheni landslide should allow easier recognition of similar features in other locations, even if only 2D data are available. A better understanding of the nature of basal shear zones in terms of physical properties is critical **for** understanding landslides in all subaqueous environments.

## Acknowledgements

The collection and processing of the P-Cable 3D volume was jointly funded by the New Zealand Ministry for Business Innovation and Employment (MBIE), NIWA and GNS Science Core funding and the Deutsche Forschungsgemeinschaft (DFG-Grant BI 404/7 | KR 2222/18). JM and GC are funded by Royal Society of New Zealand Marsden Fund Grant NIW1603. AM is funded by the European Research Council under the European Union's Horizon 2020 Programme (grant agreement n° 677898). We thank Danny Brothers and Kei Ogata for their extensive and constructive revisions. We thank the officers and crew of RV Tangaroa and all the ship board participants who made the data collection possible.

## References

Alexander, C. R., Walsh, J. P., & Orpin, A. R. (2010). Modern sediment dispersal and accumulation on the outer Poverty continental margin. *Marine Geology*, *270*(1-4), 213-226.

Baeten, N. J., Laberg, J. S., Vanneste, M., Forsberg, C. F., Kvalstad, T. J., Forwick, M., ... & Haflidason, H. (2014). Origin of shallow submarine mass movements and their glide planes—Sedimentological and geotechnical analyses from the continental slope off northern Norway. *Journal of Geophysical Research: Earth Surface*, *119*(11), 2335-2360.

Barker, D. H., Sutherland, R., Henrys, S., & Bannister, S. (2009). Geometry of the Hikurangi subduction thrust and upper plate, North Island, New Zealand. *Geochemistry, Geophysics, Geosystems*, *10*(2).

Barnes, P. M., Cheung, K. C., Smits, A. P., Almagor, G., Read, S. A., Barker, P. R., & Froggatt, P. (1991). Geotechnical analysis of the Kidnappers Slide, upper continental slope, New Zealand. *Marine Georesources & Geotechnology*, *10*(1-2), 159-188.

Barnes, P. M., Lamarche, G., Bialas, J., Henrys, S., Pecher, I., Netzeband, G. L., ... & Crutchley, G. (2010). Tectonic and geological framework for gas hydrates and cold seeps on the Hikurangi subduction margin, New Zealand. *Marine Geology*, *272*(1-4), 26-48.

Beavan, J., Tregoning, P., Bevis, M., Kato, T., & Meertens, C. (2002). Motion and rigidity of the Pacific Plate and implications for plate boundary deformation. *Journal of Geophysical Research: Solid Earth*, *107*(B10), ETG-19.

Berndt, C., Costa, S., Canals, M., Camerlenghi, A., de Mol, B., & Saunders, M. (2012). Repeated slope failure linked to fluid migration: the Ana submarine landslide complex, Eivissa Channel, Western Mediterranean Sea. *Earth and Planetary Science Letters*, *319*, 65-74.

Böttner, C., Gross, F., Geersen, J., Crutchley, G. J., Mountjoy, J. J., & Krastel, S. (2018). Marine forearc extension in the Hikurangi margin: New insights from high-resolution 3-D seismic data. *Tectonics*, *37*(5), 1472-1491.https://doi.org/10.1029/2017TC004906

Bull, S., Cartwright, J., & Huuse, M. (2009). A review of kinematic indicators from mass-transport complexes using 3D seismic data. *Marine and Petroleum Geology*, *26*(7), 1132-1151.

Carey, S. (1997). Influence of convective sedimentation on the formation of widespread tephra fall layers in the deep sea. *Geology*, *25*(9), 839-842.

Clarke, J. E. H., Marques, C. R. V., & Pratomo, D. (2014). Imaging active mass-wasting and sediment flows on a fjord delta, Squamish, British Columbia. In *Submarine Mass Movements and Their Consequences* (pp. 249-260). Springer, Cham.

Crutchley, G. J., Geiger, S., Pecher, I. A., Gorman, A. R., Zhu, H., & Henrys, S. A. (2010). The potential influence of shallow gas and gas hydrates on sea floor erosion of Rock Garden, an uplifted ridge offshore of New Zealand. *Geo-Marine Letters*, *30*(3-4), 283-303.

Crutchley, G. J., Gorman, A. R., Pecher, I. A., Toulmin, S., & Henrys, S. A. (2011). Geological controls on focused fluid flow through the gas hydrate stability zone on the southern Hikurangi Margin of New Zealand, evidenced from multi-channel seismic data. *Marine and Petroleum Geology*, *28*(10), 1915-1931.

Dugan, B. (2012). Petrophysical and consolidation behavior of mass transport deposits from the northern Gulf of Mexico, IODP Expedition 308. *Marine Geology*, *315*, 98-107.

Elger, J., Berndt, C., Rüpke, L., Krastel, S., Gross, F., & Geissler, W. H. (2018). Submarine slope failures due to pipe structure formation. *Nature communications*, *9*(1), 715.DOI: 10.1038/s41467-018-03176-1.

Ellis, S., Pecher, I., Kukowski, N., Xu, W., Henrys, S., & Greinert, J. (2010). Testing proposed mechanisms for seafloor weakening at the top of gas hydrate stability on an uplifted submarine ridge (Rock Garden), New Zealand. *Marine Geology*, *272*(1-4), 127-140.

Festa, A., Pini, G. A., Dilek, Y., & Codegone, G. (2010). Mélanges and mélange-forming processes: a historical overview and new concepts. *International Geology Review*, *52*(10-12), 1040-1105.

Field, M. E., & Barber, J. H. J. (1993). A submarine landslide associated with shallow seafloor gas and gas hydrates off Northern California. In *Submarine landslides: selected studies in the US exclusive economic zone* (Vol. 2002, pp. 151-157). Reston, Va, USA: US Geological Survey.

Flemings, P. B., Liu, X., & Winters, W. J. (2003). Critical pressure and multiphase flow in Blake Ridge gas hydrates. *Geology, 31*(12), 1057-1060.

Frey-Martínez, J., Cartwright, J., & James, D. (2006). Frontally confined versus frontally emergent submarine landslides: A 3D seismic characterisation. *Marine and Petroleum Geology*, *23*(5), 585-604.

Gorman, A. R., Holbrook, W. S., Hornbach, M. J., Hackwith, K. L., Lizarralde, D., & Pecher, I. (2002). Migration of methane gas through the hydrate stability zone in a low-flux hydrate province. *Geology*, *30*(4), 327-330.

Haeberli, W., Hallet, B., Arenson, L., Elconin, R., Humlum, O., Kääb, A., ... & Mühll, D. V. (2006). Permafrost creep and rock glacier dynamics. *Permafrost and periglacial processes*, *17*(3), 189-214.

Hampton, M. A., Lee, H. J., & Locat, J. (1996). Submarine landslides. *Reviews of geophysics, 34*(1), 33-59.

Harders, R., Kutterolf, S., Hensen, C., Moerz, T., & Brueckmann, W. (2010). Tephra layers: a controlling factor on submarine translational sliding?. *Geochemistry, Geophysics, Geosystems*, *11*(5).

Hornbach, M. J., Saffer, D. M., & Holbrook, W. S. (2004). Critically pressured free-gas reservoirs below gas-hydrate provinces. *Nature*, *427*(6970), 142.

Hungr, O., Leroueil, S., & Picarelli, L. (2014). The Varnes classification of landslide types, an update. *Landslides*, *11*(2), 167-194.

Ikeda, A., & Matsuoka, N. (2006). Pebbly versus bouldery rock glaciers: Morphology, structure and processes. *Geomorphology*, *73*(3-4), 279-296. doi:10.1016/j.geomorph.2005.07.015.

Joanne, C., Lamarche, G., & Collot, J. Y. (2013). Dynamics of giant mass transport in deep submarine environments: the Matakaoa Debris Flow, New Zealand. *Basin Research*, *25*(4), 471-488.

Locat, J., & Lee, H. J. (2002). Submarine landslides: advances and challenges. *Canadian Geotechnical Journal*, *39*(1), 193-212.

Kawamura, K., Ogawa, Y., Oyagi, N., Kitahara, T., & Anma, R. (2007). Structural and fabric analyses of basal slip zone of the Jin'nosuke-dani landslide, northern central Japan: its application to the slip mechanism of decollement. *Landslides*, *4*(4), 371-380.

Klauda, J. B., & Sandler, S. I. (2005). Global distribution of methane hydrate in ocean sediment. *Energy & Fuels*, *19*(2), 459-470.

Kuhlmann, J., Huhn, K., & Ikari, M. J. (2016). Do Embedded Volcanoclastic Layers Serve as Potential Glide Planes?: An Integrated Analysis from the Gela Basin Offshore Southern Sicily. In *Submarine mass movements and their consequences* (pp. 273-280). Springer, Cham.

Lee, S. H., & Stow, D. A.V. (2007). Laterally contiguous, concave-up basal shear surfaces of submarine landslide deposits (Miocene), southern Cyprus: differential movement of sub-blocks within a single submarine landslide lobe. *Geosciences Journal*, *11*(4), 315-321.

Li, A., Davies, R. J., & Yang, J. (2016). Gas trapped below hydrate as a primer for submarine slope failures. *Marine Geology*, *380*, 264-271.

MacKay, M. E., Jarrard, R. D., Westbrook, G. K., & Hyndman, R. D. (1994). Origin of bottom-simulating reflectors: geophysical evidence from the Cascadia accretionary prism. *Geology*, *22*(5), 459-462.

McIver, R. D. (1982). Role of naturally occurring gas hydrates in sediment transport. *AAPG bulletin*, *66*(6), 789-792.

Micallef, A., Mountjoy, J. J., Krastel, S., Crutchley, G., & Koch, S. (2016). Shallow gas and the development of a weak layer in submarine spreading, Hikurangi margin (New Zealand). In *Submarine Mass Movements and their Consequences* (pp. 419-426). Springer, Cham.

Moore, G. F., Taira, A., Klaus, A., Becker, L., Boeckel, B., Cragg, B. A., ... & Hisamitsu, T. (2001). New insights into deformation and fluid flow processes in the Nankai Trough accretionary prism: Results of Ocean Drilling Program Leg 190. *Geochemistry, Geophysics, Geosystems*, *2*(10).

Mountjoy, J. J., McKean, J., Barnes, P. M., & Pettinga, J. R. (2009). Terrestrial-style slow-moving earthflow kinematics in a submarine landslide complex. *Marine Geology*, *267*(3-4), 114-127.

Mountjoy, J. J., & Barnes, P. M. (2011). Active upper plate thrust faulting in regions of low plate interface coupling, repeated slow slip events, and coastal uplift: Example from the Hikurangi Margin, New Zealand. *Geochemistry, Geophysics, Geosystems*, *12*(1).

Mountjoy, J. J., Pecher, I., Henrys, S., Crutchley, G., Barnes, P. M., & Plaza-Faverola, A. (2014). Shallow methane hydrate system controls ongoing, downslope sediment transport in a low-velocity active submarine landslide complex, H ikurangi M argin, N ew Z ealand. *Geochemistry, Geophysics, Geosystems*, *15*(11), 4137-4156.

Ogata, K., Mutti, E., Pini, G. A., & Tinterri, R. (2012). Mass transport-related stratal disruption within sedimentary mélanges: examples from the northern Apennines (Italy) and south-central Pyrenees (Spain). *Tectonophysics*, *568*, 185-199.

Ogata, K., Mountjoy, J. J., Pini, G. A., Festa, A., & Tinterri, R. (2014). Shear zone liquefaction in mass transport deposit emplacement: A multi-scale integration of seismic reflection and outcrop data. *Marine Geology*, *356*, 50-64.

Ogata, K., Pini, G. A., Festa, A., Pogačnik, Ž., Tunis, G., Mountjoy, J. J., ... & Strasser, M. (2014). High-resolution studies of mass transport deposits: outcrop perspective for understanding modern submarine slope failure and associated natural hazards. In *Engineering Geology for Society and Territory–Volume 4* (pp. 209-213). Springer, Cham.

Orpin, A. R. (2004). Holocene sediment deposition on the Poverty-slope margin by the muddy Waipaoa River, East Coast New Zealand. *Marine Geology*, *209*(1-4), 69-90.

Netzeband, G. L., Krabbenhöft, A., Zillmer, M., Petersen, C. J., Papenberg, C., & Bialas, J. (2010). The structures beneath submarine methane seeps: seismic evidence from Opouawe Bank, Hikurangi Margin, New Zealand. *Marine Geology*, *272*(1-4), 59-70.

Pedley, K. L., Barnes, P. M., Pettinga, J. R., & Lewis, K. B. (2010). Seafloor structural geomorphic evolution of the accretionary frontal wedge in response to seamount subduction, Poverty Indentation, New Zealand. *Marine Geology*, *270*(1-4), 119-138.

Paull, C. K., Buelow, W. J., Ussler III, W., & Borowski, W. S. (1996). Increased continental-margin slumping frequency during sea-level lowstands above gas hydrate–bearing sediments. *Geology*, *24*(2), 143-146.

Pedley, K. L., Barnes, P. M., Pettinga, J. R., & Lewis, K. B. (2010). Seafloor structural geomorphic evolution of the accretionary frontal wedge in response to seamount subduction, Poverty Indentation, New Zealand. *Marine Geology*, *270*(1-4), 119-138.

Petersen, C. J., Bünz, S., Hustoft, S., Mienert, J., & Klaeschen, D. (2010). High-resolution P-Cable 3D seismic imaging of gas chimney structures in gas hydrated sediments of an Arctic sediment drift. *Marine and Petroleum Geology*, *27*(9), 1981-1994.

Plaza-Faverola, A., Pecher, I., Crutchley, G., Barnes, P. M., Bünz, S., Golding, T., ... & Bialas, J. (2014). Submarine gas seepage in a mixed contractional and shear deformation regime: Cases from the Hikurangi oblique-subduction margin. *Geochemistry, Geophysics, Geosystems*, *15*(2), 416-433.

Sibson, R. H. (1990). Conditions for fault-valve behaviour. *Geological Society, London, Special Publications*, *54*(1), 15-28.

Shedd, W., Boswell, R., Frye, M., Godfriaux, P., & Kramer, K. (2012). Occurrence and nature of "bottom simulating reflectors" in the northern Gulf of Mexico. *Marine and Petroleum Geology*, *34*(1), 31-40.

Stirling, M., McVerry, G., Gerstenberger, M., Litchfield, N., Van Dissen, R., Berryman, K., ... & Lamarche, G. (2012). National seismic hazard model for New Zealand: 2010 update. *Bulletin of the Seismological Society of America*, *102*(4), 1514-1542.

Sultan, N., Cochonat, P., Foucher, J. P., & Mienert, J. (2004). Effect of gas hydrates melting on seafloor slope instability. *Marine geology*, *213*(1-4), 379-401.

Urlaub, M., Talling, P. J., Zervos, A., & Masson, D. (2015). What causes large submarine landslides on low gradient (< 2°) continental slopes with slow (∼ 0.15 m/kyr) sediment accumulation?. *Journal of Geophysical Research: Solid Earth*, *120*(10), 6722-6739.

Vulliet, L., & Hutter, K. (1989, March). Viscous-type sliding laws for landslides: Can Geotech JV25, N3, Aug 1988, P467–477. In *International Journal of Rock Mechanics and Mining Sciences & Geomechanics Abstracts* (Vol. 26, No. 2, p. 87). Pergamon.

Wiprut, D., & Zoback, M. D. (2000). Fault reactivation and fluid flow along a previously dormant normal fault in the northern North Sea. *Geology*, *28*(7), 595-598.

Yu, Y., Kelley, C. L., Mardanova, I. M. (2015) U.S. patent no. 9,105,075. *Washington, DC: U.S. Patent and Trademark Office.*

# 6. Above the pipe – Geometry and formation processes of cold seeps in sands and sandstone derived from UAV-based analyses of an Early Eocene methane seep system, near Varna, Bulgaria.

Christoph Böttner, Ben J. Callow, Bettina Schramm, Felix Gross, Jacob Geersen, Mark Schmidt, Atanas Vassilev, Petar Petsinski, Christian Berndt

To be submitted to Solid Earth: Faults, fractures, and fluid flow in the shallow crust.

Methane seep system with vertical fluid conduits, near Varna, Bulgaria

## 6.1. Abstract

Focused fluid flow shapes the evolution of marine sedimentary basins by transferring fluids and pressure across geological formations. Natural fluid flow systems alter geological strata and the resulting fluid conduits can hydraulically connect deep strata with the seafloor. Vertical fluid conduits may form where localized overpressure breaches the sealing cap rock (permeability barrier) and thereby transport fluids and overpressure towards shallower reservoirs or the surface. However, in the Pobiti Kamani and Beloslav Quarry fluid flow system outcrops (~15 km West of Varna, Bulgaria) the largest known carbonate conduits formed in high-permeable, unconsolidated sands. Here, we use a customer-grade UAV (unmanned aerial vehicle) equipped with an optical RGB sensor camera in combination with hand-drilled rock samples to calculate geologically-calibrated ortho-rectified image mosaic, digital elevation and point clouds. Based on this data, we map fracture networks and vertical fluid conduits over kilometer-scale distances (km) and with very high accuracy (cm). Both outcrops comprise several hundred vertical calcite-cemented carbonate conduits (pipes) and sub-horizontal carbonate-cemented interbeds, which differentiate from the hosting sand formation only by their amount of cementation. Both features are remnants of a focused marine methane seepage system that developed during the Early Eocene in the marine realm of the Tethys margin. Carbonate precipitation likely took place on the periphery of point-source methane seeps, which were determined by the fractured subsurface, forming the outer walls of the pipes with a progressive inward growth, which led to self-sustaining and self-reinforcing focused fluid flow. Two different carbon and oxygen isotope signature groups likely indicate that ambient seawater and advected fresh/brine water were involved in the carbonate precipitation from biogenic methane. Current submarine groundwater discharge from sand formations may evolve a similar, where vertical fluid conduits focused flow from below.

## 6.2. Introduction

Focused fluid flow shapes the evolution of marine sedimentary basins by transferring fluids and pressure across geological formations. It alters geological strata and the resulting fluid conduits can hydraulically connect deep strata with the seafloor (Cartwright et al., 2007; Løseth et al., 2009; Andresen, 2012; Karstens & Berndt, 2015). Seismic imaging is an effective way to investigate fluid flow systems as seismic velocity and attenuation of seismic waves are highly sensitive to pore space filling (White, 1975). This sensitivity allows the imaging and interpretation of basin-scale fluid flow systems, subsurface geometries, fluid accumulations and permeability barriers (Berndt, 2005; Cartwright et al., 2007). However, there is an observational gap between seismic data (m-scale) and field geological mapping (cm-scale) of natural fluid flow systems. Furthermore, their nature, internal architecture, and hydraulic properties (especially permeability) are poorly understood and constrained.

Field observations and geological sampling from exhumed ancient fluid flow systems can add information on their internal architecture, the interaction of fluid flow with the bedrock, and physical properties of flow processes (De Boever et al., 2006a; Huuse et al., 2010; Capozzi et al., 2015; Nelson et al., 2017). To increase our understanding of fluid flow in the marine environment, the integration of field observations from ancient fluid flow systems with seismic data from modern marine sedimentary systems can help to extend the interpretation from seismic to sub-seismic scale.

Unmanned aerial vehicles (UAVs) enable us to map fluid flow features in outcrops over large distances (km-scale) at very high accuracy (cm-scale). UAVs equipped with high-resolution optical RGB sensor cameras represent a cost-effective and efficient way to map complex geological patterns in 3D (Bemis et al., 2014). Thereby, the detailed mapping adds invaluable information on the spatial distribution patterns and internal architecture. In combination with punctual (discrete) data from geological mapping enable a further insight into the interaction between fluid flow and the bedrock and hydraulic properties, especially the permeability.

Pobiti Kamani, located 20 km west of Varna, Bulgaria, hosts several hundred ancient carbonate conduits (hereafter referred to as pipes) which are up to 10 m high (De Boever et al., 2006a, 2006b). The pipes are the largest hydrocarbon carbonate conduits known globally and are well-exposed in the unconsolidated sands and sandstones of the Dikilitash Formation (Sinclair et al., 1997; De Boever et al., 2006a; Capozzi et al., 2015). In addition, at Beloslav Quarry, an old sand extraction quarry near the Village of Beloslav, the pipes crop out in a ~ 40 m cliff therewith enabling the mapping of their spatial distribution and vertical extent (De Boever et al., 2009a). The combination of both outcrops, the Beloslav Quarry and Pobiti Kamani represents an excellent target for UAV-based photogrammetry of an ancient fluid flow system.

The aim of this study is to analyze pipe-forming processes within sand formations from the combination of two outcrops (Pobiti Kamani & Beloslav Quarry), near Varna, Bulgaria. The permeability of these sand formations with high porosities should be high and support diffusive flow through the unconsolidated sediments. However, in the unconsolidated sands of the Dikilitash Formation focused fluid flow is evidenced by hydrocarbon-derived carbonate conduits (De Boever et al., 2006a, 2006b). So far, only one case study from the Kattegat, Denmark, shows similar pipe features in the marine realm (Jørgensen, 1992). Both settings oppose the current understanding of focused fluid flow in marine settings, where focused fluid flow and corresponding conduits are highly dependent on the hydraulic parameters of the hosting sediments and predominantly observed in low permeable silty to muddy sediments (e.g. Hovland and Judd, 2007; Böttner et al., 2018).

To determine the pipe-forming processes in sand formations, we first map the pipes as well as the regional distribution of fractures and carbonate slabs. The latter representing carbonate-cemented interbeds within the Dikilitash Formation. This information is used to analyze spatial patterns and interrelation of tectonic deformation and pipe formation. Secondly, we determine the processes involved in the development of pipes and characterize the involved fluids. Third, we reconstruct the history and nature of fluid flow and consequent pipe formation.

## 6.3. Geological setting

Pobiti Kamani is located 20 km west of Varna, along the eastern side of the Alpine Balkanides. It forms a section of the Moesian platform, a tectonic unit that extends from northern Bulgaria to southern Romania (Bergerat et al., 1998; Georgiev et al., 2001). The Moesian Platform was likely a part of a block-faulted Triassic to Oligocene siliciclastic shelf and carbonate succession along the northern Tethys margin (Sinclair et al., 1998). Several hundreds of calcite-cemented tubular concretions (hereafter referred to as pipes) (Figure 6.1; Botz et al., 1993; De Boever et al., 2006a, 2006b, 2009a, 2009b, 2011a, 2011b) are hosted in the Dikilitash Formation. This formation comprises unconsolidated coarse silt to sand sediments and carbonate-cemented sandstone interbeds (Figure 6.1). The Dikilitash Formation is ~ 40 m thick and was deposited in the Early Eocene in a mid to outer ramp depositional system with water depths around 100 m (De Boever et al., 2006a, 2009a, 2009b).

The pipes are 0.5-3 m in diameter and up to 10 m high. Clusters of pipes have been documented at several locations, including the Central, Strashimirovo, Beloslav quarry, Banovo and Teterlik groups (Figure 6.1; De Boever et al., 2009a, 2009b, 2011a, 2011b). The clusters align along Paleogene NNE-SSW trending transtensional faults that have up to 80 m throw (Bergerat et al., 1998; De Boever et al., 2009b). The colocation of the clusters with the Paleogene faults suggest a structural control on the location of the pipe clusters (De Boever et al., 2009b).

Geochemical analyses of the calcite-cemented tubular concretions show that they formed because of ascending methane-rich fluids resulting in precipitation of low-Mg carbonates (Botz et al., 1993; De Boever et al., 2006a, 2006b, 2009a, 2009b). The fluids likely migrated along the transtensional faults into the Dikilitash Formation (De Boever et al., 2009b). Based on oxygen isotope ratios ($\delta^{18}O$ relative to the Vienna-Pee Dee Belemnite standard [V-PDB]) the age of the pipes has been estimated to ~50 Ma (De Boever et al., 2006a). Heavily depleted $\delta^{13}C$ isotope ratios of archaeal biomarker ($\delta^{13}C$ -123‰ to -81‰ V-PDB) indicate that the exposed carbonates, including pipes and carbonate interbeds, likely formed because of microbially mediated anaerobic oxidization of methane at or below the seafloor (De Boever et al., 2009a).

There are two distinct groups of pipes with differing $\delta^{13}C$ and $\delta^{18}O$ isotope ratios. The characteristic groups show in alternating rings around the center of the carbonate conduits. Group 1 likely formed because of fluids from below that included biogenic methane and ancient sea (salt) water ($\delta^{13}C$ ~ -45 to -35‰ V-PDB & $\delta^{18}O$ ±1‰ V-PDB). Group 2 is characterized by alteration of the isotope ratios likely due to mixing of ascending methane with marine DIC ($\delta^{13}C$ ~ 0‰) and/or $\delta^{13}$-enriched $CO_2$ and recrystallization because of percolating Cenozoic meteoric water ($\delta^{13}C$ <-25‰ V-PDB & $\delta^{18}O$ <-6.5‰ V-PDB) (De Boever et al., 2009a).

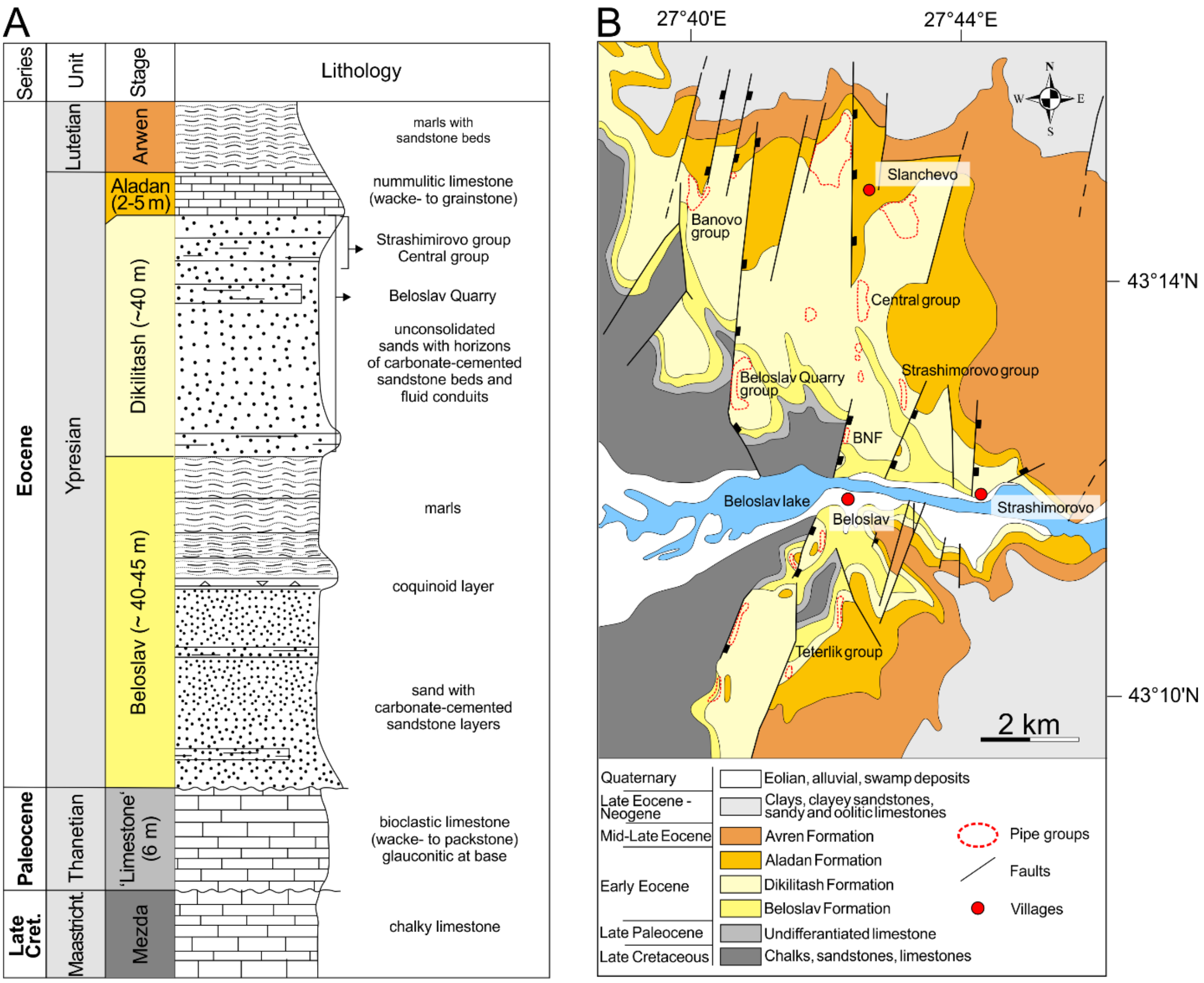

**Figure 6.1.** (a) Stratigraphic column with the main lithologies (with highlighted formations in which the pipes appear) and (b) simplified geological setting of the survey area. BNF= Beloslav North fault (modified after De Boever et al., 2009b)

## 6.4. Methods

We used the customer-grade unmanned aerial vehicle (DJI Inspire 2), equipped with a 20.8 MP Zenmuse X5S (RGB channels) camera and a DJI MFT 15mm/1.7 ASPH lens, to acquire images of the Pobiti Kamani area and Beloslav Quarry (Figure 6.2). The images were stored in jpg format and saved to a micro-SD card (64 GB) aboard the UAV. We designed the flight surveys with DJI GroundStationPro. These surveys were subsequently flown automatically by the UAV. This procedure results in a very regular flight pattern and good overlap of neighboring images. For the Beloslav Quarry, we additionally employed manually controlled surveys to achieve better coverage of the cliff which represents the surface outcrop of the transtensional faults (80 m sub-vertical relief). The average flight time was ~25 minutes with rolling shutter set to 2-3 s resulting in a data set of more than 4500 images (~42 GB) for the Pobiti Kamani area and more than 2000 images (~25 GB) for the Beloslav Quarry.

The software Pix4D (professors license, cloud computing access) was used to calculate the digital elevation model (DEM), a point cloud and an ortho-rectified mosaic (RGB) of both areas. The data were processed via cloud computing with 18 x 3 GHz and 68 GB RAM. For the

Pobiti Kamani area, the resolution of the derived ortho-rectified mosaic, point cloud and DEM is ~1 cm per pixel. We employed 10 ground control points to adjust the geo-referencing of the results. Real-time kinematic (RTK) service was not available during the acquisition campaign, resulting in a minimum accuracy of the location of the overall model of 1.3 m ± 0.6 m. The area of the Beloslav Quarry is hard to access because of the high relief and thus ground control points could not be established, resulting in an accuracy of ~ 2 m. The resolution of the Beloslav Quarry model is ~2 cm per pixel.

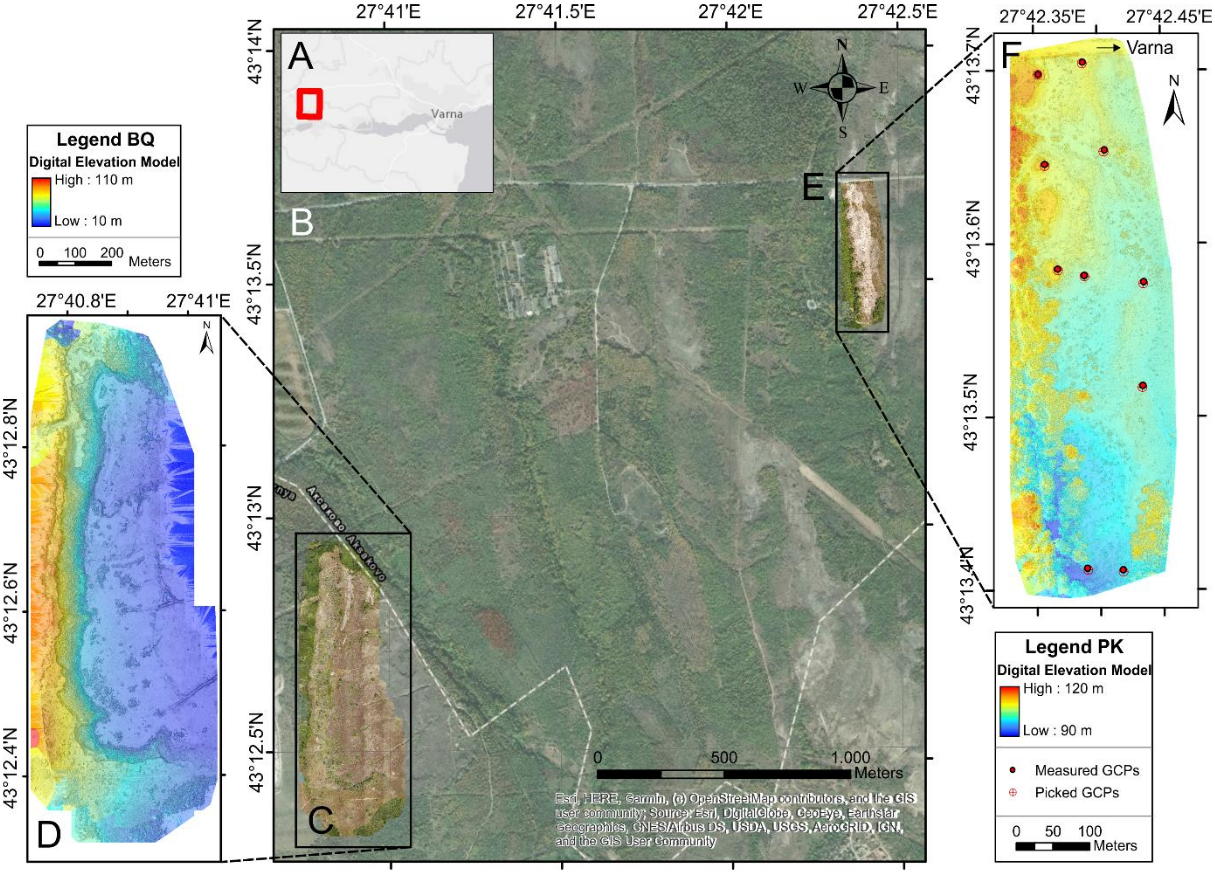

**Figure 6.2.** Overview map of the survey areas located 20 km west of Varna, Bulgaria. (A) Regional map showing the location of the investigated areas in a red box. (B) Local map of the two investigated outcrops of Pobiti Kamani and the Beloslav Quarry. (C) Ortho-rectified image mosaic of Beloslav Quarry and (D) corresponding derived digital elevation model (DEM). Photogrammetric derived digital elevation model (DEM). (E) Ortho-rectified image mosaic of Pobiti Kamani and (F) corresponding DEM. Red dots indicate measured ground control points (GCPs) and red crosses the picked GCPS.

To delineate the outlines of the pipe structures and analyze spatial distribution patterns we used multiple ArcGIS (version 10.6) geoprocessing tools. In a first step, we analyzed the spatial distribution by manually picking surface fracture patterns and pipe structures in the ortho-rectified mosaic. In a second step, we delineated the outlines of the pockmarks by calculating the curvature of the DEM and combining it with co-located manually picked pipes of the ortho-rectified mosaic image.

Geological sampling was done using a hand-held drill with a diamond-coated drill bit (32 mm diameter). The samples were taken either in vertical or horizontal transects across single well-exposed pipes to a maximum depth 25 mm into the carbonates.

## 6.5. Results

### 6.5.1. Spatial distribution

#### 6.5.1.1. Pobiti Kamani

The data set comprises 678 individual pipes, 42 individual carbonate plates covering at least 945 m² and 1016 individual fractures with a total length of 1471 m and a mean length of ~ 1.45 m (Figure 6.3). These fractures are predominantly oriented in NNE-SSW direction (Figure 6.3A). The pipes in Pobiti Kamani are highly clustered (Average nearest neighbor, z-score: -13.33) with an average distance between nearest pipes of 3.48 ± 3.39 m (Maximum 43.16 m; Figure 6.3B). The z-score of -13.33 is returned by the pattern analyses tool and indicates whether we can reject the null hypothesis (random distribution) or not. This low z-score gives that there is a less than 1% likelihood that this clustered pattern could be the result of random chance. The pipe distribution is densely spaced with a maximum of 0.11 pipes per m² (Mean: 0.035 ± 0.02 pipes per m²). There is no predominant direction of pipe orientation nor can we discern a direct relationship between fracture geometries and pipe location and orientation (Figure 6.3A vs. B, see also Figure 6.3D) as suggested by De Boever et al. (2009b). The highest pipes in the Pobiti Kamani show predominantly solidified inner cores. The majority of pipes, however, has unlithified inner cores (Figure 6.3E).

All of the investigated pipes are located within the investigated survey area. However, there are more pipes to the North and to the South, which are not part of our photogrammetric model. The fault contact that constrains the pipe location towards the West is not visible in the photogrammetric models.

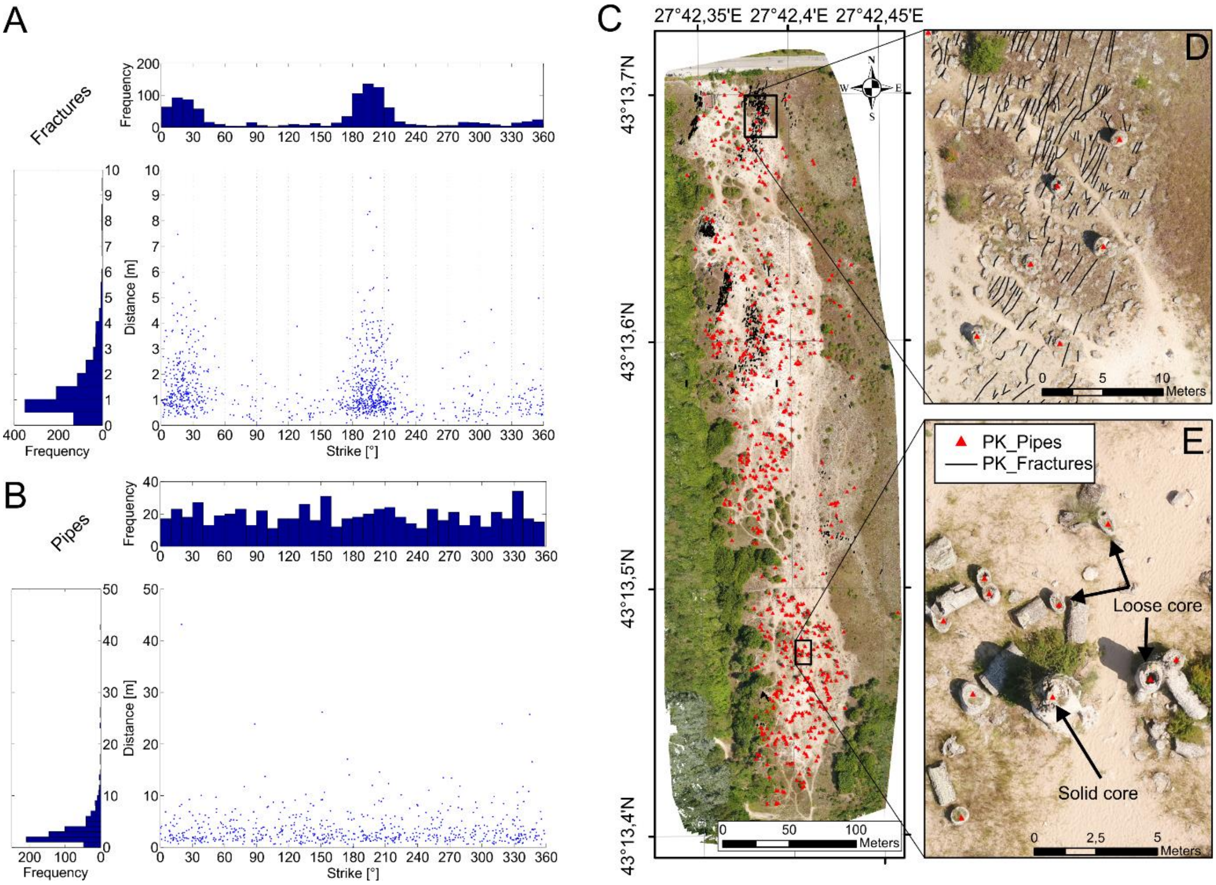

**Figure 6.3.** UAV-based photogrammetric results from Pobiti Kamani. (A) Scatterplot for fractures of their strike direction against measured distance and corresponding histograms showing the frequency of both per unit. (B) Scatterplot for pipes and their nearest neighbor direction against nearest neighbor distance and corresponding histograms showing the frequency of both per unit. (C) UAV-based ortho-rectified image of Pobiti Kamani manually picked pipes and fractures. Black boxes show the location of the insets, PK means Pobiti Kamani, red triangles show pipe location and black lines fractures. (D) The pipe location with respect to the fractures and (E) the location of pipe with respect to each other and the appearance of single pipes (loose inner core & solid inner core)

### 6.5.1.2. Beloslav Quarry

The 3D point cloud was used in combination with the original RGB-images to manually pick the pipes on different elevation levels. The point cloud shows that the pipes are separated by at least seven distinct horizons separating the pipes in tiers (color coded triangles between I1-I7, see Figure 6.4B). These interbeds show sub-horizontal bedding with slight dip of less than 10° in southeastern direction (Figure 6.4B).

The data set comprises 1066 individual pipes and large carbonate plates covering more than 1600 m², but the coarser resolution of this data set prohibits digital analyses of fractures. Spatial analyses of the pipes show that they are highly clustered (Average nearest neighbor, z-score: -37.84) and have a neighboring distance of 2.24 m ± 3.38 m (Max. 55.47 m, Min. 0.04 m). The pipes are densely spaced with an average of 0.07 ± 0.06 pipes per m² (Max. 0.22 pipes per m²). The angles between the nearest pipes show no preferred strike direction.

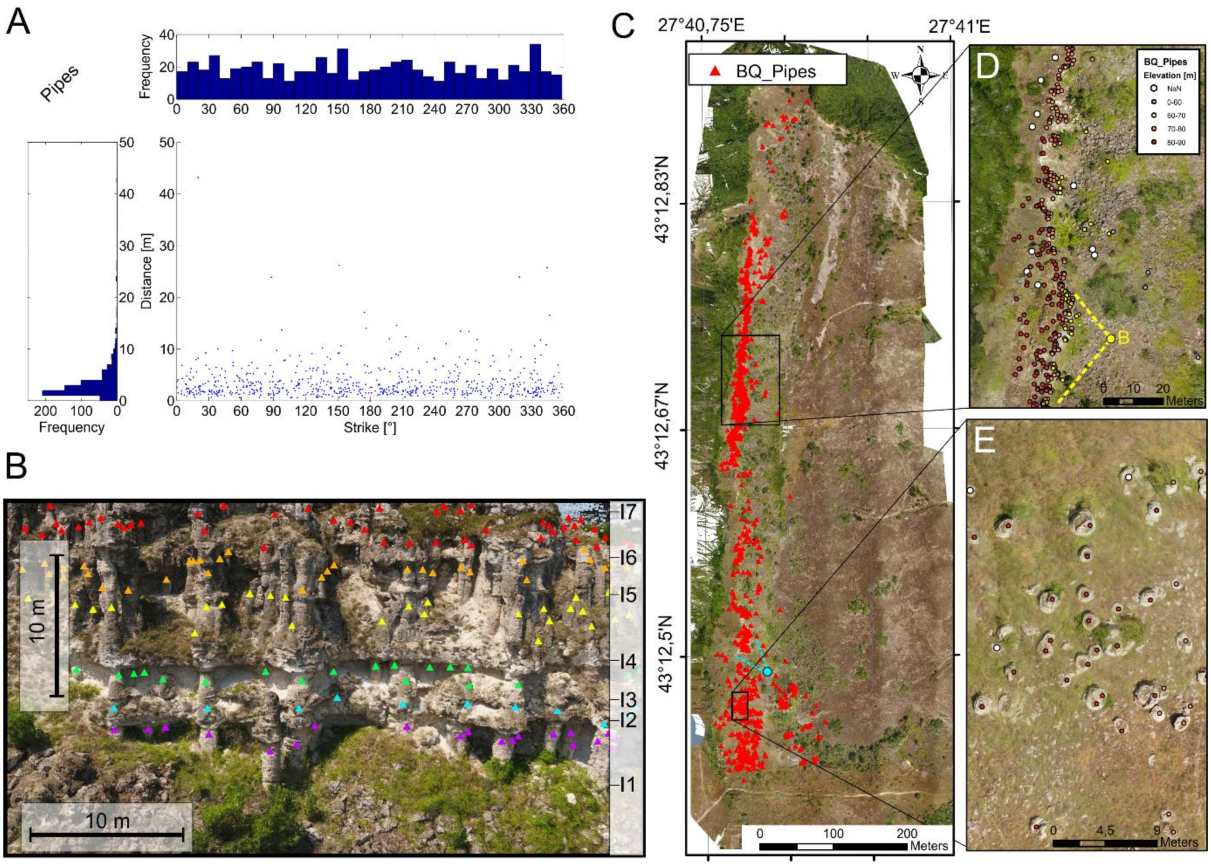

**Figure 6.4.** UAV-based photogrammetric results from Beloslav Quarry. (A) Scatterplot for pipes and their nearest neighbor direction against nearest neighbor distance and corresponding histograms showing the frequency of both per unit. (B) Point cloud image of one prominent cliff showing six tiers of pipes (colored triangles) corresponding to the intervals between the seven carbonate cemented interbeds (I1-I7). See (D) for location. (C) UAV-based ortho-rectified image of Pobiti Kamani manually picked pipes and fractures. Black boxes show the location of (D) and (E), red triangles show pipe location, turquoise circle the location of Figure 6.5. (D) Pipes picked in the point cloud separated by their elevation. Yellow dot marks the viewing location of (B). (E) Close-up of the densely-spaced pipes in the southern part of the outcrop.

### 6.5.2. Geological fieldwork

UAV-based photogrammetry allows rapid mapping of pipes and tectonic deformation structures over large areas (tens of square kilometers). However, ground-based geologic mapping and sampling is necessary to analyze the interaction of the fluids with the bedrock and reveal the internal architecture. Figure 6.5 shows a representative example of a cliff within Beloslav Quarry looking NNW towards the exposure. Figure 6.5A shows a light grey sand unit that gradually changes towards the top of the interval to sandy brown. Birds nest holes indicate that the sediment is poorly consolidated. Except for some decimeter-scale carbonate cemented horizons there is limited evidence for bedding, suggesting that the sand interval may be heavily bioturbated.

The carbonate pipes are orientated sub-vertically and perpendicular to the carbonate horizons (Figure 6.5C). Most carbonate pipes are light grey in color, which is the same color as the surrounding sandy host rock. We attribute the darker grey color of some pipes to more severe weathering (Figure 6.5C). Figure 6.5D shows that the pipes are meter-scale in width and appear to occur in discrete clusters. There is no evidence that the spatial distribution of the individual clusters follows any regular pattern and the distance between individual pipes (~2-3 m) fits the results from the UAV analyses.

Many carbonate pipes bifurcate of towards the tops (Fig. 4E) confirming interpretations based on the UAV imagery. However, convergence of pipes also occurs in some places (two pipes merging into one; see Figure 6.5). Some pipes appear intertwined, leading to more complex geometries. All pipes show a more globular or bulbous outer surface at their top, which often correlates with carbonate cemented horizons (Figure 6.5F). In some areas the overlying carbonate layer dips slightly towards the carbonate pipe indicating a genetic relationship between the pipe and carbonate horizon (Figure 6.5G). Although sub-horizontal fractures and differing color (most likely due to preferential weathering) at the interface between the pipes and upper carbonate unit are present (Figure 6.5G). There appear to be two main carbonate units of meter-scale thickness that the pipes originate from (lower unit, Figure 6.5H) and terminate into (upper unit; Figure 6.5D, G).

The host rock is composed of poorly consolidated, quartz sandstone with minor micritic cement (Figure 6.5I). The overall unit is heavily bioturbated, with an abundance of shell fragments and an abundance of Nummulites, ranging from 0.5 – 25 mm in diameter (Figure 6.5M). The carbonate pipes and the host sandstone have a similar composition and texture but differ with respect to the amount of carbonate cementation and the presence of trace fossils (Figure 6.5L). The trace fossils in the host rock consist of sub-vertically oriented burrows. They have convex shape, thin towards their base, and show sub-horizontal branching networks (Figure 6.5L). The outer boundary between the carbonate pipe and the surrounding host rock is sharp in weathered examples, but slightly more diffuse in unweathered examples (Figure 6.5I-K). The carbonate pipes and the overlying carbonate unit show the same texture and composition (Figure 6.5J).

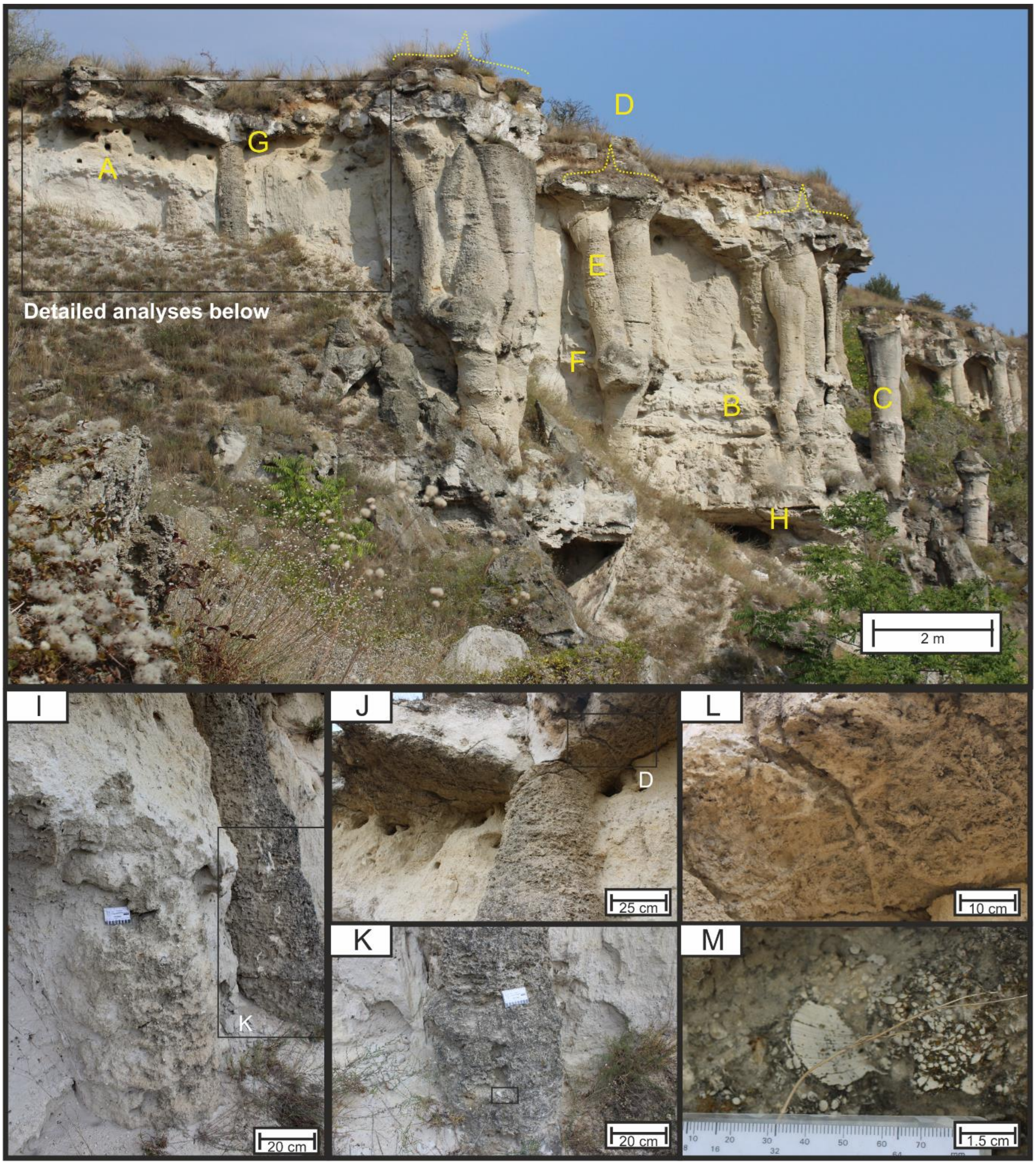

**Figure 6.5.** Vantage point looking NNW, providing an understanding of carbonate pipe geometry, and the relationship of the pipes with the surrounding sandy host rock, and the upper & lower carbonate horizons. The letters correspond to the main field observations. Detailed analyses indicated by black box: (I) Two carbonate pipes observed, one less weathered (in the foreground) and one more weathered (the dark grey colored pipe). (J) The interface between the top of the carbonate pipe and the upper carbonate unit. The carbonate pipe emanates into the upper carbonate unit, despite the false appearance of a sharp contact due to a sub-horizontal fracture and white staining of the upper carbonate unit. (K) Another view of the carbonate pipe, appearing to have intruded vertically upwards through the poorly consolidated sand host rock. (L) Horizontal branching burrow network at the base of the upper carbonate unit. (M) An abundance of shells and shell fragments 0.5-25 mm in size within the carbonate pipe, highlighting the similarity in composition between the pipe and the surrounding sandstone host rock.

To ground truth the UAV-based photogrammetric we collected information on fracture distribution, orientation, and dip in the field. For Pobiti Kamani, we measured a total of 36 fractures. They predominantly trend in NNE/SSW direction and dip at high angles towards the east, matching the NNE/SSW trend of 1016 fracture orientations measured from UAV-based data. From fracture exposure of the fracture surfaces we can measure the dip (Figure 6.6D-F), although erosion may have slightly distorted the true strike and dip directions.

At Beloslav Quarry, the resolution of the UAV imagery is not sufficient to resolve fractures. From geological field data, the metre-scale carbonate pipes display sub-vertical veining within fractures (Figure 6.6A). The veins are linear in shape, displaying no degree of sinuosity and no evidence of branching of the veins. They are also reactive to HCL, indicating a secondary infill of carbonates in previous fractures. The veins appear to display a predominant N/S orientation. Within a (lower) carbonate unit, S-shearing is observed (Figure 6.6B-C).

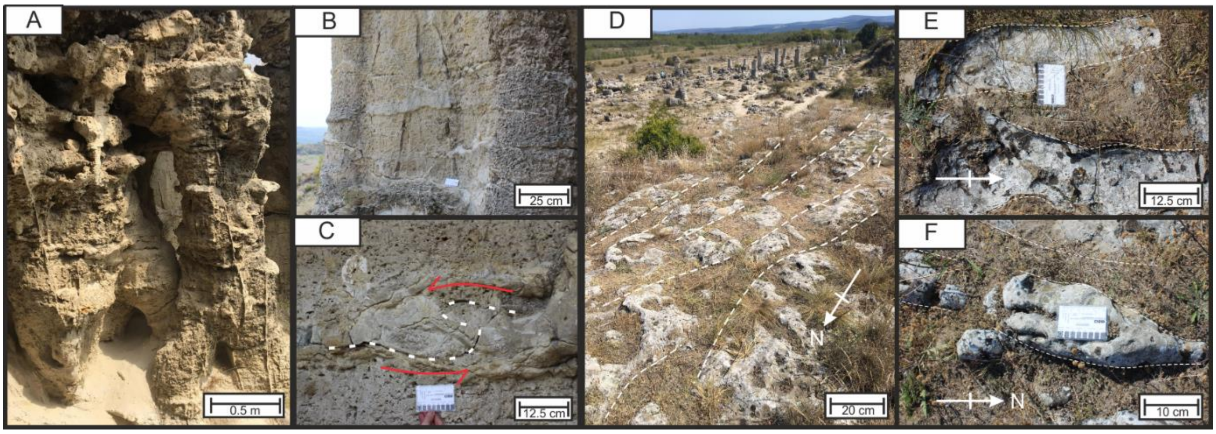

**Figure 6.6.** (A) Meter-scale carbonate pipes displaying secondary sub-vertical carbonate veining within fractures. The veins are orientated NNE/SSW. (B) Fractures and carbonate veins observed, cross cutting both the carbonate pipes and surrounding host rock, with no clear orientation trend. (C) S-shaped shear fabric within a carbonate horizon, indicating the presence of active N-S shear stress during the formation of this interval. (D) NNE trending fracture network on a carbonate slab surface, at higher elevation than the carbonate pipes observed to the East. (E, F) Zoom-ins of the measured fracture surfaces. Weathering and erosion may have slightly altered the true orientation of the fractures.

## 6.6. Discussion

### 6.6.1. Distribution of pipes

The pipe distribution in both areas is very similarly spaced with 3.43 m ± 3.31 m in the Pobiti Kamani area and 2.24 m ± 3.38 m in the Beloslav Quarry (Figure 6.3). The pipes are heavily clustered and fields are located adjacent to major transtensional faults. Fracture orientation in both areas shows a predominant N-S/NNE-SSW strike direction dipping at high-angles (Figure 6.3) and S-shearing within a carbonate interval provides evidence that the N-S stress regime was active during pipe formation (Figure 6.6), supporting the transtensional character of tectonic deformation. The tectonic deformation is probably a controlling factor for the location of the respective carbonate pipe clusters. The pipes align along the eastern side of the transtensional faults within the sediments of the Dikilitash Formation (Figure 6.3). There is no apparent preferential orientation of the pipes (nearest neighbor) within the Dikilitash Formation (Figure 6.3) and thus a direct influence of the stress regime (tectonic control) on the pipe formation along pre-existing weakness planes or the fault damage zone as suggested by De Boever et al. (2009a) is not supported by the UAV-photogrammetric results.

### 6.6.2. Pipe formation

The pipes are located in the Dikilitash Formation, which was deposited in a mid- to outer ramp environment above the storm wave base and prone to moderately frequent reworking of sediments (Sinclair et al., 1998). The sub-vertical orientation and cylindrical geometry of the pipes (Figure 6.3, Figure 6.4B, Figure 6.5) support that they formed due to the buoyancy-driven ascend of methane-rich fluids from biogenic sources (De Boever et al., 2006a; De Boever et al., 2009a).

The similar composition of the sand host rock and the carbonate pipes indicate a direct genetic relationship. The pipe forming methane-derived authigenic carbonates (MDAC) likely precipitated because of microbially mediated anaerobic oxidization of methane (AOM) within the unconsolidated sands of the Dikilitash Formation below the seafloor (De Boever et al., 2009a). The large height and the well-preserved status of the pipes (Figure 6.5) argue against a formation within the water column as bottom currents in the mid- to outer ramp environment would likely have had more destructive influence. The presence of pisoids, highly bioclastic units with Nummulite clusters (Figure 6.5M) and burrows, which are indicative of cold-seep communities (Clari et al., 2004; Wiese et al., 2015), support the sub-seabed formation of the pipes.

Towards the top of the pipes, their diameter increases and appears to emanate into the overlying carbonate layer (Figure 6.5). Bifurcation and bulging towards the pipe tops (Figure 6.5) indicate that there have been several phases of pipe formation during the Early Eocene. We can identify at least seven carbonate-cemented interbeds separating the vertically stacked tiers of pipes (Figure 6.4, Figure 6.5). If each of these interbeds represents a paleo-seafloor, we can deduce that there have been at least seven phases of methane emission from the methane seep-system.

The high-permeable, unconsolidated sands of the Dikilitash Formation should be conducive to diffusive fluid flow. Considering that the pipes have an outer layer of carbonates with a diffuse boundary to unconsolidated sands in the interior (Figure 6.5), we suggest that fluid flow was focused in pre-existing fractures beneath the Dikilitash formation (e.g. within the Beloslav Formation, Sinclair et al., 1997) and entered the Dikilitash formation at discrete points that subsequently formed the center of the pipes. The propagation of pressure waves or viscous creep of rising gas bubbles into the Dikilitash formation likely resulted in the formation of tube-shaped zone of vertical fluid flow (Boudreau et al., 2005; Räss et al., 2018). These tube-shaped zones established themselves with a positive feedback mechanism by precipitation of carbonate on the outside of the streams and likely resulted in a self-sustaining, positive feedback focused fluid flow (Clari et al., 2004). Stacking of pipes in at least seven tiers, the loose inner core and round-shaped cavities in the carbonate plates, indicate that methane flow likely persisted through time. Where flux rates were high, the focused flow of methane prevented carbonate precipitation, i.e. in the center of pipes (Luff & Wallmann, 2003). In combination with the high permeability of the hosting sediments the proposed formation process also explains the large dimensions of the pipes (height, diameter) despite their close spacing. Focused fluid flow in marine sand formations is also documented from the “bubbling reefs” in the Kattegat, offshore Denmark (Jørgensen, 1992). These pipes show ongoing discharge of methane and have formed below the seafloor. Constant erosion because of post-glacial isostatic uplift has exposed these features in 10-12 m water depth. The bubbling reef pipes only distinguish from their host sandstone by the amount of cementation. Some of the pipes are almost 4 m tall and 1.5 m in diameter (Jensen et al., 1992). Carbon-isotope studies of the pipes identified a probable link between the bubbling gas ($\delta^{13}C$ -63 to -75‰), the carbonates ($\delta^{13}C$ -26 to -63‰), and the methanotrophic bacteria ($\delta^{13}C$ -43.4‰) (Hovland & Judd, 2007). We suggest that focused fluid flow in sands and sandstone formations is not an exceptional case but also likely in other marine settings at the transition between low and higher-permeable formations (shale-sand-interface). The focusing of fluids and subsequent vertical conduit formation largely depends on the focused advection of methane from below, e.g. through pre-existing fractures, the flux rate and progressive inward growth of carbonates.

Different to previous interpretations, however, we suggest that the two alternating isotope signatures groups (group 1: $\delta^{13}C$ ~-45 to -35‰ V-PDB & $\delta^{18}O$ ±1‰ V-PDB; group 2: $\delta^{13}C$ <-25‰ V-PDB & $\delta^{18}O$ <-6.5‰ V-PDB; De Boever et al., 2009a) are not the result of a different composition of percolating meteoric waters, as this would have only affected the outside of the pipes. Instead we postulate that it represents the episodic fresh/brine water advection that fed the pipe structures from below and was captured during precipitation.

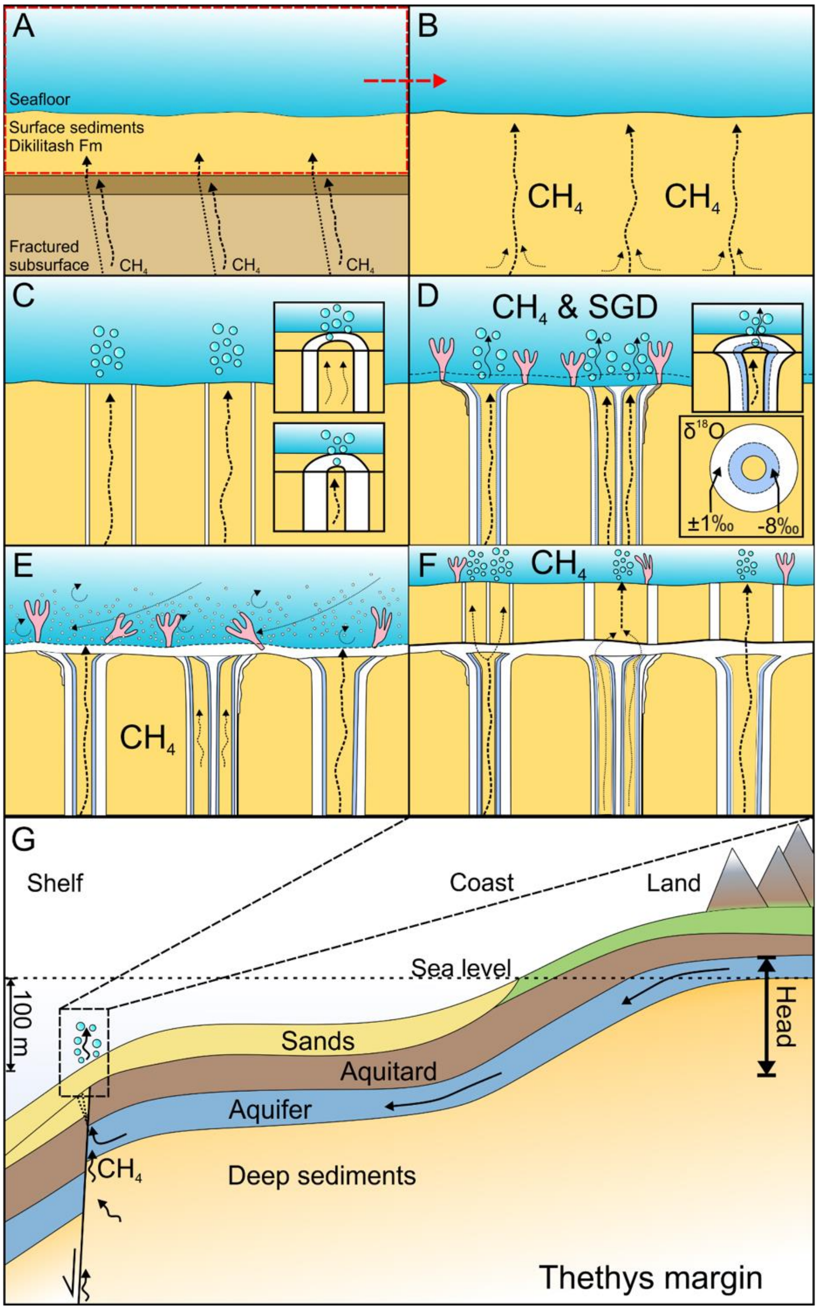

**Figure 6.7.** Schematic diagram showing the carbonate pipe formation through time. (A) Methane ascends from below possibly along pre-existing planes of weakness in the subsurface due to transtensional tectonism in the Palaeogene. (B) Buoyancy driven focused upward migration of methane through poorly consolidated sandstone of the Dikilitash Fm. (C) Carbonate precipitation on the margins of methane gas seeps, forming the outer walls of the carbonate pipe. Progressive precipitation of carbonate towards the centre of the pipe through time (1 to 2). (D) Continued carbonate precipitation, widening at the seabed interface. Cold-seep benthic communities, such as tubeworms, form at the seabed around the methane release site. Benthic organisms may form vertical burrows or roots to allow uptake of hydrogen sulphide from the seep sediments. Episodic submarine groundwater discharge leads to depleted oxygen isotope ratios in precipitated carbonates (1 to 2). (E) Bottom water currents provide additional sediment into the system, within an outer-ramp depositional setting. An outer carbonate crust forms at the seabed, interpreted to form from continued methane flux and precipitation of carbonate. (F) The process of pipe formation in the near subsurface repeats, methane continues to flow through preferential pathways created by older pipe structures. (G) Schematic model of coupled methane release and episodic submarine groundwater discharge at the shelf of the Tethys margin.

### 6.6.3. Geological model

The UAV-photogrammetry shows that the pipes do not form any lineaments or other geometrical structures that would argue for a formation of the pipes within the damage zones of major faults in the Dikilitash Formation (Figure 6.3, Figure 6.4, Figure 6.6D-F). However, the pipes cluster along regional transtensional faults (Figure 6.3, Figure 6.4; De Boever et al., 2009b). Carbonate pipes in Beloslav Quarry show S-shearing (Figure 6.6A & C) indicative for active ‘transpression’ or ‘transtension’ during their formation. The orientation of S-shears indicates that the compression/extension was orientated NNE-SSW. The S-shear itself, a type of ductile deformation, provides evidence that the carbonate unit was likely still water saturated during its formation. From this we interpret that the active transtensional faults below Dikilitash formation (1) allowed vertical flow of fluids from below towards the base of the Dikilitash Formation and (2) induced ductile shearing in the pipes during their formation.

The alternating carbonate isotope ratios in the pipes indicate that fresh or brine waters were episodically involved in the precipitation of carbonates (Figure 6.7). Considering the presence and activity of the transtensional faults below the Dikilitash Formation, we suggest that the fresh or brine water was likely sourced from an aquifer below the Dikilitash Formation (e.g. the Beloslav Formation or deeper; Sinclair et al., 1997), which advected fluids from onshore resulting in episodic submarine groundwater discharge (SGD). A similar coupled groundwater-methane discharge system is currently active along the eastern Bulgarian coastal areas documented by ongoing venting of methane (Dimitrov, 2002) and elevated Radon isotope ratios (Moore & Falkner, 1999). In order to create topography-driven groundwater flow far out into the shelf (Hughes et al., 2009; Morrissey et al., 2010; Post et al., 2013), tectonic compression in the onshore realm during the Paleogene (Sinclair et al., 1997) likely provided the necessary hydraulic head (Figure 6.7). This topography-driven groundwater flow forced episodic submarine groundwater discharge in addition to the methane emissions resulting in the two alternating characteristic isotope groups found in the carbonate pipes (Figure 6.7).

## 6.7. Conclusion

For the Pobiti Kamani area we mapped 1753 individual pipes at a mean spacing of ~3 m. Despite the dense spacing, the pipes show large heights (up to 10 m) and diameters (mean ~3.5 m). The pipes are vertically separated by at least 7 carbonate interbeds, which likely represent the paleo-seafloor. The outcropping carbonate plates cover more than 2500 $m^2$. Furthermore, we mapped more than 1000 fractures and applied ground-geological data and identified two predominant (N-S/NNE-SSW) strike directions.

The pipes formed below the seafloor as a result of anaerobic oxidation of methane (AOM) of methane-rich fluids that were advected to the Dikilitash Formation from biogenic sources. Deformation of the unit underlying the Dikilitash Formation may have focused fluid flow to certain points at which the fluids were released. The point sources have likely self-sustained themselves though carbonate precipitation on the outside of the methane streams. This would explain the large diameters and size of the pipes despite their dense spacing. The carbonate interbeds likely represent paleo-seafloors, thus, there have been at least 7 phase of methane release.

Regional tectonic deformation likely played a key role in the location of the pipe clusters on a regional scale. The pipe clusters tend to form to the eastern side of major transtensional fault in the unconsolidated sand to sandstones of the Dikilitash Formation. However, on a local scale, tectonic deformation is not governing the distribution of the pipes.

The carbonates of the conduits show two characteristic groups of carbon and oxygen isotopes that appear in rings around the center of the pipes. These groups likely represent different phases of episodic fluid release with different characters. The first group of methane-derived authigenic carbonates (MDAC) has likely formed from biogenic methane and ambient seawater. The second group of MDAC has likely formed due to the episodic release of groundwater coupled to the biogenic methane release. Groundwater was likely advected to the mid-to outer ramp shelf setting through an aquifer driven by topographic changes in the onshore realm by active deformation and uplift during the Eocene. However, we suggest that focused fluid flow in sands and sandstone formations is not an exceptional case but is also likely current marine settings at the transition between low and high-permeable formations (e.g. shale-sand-interface), especially where methane seepage is combined with submarine groundwater discharge.

## References

Andresen, K. J. (2012). Fluid flow features in hydrocarbon plumbing systems: What do they tell us about the basin evolution? *Marine Geology,* 332, 89-108.

Bemis, S. P., Micklethwaite, S., Turner, D., James, M. R., Akciz, S., Thiele, S. T., & Bangash, H. A. (2014). Ground-based and UAV-based photogrammetry: A multi-scale, high-resolution mapping tool for structural geology and paleoseismology. *Journal of Structural Geology*, *69*, 163-178.

Berndt, C. (2005). Focused fluid flow in passive continental margins. *Philosophical Transactions of the Royal Society of London A: Mathematical, Physical and Engineering Sciences*, 363(1837), 2855-2871.

Böttner, C., Berndt, C., Reinardy, B. T., Geersen, J., Karstens, J., Bull, J. M., ... & Schramm, B. (2019). Pockmarks in the Witch Ground Basin, Central North Sea. *Geochemistry, Geophysics, Geosystems, 20*(4), 1698-1719.

Boudreau, B. P., Algar, C., Johnson, B. D., Croudace, I., Reed, A., Furukawa, Y., ... & Gardiner, B. S. (2005). Bubble growth and rise in soft sediments. *Geology,* 33(6), 517-520.

Burnett, W. C., Aggarwal, P. K., Aureli, A., Bokuniewicz, H., Cable, J. E., Charette, M. A., ... & Moore, W. S. (2006). Quantifying submarine groundwater discharge in the coastal zone via multiple methods. *Science of the total Environment, 367*(2-3), 498-543.

Cartwright, J. (2007). The impact of 3D seismic data on the understanding of compaction, fluid flow and diagenesis in sedimentary basins. *Journal of the Geological Society*, 164(5), 881-893.

Cavagna, S., Clari, P., & Martire, L. (1999). The role of bacteria in the formation of cold seep carbonates: geological evidence from Monferrato (Tertiary, NW Italy). *Sedimentary Geology*, *126*(1-4), 253-270.

Dando, P. R., Austen, M. C., Burke, R. A., Kendall, M. A., Kennicutt, M. C., Judd, A. G., ... & Southward, A. J. (1991). Ecology of a North Sea pockmark with an active methane seep. *Marine Ecology Progress Series*, *70*(1), 49-63.

De Boever, E., Birgel, D., Muchez, P., Peckmann, J., Dimitrov, L., & Swennen, R. (2011a). Fabric and formation of grapestone concretions within an unusual ancient methane seep system (Eocene, Bulgaria). *Terra Nova*, *23*(1), 56-61.

De Boever, E., Birgel, D., Thiel, V., Muchez, P., Peckmann, J., Dimitrov, L., & Swennen, R. (2009a). The formation of giant tubular concretions triggered by anaerobic oxidation of methane as revealed by archaeal molecular fossils (Lower Eocene, Varna, Bulgaria). *Palaeogeography, Palaeoclimatology, Palaeoecology*, *280*(1-2), 23-36.

De Boever, E., Huysmans, M., Muchez, P., Dimitrov, L., & Swennen, R. (2009b). Controlling factors on the morphology and spatial distribution of methane-related tubular concretions–Case study of an Early Eocene seep system. *Marine and Petroleum Geology*, *26*(8), 1580-1591.

De Boever, E., Muchez, P., Swennen, R., & Dimitrov, L. (2011b). Evolution of deformation and fault-related fluid flow within an ancient methane seep system (Eocene, Varna, Bulgaria). *Geofluids*, *11*(2), 166-183.

De Boever, E., Swennen, R., & Dimitrov, L. (2006a). Lower Eocene carbonate cemented chimneys (Varna, NE Bulgaria): Formation mechanisms and the (a) biological mediation of chimney growth?. *Sedimentary Geology*, *185*(3-4), 159-173.

De Boever, E., Swennen, R., & Dimitrov, L. (2006b). Lower Eocene carbonate-cemented “chimney” structures (Varna, Bulgaria)—control of seepage rates on their formation and stable isotopic signature. *Journal of Geochemical Exploration*, *89*(1-3), 78-82.

Dimitrov, L. (2002). Contribution to atmospheric methane by natural seepages on the Bulgarian continental shelf. *Continental Shelf Research*, *22*(16), 2429-2442.

Goff, J. A. (2019). Modern and fossil pockmarks in the New England Mud Patch: Implications for submarine groundwater discharge on the middle shelf. *Geophysical Research Letters*.

Hughes, J. D., Vacher, H. L., & Sanford, W. E. (2009). Temporal response of hydraulic head, temperature, and chloride concentrations to sea-level changes, Floridan aquifer system, USA. *Hydrogeology journal*, *17*(4), 793-815.

Huuse, M., Jackson, C. A. L., Van Rensbergen, P., Davies, R. J., Flemings, P. B., & Dixon, R. J. (2010). Subsurface sediment remobilization and fluid flow in sedimentary basins: an overview. *Basin Research*, *22*(4), 342-360.

Jensen, P., Aagaard, I., Burke Jr, R. A., Dando, P. R., Jorgensen, N. O., Kuijpers, A., ... & Schmaljohann, R. (1992). 'Bubbling reefs' in the Kattegat: submarine landscapes of carbonate-cemented rocks support a diverse ecosystem at methane seeps. *Marine Ecology Progress Series*, *83*, 102-112.

Jørgensen, N. O. (1992). Methane-derived carbonate cementation of marine sediments from the Kattegat, Denmark: geochemical and geological evidence. *Marine Geology*, *103*(1-3), 1-13.

Judd, A., & Hovland, M. (2007). *Seabed fluid flow: the impact on geology, biology and the marine environment*. Cambridge University Press.

Karstens, J., & Berndt, C. (2015). Seismic chimneys in the Southern Viking Graben–Implications for palaeo fluid migration and overpressure evolution. *Earth and Planetary Science Letters*, 412, 88-100.

Maia, A. R., Cartwright, J., & Andersen, E. (2016). Shallow plumbing systems inferred from spatial analysis of pockmark arrays. *Marine and Petroleum Geology*, *77*, 865-881.

Moore, W. S. (1996). Large groundwater inputs to coastal waters revealed by 226Ra enrichments. *Nature*, *380*(6575), 612.

Moore, W. S., & Falkner, K. K. (1999). Cycling of radium and barium in the Black Sea. *Journal of environmental radioactivity*, *43*(2), 247-254.

Morrissey, S. K., Clark, J. F., Bennett, M., Richardson, E., & Stute, M. (2010). Groundwater reorganization in the Floridan aquifer following Holocene sea-level rise. *Nature Geoscience*, *3*(10), 683.

Paull, C., Ussler Iii, W., Maher, N., Greene, H. G., Rehder, G., Lorenson, T., & Lee, H. (2002). Pockmarks off Big Sur, California. *Marine Geology*, *181*(4), 323-335.

Post, V. E., Groen, J., Kooi, H., Person, M., Ge, S., & Edmunds, W. M. (2013). Offshore fresh groundwater reserves as a global phenomenon. *Nature*, *504*(7478), 71-78.

Räss, L., Simon, N. S., & Podladchikov, Y. Y. (2018). Spontaneous formation of fluid escape pipes from subsurface reservoirs. *Scientific reports*, *8*(1), 11116.

Taniguchi, M., Burnett, W. C., Cable, J. E., & Turner, J. V. (2002). Investigation of submarine groundwater discharge. *Hydrological Processes*, *16*(11), 2115-2129.

White, J. E. (1975). Computed seismic speeds and attenuation in rocks with partial gas saturation. *Geophysics*, 40(2), 224-232.

# 7. Conclusion, Recommendations and Outlook

The Southern North Sea during Alkor cruise AL512.

## 7.1. Summary of main results

Fluid flow in the Earth's crust primarily occurs within permeable beds. However, fluids can also migrate along natural and/or anthropogenic structures. Such focused fluid flow has wide implications for the formation of natural resources such as water or hydrocarbons, the occurrence of geohazards including landslides and earthquakes, or the genesis of biological seep communities. Flow of fluids often varies in both space and time and the results from my PhD thesis highlights that an interdisciplinary and multi-scale approach is helpful to analyze fluid flow and its consequences in the Earth's crust. Combining data from conventional 3D seismic data, high-resolution 3D seismic data, 2D seismic data, hydroacoustic data, sedimentological data, UAV-based photogrammetry and geochemical data, I was able to identify the sources, the migration pathways and the surface manifestations of wide range of modern and ancient marine systems. This helped to gain a better understanding of the underlying geological processes.

Fluid flow and seepage in the marine realm are primarily associated with venting of hydrocarbons. Geochemical data from the sediments and water column can help to constrain the fluid sources and can give insight into the migration pathways through the Earth's crust. Modern seep system (Chapter 2) and an ancient seep system (Chapter 6), I could show that hydrocarbons are not necessarily the exclusive fluids which migrate through marine sediments and form seabed manifestations.

In the Witch Ground Basin, Central North Sea, focused fluid flow in low-permeable sediments leads to the formation of abundant pockmarks (Chapter 2). The pockmarks can be separated into two classes dependent on their morphology, the composition of the involved fluids, and the formation processes. Large pockmarks show continuous venting of biogenic methane sourced from larger depth and advected through vertical fluid conduits over geological timescales. On the other hand, in the absence of evidence for hydrocarbon venting, smaller pockmarks may also form by purely sedimentological processes such as compaction-related dewatering in several phases over shorter periods of time. This teaches us that greenhouse gas emissions from natural geological sources cannot be based on seafloor observations and present-day fluxes but require an analysis of the involved processes through geological time.

Building on the results from the Witch Ground Basin, Chapter 6 investigates if focused fluid in the marine realm is limited to such low permeable sediments. I investigated an ancient seep system that developed during the Eocene in the marine realm of the Tethys margin. In the Pobiti Kamani area and the Beloslav Quarry (near Varna, Bulgaria) hundreds of carbonate pipes are well exposed within the Dikilitash Formation, which comprises unconsolidated coarse silt to sand sediments and carbonate-cemented sandstone interbeds. In such high-permeable sediments, fluid flow may form vertical conduits when the underlying low-permeable sedimentary unit is faulted or fractured (e.g. at a shale-sand-interface) and the resulting flux rates are high enough to cause precipitation of carbonates at the margins of the seeps. For the investigated Eocene seep system, methane seepage was likely coupled with intermittent submarine groundwater discharge as shown by geochemical and geological data. The interdisciplinary data from the North Sea (Chapter 2) and the Pobiti Kamani area (Chapter 6) highlight, that constraints on the timing of venting and constraints on the involved fluids are important for understanding the underling geological processes.

For the Eocene convergent Tethys margin, the focused seafloor seepage of groundwater was likely caused by crustal-scale faulting. Such interplay between tectonic deformation, fluid flow, and fluid seepage may be applicable to many modern active margins globally and may allow further insights on submarine groundwater discharge as well as offshore water resources. For the Hikurangi margin (New Zealand), I have used high-resolution 3D seismic reflection data in combination with hydroacoustic data to identify and analyze upper-plate normal faults (Chapter 4). These normal faults may play a crucial role for the drainage of the subduction-zone and the occurrence of submarine slope-failures within the marine forearc. They guide fluids from deeper strata towards the base of the Tuaheni Landslide Complex which may lead the development of excess fluid pressure in the sediments therewith preconditioning slope-instability (Chapter 5).

Closing the loop and going back to the North Sea, I have not only considered natural pathways through the Earth’s crust but also anthropogenic pathways through marine sediments (Chapter 3). A major contributor to regional greenhouse budgets are the inadvertent emissions from hydrocarbon wells and other subsurface operations. The exploration of hydrocarbons has left millions of wells on continental shelves, from which greenhouse gas release may counteract the effort to mitigate greenhouse gas emissions. I present an approach to investigate large numbers of wells with one single methodology, which combines seismic, hydroacoustic and geochemical data. The interdisciplinary approach enables me to assess methane release from marine decommissioned hydrocarbon wells over a large area (20,000 km$^2$). This thesis finds that there are two types of leakage associated with hydrocarbon wells and other subsurface operations. Leakage may occur through faulty casings and/or annuli of wells (Type 1), which likely affects the safety of carbon dioxide storage formations and deep hydrocarbon reservoirs, but also through the fractured surrounding along a well (Type 2). Type 2 leakage is largely dependent on the presence of shallow gas accumulation, but other factors/well attributes may be helpful to assess the propensity of wells to leak. Inadvertent greenhouse gas emissions from these anthropogenic fluid migration pathways are likely not constrained to hydrocarbon wells but also affect all other wells and subsurface operations that penetrate the shallow crust. My study shows that decommissioned hydrocarbon wells alone contribute significantly to the methane budget of the North Sea.

My results imply that natural fluid migration pathways including structure-controlled flow and vertical fluid conduits and anthropogenic fluid migration pathways such as wells and other subsurface operations may form complex fluid flow systems in the subsurface. The combination of possible pathways through the Earth’s crust may bypass permeability barriers in different tiers towards the upper strata and subsequently result in venting of fluids at the seafloor. The interdisciplinary evaluation of fluid migration pathways and the released fluids may reveal the origin of the fluids and implications for the permeability of subsurface.

These complex fluid flow systems are a global phenomenon in the Earth' crust may have significant implications for potential $CO_2$ storage formations. The injection of large volumes of $CO_2$ during industrial-scale CCS operations is necessary to effectively mitigate anthropogenic greenhouse gas emissions into the atmosphere. The storage in marine saline aquifers, which have the highest global storage potential, require the integrity of impermeable seals (cap rock) for efficient long-term storage. The injection of large volumes, however, will elevate pore pressure at depth which in turn has significant implications for the long-term storage of $CO_2$. Elevated pore pressures may lead to higher probabilities of fault reactivation and earthquakes. The degradation of permanent barriers in abandoned wells that penetrate through such formations may lead to leakage along wells. Prolonged leakage along numerous abandoned wells may counteract efficient long-term storage of $CO_2$. Seismic pipes and chimneys are common features in seismic reflection data and their interpretation as focused fluid flow conduits is well established, however, their nature and in particular their permeability is poorly understood, which are both crucial for a proper assessment of the risk they pose for $CO_2$ storage formations. Though leakage through these pathways is possible and they should be avoided when possible, my findings do not necessarily imply that saline aquifers are not suitable for $CO_2$ storage. My results highlight the importance of careful evaluation of the particular storage formation overburden with geophysical and geochemical methods prior to injection as well as effective monitoring strategies of the subsurface and seafloor during—and after— $CO_2$ injection at reasonable cost and appropriate temporal and spatial resolutions.

## 7.2. Recommendations & Outlook

This thesis highlights that the nature and internal architecture of fluid flow systems, especially their hydraulic properties, are poorly constrained by direct observations (Chapter 2, 3, 6). The permeability, however, is the one parameter that determines the relevance of fluid flow systems for the safety of $CO_2$ storage formations. The geological sequestration of anthropogenic $CO_2$ is an important step towards a low carbon future. In order for $CO_2$ sequestration to have a global climate impact, large-scale $CO_2$ storage sites in the range of tens of megatons per year are necessary both offshore and onshore, which require careful monitoring prior, during and after $CO_2$ injection. The STEMM-CCS (EU), CHIMNEY (NERC) and SENSE (ACT) projects create new knowledge with regard to our understanding of leakage through the overburden of $CO_2$ storage formations and will likely benefit from the results of my thesis. Within the framework of these projects, I recommend the following steps forward:

First, direct probing of a seismic pipe structure in the marine realm to determine their internal architecture was planned during my thesis. My thesis shows the geometries, stratigraphic framework and surface manifestation of the active fluid conduit beneath the Scanner Pockmark, which manifests itself in seismic data as seismic pipe. After technical problems at the first attempt, the second attempt was successful and will deliver valuable information on the permeability of focused fluid conduits and their internal architecture. The combination of both, the geometries, stratigraphic framework and surface manifestation and the sediment properties and internal architecture will feed numerical two-phase flow models conducted at the Heriot-Watt University, Edinburgh, UK.

Second, the ongoing CHIMNEY project at the National Oceanography Centre, Southampton, including a multi-scale seismic investigation of the same pipe will benefit from my results and additionally derive important knowledge on the seismic manifestation of vertical fluid conduits as well as give insight into their nature and internal architecture.

Third, to further constrain permeabilities of vertical fluid conduits and their formation processes, the blowout site in the North Sea such as 22/4B in the British sector or B1 in the German sector represent good targets for future research, because they are very young and the involved fluids are well known. The Figge Maar blowout was targeted during RV Alkor cruise AL512 in 2018. My results on leakage from decommissioned hydrocarbon wells (Chapter 3), structure-controlled flow and pipe structures (Chapter 2 & 6) may help to untangle the complex fluid flow systems that evolved during the blowout, constrain their effective permeabilities, study their long-term behavior and to calculate the amount greenhouse gases that have been released over the period of activity.

Fourth, my thesis highlights that in the early stage of pockmark formation, the seafloor is likely deforming (Chapter 2), which will be further investigated within the SENSE project, which includes the injection of $CO_2$ into suitable formations (e.g. sand bodies) as well as the development of cost-effective and efficient monitoring technologies to observe seafloor deformation offshore.

In general, I recommend an integrated, interdisciplinary approach similar to what I have shown in this thesis. Direct probing, seismic multi-scale and interdisciplinary investigations of the particular fluid conduit beneath Scanner pockmark or the B1/”Figge Maar” may only provide site specific information, which is only representative for the current status. However, by integrating the results from various targets representative of different stages of fluid flow evolution, the study of focused fluid flow conduits will gain a better understanding.

Based on my work, I also recommend to further substantiate the seismic analyses of chimney and pipe structures in seismic data. In particular, I recommend to use industry pre-stack seismic data of seismic pipes and chimney structures in sedimentary basins. During the time of this thesis, I have re-processed pre-stack seismic data provided by PGS to investigate the pipe structure beneath the Scotia pockmark. The evaluation of reflections in far- and near-offset should give rise whether the observed anomalies are induced by the overlying gas and subsequent distorted propagation of the wave field or if they are induced by local geology, i.e. by a fracture network. However, the pipes are located in shallow depth and the geometries of pre-stack seismic data provided by the industry do not allow imaging the target area appropriate to fulfil this task. I recommend to use other (new) seismic data sets with high quality seismic data above pipe features that are located in larger depth, i.e. at Nyegga pockmark field offshore Norway or 1000 m long blow-out pipes offshore Nigeria. Both areas comprise promising targets for which pre-stack seismic data may be able to constrain the knowledge on seismic pipe and chimney structures and give rise whether these features are a seismic artifact induced by the overlying gas or real geological features.

Greenhouse gas emissions from wells and other subsurface operations are now in the focus of the Federal Ministry of Education and Research within their “Mare:N – Coastal, Marine and Polar Research for Sustainability" German Federal Government research program (see also concept paper “Blauer Ozean”). I have shown, that seismic data in combination with hydroacoustic, geochemical and well attribute data is useful to assess the propensity of wells to leak (Chapter 3). The described method can be applied to marine settings around the world’s hydrocarbon provinces to further substantiate the knowledge on fugitive emissions from oil and gas infrastructure and natural geological sources. The discussed pre-conditions and processes, however, are not necessarily constrained to the marine realm but also apply for onshore wells. In this context, the monitoring of wells during and after abandonment is crucial for a better understanding of the involved processes. Monitoring may help attribution of released fluids to the shallow subsurface or the deep reservoirs. Detailed knowledge on the release fluids helps to understand how barriers in the subsurface degrade over time and help improve the materials and methods used for permanent plugging. For the offshore realm, such monitoring may include indirect methods such as hydroacoustic surveys and evaluation of existing seismic data but also direct methods such as the sampling of the released fluids by a remote operated vehicle (ROV).

I have shown that steps towards fully automated analyses methods of seismic, hydroacoustic and UAV-based data can lead to progress in understanding of the particular geological processes (Chapter 2, 3 & 6). Methods including machine learning applications and (semi-) automated processes represent efficient and cost-effective way to analyze existing and new data sets. For this purpose, however, existing and future data sets have to be made available and stored in formats that allow easy access, homogeneous archiving and integrated approaches. Within this thesis there are multiple applications, where such methods would advance the knowledge in the respective field of research:

First, machine-learning algorithms can be used on available information of wells to predict the propensity of wells to leak. In the Netherlands, analyses of well attributes, i.e. location, age, spud date, depth) and corresponding reservoir fluids with machine learning approaches (decision tree) have led to a high degree of certainty in prediction of emissions from hydrocarbon wells. In combination with existing seismic data, this would largely improve the assessment process.

Second, if existing bathymetric data sets were stored in a unified format and easily accessible, one could use various geoprocessing tools (i.e. ArcGIS) to apply these for quantitative geomorphology and analyze existing and new data. This would provide scientific basis to draw conclusions for geological settings around the world. If done properly, this would allow research solely based on existing data and the implementation of various data sets, i.e. surface, sub-surface and sediment properties, for one study. The re-evaluation of old data in combination with new data will allow a synthesis that will likely drive scientific progress in the near future.

Third, leakage rates are much higher were pre-existing fracture networks are present in the subsurface around wells. I recommend to use a machine learning approach to identify areas where wells are co-located with seismic pipes and chimneys as they are proven to enhance fluid flow. This approach would make use of training algorithms with small training data sets of seismic pipes and chimneys and applying them to large data sets as presented in this thesis. This approach would require large quantities data storage and computational power. The University Computing Centre at the CAU could provide such computational power and storage with their high-performance computing (HPC) service.

My thesis highlights the importance of scientific drilling for geological investigations of fluid flow (Chapter 2, 4, 5, & 6). The IODP372 drilling campaign to Tuaheni Landslide Complex and the underlying normal fault network benefited from my thesis and the results of the drilling will likely refine our understanding of the geological processes (Chapter 4 & 5). I recommend to use borehole deviation data to derive the current stress regime and compare it with the seismic analyses of the extensional system. In combination, the seismic data and the drilling campaign provide excellent basis for future work on the complex and often intertwined relationship between fluid flow and fault activity (fault reactivation, modes of seismic activity) but also for the emplacement history of the landslide complex.

I show that customer-grade UAVs, equipped with high-resolution optical RGB sensor cameras, represent a cost-effective and efficient way to map outcrops of fluid flow systems over large areas (several km²) with very high accuracy (down to 1 cm; Chapter 6). The drone group at GEOMAR provides excellent infrastructure to investigate a multitude of geological problems onshore, offshore and across shorelines. I would recommend using UAVs equipped with RGB sensor cameras may be used for shallow marine water down 5 m but at maximum to the Secchi depth to quantify the seasonal changes in biology or the evolution of landslides. In addition, UAVs equipped with real-time-kinematic (RTK)-systems and coupled RGB/infrared cameras can help identify areas of methane venting and/or submarine groundwater discharge.

Integrated, interdisciplinary research of natural and anthropogenic fluid migration pathways through the Earth’s crust and especially marine sediments including direct probing (drilling), existing and future seismic surveys (4D, 3D, high-resolution 3D, 2D), geochemical analyses, numerical modelling and fieldwork at outcrops will help untangle complex fluid flow systems and give insight on their spatial and temporal evolution. A better understanding of these systems will make sub-seabed operations much safer and help us to reduce offshore emissions of greenhouse gases. The findings will also help us understand the occurrence of natural resources such as water or hydrocarbons in the offshores and investigate their interrelation with current climatic processes in order to estimate the effect of global warming and its consequences on the global carbon cycles with wide implications for the geosphere, cryosphere, hydrosphere, and atmosphere.

# 8. Acknowledgements

There are very little words that can describe how thankful I am for the last 3 year supervised by Christian Berndt. A special thank you to Christian Berndt for being the main supervisor, the fruitful discussions, encouragement and reading of my drafts. I have learned so much from you, some of which goes beyond my scientific career. You have always supported me and encouraged me to question existing knowledge and develop my own ideas. I will be always grateful for this. Thank you, Christian!

I would like to thank Lars Rüpke for being my co-supervisor during my PhD. Thank you for your support and helpful advice. Your constructive input, opinions on scientific work, ideas on career planning and motivation were very valuable. Thank you, Lars!

A special thanks to Jacob Geersen, who was patient enough to help improve my writing and analyses skills and was an excellent mentor throughout the whole time here at GEOMAR. Thank you, Jacob!

I would like to thank Bettina Schramm, who managed to spend three years across the table in our office. Thank you for the nice conversations, the many collaborative research cruises, our joint proposal, vacations, sport workouts, the good working climate, the hectoliters of good coffee and for tolerating my jumping mind.

Many thanks to Jens Karstens and Gareth Crutchley for constant support during my doctorate, insightful discussions, and proof-reading of this thesis. A special thanks to Dirk Klaeschen, for his input, supervision and patients in teaching me seismic data processing.

The post- and pre-stack 3D seismic data, which I analyzed and processed during my doctorate, was kindly provided by PGS (Petroleum GeoService). I would like to thank them for their permission to interpret the data and publish the results. The seismic data interpretation was carried out with the software package IHS Kingdom Suite, thanks for granting access to the software through educational licenses.

I would like to thank the GEOMAR and STEMM-CCS project for financing my doctorate. GEOMAR and STEMM-CCS enabled me to visit various research conferences (EGU, AGU, STEMM-CCS annual meet, STEMM-CCS Early Career Researcher meeting), various research cruises to the North Sea and broadened my scientific network for the future. Many thanks to ECORD for granting me financial support to visit the IODP Petrophysics summer school in Leicester, 2017. A special thanks to ISOS and Avan Antia for providing the Miniproposal framework and granting financial support to conduct fieldwork in Varna, Bulgaria. Many thanks to the captains and crews of research cruises MSM63, MSM78, POS518, POS534, AL512 and M154.

Many thanks to the entire geodynamics group for the nice atmosphere and fruitful discussions. I had the privilege to be involved in many research projects and scientific publications but also to join many research cruises around the world. Many thanks to my co-authors and colleagues, who supported me during the preparation of the manuscripts and proposals. Special thanks to Mark Schmidt, Matthias Haeckel, Benedict Reinardy, Aaron Micallef, Joshu Mountjoy, Jens Schneider von Deimling, Jörg Bialas, Christian dos Santos Fereira and Nico Augustin. Many thanks to my colleagues within the STEMM-CCS framework, including Ben J. Callow, Jon Bull, Anita Flohr, and Anna Lichtschlag for fruitful discussions and support during the past years. A special thanks to Ismael Falcon-Suarez, for he is a "beast" not only in science but more importantly with his voice and guitar.

This thesis could not have been completed without the assistance of Gero Wetzel, Tim Weiß, Florian Beeck, Asmus Petersen, Florian Evers, Bettina Domeyer, Anke Bleyer, Andrea Bodenbinder, and Regina Surberg. A special thanks goes out to Anne Völsch, Jasmin Mögeltönder, Stefan Kontradowitz, and Julia Schätzel, who made not only my lunch break an everyday pleasure but also helped me greatly in dealing with cruise/research/conference/travel paperwork and preparation.

I would like to thank my friends and family for supporting me during my time in Kiel. The last decade in Kiel was a very exciting time and I would not be here without you.

Many thanks to Judith Elger, for taking chances and good times. I am looking forward to our future. I would like to thank Felix Gross, Sandra Gross and Florian Petersen for being the guiding light in darker times, spending holidays, sharing a flat, insightful discussions, support and being close friends. I would like to thank Jasper Hoffmann for insightful discussion and spending quality time in Kiel despite being on the other side of the world. Many thanks to Jakob Kutsch, Büsra Tokuc, Thade and Lena Wunderlich, for their steady support and gentle reminder that life outside academia exists.

I would like to thank Michel Kühn, who I could convince to join me on hiking adventures and for proof-reading my German abstract. Many thanks to Christopher Schmidt, for being similarly insane and sharing pain but also joy on long distance races as well as triathlons. I had a great time with both of you.

Many thanks to Burkhart Wilm and Kathrin Lange for encouraging me to go the long way and raising my interest in science.

Many thanks to family, Bernd Böttner, Monika Böttner, Katharina Garben, Johannes Böttner, Luisa-Marie Böttner for their support, shelter and advice during the long way to my doctorate.

So long and thanks for all the fish.

# 9. Curriculum Vitae

Removed for data protection reasons.

Aus datenschutzrechtlichen Gründen entfernt.

# 10. Publication list

Please find a digital list and access to all publications on OceanRep:

http://oceanrep.geomar.de/view/creators/ec39004b-8d74-478c-a4ab-6454050ee48d.html

## 10.1. Peer-reviewed publications

**Böttner, C.,** Haeckel, M., Schmidt, M., Berndt, C., Vielstädte, L., Karstens, J., & Weiß, T. (2019, **in Review**). Decommissioned hydrocarbon wells as a source for greenhouse gas release: sources, rates, and mitigation strategies. *International Journal of Greenhouse Gas Control*.

Couvin, B., Georgiopoulou, A., Mountjoy, J. J., Amy, L., Crutchley, G. J., Brunet, M., Cardona, S., Gross, F., **Böttner, C.**, Krastel, S., & Pecher, I. (2019, **accepted**). Depositional History of the Tuaheni Landslide Complex, Hikurangi Margin, New Zealand. *Geological Society, London, Special Publications*.

**Böttner, C.,** Berndt, C., Reinardy, B.T.I., Geersen, J., Karstens, J., Bull., J.M., Callow, B.J., Lichtschlag, A., Schmidt, M., Elger, J., Schramm, B., & Haeckel, M. (2019). Pockmarks in the Witch Ground Basin, Central North Sea. *Geochemistry, Geophysics, Geosystems*, *20*(4), 1698-1719.

Karstens, J., Berndt, C., Morelia, M., Watt, S.F.L., Micallef A., Ray, M., Klaucke, I., Kühn, M., Klaeschen, D., Muff, S., Roth, T., **Böttner, C.,** Schramm, B., Elger, J., & Brune, S. (2019). From gradual spreading to catastrophic collapse–Reconstruction of the 1888 Ritter Island volcanic sector collapse from high-resolution 3D seismic data. *Earth and Planetary Science Letters*, *517*, 1-13.

Watt, S.F.L., Karstens, J., Micallef A., Berndt, C., Morelia, M., Ray, M., Desau, A., Sammartini, M., Klaucke, I., **Böttner, C.,** Day, S., & Downes, H. (2019). From catastrophic collapse to multi-phase deposition: Flow transformation, seafloor interaction and triggered eruption following a volcanic-island landslide. *Earth and Planetary Science Letters*, *517*, 135-147.

**Böttner, C.,** Gross, F., Geersen, J., Crutchley, G. J., Mountjoy, J. J., & Krastel, S. (2018). Marine Forearc Extension in the Hikurangi Margin: New Insights From High-Resolution 3-D Seismic Data. *Tectonics*, 37(5), 1472-1491.

Gross, F., Mountjoy, J. J., Crutchley, G. J., **Böttner, C.,** Koch, S., Bialas, J., ... & Huhn, K. (2018). Free gas distribution and basal shear zone development in a subaqueous landslide–Insight from 3D seismic imaging of the Tuaheni Landslide Complex, New Zealand. *Earth and Planetary Science Letters*, 502, 231-243.

Krastel, S., Wynn, R. B., Feldens, P., Schürer, A., **Böttner, C.,** Stevenson, C., ... & Unverricht, D. (2016). Flow behaviour of a giant landslide and debris flow entering Agadir Canyon, NW Africa. In *Submarine Mass Movements and their Consequences* (pp. 145-154). Springer, Cham.

Berndt, C., Hensen, C., Mortera-Gutierrez, C., Sarkar, S., Geilert, S., Schmidt, M., Liebetrau, V., Kipfer, R., Scholz, F., Doll, M., Muff, S., Karstens, J., Planke, S., Petersen, S., **Böttner, C.,** Chi, W. C., Moser, M., Behrendt, R., Fiskal, A., Lever, M. A., Su, C. C., Deng, L., Brennwald, M. S., & Lizarralde, D. (2016). Rifting under steam – how rift magmatism triggers methane venting from sedimentary basins. *Geology,* 44 (9), 767-770.

## 10.2. Scientific communication

**Böttner, C.,** Callow, B.J., Schramm, B., Gross, F., Vasilev, A., Petsinski, P., Karstens, J., Berndt, C., & Bull, J. (2019). GRAPA – Quantifying features of a fluid flow systems using customer-grade UAV imagery. [Talk] *In STEMM-CCS ECR Meeting*, 04.11.-7.11.2019, Winchester, United Kingdom.

**Böttner, C.,** Schramm, B., Berndt, C., Karstens, J., Bull, J., Callow, B.J., & Gross, F. (2019). GRAPA–Quantifying fractures using drone imagery. [Poster] In*: STEMM-CCS 3. Annual Meeting,* 27.2.-1.3.2019, Amsterdam, Netherlands.

Schramm, B., Berndt, C., Dannowski, A., Bayrakci, G., **Böttner, C**. & Minshull, T. (2019). Imaging the 3D seismic velocity structure of the Scanner pockmark, central North Sea. [Poster] In: *STEMM-CCS 3. Annual Meeting,* 27.2.-1.3.2019, Amsterdam, Netherlands.

Schramm, B., Berndt, C., Dannowski, A., Bayrakci, G., Minshull, T., & **Böttner, C.** (2019). Imaging the 3D seismic velocity structure of the Scanner pockmark, central North Sea. [Poster] In: *79. Jahrestagung der Deutschen Geophysikalischen Gesellschaft (DGG),* 5.3. - 8.3.2019, Braunschweig, Germany.

Gehrmann, R., Yilo, N., Haroon, A., Morton, M., Djanni, A., Bull, J., Provenzano, G., **Böttner, C.,** Schwalenberg, K., Berndt, C. & Minshull, T. (2019). Effect of acquisition uncertainties on interpretation of resistivity estimates from marine electromagnetic data. [Poster] *IUGG*, Montreal, Canada.

Yilo, N., Gehrmann, R., Bull, J., Minshull, T., Provenzano, G., Bayrakci, G., Böttner, C., Schramm, B., & Berndt, C. (2019). Controlled Source Electromagnetics data analysis to evaluate fluid flow pathways associated with CCS sites. [Talk] *Marelec*, Woods Hole, MA, USA.

Bull, J., Minshull, T., Henstock, T., Bayrakci, G., Gehrmann, R., **Böttner, C**., ... & Chen, B. (2018, October). Constraining leakage pathways through the overburden above sub-seafloor CO2 storage reservoirs. [Poster] In *14th Greenhouse Gas Control Technologies Conference Melbourne* (pp. 21-26), Melbourne, Australia.

**Böttner, C.,** Schramm, B., Berndt, C., Karstens, J., Schmidt, M., Haeckel, M., ... & Reinardy, B. (2018, April). Pockmark formation in the Witch Ground Basin, central North Sea. [Talk] In *EGU General Assembly Conference Abstracts* (Vol. 20, p. 8536), Vienna, Austria.

Micallef, A., Watt, S., Berndt, C., Urlaub, M., Brune, S., Klaucke, I., **Böttner, C.,** Karstens, J., & Elger, J. (2017). An 1888 Volcanic Collapse Becomes a Benchmark for Tsunami Models. [Article] Eos: Earth & Space Science News, 48.

**Böttner, C.,** Gross, F., Geersen, J. M., Mountjoy, J., Crutchley, G., & Krastel, S. (2017). An analysis of marine forearc extension on the northern Hikurangi subduction margin using high-resolution 3D seismic data. [Poster] *In EGU General Assembly Conference Abstracts* (Vol. 18), Vienna, Austria.

Yilo, N., Gehrmann, R., Bull, J., Minshull, T., Provenzano, G., Bayrakci, G., **Böttner, C.,** Schramm, B. & Berndt, C. (2017). Controlled Source Electromagnetics data analysis to evaluate fluid flow pathways associated with CCS sites. [Poster] *Electromagnetic induction workshop*, Copenhagen, Denmark.

Gross, F., Mountjoy, J., Crutchley, G., Koch, S., Bialas, J., Pecher, I., ... & **Böttner, C.** (2016, April). Submarine creeping landslide deformation controlled by the presence of gas hydrates: The Tuaheni Landslide Complex, New Zealand. [Talk] *In EGU General Assembly Conference Abstracts* (Vol. 18), Vienna, Austria.

Berndt, C., Hensen, C., Mortera-Gutierrez, C., Sarkar, S., Geilert, S., Schmidt, M., Liebetrau, V., Kipfer, R., Scholz, F., Doll, M., Muff, S., Karstens, J., Planke, S., Petersen, S., **Böttner, C.,** Chi, W. C., Moser, M., Behrendt, R., Fiskal, A., Lever, M. A., Su, C. C., Deng, L., Brennwald, M. S., & Lizarralde, D. (2015, December). Hydrothermal Activity in the Northern Guaymas Basin. [Poster] In *AGU Fall Meeting Abstracts*, San Francisco, USA.

## 10.3. Scientific reports

Karstens, J. , **Böttner, C.** , Edwards, M., Falcon-Suarez, I., Flohr, A., James, R., Lichtschlag, A., Maicher, D. , Pheasant, I., Roche, B., Schramm, B. & Wilson, M. (2019). *RV MARIA S. MERIAN Fahrtbericht / Cruise Report MSM78 - PERMO 2, Edinburgh – Edinburgh (U.K.), 16.10. – 25.10.2018*. Open Access. GEOMAR Report, N. Ser. 048 . GEOMAR Helmholtz-Zentrum für Ozeanforschung Kiel, Kiel, Germany, 60 pp. DOI 10.3289/geomar_rep_ns_48_2019.

Berndt, C. , **Böttner, C.** , Elger, J. , Kontradowitz, S., Kühn, M., Müller, S., Schramm, B. & Stelzner, M. (2019). *Sector collapse kinematics and tsunami implications - SEKT, Cruise No. M154/1, April 3 - April 25, 2019, Mindelo (Cape Verde) - Point-á-Pitre (Guadeloupe)*. Open Access. METEOR-Berichte, M154/1 . GEOMAR Helmholtz Centre for Ocean Research Kiel, Kiel, Germany, 47 pp. DOI 10.2312/cr_m154_1.

Karstens, J., Schneider von Deimling, J., **Böttner, C.**, Elger, J., Hilbert, H. S., Kühn, M., Kühn, R., Müller, P., Reinardy, B. & Schramm, B. (2018). *R/V ALKOR Cruise Report 512 [AL512] - North Sea Blowouts, 15th July - 26th July, 2018, Cuxhaven - Kiel (Germany)*. Open Access. GEOMAR, Kiel, Germany, 39 pp. DOI 10.3289/CR_AL512.

Berndt, C., Elger, J., **Böttner, C.,** Gehrmann, R., Karstens, J., Muff, S., Pitcairn, B., Schramm, B., Lichtschlag, A. & Völsch, A. (eds.) (2017*). RV MARIA S. MERIAN Fahrtbericht / Cruise Report MSM63 - PERMO, Southampton – Southampton (U.K.) 29.04.-25.05.2017*. Open Access. GEOMAR Report, N. Ser. 037 . GEOMAR Helmholtz-Zentrum für Ozeanforschung Kiel, Kiel, 137 pp. DOI 10.3289/GEOMAR_REP_NS_37_2017.

Berndt, C. , Muff, S., Klaucke, I. , Watt, S., **Böttner, C.** , Schramm, B., Völsch, A., Bennecke, S., Elger, J. , Chi, W. C., van Haren, J., Micallef, A. & Roth, T. (2017). *RV SONNE 252 Cruise Report / Fahrtbericht, Yokohama: 05.11.2016 - Nouméa: 18.12.2016. SO252: RITTER ISLAND Tsunami potential of volcanic flank collapses*. Open Access. GEOMAR Helmholtz Centre for Ocean Research, Kiel, Germany, 148 pp. DOI 10.3289/CR_SO252.

Berndt, C. , Hensen, C., Muff, S., Karstens, J. , Schmidt, M. , Liebetrau, V., Kipfer, R., Lever, M., **Böttner, C.** , Doll, M., Sarkar, S. & Geilert, S. (2015). *RV SONNE 241 Cruise Report / Fahrtbericht, Manzanillo, 23.6.2015 – Guayaquil, 24.7.2015: SO241 - MAKS: Magmatism induced carbon escape from marine sediments as a climate driver – Guaymas Basin, Gulf of California*. Open Access. GEOMAR Helmholtz Centre for Ocean Research Kiel, 74 pp. DOI 10.3289/CR_S241.

## 10.4. Publications in preparation

Augustin, N., Devey, C.W., van der Zwan, F.M., Herrero, T., **Böttner, C.,** … et al. (**in prep.**). The Balerion Lava Fields at the Mid-Atlantic Ridge. *Nature Geoscience*.

**Böttner, C**., Callow, B.J., Schramm, B., Gross, F., Geersen, J., Schmidt, M., Vasilev, A., Petsinski, P., & Berndt, C. (**in prep.**). Above the pipe – Geometry and formation processes of cold seeps in sands and sandstone derived from UAV-based analyses of an Early Eocene methane seep system, near Varna, Bulgaria. *Solid Earth, Faults, fractures, and fluid flow in the shallow crust – Special Issue, European Geosciences Union, Munich, Germany.*

Callow, C. J., Robinson, A. H., **Böttner, C.** … et al. (**in prep.**). Multiscale characterisation of chimney/pipe-structures within sedimentary basins. *Journal of Greenhouse Gas Control, STEMM-CCS Special Issue*.

Flohr, A., Schaap, A., ... et al. (**in prep.**). STEMM-CCS release experiment design and implementation. *Journal of Greenhouse Gas Control, STEMM-CCS Special Issue*.

Reinardy, B.T.I., **Böttner, C.,** Berndt, C., Karstens, J., Bull, J.M., Callow, B.J., Lichtschlag, A., … et al. (**in prep.**). Late Pleistocene depositional environments of the Witch Ground Basin, central North Sea. *Quaternary Science Reviews*.

Schramm, B., Berndt, C., Dannowski, A., Bayrakci, G., **Böttner, C.,** … et al. (**in prep.**). 3-D refraction seismic investigation of a pipe structure in the Witch Ground Basin, central North Sea. *Journal of Geophysical Research: Solid Earth.*

Schramm, B., Karstens, J., **Böttner, C**., Schneider von Deimling, J., Gross, J., Schmidt, M., Haeckel, M., Kühn, M., & Berndt, C. (**in prep.**). Quantifying the permeability of a focused fluid conduit with multi-resolution hydroacoustic data. *Journal of Greenhouse Gas Control, STEMM-CCS Special Issue*.

# 11. Appendix

## Appendix for Chapter 3

Böttner, C., Haeckel, M., Schmidt, M., Berndt, C., Vielstädte, L., Karstens, J., Weiß, T. (2019, in Review). Decommissioned hydrocarbon wells as a source for greenhouse gas release: sources, rates, and mitigation strategies. *International Journal of Greenhouse Gas Control*.

Table S2| Source data of the North Sea well inventory.

| **Country** | **Data Source (Date)** | **Link** |
|---|---|---|
| Norway (NOR) | Norwegian Petroleum Directorate (Dec. 2018) | https://www.npd.no/en/about-us/information-services/available-data/map-services/ |
| United Kingdom (UK) | Oil and Gas Authority (Dec. 2018) | https://data-ogauthority.opendata.arcgis.com/datasets/oga-wells-ed50 |
| Germany (GER) | Niedersächsisches Landesamt für Bergbau Energie und Geologie (Dec. 2018) | https://nibis.lbeg.de/cardomap3/?TH=BOHRKW |
| Denmark (DK) | Danish Energy Agency (Dec. 2018) | https://ens.dk/en/our-services/oil-and-gas-related-data/shape-files-maps |
| Netherland (NL) | Netherland Oil and Gas Portal (Dec. 2018) | https://www.nlog.nl/en/boreholes |

Table S3| Well selection for offshore North Sea (NSEA) wells.

| **Country** | **Onshore** | **Offshore** | **Multilateral** | **NSEA** | **NSEA (non-sidetracked)** | **Decommissioned** |
|---|---|---|---|---|---|---|
| **UK** | n/a | 12040 | 3071 | 11672 | 8655 | 4048 |
| **NOR** | n/a | 7769 | 764 | 6254 | 5551 | 1891 |
| **NL** | 6481 | 2108 | 661 | 2108 | 1447 | 750 |
| **DK** | 102 | 269 | n/a | 269 | 264 | n/a |
| **GER** | 21100 | 204 | n/a | 204 | 204 | n/a |
| **Total** | **27683** | **22390** | **4496** | **20507** | **16121** | **6689** |

Table S4| Investigated wells during POS518 and POS534. The table shows field identification number (FID), well identification number (well ID), latitude (WGS84), longitude (WGS84), flare identification index (1 positive detection), corresponding cruise number, distance to bright spot with polarity reversal from seismic data, the mean root-mean-square (RMS) amplitude for a 300 m circular buffer around the well location, the corresponding RMS standard deviation (RMS STD), well spud year (start date of drilling) and well intent.

| FID | Well ID | Lat. [°] | Lon. [°] | Cruise | Flare | Distance to polarity reversal [m] | RMS amplitude (300 m buffer mean) | RMS STD (300 m buffer mean) | Spud date [Year] | Well intent |
|---|---|---|---|---|---|---|---|---|---|---|
| **1** | 15/30-1 | 58.081721 | 0.839666 | POS518 | 1 | 240 | 988 | 180 | 1975 | Exploration |
| **2** | 15/30-11Z | 58.110768 | 0.846873 | POS518 | 0 | 780 | 1111 | 202 | 1995 | Exploration |
| **3** | 15/30-12 | 58.100815 | 0.858856 | POS518 | 1 | 100 | 1241 | 142 | 2003 | Appraisal |
| **4** | 15/30-2 | 58.102421 | 0.841843 | POS518 | 1 | 400 | 1029 | 244 | 1977 | Appraisal |
| **5** | 15/30-7 | 58.068499 | 0.839686 | POS518 | 0 | 960 | 975 | 201 | 1990 | Exploration |
| **6** | 16/26-24 | 58.040716 | 1.181016 | POS518 | 0 | 950 | 721 | 147 | 1992 | Exploration |
| **7** | 16/26-3 | 58.061740 | 1.166899 | POS518 | 1 | 570 | 956 | 98 | 1981 | Exploration |
| **8** | 16/27a-6 | 58.053665 | 1.225865 | POS518 | 1 | 250 | 896 | 197 | 1991 | Exploration |
| **9** | 16/27b-5 | 58.045337 | 1.210067 | POS518 | 1 | 570 | 784 | 176 | 1986 | Exploration |
| **10** | 21/03-2 | 57.960323 | 0.594846 | POS518 | 1 | 0 | 1213 | 288 | 1975 | Appraisal |
| **11** | 21/04b-5 | 57.987966 | 0.648638 | POS518 | 1 | 150 | 1044 | 316 | 1991 | Exploration |
| **12** | 22/02b-15 | 57.943307 | 1.388942 | POS518 | 1 | 100 | -9999 | -9999 | 2008 | Exploration |
| **13** | 22/02c-10 | 57.950753 | 1.355541 | POS518 | 0 | 300 | -9999 | -9999 | 1994 | Exploration |
| **14** | 22/03a-2 | 57.944971 | 1.439124 | POS518 | 1 | 0 | 717 | 182 | 1988 | Exploration |
| **15** | 22/03a-3 | 57.932767 | 1.426663 | POS518 | 1 | 100 | 637 | 174 | 1991 | Exploration |
| **16** | 23/26a-11 | 57.005108 | 2.164740 | POS518 | 1 | 0 | 973 | 313 | 1988 | Exploration |
| **17** | 29/01c-4 | 56.986807 | 1.128700 | POS518 | 1 | 570 | 693 | 90 | 1990 | Exploration |
| **18** | 29/01c-9z | 56.991495 | 1.094668 | POS518 | 0 | 500 | 840 | 100 | 2012 | Exploration |
| **19** | 30/01a-7 | 56.998989 | 2.165184 | POS518 | 1 | 0 | 985 | 362 | 1988 | Exploration |

| | | | | | | | | | | |
|---|---|---|---|---|---|---|---|---|---|---|
| **20** | 30/01f-8 | 56.954942 | 2.049750 | POS518 | 1 | 0 | 1027 | 183 | 1991 | Exploration |
| **21** | 20/10-2 | 57.668590 | -0.146838 | POS534 | 0 | 1040 | 1025 | 156 | 1976 | Appraisal |
| **22** | 20/10b-4 | 57.681923 | -0.145130 | POS534 | 0 | 810 | 879 | 124 | 1997 | Exploration |
| **23** | 20/15-1 | 57.560452 | -0.076122 | POS534 | 1 | 310 | 917 | 217 | 1985 | Exploration |
| **24** | 21/06-1 | 57.826023 | 0.108633 | POS534 | 1 | 35 | 882 | 247 | 1977 | Appraisal |
| **25** | 21/06-2 | 57.804332 | 0.000688 | POS534 | 1 | 0 | 907 | 224 | 1977 | Appraisal |
| **26** | 21/06a-3 | 57.778930 | 0.071013 | POS534 | 1 | 0 | 1086 | 330 | 1989 | Exploration |
| **27** | 21/06b-6 | 57.768707 | 0.052362 | POS534 | 0 | 620 | 651 | 219 | 2005 | Exploration |
| **28** | 21/08-2 | 57.750513 | 0.405838 | POS534 | 0 | 730 | 747 | 111 | 1987 | Exploration |
| **29** | 21/11-5 | 57.520818 | 0.005042 | POS534 | 1 | 330 | 668 | 177 | 1995 | Exploration |
| **30** | 21/12-1 | 57.559972 | 0.306242 | POS534 | 1 | 0 | 1313 | 270 | 1973 | Exploration |
| **31** | 21/12-2B | 57.646800 | 0.336925 | POS534 | 1 | 260 | 1175 | 141 | 1981 | Exploration |
| **32** | 21/12-4 | 57.514748 | 0.335738 | POS534 | 0 | 1000 | 1238 | 147 | 2001 | Exploration |
| **33** | 21/13a-3 | 57.544567 | 0.421852 | POS534 | 1 | 1000 | 1202 | 187 | 1990 | Appraisal |
| **34** | 21/13b-2 | 57.565747 | 0.585255 | POS534 | 0 | 1100 | 952 | 127 | 1983 | Exploration |
| **35** | 21/13b-4 | 57.500018 | 0.432610 | POS534 | 0 | 3300 | 1307 | 149 | 1992 | Exploration |
| **36** | 21/14b-3 | 57.539863 | 0.668117 | POS534 | 0 | 1800 | 1070 | 158 | 1986 | Exploration |
| **37** | 21/15b-5 | 57.659193 | 0.848283 | POS534 | 1 | 200 | 738 | 157 | 1985 | Exploration |
| **38** | 21/16-1 | 57.468655 | 0.148182 | POS534 | 0 | 500 | 696 | 98 | 1993 | Development |
| **39** | 21/16-4 | 57.416752 | 0.131247 | POS534 | 1 | 310 | 762 | 140 | 1995 | Appraisal |
| **40** | 21/16-A1 | 57.464052 | 0.158402 | POS534 | 1 | 180 | 651 | 165 | 1996 | Exploration |
| **41** | 21/17-4 | 57.462742 | 0.264408 | POS534 | 1 | 270 | 1417 | 190 | 1986 | Exploration |
| **42** | 21/17a-6 | 57.468530 | 0.307422 | POS534 | 0 | 2400 | 1482 | 168 | 2011 | Exploration |
| **43** | 21/19-1A | 57.481067 | 0.622222 | POS534 | 1 | 100 | 516 | 118 | 1980 | Appraisal |